Understanding the role of HACD enzymes and very long chain fatty acids in muscle development and disease

Thesis submitted in accordance with the requirements of the University of Liverpool for the degree of Doctor in Philosophy

By

Miss Rhiannon Morgan

May 2019

Abstract

3-hydroxyacyl-coA dehydratase (HACD) enzymes form part of a complex that elongates fatty acids with very long carbon chain length (VLCFA) (>20C). There are four paralogous HACD enzymes in mammals (encoded by *HACD1-4*), each with a distinct tissue distribution: HACD1 is specifically expressed in striated muscles and mutations in *HACD1* cause congenital myopathies in humans, dogs and mice. The canine autosomal recessive centronuclear myopathy, HACD1-CNM, is the most prevalent neuromuscular disorder in dogs with 15-20% of the Labrador retriever breed carrying the causative mutation. The pathogenesis of HACD1-associated myopathies and the roles of VLCFA in developing and mature muscle remain poorly understood. Membranous abnormalities, particularly affecting excitation-contraction coupling apparatus at the triad, are an important feature of CNMs due to other genetic causes and progressive t-tubule disorganisation has recently been documented in CNM affected dogs.

We hypothesised that HACD1-deficiency reduces levels of specific VLCFA and impacts upon normal triad structure and function. We further hypothesised that *hacd1*-mutant zebrafish embryos can be used to model HACD1-associated myopathies. I aimed to: characterise expression of HACD enzymes in developing and adult zebrafish, and also a murine myoblast cell line during normal myogenesis and HACD1-deficiency; establish techniques for studying the impact of HACD1-deficiency on the lipidome and excitation-contraction coupling in these models; validate a novel model of HACD1-deficiency in zebrafish embryos generated using CRISPR/Cas9 genome editing.

First I identified the zebrafish orthologues of mammalian HACD1-4 and evaluated their expression. The major findings confirmed *hacd1* as the major HACD enzyme in developing and mature zebrafish muscle with *hacd1-fl* strongly upregulated during myogenesis as seen in mammals. A murine *Hacd1*-knockdown model in C2C12 was used to investigate the effect of *Hacd1*-deficiency upon membrane systems and lipid profiles - *Hacd1* knockdown was significant in later stages of differentiation and no compensatory upregulation of *Hacd2-4* could be observed. Electrophysiological and NMR-lipidomic studies were established and optimised in this cell culture model and significant changes to the lipidome were detected in *Hacd1*-deficient myotubes in comparison with controls. NMR-lipidomics was then implemented on wildtype zebrafish embryos to establish their lipid phenotype. Finally, I characterised the phenotype and mutation spectrum in F_0 *hacd1*-mutant embryos and documented functional motor impairment alongside gross and microscopic muscle abnormalities including disorganisation of RYR1 staining – a marker of junctional sarcoplasmic reticulum. These findings recapitulate those in dogs with HACD1-CNM and zebrafish embryo models of CNMs due to other genetic causes.

In conclusion, embryonic zebrafish are a relevant model of HACD1-CNM due to their comparable HACD enzyme expression and myopathic phenotype in *hacd1*-mutant embryos. This will be a valuable asset and complement existing cell and mammalian models for future research to study the roles of HACD enzymes in muscle development and disease and the pathogenesis of HACD1 associated myopathies.

Acknowledgements

I have thoroughly enjoyed this whole experience, and for that I am indebted to a number of people. I would first like to thank the Institute of Ageing and Chronic Disease for funding this project.

To my supervisory team, thank you for all your support over the past few years. Dr. Gemma Walmsley, thank you for securing the funding for this project, for your unwavering guidance and support and for introducing me to the world of zebrafish! I feel lucky to have been a part of this research, thank you. Dr. Richard Barrett-Jolley, thank you for welcoming me into your group and for imparting a tiny fraction of your electrophysiology knowledge upon me. Prof. Mandy Peffers, thank you for your advice throughout this project and for all the thesis reading! From the NMR centre: Dr. Marie Phelan, thank you for your endless help regarding my lipidomic work, and for always finding the time.
Thank you to everyone in IACD who has helped me along the way, including the girls in the write up office and a special thank you to the RBJ lab group: thank you so much for helping me with all things patch-clamp. Clare and Niamh: for going through the whole process alongside me, and for being there for me when you were both dealing with your own PhD stress. Rachel, Caroline and Fiona, thank you for your help with lab work and analysis but mainly for our lunch breaks, the laughs… and sneaking me into the staff awards.

To all my friends outside of academia, thank you so much for being my cheerleaders, for being so understanding and for always being there. There are too many of you to name individually (which I am incredibly lucky for) but I would like to give a special thank you to Elin: you've checked in almost daily for the past few months, and for that I owe you a huge thank you… and a (lot of) prosecco!

My family (A.K.A proof reading team), Dad thank you for knowing before I did that I would gain so much from a PhD, Mum thank you for knowing I could do this even when I wasn't sure, and Kat (and Trev), thank you for keeping me smiling, for encouraging me to get outside and run off the stress and just generally being a wonderful sister.
Lastly, Alex: you have been my rock these past few years and I simply can't put into words how much your support means to me.

Contents

List of Figures

List of Figures in Appendices

List of Tables

Abbreviations

^{1}H-NMR	Proton nuclear magnetic resonance
AD	Autosomal dominant
ANOVA	Analysis of variance
AR	Autosomal recessive
ATP	Adenosine triphosphate
BIN1	Amphiphysin
BSA	Bovine serum albumin
Ca^{2+}	Ionic calcium
CE	Cholesteryl ester
cDNA	Complementary DNA
$CDCl_3$	Dueturated chloroform
$CHCl_3$	Chloroform
CICR	Calcium induced calcium response
Cl^-	Ionic chloride
CNM	Centronuclear myopathy
CNS	Central nervous system
CSQ	Calsequestrin
DAPI	4’,6-Diamidino-2-phenylindole
DEPC	Diethyl pyrocarbonate
DHPR	Dihydripyridine receptor
DIG	Digoxin
DMEM	Dulbecco’s modified eagles medium
DMSO	Dimethyl sulfoxide
DNA	Deoxyribonucleic acid
DNM2	Dynamin 2
DPD	Days post differentiation
DPF	Days post fertilisation
ECC	Excitation-contraction coupling
ER	Endoplasmic reticulum
FA	Fatty acid
FC	Free cholesterol
GPL	Glycerophospholipids
HACD	3-Hydroxyacyl-CoA dehydratase
HACD1-fl	HACD1 full length isoform
HPF	Hours post fertilisation
ICC	Immunocytochemistry
IHC	Immunohistochemistry
ISH	*In situ* hybridisation
JP	Junctophilin
K^+	Ionic potassium
KD	Knockdown
KO	Knockout
LCFA	Long chain fatty acid
LPC	Lysophosphatidylcholine

MHC	Myosin heavy chain
MS	Mass spectrometry
MUFA	Monounsaturated fatty acid
MND	Myonuclear domain
MRF	Myogenic regulatory factors
MTM1	Myotubularin
MTMR14	Myotubularin related protein 14
Na^+	Ionic Sodium
NMJ	Neuromuscular junction
NMR	Nuclear magnetic resonance
PBS	Phosphate buffered saline
PC	Phosphatidylcholine
PCA	Principal component analysis
PFA	Paraformaldehyde
PLS-DA	Partial least squares- discriminant analysis
PTPL	Protein tyrosine phosphatase like
PUFA	Polyunsaturated fatty acid
qRT-PCR	Quantitative reverse transcriptase-polymerase chain reaction
RMP	Resting membrane potential
RNA	Ribonucleic acid
RYR1	Ryanodine receptor 1
SERCA	Sarcoplasmic reticulum calcium ATPase
SFA	Saturated fatty acid
sh-RNA	Short hairpin RNA
SINE	Short interspersed nuclear element
SR	Sarcoplasmic reticulum
SSC	Saline-sodium citrate
T-tubule	Transverse tubule
TAG	Triacylglycerides
TALENs	Transcription activator-like effector nucleases
TRP	Transient receptor potential
TRPA	Transient receptor potential ankyrin
TRPC	Transient receptor potential canonical
TRPM	Transient receptor potential melastatin
TRPV	Transient receptor potential vanilloid
VLC	Very long chain
VLCFA	Very long chain fatty acid
WT	Wild type
XLMTM	X-linked myotubularin myopathy
ZFN	Zinc finger nucleases

1 Introduction

1.1. Overview of mammalian muscle development, anatomy and physiology

Movement is a key feature of all animals, which vertebrates achieve through the contraction of skeletal muscle fibres. Over a quarter of adult human body mass is accounted for by skeletal muscle which must provide functional strength, movement and flexibility. The highly structured, repetitive nature of the muscle cells and their intracellular architecture has been specifically adapted to allow the muscles to function efficiently (Keynes *et al*., 2011).

1.1.1. Muscle development

Skeletal muscle is a complex and highly specialised tissue which develops initially during embryogenesis via strict sequential expression of a number of transcription factors called myogenic regulatory factors (MRFs) during myogenesis (Figure 1.1) (Braun & Gautel, 2011; Buckingham, 1992).

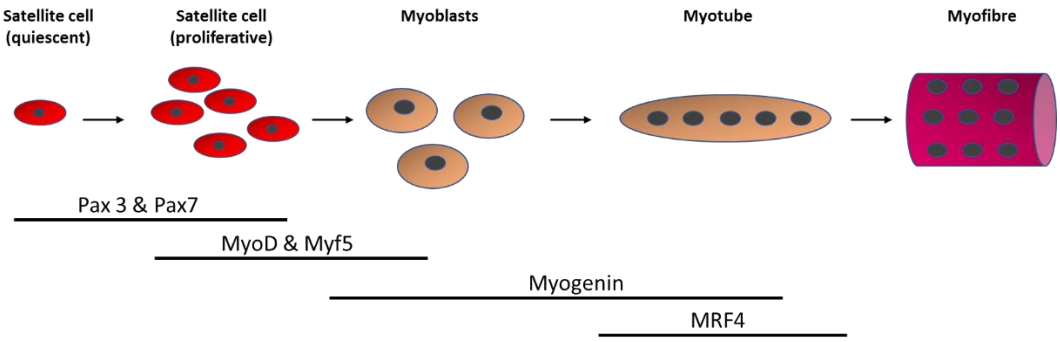

Figure 1.1: Schematic of mammalian (vertebrate) muscle differentiation.
Muscle progenitor cells, termed satellite cells, are triggered by transcription factors Pax3 and Pax7. The upregulation of other muscle transcription factors, MyoD, Myf5, Myogenin and MRF4 further induce these cells into mature myotube differentiation (Adapted from Tidball *et al*., 2014).

Myogenesis in mammals, and all vertebrates, can be divided into three parts – stages one and two occur during development (primary myotome formation and muscle growth respectively) and the third stage (adult myogenesis) is adapted for the repair of post-natal mature myofibres (Bryson-Richardson & Currie, 2008). The first stage begins in the mesoderm during gestation, more specifically the dermomyotome, from which the majority of the skeletal muscle forms through the alignment and fusion of early muscle cells, termed myoblasts. In phase two the myoblasts differentiate further on either side of the neural tube, which runs along the centre of the embryo during development in vertebrates (Bryson-Richardson & Currie, 2008). This

stage produces the mature musculature of the organism (Braun & Gautel, 2011). Transcription factors Pax3 and Pax7 are critical in this stage of early development to induce stem cell populations down a myogenic lineage (determination) (Kassar-Duchossoy *et al*., 2005). Subsequently other MRFs including MyoD, myogenin, Myf5, MRF4 are expressed – all of which are important for the differentiation and maturation of skeletal muscle (Bentzinger *et al*., 2012; Kassar-Duchossoy *et al*., 2005). During embryogenesis muscle mass originates from myoblast proliferation, and once developed, muscle is a terminally differentiated tissue. Postnatal growth occurs mostly through hypertrophy (increase of protein content), therefore increasing the size of fibres already present (Alnaqeeb & Goldspink, 1986). Muscle fibre number reaches its maximum shortly after birth and thereafter remains mostly unchanged. Increase in fibre size and increased myofibril number are the mechanisms by which the contractile force of a muscle is increased. (Alnaqeeb & Goldspink, 1986).

The third stage of myogenesis is designed to repair damaged mature muscle by the muscle specific stem-cells; satellite cells (Bryson-Richardson & Currie, 2008). Satellite cells are found on the surface of muscle fibres and once activated work to generate new myoblasts that will differentiate into myotubes and produce new myonuclei for the fibres (Zammit, 2008). Pax7 is activated with the satellite cells and has been reported to be important in driving the differentiation of satellite cells (Zammit *et al*., 2006). The post mitotic nature of skeletal muscle fibres, means the capability of muscle to repair itself is limited; therefore, the satellite cells provide regenerative assistance through the fusing of newly differentiated myotubes into the myofibres to aid in muscle repair (Conceição *et al*., 2018; Shenkman *et al*., 2009; Zammit, 2008).

Vertebrate muscle can be divided into five sub-types: trunk, limb, branchial, oral (tongue and laryngeal) and extraocular. These sub-types require different combinations of MRF regulation for development but commonly all require MyoD and myogenin (Braun & Gautel, 2011). The differences in the network of regulatory genes within development provides a level of heterogeneity to muscles developed within an organism (Braun & Gautel, 2011).

1.1.2. Muscle anatomy

Skeletal muscle is composed of many elongated intracellular, contractile myofibrils, together within a single muscle fibre (Figure 1.2). Myofibres are bound together by connective tissue into a muscle bundle and several of these together form a muscle. Mature muscle fibres can be as long as the muscle itself and are between 10-100µm in diameter (Braun & Gautel, 2011; Ehler & Gautel 2008; Keynes *et al*., 2011). Skeletal muscle myofibres are complete contractile systems that are under the control of motor neurons and carry out a variety of motor functions

within an organism from finer motions of facial expressions and the larynx during vocalisation to gross movements such as running or lifting weights (Fregosi & Ludlow, 2013; Keynes *et al*., 2011).

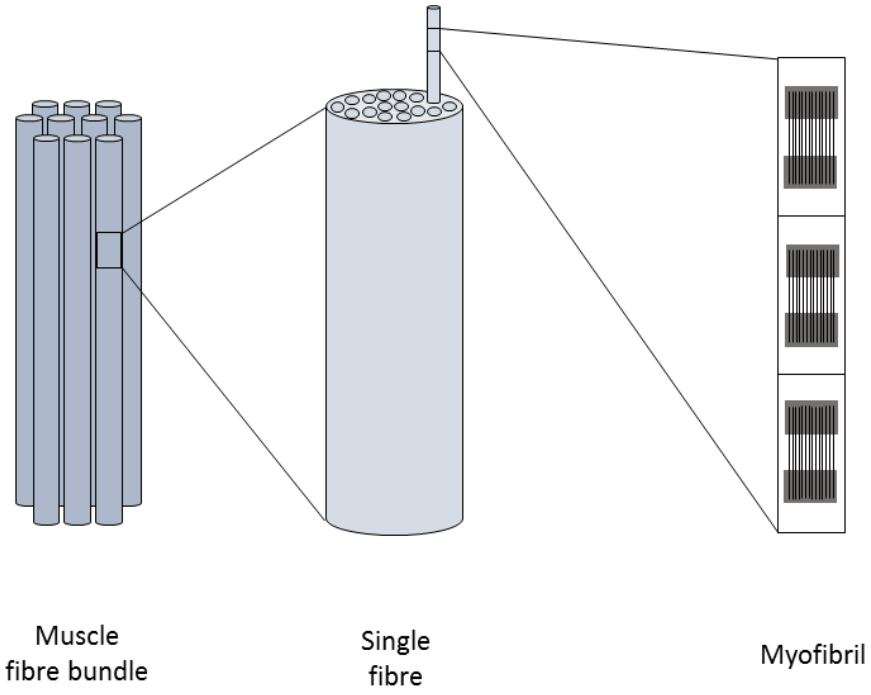

Figure 1.2: Structure of skeletal muscle (Redrawn from Keynes *et al*., 2011).

1.1.2.1. Myofibre types

Mammalian skeletal muscle is comprised of broadly two types of fibre: slow twitch (type I) and fast twitch (type II) (Blaauw *et al*., 2013; Schiaffino & Reggiani, 2011; Scott *et al*., 2001). The presence of different fibre types provides more heterogeneity, allowing one muscle to perform different tasks effectively according to varying functional demands (Schiaffino & Reggiani, 2011). Muscle fibre types are categorised by their metabolism and contractile response: type I fibres are commonly known as oxidative slow twitch fibres, and they are high in myoglobin giving them a red coloured appearance (Schiaffino & Reggiani, 2011). Type I fibres are adapted for endurance: they have a longer duration contraction and fatigue slowly. Conversely; type II fibres do not require oxygen for energy and so do not have the rich blood supply that type I fibres have. Type II fibres are specialised for quick and powerful contraction and fatigue quickly. (Essén *et al*., 1975; Schiaffino & Reggiani, 2011). Proportions of myofibre types varies between different muscles: those required for fast movement, such as those in the leg, are predominantly type II whereas other muscles such as those located around the spine for posture are predominantly type I myofibres (Schiaffino & Reggiani, 2011).

Proportional changes in the types of myofibres within a muscle have been documented as a secondary pathology in a number of congenital myopathies including nemaline myopathy, central core myopathy, congenital fibre-type disproportion and centronuclear myopathy (North & Clarke, 2003; Clarke, 2011; North *et al*., 2014).

1.1.2.2. Myonuclei

Myofibres are unique in their nuclear architecture and a single muscle fibre can contain hundreds of nuclei due to a high number of myoblasts fusing to form the myofibre (Roman & Gomes, 2018). The myonuclei within mammals are uniquely located at the periphery of the myofibres, to provide maximum room for the contractile apparatus (Cadot *et al*., 2015). The nuclei are located evenly across the periphery, and the finite volume of cytoplasm they control through the transport of gene products and protein synthesis, is termed the myonuclear domain (MND) (Allen *et al*., 1999). Microtubules from nuclear envelopes act mechanically on neighbouring nuclei and cell boundaries to provide this even distribution of myonuclei along the myofibre (Manhart *et al*., 2018). This nuclear positioning is mediated by a number of proteins including Map7, nesprins and amphisphysin-2: of which the latter is also involved in triad organisation (Falcone *et al*., 2014). The elongated shape of myofibres provides reason for their requirement of multiple, precisely spaced nuclei - it is thought that clusters of myonuclei would leave areas of the myofibre without the appropriate transcription and translation to maintain a healthy myofibre (Pavlath *et al*., 1989; Ross *et al*., 2008).

This peripheral positioning of nuclei is an important and well-established feature of mammalian muscle cells and their displacement to the centre of fibres correlates with muscle dysfunction and has been documented in a number of myopathies (Folker & Baylies, 2013). It is unknown whether nuclear centralisation is a primary or secondary factor of muscle disease and is likely to depend greatly upon disease aetiology. Centralised nuclei are also seen in regenerating fibres, suggesting that the centralised nuclei in certain diseased fibres may be due to attempted repair of damaged fibres and therefore secondary to the disease pathology (Folker & Baylies, 2013; Roman & Gomes, 2018; Shenkman *et al*., 2009).

1.1.2.3. Sarcomeres

The contractile unit; the sarcomere, is approximately 2µm in length, and up to 250 sarcomeres may be found per mm of muscle fibre (Infantolino *et al*., 2010). Sarcomeres consist of two main proteins: the ‘thin’ actin and ‘thick’ myosin filaments of approximately 5nm and 11nm diameter respectively, which lie repetitively side by side against one another (Keynes *et al*., 2011). Interaction between these two filaments allow skeletal muscle fibres to contract and generate force (Keynes *et al*., 2011). Myofibres have a distinct and recognisable striated

appearance derived from the highly organised layout of the actin and myosin within the sarcomeres (Figure 1.3) and these are one of the most consistent structures within animal cells (Ehler & Gautel, 2008).

The repetitive patterning of the sarcomere is described by the bands and lines that the actin and myosin form together (Huxley & Hanson, 1954). The A band of the sarcomere appears darker using electron microscopy due to the presence of both thick myosin and thin actin filaments located there. In comparison, the I band of just actin filaments appears significantly lighter. The H band lies within the A band in an area of just the myosin filaments, and is bisected down the middle of the sarcomere by the M line which represents the cross links of myosin filaments. The actin filaments are attached by the Z line which is found in the middle of the I band (Huxley & Hanson, 1954).

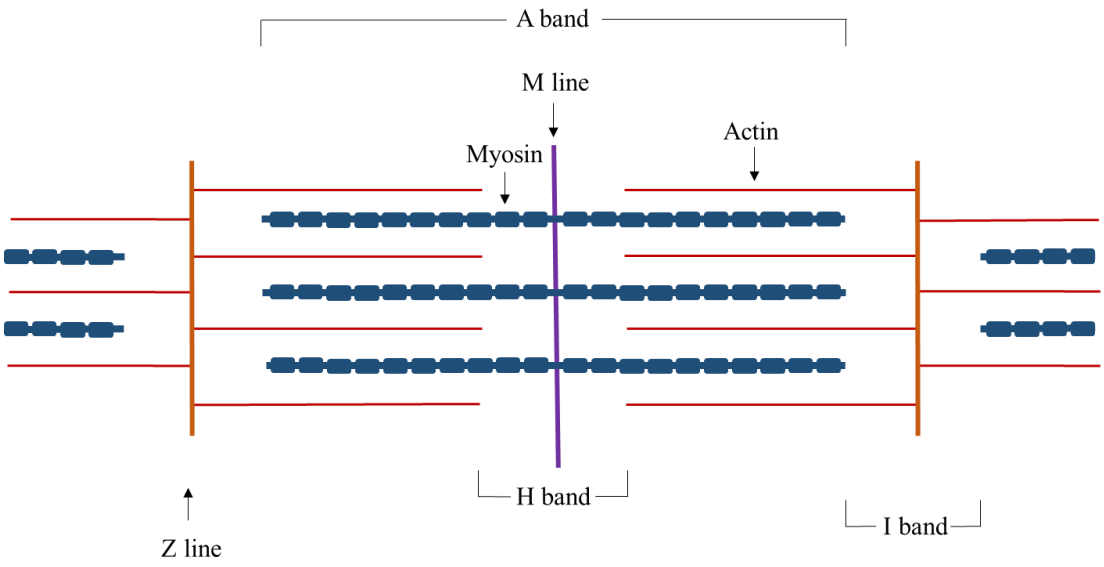

Figure 1.3: Diagram of the mammalian sarcomere.

1.1.3. Muscle contraction

Muscle contracts according to Huxley's sliding filament theory which explains shortening of the sarcomeres and hence the overall length of the muscle. Huxley & Hanson, (1954) and Huxley & Niedergerke, (1954) first observed that while one section of the sarcomere, the A band, remained consistent throughout contraction, the other notable section, the I band, changed in length (Huxley & Hanson, 1954; Huxley & Niedergerke, 1954). From this they concluded that the actin filaments were "sliding" past filaments of myosin. This mechanism occurs through the formation of cross bridges between the actin filament and myosin heads, pulling along and shortening the sarcomere and therefore causing muscle fibre contraction (Huxley & Hanson, 1954; Huxley & Niedergerke, 1954).

As well as myosin and actin there are a number of other important proteins involved in regulating muscle contraction including the protein complex troponin-tropomyosin that inhibits direct interaction between actin filaments and myosin heads at rest (Bailey, 1946). Tropomyosin is distributed along the myosin filaments and mediates the effect of calcium on actin-troponin binding (Bailey, 1948); troponin is bound to both tropomyosin and the actin filament and it is thought the binding of calcium ions (Ca^{2+}) molecules causes a structural change in troponin which draws the tropomyosin away from the binding sites allowing myosin-actin cross bridges to form (Ebashi & Kodama, 1965; Keynes *et al*., 2011).

ATP is essential for the contraction of skeletal muscle and adequate levels are maintained in muscle (Cooke, 1986; Widen & Barclay, 2006). The conversion of electrical stimulus into contractile response from the muscle is termed excitation-contraction coupling (ECC), and once this is initiated, Ca^{2+} is released from internal stores and binds troponin allowing actin and myosin to interact and utilise the ATP already present (Sandow, 1952). Conversely; with calcium present but ATP absent, actin and myosin can bind but there is no energy for movement, as seen in rigor mortis (Bate-Smith & Bendall, 1947). Hydrolysis of ATP provides the energy for cross-bridge cycling and contraction and occurs at the rate of one ATP per cycle - this repeats along the filaments during contraction. (Widen & Barclay, 2006).

1.1.3.1. Excitation-contraction coupling (ECC)

Excitation-contraction coupling is the work of the entire motor unit: a single motor unit describes a motor neuron providing stimulation to a bundle of myofibres, of which hundreds can be found within a muscle (Celichowski, 2000), a schematic of ECC is shown in Figure 1.4. The motor neuron provides an electrical signal that is received by the muscle at the neuromuscular junction (NMJ), a chemical synapse (Hall & Sanes, 1993). Depolarisation of the pre-synaptic nerve terminus results in Ca^{2+} influx, vesicle binding and release of acetylcholine which diffuses across the synaptic crest to post-synaptic receptors on the muscle endplate. This causes ligand-gated ion channels in the muscle cell membrane, the sarcolemma, to open and allow the influx of sodium ions (Na^{+}) into the fibre (Hall & Sanes, 1993). The influx of positive ions into the cell depolarises the sarcolemma and triggers a muscle action potential. The action potential then propagates over the entire surface of the muscle fibre (Barnett & Larkman, 2007; Hall & Sanes, 1993) and into the fibre via sarcolemmal membrane invaginations known as transverse (t)-tubules. The positive increase in sarcolemmal charge (membrane potential) activates the voltage-sensitive calcium channel, the dihydropyridine receptor (DHPR), also known as $Ca_v1.1$, to open and allow Ca^{2+} influx (Corry, 2006; Hall & Sanes, 1993). The DHPR channels are in allosteric contact with another type of calcium channel found on the sarcoplasmic reticulum (SR) (muscle specific endoplasmic reticulum

and calcium store), the ryanodine receptor 1 (RYR1) and the physical interaction and conformational coupling between these two Ca^{2+} channels is crucial to the control of ECC (Paolini *et al*., 2004). DHPR and RYR1 bind via the DHPR cytoplasmic β_{1a} subunit and the RYR1 α_{1s} subunit (deletion of either of these subunits prevents ECC, DHPR subunit loss has been reported in β_{1a}-null murine and zebrafish models) (Rebbeck, 2011; Karunasekara *et al.*, 2012) and the positioning of these channels permits bidirectional interactions (Lanner *et al*., 2010). The final step of ECC is the Ca^{2+} release from the SR. Here the RYR1 channels are opened in response to a structural change in DHPR (Hernandez-Ochoa & Schneider, 2018). Local cytosolic calcium concentrations often increase by 100-fold during this process and result in muscle contraction by allowing myosin and actin to interact (Corry, 2006; Dulhunty, 2006; Smith, 2007).

The ECC machinery is similar between skeletal, smooth and cardiac muscle however the mechanism by which the cytosolic calcium is increased differs. In smooth and cardiac muscle calcium induced calcium release (CICR) via the influx of Ca^{2+} ions is the mechanism by which ECC is conducted. In skeletal muscle the RYR1 channel does not rely upon the influx of external calcium, due its large store of intracellular calcium within the SR (~1mM Ca^{2+} within the SR lumen at rest with cytosolic Ca^{2+} ~50nM) (Dulhunty, 2006; Rossi, 2008; Berchtold *et al*., 2000) and it is well established that RYR1 is activated during ECC by a structural change in DHPR (Dayal *et al*., 2017). This is corroborated by the speed of ECC, as it requires a rapid response and chemical messengers are simply not quick enough (Hernandez-Ochoa & Schneider, 2018).

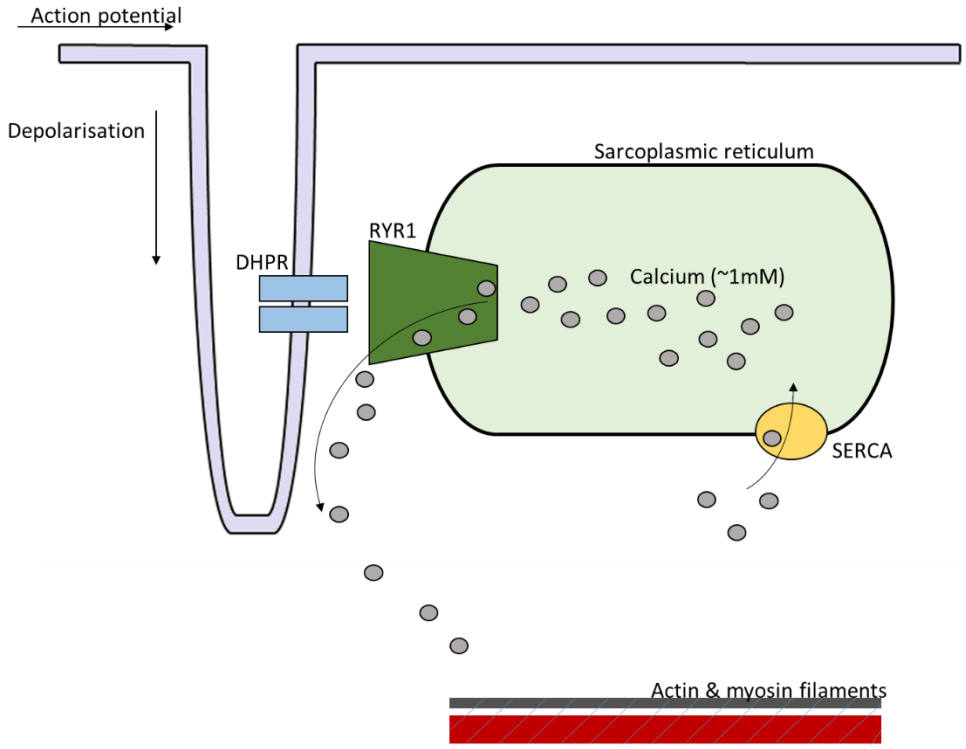

Figure 1.4: Schematic demonstrating the basis of excitation-contraction coupling (ECC) and its machinery.
RYR1 = ryanodine receptor 1, DHPR = dihydropyridine receptor, SERCA = sarcoplasmic reticulum calcium-ATPase.

1.1.3.2. Triads

Excitation-contraction coupling in mammals is reliant upon communication between two highly specialised membrane domains and their aforementioned ion channels: invaginations of the sarcolemma called the t-tubules where the DHPR localise and the SR with their RYR1 channels (Franzini-Armstrong & Jorgensen, 1994). Two SR termini and one t-tubule meet at the A-I band junction of the sarcomere in mammals, and this set of membranes is called the triad (Rossi, 2008). Development of the mammalian triad begins in a disorganised manner during gestation before becoming strict in organisation providing the most efficient layout of membrane systems for ECC. SR membranes appear early on in development and in a regular manner and t-tubules are for the most part formed postnatally. In mice this organisation happens early in life (3-4 weeks) (Franzini-Armstrong & Jorgensen, 1991; Flucher *et al*., 1993; Takeshima *et al*., 1994).

The t-tubule membrane system accounts for 80% of plasma membrane surface in skeletal muscle; and it functions to rapidly conduct the electrical signal from the sarcolemma to arrive close to the SR. Without the specialised t-tubule membrane system the surface action potential would be insufficient to activate contraction (Barrientos *et al*., 2017; Bers, 2014; Keynes *et*

al., 2011). The DHPR channels found along the t-tubules are L-type Ca^{2+} channels, which refers to its high-voltage activation and the length of which activation lasts a "L=long" time (Denniss *et al*., 2018; Hernandez-Ochoa & Schneider, 2018).

The primary role of the SR is to store and regulate calcium homeostasis including the release of intracellular calcium into the cytosol during ECC via the RYR1 channel (Bers, 2014). RYRs are homotetrameric proteins weighing over two million Daltons, of which there are three isoforms that are found in numerous cell types including striated (skeletal and cardiac) and smooth muscle, testis, neurons and ovaries (Hamilton, 2005). RYR1 is specific to striated muscle with low levels found within cardiac and smooth muscle, RYR2 is expressed within cardiac muscle predominantly and RYR3 is expressed within the brain at high levels (Lanner *et al*., 2010). As part of its role in calcium homeostasis, the SR also communicates back to the DHPR via the release of Ca^{2+} in order to regulate the calcium influx through the DHPR (Paolini *et al*., 2004; Balog & Gallant, 1999). Calcium reuptake back into the SR is also imperative to regulate ECC and control the rate of muscle relaxation following contraction (Rossi & Dirksen, 2006). The sarcoplasmic reticulum Ca^{2+}-ATPase (SERCA) pump is efficient at returning this calcium back into the SR (Rossi & Dirksen, 2006).

Calcium homeostasis within the SR also depends upon a number of calcium binding proteins within the SR lumen, including calsequestrin (CSQ), which makes up ~27% of junctional SR protein (Beard, 2005). CSQ is important for calcium homeostasis within muscle fibres, it binds calcium within the SR, keeps cytoplasmic levels of Ca^{2+} low when at rest and has a role in calcium sensing within the lumen of the SR (Beard, 2005; Berchtold *et al*., 2000).

The formation of the triad requires a number of proteins that assist in coordinating this process. Junctophilins and triadins (transmembrane proteins expressed in excitable cells) are examples of the proteins critical for this, and therefore essential for ECC to function. By spanning both t-tubule and SR membranes junctophilins aid in triad formation, and indirectly assist with conversion of the cell membrane depolarisation into the intracellular Ca^{2+} signalling (Ito *et al*., 2001). Knock out of the junctophilin-1 gene (*JP-1*) in mice leads to the formation of diads instead of triads (Ito *et al*., 2001; Komazaki *et al*., 2001; Osseni *et al*., 2016). STAC3, another important protein for ECC, has been reported to be involved in linking the two calcium channels (Campiglio *et al*., 2018; Polster *et al*., 2018). It has been reported that *STAC3* knockout mice have defective ECC and that the activation of RYR1 relies on STAC3 being bound correctly (Cong *et al*., 2016; Polster *et al*., 2018).

1.2. Muscle membrane systems and disease

The organisation of the highly specialised muscle membranes is imperative for muscle to function normally and in healthy muscle ECC is extremely robust, but many diseases are now known to result from mutations that lead to abnormalities in the ECC machinery (Jungbluth *et al*., 2018). This is an important pathogenic mechanism in congenital myopathies which leads to muscle dysfunction with little to no contractile force and often presents as progressive muscle weakness and therefore ultimately paresis (Allard, 2018). These ECC abnormalities can occur through a number of mechanisms: mutation of proteins within the Ca^{2+} release, alteration in triad structure, alterations in ion channels, abnormalities within calcium store (Marty & Fauré, 2016).

1.2.1. Congenital myopathies

Congenital myopathies are a heterogeneous group of neuromuscular disorders that are grouped broadly based on their pathological features (North, 2008). Defining features of the congenital myopathies include: abnormal morphology of muscle tissues when examined histopathologically, abnormalities from within the myofibres (compared to dystrophies where pathology stems from the sarcolemma and extracellular matrices), and early onset clinical weakness and hypotonia that may be progressive (Cassandrini *et al*., 2017; North, 2008).

1.2.1.1. Histopathology of the congenital myopathies

The congenital myopathies have been subcategorised into five major forms: nemaline myopathies, core myopathies, centronuclear myopathies, myosin storage myopathies and congenital fibre-type disproportions (North *et al*., 2014). Histopathology of these congenital myopathies is shown in Figure 1.5 and pathology of muscle biopsies has classically been used for diagnostics of the congenital myopathies (Goebel, 2003).

Nemaline myopathy is characterised by rod-like inclusions within myofibres consisting of alpha-actinin (Wallgren-Petterron & Laing, 1999). Core myopathies are categorised due to the presence of circular structures, lacking both mitochondria and glycogen, seen within myofibres, “cores” and these can be present in multiples within one fibre (termed multi-minicores diseases) (Cassandrini *et al*., 2017; Engel *et al*., 1971). Centronuclear myopathy is characterised by the presence of mislocalised and internalised myonuclei within the centre of myofibres (Spiro *et al*., 1966). Myosin storage myopathies lead to an accumulation of myosin heavy chain inclusions within fibres (Tajsharghi *et al*., 2003). The final category of congenital myopathies, congenital fibre-type disproportion is described by

type I fibres which are consistently smaller than the type II fibres and predominate within the muscle (Clarke, 2011).

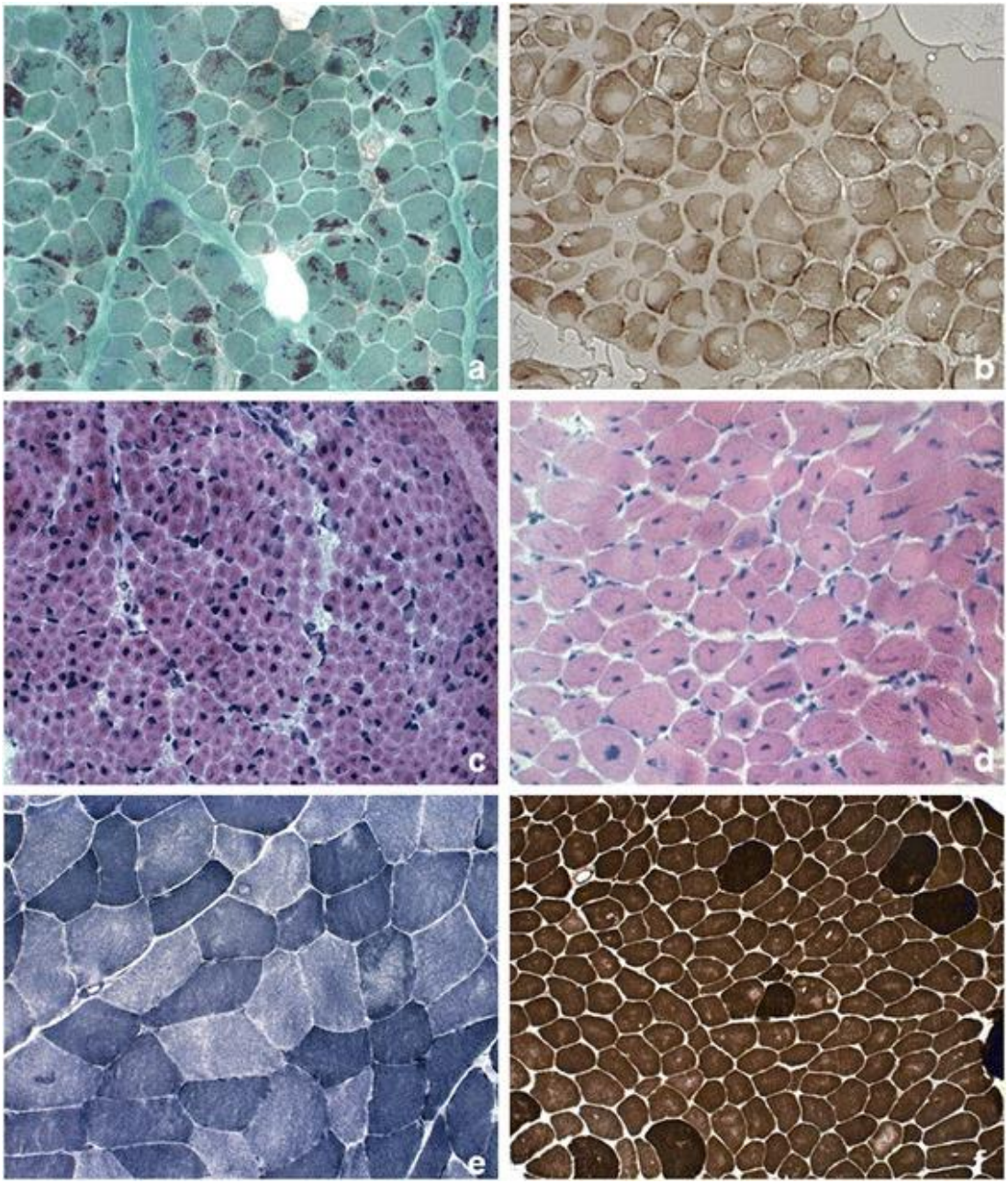

Figure 1.5: Histology of the congenital myopathies.
(a) (nemaline myopathy) Gomori trichrome stain of alpha-actinin rods within myofibres (purple) seen both at the periphery or centre. (b) (core myopathy) Cytochrome C oxidase stain highlighting the "cores" within fibres by lack of stain. (c and d) (Centronuclear myopathy (CNM)) H&E (haemotoxylin and eosin) stain showing nuclei in purple which a large proportion have migrated from the periphery of fibres into the centre. (c) CNM patient with a myotubularin mutation and (d) from a CNM patient with a dynamin2 mutation. (e) (multi-minicores myopathy) NADH-TR stain indicates areas with no oxidative stain, indicative of the cores. (f) (Congenital fibre-type disproportion) ATPase stain indicating the lighter stained type I fibres to be smaller in size and the predominating fibre within the muscle sample. (Figure taken from Cassandrini *et al*., 2017).

1.2.1.2. Genetics of congenial myopathies

The histopathology of muscle biopsies from myopathy patients provides initial insight for patient diagnosis, however the genetic and phenotypic heterogeneity of congenital myopathies means that it cannot be used alone in order to successfully diagnose patients (Bohm *et al*., 2013). Table 1.1 displays a recent cataloguing of the congenital myopathies and their associated genes; the table highlights the heterogeneity within the myopathies (Jungbluth *et al*., 2018). Performing mutation analysis is crucial in the diagnosis of patients due to the vast number of genes associated with disorders which greatly overlap in phenotype: it can provide a greater clarity (Goebel, 2003; Bohm *et al*., 2013).

Table 1.1: Genes associated with human congenital myopathies, adapted from Jungbluth *et al*., 2018.

(Bitoun *et al*., 2005; Coste *et al*., 2013; Jungbluth *et al*., 2018; McMillin *et al*., 2013; O'Grady *et al*., 2016; Schnartner *et al*., 2017; Zhou *et al*., 2007).

Gene symbol	Protein	Condition
ECC, SR Ca^{2+} release or triad assembly		
RYR1	Ryanodine receptor 1	Central core disease, Multi-minicores disease, Centronuclear myopathy, Congenital fibre-type disproportion, King–Denborough syndrome
STAC3	SH3 and cysteine-rich domain-containing protein 3	North American myopathy
ORAI1	Ca^{2+}-release-activated Ca^{2+} channel protein 1	Tubular aggregate myopathy
STIM1	Stromal interaction molecule 1	Tubular aggregate myopathy, Stormorken syndrome
MTM1	Myotubularin	X-linked myotubular myopathy
BIN1	Amphiphysin II	Centronuclear myopathy
DNM2	Dynamin 2	Centronuclear myopathy
SPEG2	Striated muscle preferentially expressed protein kinase	Centronuclear myopathy with central nuclei and cardiomyopathy
CCDC78	Coiled-coil domain-containing protein 78	Centronuclear myopathy with cores and central nuclei
CACNA1S/DHPR	Voltage-dependent L-type Ca^{2+} channel subunit-α1S	Centronuclear myopathy with extraocular muscle involvement
SEPN1	Selenoprotein N	Multi-minicores disease, Congenital fibre-type disproportion
Thin-thick filament assembly and/or interaction, myofibrillar force generation and protein turnover		
NEB	Nebulin	Nemaline myopathy
ACTA1	Actin, α-skeletal muscle	Nemaline myopathy, Cap myopathy, Congenital fibre-type disproportion
TNNT1	Troponin T, slow skeletal muscle	Nemaline myopathy
TPM2	Tropomyosin β-chain	Nemaline myopathy, Cap myopathy, Escobar syndrome, Distal arthrogryposis
TPM3	Tropomyosin α3-chain	Nemaline myopathy, Cap myopathy, Congenital fibre-type disproportion

MYH2	Myosin 2	Centronuclear myopathy with extraocular muscle involvement
MYH3	Myosin 3	Distal arthrogryposis
MYH7	Myosin 7	Congenital fibre-type disproportion, Multi-minicores disease, Myosin storage myopathy
MYH8	Myosin 8	Trismus-pseudocamptodactyl syndrome, Carney complex
KBTBD13	Kelch repeat and BTB domain-containing protein 13	Nemaline myopathy with cores
KLHL40	Kelch-like protein 40	Nemaline myopathy
KLHL41	Kelch-like protein 41	Nemaline myopathy
LMOD3	Leiomodin 3	Nemaline myopathy
MYBPC3	Myosin binding protein C, cardiac-type	Congenital myopathy with cardiomyopathy
MYPN	Myopalladin	Nemaline myopathy with cardiomyopathy
TTN	Titin	Centronuclear myopathy, Multi-minicores disease
Other cellular processes		
CFL	Cofilin 2	Nemaline myopathy with cores
CNTN1	Contactin 1	Congenital myopathy (lethal)
ECEL1	Endothelin-converting enzyme-like 1	Distal arthrogryposis
PIEZO2	Piezo-type mechanosensitive ion channel component 2	Distal arthrogryposis, Marden-Walker syndrome
MEGF10	Multiple epidermal growth factor-like domains protein 10	Congenital myopathy with minicores, Congenital myopathy with areflexia, respiratory distress and dysphagia
HACD1	3-hydroxyacyl-CoA dehydratase 1	Congenital myopathy
SCN4A	Sodium channel, protein type 4 subunit-α	Congenital myopathy
TRIM32	E3 ubiquitin–protein ligase TRIM32	Sarcotubular myopathy
PYROXD1	Pyridine nucleotidedisulfide oxidoreductase domain-containing protein 1	Congenital myopathy

The RYR1-associated congenital myopathies provide a strong example of the variability of disease phenotypes even within the dysfunction of one protein (Todd *et al*., 2018). *RYR1* mutations contribute to a number of congenital myopathies including CNM, central core disease, malignant hypothermia, multi-minicore disease (Avila *et al*., 2001; Bevilacqua *et al*., 2011; Jungbluth *et al*., 2018; Zhang *et al*., 1993). Todd *et al*., (2018) reported six novel variants of *RYR1*, of which had previously been documented in numerous other cases of congenital myopathy (Jungbluth *et al*., 2018; Todd *et al*., 2018).

Other important ECC proteins have been linked to musculoskeletal disorders including caveolin-3 (*CAV3*) and amphiphysin-2 (*BIN1*) which are both involved in t-tubule biogenesis (Nicot *et al*., 2007; Sotgia *et al*., 2003). Junctophilin-2 mutations have been linked to cardiomyopathies and Charcot-Marie-Tooth disorder due to perturbed calcium handling (Takeshima *et al*., 2000).

Mutations in the CNM causing gene, *HACD1*, have shown to cause tubuloreticular membrane abnormalities in Labrador retrievers (Walmsley *et al*., 2017). HACD1-CNM is discussed in more detail in Section 1.3.1.

1.2.2. Centronuclear myopathies

The centronuclear myopathies are a subset of congenital myopathy that are characterised by the mislocalisation of nuclei to the centre of >25% myofibres with no signs of regeneration, infiltration of fat into muscle tissue, a shift in fibre type proportions and inconsistency in myofibre size among other features (Spiro *et al*., 1966). The centralised nuclei in the CNMs are distinct to those found in dystrophies – in the latter, centralised nuclei are present within regenerating fibres (Dowling *et al*., 2009). Clinically, CNM patients have progressive weakness and hypotonia but may also present with breathing troubles or difficulty moving the eyes in severe cases (Jungbluth *et al*., 2008).

Mutations in myotubularin, the lipid phosphatase, cause the severe X-linked form of CNM, termed myotubular myopathy (XLMTM) (Laporte *et al*., 1996). Biopsies of affected individuals show hypertrophy and a significant number of fibres with the characteristic centralised nuclei (Laporte *et al*., 1996; Pierson *et al*., 2005). Over half the XLMTM mutations inactivate the enzyme by missense mutations or protein truncation. XLMTM mice develop a progressive myopathy from around 4 weeks of age and their lifespan is severely reduced (Buj-Bello *et al*., 2002; Laporte *et al*., 1997). Mutations in a myotubularin related protein (*MTMR14*) also cause an autosomal recessive form of CNM (Tosch *et al*., 2006). Both *MTM1* and *MTMR14* deficiencies result in defective ECC, decreased triad number and abnormally

formed t-tubules (Al-Qusairi *et al*., 2009; Buj-Bello *et al*., 2002; Dowling *et al*., 2009). Myotubularin expression increases postnatally, after the development of the t-tubules, hence it has been suggested that myotubularin is essential for the maintenance and maturation of t-tubules (Al-Qusairi & Laporte, 2011).

An autosomal-dominant form of CNM is caused by mutations in the gene for dynamin 2 (*DNM2*) which is involved in membrane trafficking (Bitoun *et al*., 2005). DNM2 localises to the I band of the sarcomere and perinuclear areas of the myofibre – areas of high levels of membrane trafficking (Durieux *et al*., 2010). Heterozygous *DNM2* mutations have a large spectrum of severity and differ in their onset, from neonatal to childhood and DNM2-CNM presents with muscle weakness and delayed motor milestones (Bitoun *et al*., 2005; Bitoun *et al*., 2007; Jungbluth *et al*., 2010). Histologically, the nuclei mislocalise to the centre of fibres and slow type fibres predominate. Introducing a *DNM2* mutation into mice resulted in altered mitochondrial staining as well as nuclear mislocalisation (Cowling *et al*., 2011; Durieux *et al*., 2010; Jungbluth *et al*., 2008).

Mutations in amphiphysin (*BIN1*), which is involved in membrane sensing and remodelling within cells causes an autosomal recessive CNM with triad disorganisation (Nicot *et al*., 2007; Toussaint *et al*., 2011). BIN1 is involved in the tubulation of membranes due to its membrane bending functions (Al-Qusairi & Laporte, 2011). The *BIN1* gene is expressed highly within skeletal muscle and expression increases over the differentiation of the myogenic cell line, C2C12, in line with the development of internal membranes (Al-Qusairi & Laporte, 2011; Lee *et al*., 2002). The mechanism by which BIN1 deficiency causes CNM is likely to be the lack of proper t-tubule formation within the myofibres. This suggests that BIN1 is crucial to the development of the t-tubules at an earlier developmental stage than that of myotubularin. It has been hypothesised that both BIN1 and DNM2 proteins may need to functionally interact for normal nuclei positioning and muscle function therefore linking two of the CNM disease proteins (Cowling *et al*., 2017; Nicot *et al*., 2007).

A dominant mutation in the calcium channel gene *RYR1* causes CNM with a broad spectrum of phenotypes including disturbed DHPR function and significantly disrupting ECC (Jungbluth *et al*., 2007).

The genes discussed above, in particular MTM1, DNM2 and BIN1 are those classically associated with CNM. Recently, other mutations have been associated with this phenotype (see Table 1.2). The large contractile protein, titin, has also been associated with CNM, as titin mutations were seen in five patients with CNM-like clinical pathology (Ceyhan-Birsoy *et al*.,

2013). A mutation in *CCDC78*, a gene of unknown function, has also been found to be associated with CNM, and when modelled in zebrafish the characteristics mirror the human CNM pathology, (see Table 1.2) (Majczenko *et al*., 2012).

Most if not all affected proteins fit into the membrane remodelling/ECC pathways, and in particular they are primarily involved with the formation and organisation of triads (Cowling *et al*., 2012).

Table 1.2: Centronuclear myopathies including congenital myopathies with central nuclei.
AR = autosomal recessive, AD = autosomal dominant. (Jungbluth *et al*., 2018; Schnartner *et al*., 2017).

Gene symbol	Protein	Type	Inheritance
RYR1	Ryanodine receptor	CNM	AR
MTM1	Myotubularin	X-linked myotubular myopathy	X-linked
BIN1	Amphiphysin II	CNM	AR, AD
DNM2	Dynamin 2	CNM	AD
TTN	Titin	CNM	AR
HACD1	3-hydroxyacyl-CoA dehydratase 1	Canine CNM and poorly defined congenital myopathy in humans	AR
CCDC78	Coiled-coil domain-containing protein 78	Congenital myopathy with cores and central nuclei	AD
SPEG	Striated muscle preferentially expressed protein kinase	Congenital myopathy with central nuclei and cardiomyopathy	AR
DHPR	Dihydropyridine receptor	Congenital myopathy with central nuclei	AR, AD

1.3. HACD1 mutations and congenital myopathies

Mutations in 3-hydroxyacyl-coA dehydratase 1 (HACD1) (previously PTPLA based on presence of a putative phosphatase-like domain (protein tyrosine phosphatase; proline instead of catalytic arginine) which lacks activity due to amino acid change in the active site) (Li *et al*., 2000; Uwanogho *et al*., 1999) also cause congenital myopathies in dogs, humans and mice (Blondelle *et al*., 2015; Maurer *et al*., 2012; Muhammed *et al*., 2013; Pelé *et al*., 2005; Toscano *et al*., 2017). HACD1, alongside other HACD and elongase enzymes functions in the biosynthesis of very long chain fatty acids (VLCFAs) (Ikeda *et al*., 2008).

1.3.1. Canine centronuclear myopathy and HACD1

The clinical condition now known as canine CNM was first described by Kramer *et al*., (1976) - but its nature as a centronuclear myopathy was only described by Tiret *et al*., (2003).

Labrador retrievers with HACD1-CNM present with similar clinical and histopathology to that of other CNMs (Figure 1.7 shows the histopathology of HACD1-CNM). Clinically the dogs present with progressive symptoms, initially hypotonia, weakness and exercise intolerance (Blot *et al*., 2002). The dogs also present with decreased skeletal muscle mass, poor posture (shown in Figure 1.6) and a stiff gait leading to a 'hopping' style walk in the dogs (Blot *et al*., 2002; Tiret *et al*., 2003). Pathologically muscle fibres from CNM dogs have increased prevalence of centralised nuclei, fibre type proportional shift to type I predominance, fibrosis, fat infiltration and progressive tubuloreticular disorganisation (Blot *et al*., 2002; Kramer *et al*., 1976; McKerrell & Braund, 1987; Pelé *et al*., 2005; Tiret *et al*., 2003; Walmsley, 2013; Walmsley *et al*., 2017).

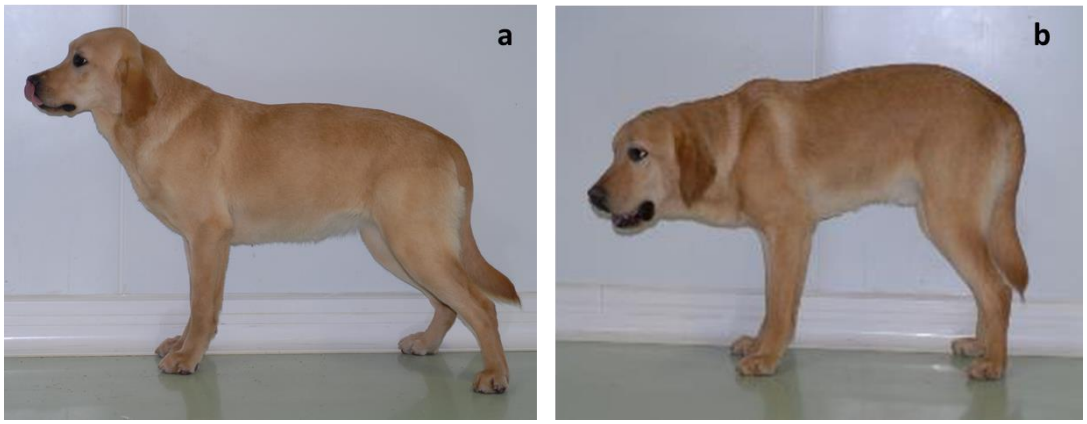

Figure 1.6: Clinical features of centronuclear myopathy (CNM) within Labrador retrievers.
(a) Clinically normal Labrador and a CNM-affected littermate (b) which present with generalised weakness shown by inability to hold up head. (Pictures courtesy of Laurent Tiret and Stéphane Blot).

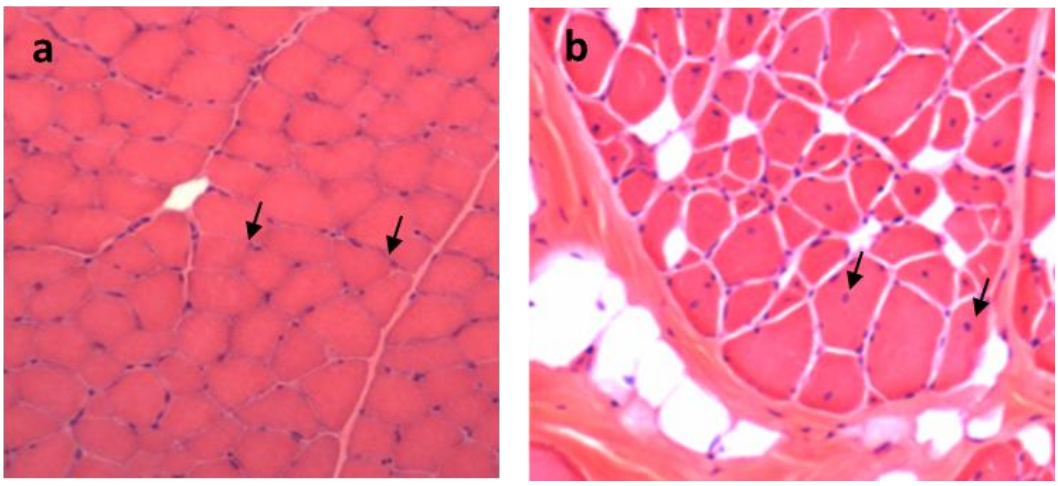

Figure 1.7: Canine muscle biopsy of both control (a) and HACD1-CNM (b) canines.
(a) Control muscle biopsy cross section annotated with black arrows pointing to the peripherally located nuclei. Myofibres are consistent in size and uniformly organised (b) centronuclear myopathy affected muscle biopsy cross section with black arrows annotating the nuclei that have mislocalised to the centre of fibres. Samples also show great disorganisation with huge myofibre size disorganisation and fatty infiltrates (white spaces).

The genetics underlying the disorder were unknown for some 30 years until its autosomal recessive inheritance pattern was discovered in 2002, followed shortly after by the discovery of a mutation within the *HACD1* gene, (*PTPLA)* within the disorder in 2005 (Bley *et al*., 2002; Pelé *et al*., 2005). The *HACD1* gene was mapped to a locus on chromosome 2 initially, which is orthologous to the human chromosome 10p (Tiret *et al*., 2003). Further work identified a tRNA-derived short interspersed repeat element (SINE) insertion within exon two of the gene (Figure 1.8) and this had a significant effect on the expression of *HACD1* mRNA (Pelé *et al*., 2005). This mutation lead to abnormal splicing and/or exon-skipping resulting in <1% of normal transcript being expressed in the canine muscles (Pelé *et al*., 2005). The function of HACD1 was unknown at the time of its association with CNM in 2005 and it was research by Ikeda *et al*., (2008) that identified this CNM causing gene to be involved in VLCFA biosynthesis (Ikeda *et al*., 2008). This SINE insertion was shown to be present in carrier dogs within 13 countries and HACD1-CNM is globally, the most common inherited neuromuscular disorder within dogs (Maurer *et al*., 2012).

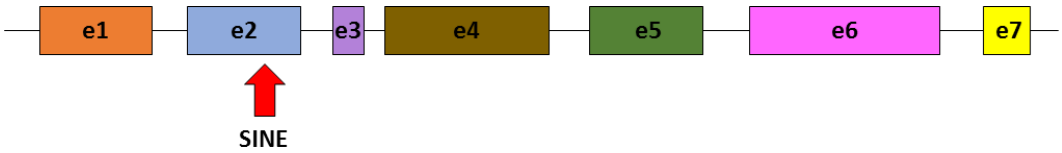

Figure 1.8: Diagram of the canine *HACD1* gene with the centronuclear myopathy (CNM) causative mutation annotated.
Gene is mutated by the insertion of a short interspersed nuclear element (SINE) causing a frame shift in the transcript. Exons1-7 are labelled as 'e1-7'. (Adapted from Pelé *et al*., 2005).

1.3.2. Human congenital myopathies and *HACD1*

The discovery of mutations in *HACD1* as a cause of congenital myopathies in humans has emerged in the past few years. A non-sense mediated decay in *HACD1* reduced gene expression to approximately 30% within a Bedouin family with a congenital myopathy (Muhammed *et al*., 2013). The clinical findings in this family linked *HACD1* to human myopathies for the first time (Muhammed *et al*., 2013). A second, Caucasian, family with myopathic phenotype has more recently been identified to have a mutation within the *HACD1* gene affecting the active site (Toscano *et al*., 2017).

The human congenital myopathies have many features in common with CNM however centralised nuclei have not been established as a disease phenotype within these human patients (Muhammed *et al*., 2013; Toscano *et al*., 2017). Canines with CNM present with a clinical phenotype at six months of age, yet the dogs are two years of age when the centralised nuclei are a prominent feature within the fibres (Blot *et al*., 2002; Tiret *et al*., 2003). The detection of the centralised nuclei and recognition of the condition in dogs as a CNM (defined by the presence of centralised nuclei in >25% of myofibres (Ramero & Laporte, 2013) was the product of serial muscle biopsies of affected dogs in a colony; this would be difficult to achieve in human patients. It therefore possible that *HACD1* mutations in humans cause a CNM rather than CFTD and that biopsies later in life are required from this diagnosis. Ultrastructural analyses and evaluation of ECC apparatus are also lacking in human patients (Blot *et al*., 2002; Muhammed *et al*., 2013; Tiret *et al*., 2003; Toscano *et al*., 2017).

1.3.3. HACD enzymes

There are four paralogous HACD enzymes within mammalian species that are associated with the dehydration step of VLCFA biosynthesis: HACD1 (formerly known as: protein tyrosine phosphatase-like A; PTPLA), HACD2 (formerly: protein tyrosine phosphatase-like B; PTPLB), HACD3 (formerly: protein tyrosine phosphatase-like A domain-containing 1; PTPLAD1) and HACD4 (formerly: protein tyrosine phosphatase-like A domain-containing 2; PTPLAD2) (Ikeda *et al*., 2008). The HACD enzymes have been historically referred to as the

PTPLs due to the presence of a PTP like domain; though, they lack the important catalytic sequence that allows the PTPs to regulate the level of cellular tyrosine-phosphorylation (Li & Dixon, 2000). The need for four HACD isoforms in mammals is poorly understood (Yazawa *et al*., 2013).

1.3.4. HACD conservation

The HACD enzymes sequences are highly conserved, both between isoforms and also between species. HACD orthologues have been studied in both plants and yeast. The study of the HACD orthologue (Phs1) in yeast, or *S. cerevisiae* has been crucial in the characterisation of the HACD enzymes (Ikeda *et al*., 2008). Phs1 was first understood to be involved in sphingolipid metabolism (Schuldiner *et al*., 2005) and it has been demonstrated that decreases in Phs1 lead to accumulation of fatty acids of C20 chain length due to the disruption of further elongation steps and VLCFA synthesis (Kihara *et al*., 2008). Its high conservation and homology, between isoforms and species, does not extend to that of other protein families (Denic & Weissman, 2017; Yazawa *et al*., 2013).

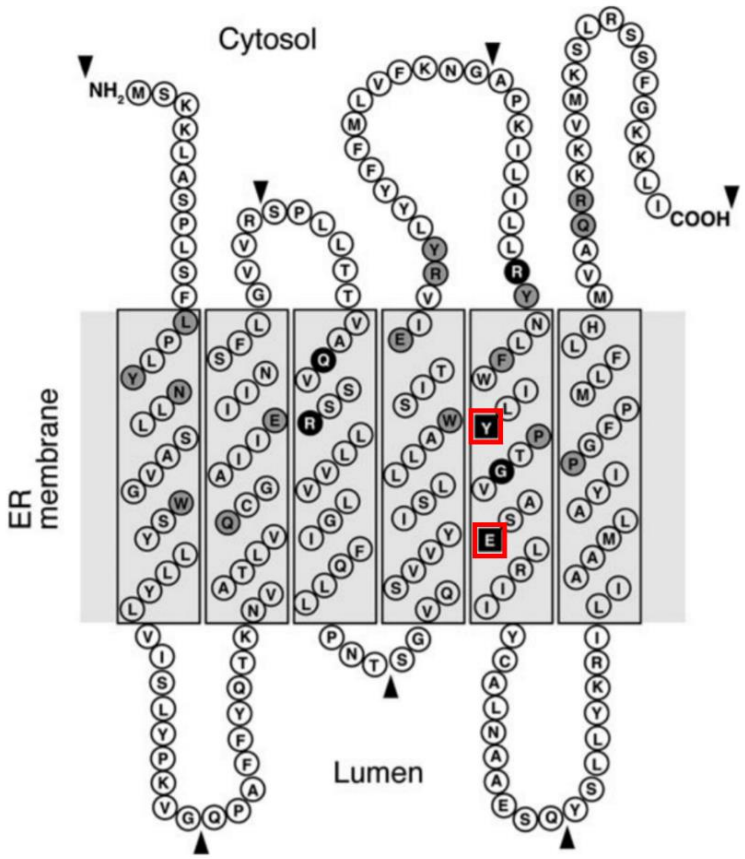

Figure 1.9: Simplistic diagram of the transmembrane Phs1 enzyme in yeast.
Essential amino acids for HACD activity are labelled with red boxes and found in the 5th transmembrane region (adapted from Kihara *et al*., 2008).

By mutating the 22 conserved residues in Phs1, Kihara *et al*., (2008) identified two essential amino acids for life, Tyr-149 and Glu-156, required for Phs1 function and these are conserved between species (essential amino acid residues highlighted by red boxes in Figure 1.9). There were another four mutations within residues that stopped growth in the yeast but these mutations were not fatal and so these were classed as important amino acids (Kihara *et al*., 2008). A point mutation in the conserved glutamine residue in humans has since been found within CNM patients (Toscano *et al*., 2017). This suggests that these two amino acids are likely to be essential for HACD activity across species. This CNM causing mutation in a conserved amino acid, known to be essential is yeast, provides evidence that the HACD activity may be conserved within these amino acids (Toscano *et al*., 2017).

Plants also require VLCFAs for cytokinesis and membrane fusion and the Arabidopsis orthologue of HACD/Phs1 is PASTICCINO2 (PAS2) is capable of rescuing the effects of Phs1 deficiency in yeast. A deficiency in PAS2 itself caused a reduction of VLCFAs in Arabidopsis seeds (Bach *et al*., 2008; Molino *et al*., 2014).

1.3.5. HACD1

Expression patterns for HACD1 found it to be highly expressed in both skeletal and cardiac muscle, therefore suggesting perhaps a role in muscle development and maintenance (Li *et al*., 2000; Uwanogho *et al*., 1999). Work by Ikeda *et al*., (2008) as previously mentioned, demonstrated that HACD1 could sufficiently rescue Phs1-knockout yeast strains and interacted with the ELOVL enzymes, confirming the role as a dehydratase (Ikeda *et al*., 2008).

The gene was initially mapped in humans to a locus responsible for arrhythmic right ventricular dysplasia (ARVD) seemingly confirming its role within cardiac muscle (Li *et al*., 2000). Conversely, a study by Konishi *et al*., (2010) discovered that the K46Q mutation in ARVD patients had no effect on the activity of the HACD enzyme and that the VLCFA synthesis cycle was unaffected.

In Labrador retrievers it was discovered that the *HACD1* gene expressed three differently spliced isoforms: including that of the full length *HACD1* expressed in striated muscle, termed *HACD1-fl*; one transcript missing exon 5 that was translated into a truncated protein that was more ubiquitously expressed, termed *HACD1-d5*; and a transcript of only HACD exons 1, 6 and 7, named *HACD1-167* (Maurer *et al*., 2010; Pelé *et al*., 2005). The HACD1-d5 isoform has been reported to lack interaction with the *trans*-2,3-enoyl CoA reductase (TER) proteins of the elongase complex and the HACD1-167 isoform accumulates in the muscles of HACD1-CNM dogs (Blondelle *et al*., 2015; Pelé *et al*., 2005). HACD1 has also been

documented to have additional isoforms that do not encode the essential amino acids for HACD activity therefore function is unknown in other tissues, including haematopoietic cells and teeth (Tondeur *et al*., 2010; Valdés De Hoyos *et al*., 2012).

A difficulty in understanding and characterising function of HACD1 in mammalian skeletal muscle and disease is the coding of four paralogues in mammals that express tissue specificity (HACD1-4). HACD2-4 have not been characterised in detail at a transcriptome level and little evidence exists for splice variants of these HACD enzymes (Ikeda *et al*., 2008; Maurer *et al*., 2010; Pelé *et al*., 2005; Tondeur *et al*., 2010; Valdés De Hoyos *et al*., 2012).

1.3.6. Previous work on HACD1 in muscle

HACD1 has been previously studied with respect to both human and canine CNM. *Hacd1*-knockout (ko) mice presented with reduced muscle mass, reduced and inconsistent myofibre size and maximal force, with phenotypes similar to CNM affected Labradors (Blondelle *et al*., 2015).

To investigate the function of *HACD1-fl* in more detail, the gene was knocked down *in vitro* in the myogenic C2C12 cell line and it was found that myoblast fusion was significantly impaired and myotubes were unable to differentiate properly (Blondelle *et al*., 2015, Lin *et al*., 2012). With regards to the HACD1 function and VLCFA synthesis it was found that *HACD1-fl* in the cells increased the ratio of C18-26:C10-16 in the cells (Blondelle *et al*., 2015). A different clone of HACD1-deficient C2C12 myotubes (and using optimised cell culture conditions to allow for cell fusion) has been used to research HACD1 and these *Hacd1*-knockdown (kd) cells were found to have disruption in their internal membrane systems (Walmsley, 2013; Walmsley *et al*., 2017). *Hacd1*-kd myotubes differentiated unlike the previous knockdown used by Blondelle *et al*., (2015) and the myotubes formed with an increased number of intracellular vacuoles and increased number of abnormally clustered nuclei (Walmsley *et al*., 2017). A recent study using *Hacd1*-null mice, which presented with reduced body and muscle weight, only a ~40% HACD activity reduction was seen and there was no change in lipid membrane composition; therefore, suggesting compensation may have occurred by another HACD enzyme within this *Hacd1*-null mouse model (Sawai *et al*., 2017).

1.3.7. HACD2

HACD2 (previously PTPLB) is localised to the endoplasmic reticulum (ER) whereby it undergoes a fast turnover via the ERs proteasome system through significant interaction with the chaperone protein, BAP31 (Wang *et al*., 2004). The role of HACD2 in VLCFA synthesis was reported by Ikeda *et al*., (2008) due to its sequence homology with Phs1 - and it was

shown to interact with the elongase complex (Ikeda *et al*., 2008). HACD2 has high redundancy with HACD1 and they have been reported to elongate the same forms of VLCFA; as well as both HACD1 and HACD2 having functional redundancy with the yeast paralogue, Phs1 (Ikeda *et al*., 2008; Sawai *et al*., 2017). Sawai *et al*., (2017) disrupted HACD2 in a human cell line which prevented the elongation of both saturated and unsaturated FAs and when disrupting HACD1 activity this also led to further reductions in the same VLCFAs. HACD2 may therefore have the potential to compenstate for HACD1-deficieny.

1.3.8. HACD3

HACD3 was shown to compartmentalise to golgi/endosome fractions in response to insulin, leading to the initial hypothesis that HACD3 might play a role in insulin signalling and diabetes (Boutchueng-Djidjou *et al*., 2015; Boutchueng-Djidjou *et al*., 2018). HACD3 (referred to as BIND1 and PTPLAD1 previously) was shown to have strong expression in mouse testis, kidney, brain and liver, with weaker signals in skeletal muscle, spleen and heart (Courilleau *et al*., 2000). HACD3 also shares sequence homology with Phs1, although it was unable to rescue Phs1 defiency in yeast (Ikeda *et al*., 2008) and the overexpression of HACD3 in the HACD2-disrupted cell line exhibited a weak activity in elongating saturated and monounsaturated VLCFAs suggesting it has less redundancy with HACD1 and HACD2 than they have with each other (Sawai *et al*., 2017).

1.3.9. HACD4

HACD4 (previously PTPLAD2) was mapped in humans to locus 9p21.3 (Zhu *et al*., 2014), which harbours a number of tumour suppressor genes; the loss of the HACD4 loci has been associated with oesophageal squamous cell carcinoma and frameshift mutations in HACD4 have been associated with colon cancers (Yeon *et al*., 2017; Zhu *et al*., 2014). The HACD4 haplotype has also been linked to accelerated atherosclerosis and myocardial infarction in a Serbian, male population (Zivotic *et al*., 2018a; Zivotic *et al*., 2018b). HACD4 was also shown to be involved in VLCFA synthesis through its sequence homology, however both HACD3 and HACD4 are less homologous to Phs1 than HACD1 and HACD2 (Ikeda *et al*., 2008). As with HACD3, HACD4 also could not rescue Phs1 deficiency in yeast (Ikeda *et al*., 2008). The study by Sawai *et al*., (2017) found no HACD activity in the HACD2-disrupted human cell line even once HACD4 had been overexpressed.

1.4. Lipids in skeletal muscle membranes

Due to the involvement of HACD1 in the synthesis of VLCFA (Ikeda *et al*., 2008), this section will discuss fatty acids and lipids, and their roles within mammals; specifically within muscle and plasma membranes.

Lipids are an abundant class of molecules within all living organisms and they are diverse in both structure and function, with cells using ~5% of genes to synthesise lipids (Cox & Nelson, 2012; van Meer *et al*., 2008). Complex, polar lipids such as phospholipids and sterols provide structure within plasma membranes whereas simpler fats and oils provide energy and may have important roles in processes such as signalling or membrane trafficking (Cox & Nelson, 2012). The lipid bilayer is the key component of skeletal muscle membranes, providing both structural support and fluidity as well as forming a barrier, contributing to the biophysical properties of the cell and aiding membrane fusion (van Meer *et al*., 2008).

1.4.1. Fatty acids

Fatty acids (FAs) are the simplest form of lipids structurally and are composed of a hydrocarbon chain, ranging in length from 4-36 carbons (C4-C36) with a carboxylic group (COOH) positioned at one end of the chain (Cox & Nelson, 2012). FAs predominantly have even numbers of carbons in their chain. These may be single chains or may branch out into numerous chains: this structure forms the fundamental basis of most biological lipids from which the synthesis of more complex lipids is built (Cox & Nelson, 2012). The hydrocarbon chain backbone may: a) be entirely saturated with only single bonds present between atoms (the carbon atoms available bonds are saturated with carbon or hydrogen atoms) (SFA); b) include only one double bond in their chain (MUFAs, mono-unsaturated fatty acid); or c) have more than one double bond along the hydrocarbon chain (PUFA) (Figure 1.10) (Jakobsson *et al*., 2006; Kihara *et al*., 2012; Cox & Nelson, 2012).

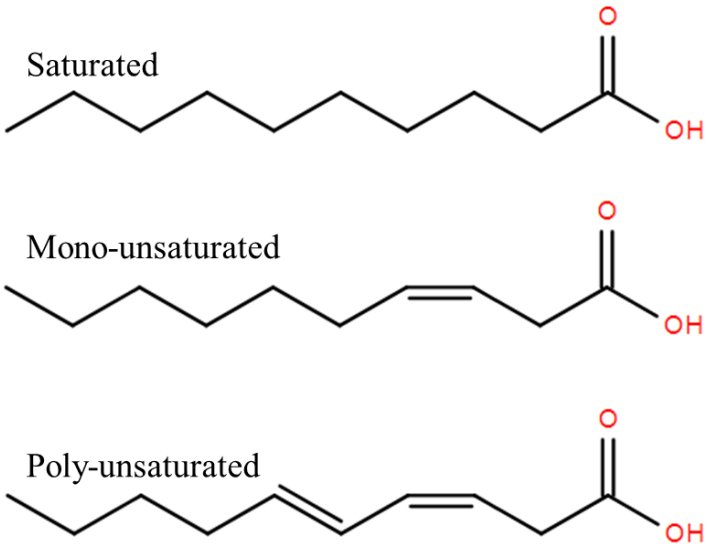

Figure 1.10: Example lipid saturation in a C10 fatty acid (carbon chain length = 10).
The right end of hydrocarbon chain represents the carboxyl group (COOH) and unsaturated bonds are represented by an extra line along the hydrocarbon chain. Figure created using LIPID MAPS (https://lipidmaps.org).

Fatty acids can either be taken up into the body through the diet, or synthesised by the fatty acid synthase (FAS) enzyme, up to 16 carbons in chain length (Jakobsson *et al*., 2006). It has been reported that 90% of fatty acids in mammals are synthesised *de novo*, indicating the importance of efficient fatty acid synthesis as well as diet (Moon & Horton, 2003).

1.4.2. Fatty acid classes and function

Fatty acids can be classified according to their carbon chain length and are required for normal physiology; deficiency of FAs can lead to infertility, dermatitis and stunted growth (Lauritzen *et al*., 2001). Shorter fatty acids (C4-10) are absorbed for use as an energy source very readily and have also been shown to activate leukocytes through signalling pathways (Kinsella, 1990; Le Poul *et al*., 2003). Long chained fatty acids (LCFAs) range from 10-20 carbon chain length and are the most abundant FA species in mammalian cells (Leonard *et al*., 2004). LCFAs often act as precursors and can be modified into more complex structural molecules that are also highly valuable to the cell (Abedi & Sahari, 2014; Leonard *et al*., 2004). LCFAs, when not synthesised further, can be used for energy during exercise, whereby there is a large increase in the metabolism of LCFA in muscle (Kiens, 2006).

Very long chain fatty acids are classified as FAs with a carbon chain length of over 20 and are far less abundant than shorter length FAs, and relative to their own expression, are highly abundant in the skin, retina, testis and brain (Monroig *et al*., 2010). VLCFAs have important

functions that LCFAs cannot compensate for, such as functions in inflammation resolution, sphingolipid biogenesis and vesicular transport (Kihara *et al*., 2012; Obara *et al*., 2013).

1.4.3. Very long chain fatty acids (VLCFAs)

1.4.3.1. VLCFA function

The VLCFAs play important roles in the eye, skin, testis and CNS that have been well documented: their functions include barrier formation, inflammation, retinal function, spermatogenesis and maintenance of the nuclear envelope (Monroig *et al*., 2010; Schneiter *et al*., 1996). Their length is thought to aid in the lipids ability to match up with increasingly thick areas of the lipid bilayer (Gaigg *et al*., 2005).

Docosahexanoic acid (DHA, C22) is important in the nervous system and decreased levels affect learning, cognition and emotions. DHA makes up 50-60% of the FA composition of the retina, it activates retinal signalling and decreased levels of DHA reduce vision (Tanaka *et al*., 2015). DHA is also present within testis and brain and one of its main functions is to generate lipid mediators that turn off inflammation response (Sassa & Kihara, 2014). Cognitive function correlated positively with mothers taking VLC-PUFA supplements during pregnancy and lactation: this has been observed in a number of studies including one correlating DHA levels in pregnancy with infant cognition (Braarud *et al*., 2018; Helland *et al*., 2003). Ceramide is critical in spermatazao and cells have been reported to apoptose in its absence and VLC sphingolipids are required for cell proliferation (Rabionet *et al*., 2015; Tvrdik *et al*., 2000). In mammals, VLCFAs with carbon chain lengths above 30 form permeability barriers (including the water permeability barrier of the epidermis) that are required for formation of the skin (Denic & Weissman, 2007).

Although no clear overall function for VLCFAs has been established they seem to be critical for functioning of membranes, either by formation of membranes themselves and the maintenance of said membranes, or trafficking and signalling via membranes (Monroig *et al*., 2010; Schneiter *et al*., 1996).

1.4.3.2. VLCFA in muscle

The localisation of a muscle specific enzyme, HACD1, now known to be involved in the elongation of VLCFA has highlighted their importance within muscle, despite this VLCFA functions are still poorly understood (Ikeda *et al*., 2008; Kihara *et al*., 2012).

1.4.3.3. VLCFA synthesis

The elongation of VLCFAs requires a set of endoplasmic reticulum (ER) bound enzymes (Kihara *et al*., 2012). The elongation is a cyclical process of four sequential steps (displayed in Figure 1.11): condensation of long chain fatty acids, reduction, dehydration and a further reduction step, resulting in the addition of two carbons per cycle to the carboxylic acid side of the FA (Kihara *et al*., 2012).

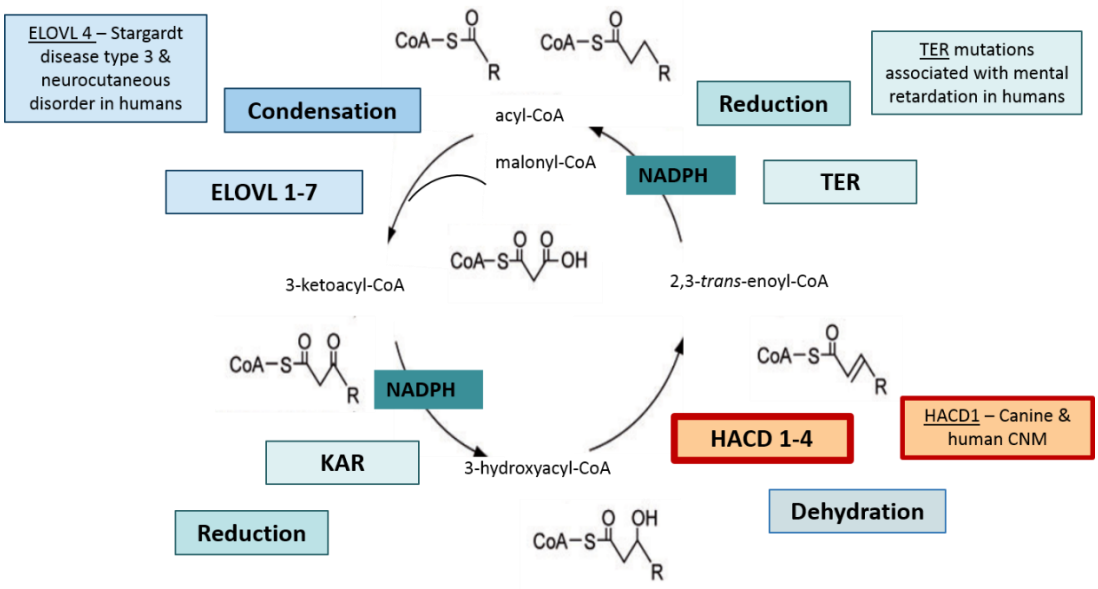

Figure 1.11: Cyclic process of very long chain fatty acid (VLCFA) synthesis (Adapted from Kihara *et al*., 2012).

The initial condensation step in this cycle was found to be a rate limiting step, in which the carbon donor of malonyl-CoA is introduced to the fatty acid, resulting in β-ketoacyl-CoA (Nugteren, 1965). The ELONGASE protein family is responsible for catalysing this step and there are 7 mammalian isoforms (ELOVL1-7) which favour the elongation of different fatty acid chain lengths/saturations, and have been extensively researched (Kihara *et al*., 2012; Sassa & Kihara, 2014).

ELOVL1 is highly involved with the synthesis of C24 sphingolipids, and *Elovl1*-ko mice have severe and lethal epidermal defects (Ohno *et al*., 2010, Sassa *et al*., 2013). Knockout in *Elovl2* leads to the absence of C26 VLCFAs in the testis of mice which lead to infertility (Zadravec *et al*., 2011). ELOVL4 favours the elongation of VLC-PUFAs and is critical for both retinal function and the formation of the water permeable barrier (Harkewicz *et al*., 2012). Mutations in *Elovl4* result in loss of formation of the skin barrier in mice, the depletion of ceramide and

of retinal glycerophospholipids containing VLC-PUFAs (Harkewicz *et al*., 2012; Li *et al*., 2007; Vasireddy *et al*., 2007). ELOVL5 was reported to elongate long chain C18 FAs for the liver and *Elovl5-ko* has been reported to cause hepatic stress in mice (Moon *et al*., 2009). ELOVL6 also elongates shorter chain lengths, with no apparent role in elongating VLCFAs: it is reported to elongate fatty acids of C12-C16 chain length (Moon *et al*., 2001). ELOVL3 and 7 elongate C16-C22 FAs with particular affinity towards C18 chain lengths and so elongate both LCFA and VLCFA (Ohno *et al*., 2010; Zadravec *et al*., 2010). The ELOVL proteins have been documented to show a degree of tissue specificity within mammals: ELOVLs 1, 2, 3, 5 and 6 have been reported in the liver (Brolinson *et al*., 2008; Wang *et al*., 2005) and ELOVLs 1, 5 and 6 in the heart (Igarashi *et al*., 2008).

The first reduction step, and second in the cycle, requires nicotinamide adenine dinucleotide phosphate (NADPH) as a cofactor. The 3-ketoacyl-CoA is converted to 3-hydroxyacyl-CoA by the 3-ketoacyl-CoA reductase (KAR) enzyme (Moon and Horton, 2003.) In the third step the fatty acid chain is dehydrated to become an enoyl-CoA, and this is catalysed by the 3-hydroxyacyl-coA enzymes dehydratase (HACD) enzyme (Ikeda *et al*., 2008; Kihara *et al*., 2012). This step has also shown to be rate-limiting due to the accumulation of these 3-hydroxyacyl-CoA molecules during *in vitro* FA elongation assays (Kihara *et al*., 2012). The TER enzyme catalyses the final reduction step to generate the extended acyl chain, also using NADPH as a cofactor (Moon & Horton, 2003). The TER enzymes are also involved in the degradation of sphingosine (Wakashima *et al*., 2014).

1.4.4. Membrane lipids

The composition of lipids within membranes is extremely varied both between organisms and within them, including variation between organelle membranes, as the lipid composition is highly important for each specific membrane's functions (Harayama & Riezman, 2018; Nicolson & Ash, 2017). The diversity of different membrane lipids is shown in Figure 1.12.

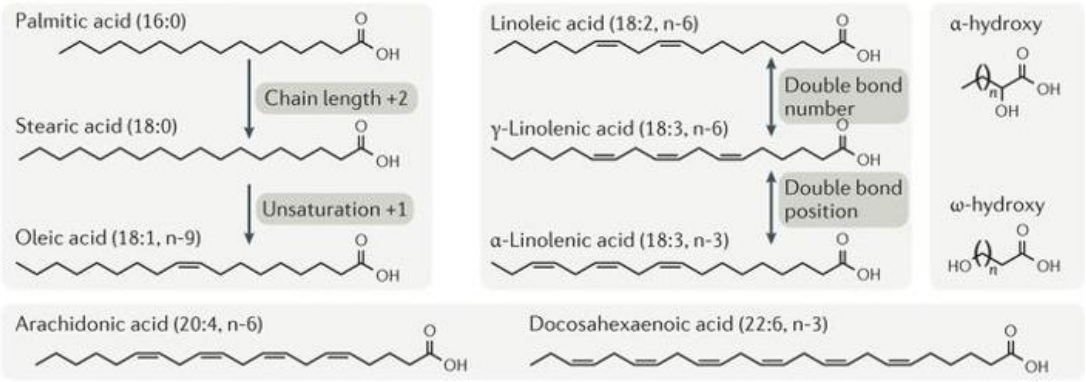

Figure 1.12: Diversity of fatty acids found in membranes (Adapted from Harayama & Riezman, 2018).

Membrane lipids self-assemble in accordance to the cellular environment and the main membrane lipids are sphingolipids, glycerophospholipids and sterols, particularly cholesterol (Blanco, 2017; van Meer *et al*., 2008). Poly-unsaturated fatty acids (PUFAs) and glycerophospholipids (GPLs) are important for providing membrane fluidity and selective permeability. In contrast saturated fatty acids (SFAs) provide the cell membrane with more rigidity and organisation (Harayama & Riezman, 2018; Leonard *et al*., 2004.). Lipids modulate membrane properties and can affect the activity of membrane proteins – for example ion channel activity (Rosenhouse-Dantsker *et al*., 2012). Cholesterol, phosphoinitols and sphingolipids are known to regulate ion channel function through lipid-protein interaction and through physically altering membranes. (Ciardo & Ferrer-Montiel, 2017; Rosenhouse-Dantsker *et al*., 2012). Lipids within the membrane undergo constant maintenance and their homeostasis is crucial as evidenced by the vast number of genetic diseases associated with lipids (Harayama & Riezman, 2018). Lipid accumulation in a number of disorders has been linked with muscle weakness; such as the lipid storage myopathies and dysferlin deficient myopathies (Grounds *et al*., 2014; Laforêt & Vianey-Saban, 2010).

1.4.4.1. Sarcolemmal membrane lipids

In skeletal muscle, lipid composition of the sarcolemmal membranes is important for structure and for the fusion of myoblasts (Mukai *et al*., 2009). Cholesterol is important for preventing ionic leak through ion channels, modifying lipid organisation and playing a role in membrane fluidity (Barrientos *et al*., 2017; Briolay *et al*., 2013; Mukai *et al*., 2009). Membrane cholesterol has been documented to modulate DHPR activity, potentially through interactions with Caveolin-3 (Barrientos *et al*., 2017). GPLs, the other highly abundant class of lipids within skeletal muscle membranes, are associated with providing structure for the membranes

and GPLs were reported to contribute for up to 50% of membrane lipids in the L6 muscle cell line (Briolay *et al*., 2013).

1.4.4.2. Internal skeletal muscle membrane lipids

T-tubule membranes are composed largely of sphingolipids and cholesterol which creates a highly ordered lipid membrane; t-tubules are reported to be less fluid than other mammalian plasma membranes (Al-Qusairi & Laporte, 2011; Barrientos *et al*., 2017). Lipid composition within internal membranes varies between fibre types: type II SR membrane contains more phosphatidylcholine (PC) (64%) and less sphingomyelin (SM) (5%) than SR from type I fibres (37% and 15% respectively (Borchman *et al*., 1999). The PC: SM ratio is hypothesised to be related to membrane fluidity, suggesting type II fibres have more fluid SR membranes (Borchman *et al*., 1999).

1.4.5. Lipidomic techniques

Studying the lipidome within HACD1-deficient muscle will be instrumental in understanding which lipids are affected, due to HACD1's role in elongating VLCFA (Ikeda *et al*., 2008). Developments in techniques such as mass spectrometry (MS) and nuclear magnetic resonance (NMR) have allowed lipidomics as a field of research to advance greatly, however as it is a developing field there are limitations yet to be overcome (van Meer *et al*., 2009). For example: low concentrations of lipids within samples, halting enzymatic and oxidative processes of samples and a lack of lipid standards making the identification of lipids in samples difficult (Li *et al*., 2017; Vuckovic, 2018). Table 1.3 compares a number of methods currently in use for lipidomic studies including MS and NMR methods. MS as a technique is highly sensitive however, the level of ionisation of lipids is variable and therefore loses reproducibility (Li *et al*., 2017). MS is destructive to samples and therefore complementary analyses cannot be performed, unlike with NMR in which samples stay intact and available for further study: therefore making NMR desirable as an initial experimental choice (Li *et al*., 2017).

Table 1.3: Brief overview of lipidomic analyses techniques (Adapted from Yang *et al*., 2016).

Technique	Types	Key features	Advantages	Disadvantages	References
Lipid chromatography based-mass spectrometry (MS)	LC-MS MS/MS	Chromatographic separation	Reproducible, high resolving power, high sensitivity for focused analysis	Low throughput, complex data processing, destruction of sample	Pitt 2009; Yang *et al*., 2016
	Matrix-assisted laser desorption/ ionisation (MALDI) MS	Samples mixed with matrix material and applied to metal plate Samples then pulsed with laser and desorbed before molecules are ionised	Tolerant to contaminations, extraction is not required and off-line sample preparation allows for focused analyses	Low throughput, destruction of sample, low sensitivity for low abundance molecules	Cramer 2009, Yang *et al*., 2016
	Ion mobility MS	Gas phase separation of ions by size, shape and charge	Increased signal: noise ratio and ion separation	Loss of sensitivity, destruction of sample	Paglia *et al*., 2015; Wang *et al*., 2015; Yang *et al*., 2016
Shotgun MS	Tandem MS	Internal standards added for lipids of interest, focused technique	Simple, fast and quantitative, a focused technique	Selection of standards difficult due to availability, destruction of sample	Yang *et al*., 2016

	High mass accuracy MS	Highest possible mass resolution	Sensitive analysis	Differential fragmentation and ionisation makes quantitation difficult, destruction of sample	Marshall *et al*., 2013; Yang *et al*., 2016
Spectroscopy	Nuclear magnetic resonance (NMR)	Nuclear magnetic fields are perturbed by magnetic field and produce spectral characteristics dependent upon their environment ^{1}H-NMR, ^{13}C-NMR and ^{31}P-NMR combinations can provide increasingly more informative spectra Used often as an exploratory method	Time efficient, reproducible, samples preserved, instruments are robust	Crowded spectra due to lack of separation, low resolution for lipids of the same class, requires sample preparation/extraction of lipids	Li *et al*., 2013; Li *et al*., 2017
	Ramen spectroscopy	Uses scattering of light source to provide information about vibrations within sample Used for a targeted approach	Quantitative, samples preserved, fast and reliable, single-cell applications, can be used as a focused technique	Requires highly sensitive and optimised equipment	Buzgar *et al*., 2009; Wu *et al*., 2011; Li *et al*., 2013;

1.5. Current HACD1-CNM models

Animal and cellular muscle models in research have greatly enhanced our understanding of CNM, as well as a number of other musculoskeletal disorders including muscular dystrophies (Blondelle *et al*., 2015; Buj-Bello *et al*., 2002; Cowling *et al*., 2017; Dowling *et al*., 2009; Dowling *et al*., 2010; Durieux *et al*., 2010; Nance *et al*., 2012; Sabha *et al*., 2016; Sawai *et al*., 2017; Smith *et al*., 2014; Walmsley, 2013; Walmsley *et al*., 2017; Ytterberg, 1991).

1.5.1. HACD1-CNM Labrador retrievers

In 1992, a colony of HACD1-CNM dogs was established in Alfort Veterinary School, France, and using these dogs the genetics and pathology of canine CNM was characterised using these dogs (Blot *et al*., 2002; Maurer *et al*., 2012; Pelé *et al*., 2005; Tiret *et al*., 2003). However, the use of dogs for further research is less practical due to size, cost and ethics (Collins & Morgan, 2003).

1.5.2. *Hacd1*-null mice

Mice have been used as a longstanding model for neuromuscular diseases, including CNM (Nance *et al*., 2012; Vainzof *et al*., 2008). The *mdx* mouse is a widely used model of Duchenne muscular dystrophy (DMD) and has provided great insight into the disease, but their phenotype is very mild and this is not representative of DMD in both humans and canines (Cox *et al*., 1993) and so are not necessarily the most appropriate model of muscle disease.

Mice models have also been used in the study of HACD1-CNM providing a greater understanding of the mechanisms in which HACD1 might be involved in (Blondelle *et al*., 2015; Sawai *et al*., 2017). *Hacd1*-null mice (*Hacd1*-/-) presented with reduced body weight gain after birth and into adulthood due to a 29% reduction in muscle mass; these mice had a 27.5% reduction in absolute maximal force, although specific force (force per unit mass) was unchanged (Blondelle *et al*., 2015). These phenotypes are comparable to the phenotype of HACD1-CNM dogs (Maurer *et al*., 2012; Tiret *et al*., 2003). Blondelle *et al*., (2015) hypothesised that a defect in myoblast fusion was present as a result of HACD1-deficiency as they exhibited smaller fibres with fewer nuclei within their *Hacd1*-/- mice (Blondelle *et al*., 2015). Sawai *et al*., (2017) also used a *Hacd1*-/- mouse model in their research and found corroborating results in terms of reduced body and muscle mass. It was also documented that the reduction in HACD activity was only ~60% of the control which was less severe than expected - they proposed HACD2 was responsible for this remaining HACD activity within the muscles (Sawai *et al*., 2017).

1.5.3. *Hacd1*-deficient C2C2 cell line

Skeletal muscle cell lines allow the study of muscle without the need for live animal models and so complies with the NC3Rs guidelines by reducing the number of animals required within research. The mouse muscle cell line, C2C12, and the rat muscle cell line, L6 are used within research and promoted to differentiate into multinucleated myotubes through the removal of serum high in growth factors (Yaffe, 1968; Yaffe & Saxel, 1977).

C2C12 cells have been widely documented within muscle research and shown to have a number of characteristics making them a suitable resource. These characteristics include: the measurement of force and contraction and the measurement of ECC and its apparatus including RYR1, DHPR and SERCA channels (Manabe *et al*., 2012; McMahon *et al*., 1994).

Blondelle *et al*., (2015) used a *Hacd1*-knockdown (*Hacd1*-kd) C2C12 cell line alongside their *Hacd1*-/- mouse model and found a reduction in myotube fusion in these cells. They also found defects in membrane properties such as fluidity and abnormal cell lipid profiles (Blondelle *et al*., 2015). A different clone of HACD1-deficient C2C12 myotubes (using optimised cell culture conditions to allow for cell fusion) has been used to study ECC defects and these *Hacd1*-kd cells were found to have disruption in their internal membrane systems including abnormal nuclei clustering (often developed in ring formations) and development of internal vacuoles (Walmsley, 2013; Walmsley *et al*., 2017).

1.6. Zebrafish as a potential HACD1-CNM model

Zebrafish are an established model organism for studying mammalian disease and have been used in biomedical research for approximately 40 years, when they were first used in an experiment to study mutations affecting their nervous system (Streisinger *et al*., 1981). They are now used widely for drug and genetic screening as well as for modelling mammalian diseases (Den Hertog, 2005; Dooley & Zon, 2000). DMD has been studied in zebrafish extensively since the generation of the *sapje* DMD zebrafish model (Bassett & Currie, 2004). The model has an extremely close phenotype to DMD phenotype and the translatability of using zebrafish as a myopathy model has arisen from the high similarity in their muscular characteristics to that of mammals (Guyon *et al*., 2007).

As a model organism the zebrafish has a number of advantages over other models. Invertebrate organisms such as *Drosophila* and *C.elegans* are powerful models and can be used in large numbers, but as invertebrates, they lack basic homology of anatomy with mammals, for example, the absence of kidneys (Dooley & Zon, 2000; Wilson-Sanders, 2011). For this

reason, they are limited in the issues they can address in mammalian physiology. Mice are also widely used and as mammals they offer a clear advantage in terms of translatable results: however studying mice also comes with disadvantages to which zebrafish offer a valid solution. Mice are expensive to house and maintain and often lack key phenotypes in their disease models compared to zebrafish models which are often good representative for mammalian disease (Dooley & Zon, 2000; Guyon *et al*., 2007; Kasher *et al*., 2015). Zebrafish provide a bridging of this gap between the invertebrate and mammalian models (Dooley & Zon, 2000; Kabashi *et al*., 2011; Phelps & Neely, 2005).

Zebrafish have high fecundity and females may spawn up to 300 eggs per week which undergo rapid development: the cardiovascular and nervous systems among other organs are fully developed by 1-week post fertilisation (Kimmel *et al*., 1995). Thus, making them a valuable resource for studying neurological and musculoskeletal disorders within development (Crilly *et al*., 2018; Sarasamma *et al*., 2017), Figure 1.13 presents embryos from 1-3 days post fertilisation (dpf). Zebrafish models allow for the study of early development as the embryos develop separately from the mother and so are highly accessible and non-invasive to attain (Phelps & Neely, 2005). This external development also allows for easier genetic manipulation through the injection of RNA/DNA at a single cell stage (Liu *et al*., 2017).

A potential limitation of using zebrafish to study genetics is the genome duplication that the ancestral zebrafish lineage underwent, over 500 million years ago (Meyer & Schartl, 1999). While this is a potential set back with zebrafish genetic studies, comparative mapping against the human genome has been completed to identify segments that may have arisen due to this (Howe *et al*., 2013). These duplicated genes may have lost function over time, and it has been documented that larger families of genes with more paralogues are present within zebrafish compared to the mammalian orthologues (Postlethwrait *et al*., 1999). Despite this potential limitation, zebrafish share over 75% of human disease genes making them a suitable model for the diversity of human and mammalian disease (Howe *et al*., 2013; Sarasamma *et al*., 2017). Zebrafish embryos are also valuable in biomedical research as they have high optical clarity due to their transparency - allowing developing cells and organs to be observed throughout embryogenesis (Guyon *et al*., 2007).

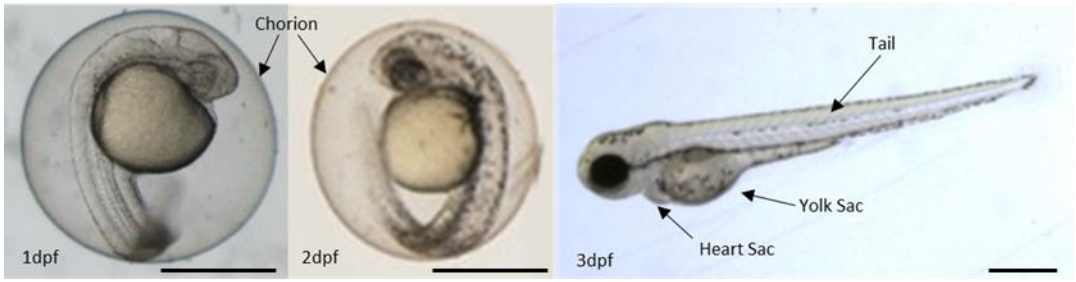

Figure 1.13: Images of developing zebrafish from 1dpf – 3dpf (days post fertilisation).
Anatomy including heart sac, yolk sac, tail and chorion are labelled, scale bar indicates 0.5cm.

1.6.1. Muscle in developing zebrafish embryos

Neurogenesis begins at around 10 hours post fertilisation (hpf) and within the first 24 hours key components of the CNS are present within the embryos (Kabashi *et al*., 2011). Zebrafish embryos develop somites from approximately 10-24hpf and shortly after somite formation the first muscle cells are present within the embryos (Devoto *et al*., 1996; Kimmel *et al*., 1995). Devoto *et al*., (1996) reported that by using cell fate mapping, the type of myofibre (type I or type II) could be recognised before the formation of the somites. At approximately 17hpf embryo tails begin to twitch, confirming the connection between nerve and muscle (Saint-Amant & Drapeua, 1998). Muscle function is commonly evaluated within zebrafish muscle due to the rapid development of the musculoskeletal and nervous systems (Saint-Amant & Drapeua, 1998). This optical clarity of the embryos has allowed zebrafish embryos to be utilised in the study of calcium signalling within muscle through the use of fluorescence imaging. Calcium homeostasis and signalling are highly regulated throughout development; including the expression of RYR1 from early stages of development (Ashworth *et al*., 2005; Brennan *et al*., 2005; Wu *et al*., 2011). The developed myofibres within 2dpf zebrafish tails are shown in Figure 1.14, with positive RYR1 staining present by 3dpf.

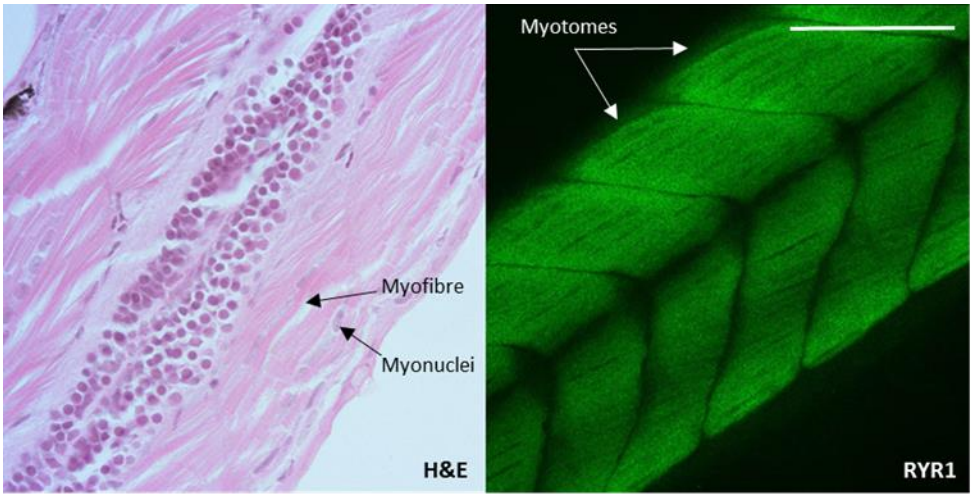

Figure 1.14: Images of 3dpf (days post fertilisation) zebrafish embryo tails stained with both haemotoxylin & eosin (H&E) and RYR1 immunofluorescence showing the developed myofibres. White scale bar represents 100µm.

1.6.2. Comparisons between mammalian and zebrafish muscle

Although zebrafish are a non-mammalian model there a number of important similarities between two sets of musculoskeletal systems. Zebrafish have the presence of both type I and type II myofibres, and these are topologically separate, unlike mammals (Devoto *et al*., 1996; Sparrow *et al*., 2008). As mammalian myopathies often only effects one fibre type the separation of fibre types may be seen as advantageous (Devoto *et al*., 1996; Sparrow *et al*., 2008). Their muscle also develops from the dermomyotome in three stages, as seen in mammalian muscle development, and zebrafish muscle development utilises satellite cells comparable to the satellite cells of mammals (Bryson-Richardson & Currie, 2008; Devoto *et al*., 2006; Sparrow *et al*., 2008). The zebrafish satellite cells express orthologues of Pax7 and Pax3 which are required in mammalian muscle development and present within mammalian satellite cells. The development of a *pax7*-mutant zebrafish confirmed its role in adult muscle repair (Berberoglu *et al*., 2017). Zebrafish provide incredibly useful tools for studying mammalian muscle, and this is supported by the *sapje* zebrafish DMD model (Bassett & Currie, 2004). The *sapje* zebrafish phenotype is representative of the human disease phenotype whereas the mouse DMD model, the *mdx* mouse, has a much milder phenotype than is seen in DMD (Bassett & Currie, 2004).

1.6.3. Methods of zebrafish genome editing

There are a number of ways to genetically alter the *hacd1* gene within zebrafish embryos to create a *hacd1*-mutant model and investigate the role of HACD1: the method favoured and used in this thesis will be CRISPR/Cas9 genome editing.

Morpholinos are another common genome editing tool within zebrafish and have been used widely within zebrafish in the past due to their ability to phenotypically mimic characterised mutants (Stainer *et al*., 2017). Morpholinos are composed of synthetic nucleic acid oligonucelotides that bind to RNA and block further binding or interactions from molecules therefore blocking translation (Heasman, 2002). However; morpholinos often degrade, have many uncertain off-target effects and exhibit low sequence specificity (Summerton, 1999). When comparing morpholino zebrafish to the Sanger Zebrafish Mutation Project Kok *et al*., (2015) found that approximately 80% of known morphant phenotypes were not seen in the morpholino zebrafish suggesting a lack of efficiency in the genome editing (Kok *et al*., 2015). Where morpholino genome editing was shown to be inefficient, CRISPR/Cas9 efficiency in zebrafish has reported to reach up to 86% and be hereditable (Hruscha *et al*., 2013).

Other methods include zinc finger nucleases (ZFN), transcription activator-like effector nucleases (TALENS) and morpholinos. ZFN works by cleaving targeted DNA and inducing DSB (Carroll, 2011). TALENS also works via DNA cleaving, using nucleases that target single nucleotides to provide high levels of specificity (Joung & Sander, 2013). CRISPR/Cas9 has a comparable rate of mutagenesis compared to ZFNs or TALENs and is better adapted than that of TALENs or ZFNs (Gagnon *et al*., 2014).

CRISPR DNA sequences are found naturally within prokaryotic organisms and originate from their adaptive immune response to degrade DNA from invading viruses, and these sequences have been found in approximately 50% of bacteria genomes (Hille *et al*., 2018). The Cas9 (CRISPR-associated 9) enzyme utilises the CRISPR sequences as a guide to introduce double strand breaks (DSB) into the sequence specific DNA, which therefore destroys the virus. These DSB occur adjacent to a specific 3-5bp (base pairs) sequence within the genome known as a protospacer adjacent motif (PAM), and are now utilised in order to mutate gene sequences of choice (Sander *et al*., 2014). CRISPR/Cas9 is a rapidly developing method of editing genomes and due to the frequency of the PAM sequences within the genome a primary advantage of CRISPR/Cas9 is the allowance to direct mutagenesis to almost anywhere within the genome simply by editing the sequence of the single-guide RNA (sgRNA); this provides great flexibility in the technique.

1.6.4. Current zebrafish CNM congenital myopathy models

Due to the benefits of using zebrafish embryos; several zebrafish models of CNMs have been developed to study different genetic causes, more specifically mutations in: *MTM1*, *MTMR14*, *BIN1* and *DNM2* (Dowling *et al*., 2009; Dowling *et al*., 2010; Gibbs *et al*., 2013a; Sabha *et al*., 2016; Smith *et al*., 2014). Dowling *et al*., (2009) demonstrated that *mtm1*-morphant

zebrafish presented with early muscle phenotype including: mislocalised, rounded nuclei and a disorganised t-tubule network. This model was suggested to be more translatable to the disease than the mouse model of MTM1-deficiency in which the mouse phenotype appeared after a period of normal muscle growth and function (Dowling *et al*., 2009).

Dowling *et al.*, (2010) then investigated the other myotubularin-related gene (*mtmr14*) knockdown in zebrafish which resulted in, similar to *mtm1*-knockdown, an abnormal motor phenotype including diminished spontaneous contractions and impaired ECC function (Dowling *et al*., 2010). Gibbs *et al.*, (2013a) characterised two isoforms of dynamin 2 in zebrafish embryos of which they hypothesised to be due to the genome duplication. When knocking expression of these isoforms down they found morphological defects in embryos, including shortened somites and body axis, by 1-day post fertilisation (dpf) comparable to mammalian centronuclear myopathy (Gibbs *et al*., 2013a). The BIN1-CNM zebrafish model generated by Smith *et al*., (2014) displayed structural defects in the muscle comparable to those seen in human biopsies and they reported abnormal calcium homeostasis (Gibbs *et al*., 2013a).

The current zebrafish CNM models have furthered the understanding of CNM pathogenesis and the function of some of the genes within the disease (Dowling *et al*., 2009; Dowling *et al*., 2010; Gibbs *et al*., 2013a; Smith *et al*., 2014). Zebrafish embryos bridge the gap between the ease of using invertebrate models and the translatability of mammalian models (Dooley & Zon, 2000; Kabashi *et al*., 2011; Phelps & Neely, 2005). For this reason, zebrafish should make a relevant model for HACD1-CNM and once generated will have great potential for the research into both HACD1 and VLCFA within muscle.

1.7. Aims and hypotheses

Mutations in *HACD1* cause spontaneous congenital myopathies in dogs and humans, and *Hacd1*-deficient mouse and myogenic cell culture models demonstrate similar characteristics. Muscle membrane abnormalities are a key feature of CNMs, including canine HACD1-CNM, however the role of HACD1 and VLCFA in the development and maintenance of skeletal muscle membrane systems is poorly understood. The overall aim of this project was to validate and characterise a zebrafish embryo model with *hacd1* mutations and develop techniques (initially using a mammalian cell culture model) to study the effects of HACD1-deficiency on muscle membrane development, structure and function. Our specific aims were as follows:

1) Determine the zebrafish homologue of HACD1 and investigate the hypothesis that HACD enzyme genes are evolutionarily conserved with comparable expression patterns in zebrafish to those documented in mammals;

2) Utilise a murine myoblast cell culture model to evaluate the effect of *Hacd1*-knockdown on differentiation and function via an electrophysiological study of the cell membranes;

3) Explore the effects of HACD1 expression (by examining samples in early development prior to HACD1 upregulation and after) and deficiency on the lipidome of cell and embryonic zebrafish models using ^{1}H-NMR;

4) Investigate the hypothesis that zebrafish embryos with mutations in *hacd1*, introduced by CRISPR-Cas9 genome editing, will produce a relevant model of HACD1-CNM.

2 Spatial and temporal evaluation of HACD enzyme expression in zebrafish

2.1. Introduction

Expression of HACD1 in developing and mature skeletal and cardiac muscle was first reported several decades ago (Uwanogho e*t al*., 1999). Linkage analysis in a pedigree of Labrador retrievers with CNM documented a hypomorphic mutation and confirmed the protein's importance for normal muscle function (Maurer *et al*., 2012; Pelé *et al*., 2005). However, the role of HACD enzymes in VLCFA biosynthesis was only discovered more recently after elucidation of fatty acid elongation pathways in yeast allowed identification of the elongase complex enzymes and their mammalian orthologues (Denic & Weissman, 2007; Riezman, 2007). Yeast Phs1 and the four mammalian HACD enzymes (HACD1-4) share sequence similarities, in particular two conserved amino acids are thought to be essential for the enzymes active site and dehydratase activity in the elongation cycle of VLCFAs (Ikeda *et al*., 2008; Kihara *et al*., 2008).

A bottleneck in understanding the precise function of individual HACD enzymes in mammals has been the presence of paralogues which are differentially expressed between tissues. HACD1 is predominantly expressed in skeletal and cardiac muscle (Ikeda *et al*., 2008; Li *et al*., 2000), HACD4 in leukocytes (Ikeda *et al*., 2008) and both HACD2 and 3 are expressed ubiquitously (Courilleau *et al*., 2000; Ikeda *et al*., 2008; Wang *et al*., 2004). This suggests tissue-specific requirements for HACD enzymes and VLCFA. Hence, to evaluate the specific roles of HACD1 in skeletal muscle we cannot consider it in isolation: a recent report found HACD1 and HACD2 to have functional redundancy therefore suggesting compensatory mechanisms might be possible (Sawai *et al*., 2017).

Two main transcripts of *HACD1* are recognised: specifically, in striated muscles *HACD1-fl* (full length isoform) is expressed and ubiquitously expressed *HACD1-d5* (excluding exon 5) has a different reading frame in the 3' sequence therefore this does not code for the essential amino acids and does not have HACD activity (Blondelle *et al*., 2015; Kihara *et al*., 2008; Maurer *et al*., 2010; Pelé *et al*., 2005). Other splice variants include 'HACD1-CAP' encoding 140 of the full length 288 amino acids, which was reported to be expressed in teeth cementum, heart and liver (Valdés de Hoyos *et al*., 2011), and a transcript encoding only exon 1 of the transcript in haematopoietic stem cells (Tondeur *et al*., 2010). In CNM affected dogs the SINE insertion results in multiple splice variants (Maurer *et al*., 2010; Pelé *et al*., 2005), only one of

these *HACD1-167* expresses exon 6 in frame with the potential for HACD activity (Pelé *et al*., 2005). It is unknown if the other three HACD enzymes are also prone to multiple splicing.

To determine whether zebrafish embryos could be a relevant model for HACD1-deficient myopathies and used to evaluate the role of HACD enzymes in muscle development and disease, normal expression pattern of these enzymes in zebrafish were evaluated to determine whether their functions are likely to be evolutionarily conserved.

Previous work on *hacd1* in zebrafish embryos (Walmsley, 2013) identified the two major *hacd1* transcripts, (*hacd1-fl* and *hacd1-d5)* already characterised in mammals (Maurer *et al*., 2010; Pelé *et al*., 2005; Walmsley, 2013). Zebrafish embryos were seen to have a number of different isoforms in early embryogenesis including *hacd1-fl* following the onset of muscle development in somites (Walmsley, 2013). Preliminary evaluation by whole-mount *in situ* hybridisation (ISH) found expression of *hacd1* within somites from 24hpf and myotome and heart from 72hpf (Walmsley, 2013). We aimed to provide more detail regarding the expression of *hacd1-4* within zebrafish embryos.

2.1.1. Chapter aims

The work of this chapter aimed to characterise the HACD enzymes within developing zebrafish embryos and adult tissues, more specifically to:

1) Identify the zebrafish orthologues to mammalian HACD1-4;
2) Design conventional RT-PCR assays to clone each of these genes to evaluate for alternatively spliced transcripts and as templates to synthesise probes for ISH;
3) Investigate the localisation of *hacd* enzyme transcripts in developing zebrafish embryos by ISH;
4) Develop quantitative RT-PCR assays, including validation of reliable housekeeping genes, to assess the expression levels of *hacd* genes during zebrafish embryo development.

2.2. Methods

2.2.1. Bioinformatics

ENSEMBL and NCBI databases were utilised to identify zebrafish (*Danio rerio*) HACD genes and previously documented transcripts. Coding sequence and amino acid sequence, transcript length, exon arrangement and structure were compared between putative zebrafish HACD enzyme and those from humans, mice and dogs as genome databases for these mammalian species have more in-depth annotation. BLAST search of HACD1 coding sequence was performed to evaluate for other common sequences that might be additional paralogues. Synteny of surrounding areas on chromosomes was also evaluated to obtain evidence for homology which was particularly important considering the ancestral zebrafish genome duplication (Meyer & Schartl, 1999).

2.2.2. Alignments

CLC Workbench (Qiagen) was used to align the *hacd* cDNA transcripts and amino acid sequences with human and murine counterparts. All four zebrafish *hacd* cDNA transcripts and Hacd amino acid sequences were also aligned to evaluate similarity between the four genes and proteins, as any area of high sequence homology would need to be considered later when designing primers and probes. CLC Workbench was also used to annotate and store this data (CLC Bio).

2.2.3. Zebrafish husbandry

Adult AB wild type zebrafish were housed in a licensed facility under a 12 hour light – 12 hour dark cycle and at 28^{o}C. Embryos were staged in accordance to Kimmel *et al*., (1995). Fish were fed a diet of basic grade 230 artemia (ZM systems), tetramin flake (Tetra) and hikari pellets (Hikari) to provide optimised diet for zebrafish breeding. Facility management and handling of fish and embryos was in accordance with local rules and UK Home Office regulations.

2.2.4. Zebrafish rearing

As the optimal age for embryo production in zebrafish is between 6-18 months a stock was bred and reared to breeding age for the purposes of experiments (Nasiadaka & Clark, 2012). Embryos were housed in 5L tanks with constant water flow, and fed on a diet of both live brine shrimp and fish feed tailored to the size of the growing fry (ZM systems).

2.2.5. RNA extraction from zebrafish embryos

Embryo pools of 20 at set embryonic stages were collected in microcentrifuge tubes, system water was removed and then replaced with 1ml TRIzol (Life Technologies). Embryos were then homogenised using a 25g syringe and passed through this 10 times before storage at -80^{o}C until extraction was carried out.

Once thawed, samples in TRIzol were first incubated at room temperature for five minutes. 200µl chloroform (Sigma Aldrich) was added to each sample and agitated for 15 seconds before a two-minute incubation again at room temperature. Samples were then centrifuged at 12,000g for 15 minutes at 4^{o}C. This separated the embryo homogenate into several layers: an upper aqueous phase (containing RNA), an interphase containing DNA and a lower organic protein containing phase. The aqueous phase from each sample was then transferred to new, clean tubes and 500µl isopropanol (Sigma Aldrich) was added to precipitate RNA. These samples were left to incubate for 10 minutes at room temperature (~22^{o}C) before centrifugation at 12,000g for 10 minutes at 4^{o}C. Supernatant was removed and the pellet washed with 1ml of 75% molecular grade ethanol (Sigma Aldrich) and mixed gently. Samples were then centrifuged at 7,500g for five minutes at 4^{o}C. Ethanol supernatant was removed and RNA pellets allowed to air dry for 10 minutes before re-suspension in 20µl RNase-free water.

RNA samples were analysed on the Nanodrop to ascertain concentration (ng/µl) and purity of extracted RNA as measured by the 260/280 and 260/230 absorbance ratios. These provide information on contamination by protein or phenol (260/280 and 260/230 ratios), phenol contamination may arise from TRIzol used during extraction (260/230). A proportion of RNA samples were also sent to the Centre for Genomic Research within the University of Liverpool for samples to be analysed on the Qubit (Thermo Fisher) and Bioanalzyer (Agilent) for further information on RNA quality.

2.2.6. RNA extraction from adult zebrafish tissues

Adult tissues obtained from zebrafish over 12 months of age. Zebrafish were culled via the "concuss and pith" method (Valentim *et al*., 2016). Samples were either snap frozen in liquid nitrogen or stored in RNA Later (Life Technologies).

2.2.6.1. Muscle

Due to the fibrous nature of mature muscle, a fibrous tissue specific RNA extraction kit (Qiagen, catalogue number 74104) was used. The muscle was first ground in liquid nitrogen to a powder before addition of 350µl buffer RLT (containing β-mecaptoethanol to denature RNases). This was then transferred to the QIAShredder column and centrifuged at 13,000rpm

for two minutes at 4ºC. Proteinase K (Qiagen) diluted in RNase-free water (600µl total) was then added to debris and incubated for 10 minutes at 55ºC. Following steps were all carried out at room temperature. Incubated samples were then centrifuged at 10,000rpm for three minutes before supernatant was collected and combined with 500µl of 96-100% ethanol. Solution was then transferred to the Qiagen RNeasy columns and centrifuged at 8,000g for 15 seconds and flow through discarded: this was done twice to ensure flow through was eliminated from column. 350µl buffer RWI was added and columns centrifuged at 8,000g for 15 seconds and again flow through discarded. 80µl of buffer RDD and Dnase solution was added to column and incubated at room temperature for 15 minutes. Columns were then centrifuged again at 8,000g for 15 seconds and 500µl buffer RPE added before another centrifuge step at 8,000g for 15 seconds and flow through discarded, this was repeated again as well as an extra centrifuge step with no addition of buffer RPE to completely remove leftover buffer. 30µl RNase free water was then added and columns were spun at 8,000g for one minute to elute through RNA. Samples were also assessed for purity on the Nanodrop as described in Section 2.2.6.

2.2.6.2. Other (non-fibrous) tissues

All other adult tissues were ground in liquid nitrogen as in Section 2.2.6 and RNA was then extracted using the TRIzol method described in Section 2.2.5.

2.2.7. cDNA synthesis from zebrafish embryo and adult RNA for RT-PCR

cDNA was synthesised by reverse transcription (RT) (SuperScript III, Invitrogen) using 8µl of approximately 1µg RNA (isolated by protocols in sections 2.2.6.1 and 2.2.6.2) and was combined with 1µl random primers (50ng/µl) and 1µl of 0.5mM dNTPs. The reaction was run for five mins at 65ºC followed by one minute at 4ºC before the addition of 10mM DTT, 1x RT buffer, 2.5mM MgCl2, 40U/µl RNase out and 200U/µl SuperScript III reverse transcriptase. Reaction was then run for a further 10 minutes at 25ºC, 50 mins at 50ºC and 85ºC for five minutes before the addition of RNase (2U/µl) and run at 37ºC for 20 minutes to remove any residual RNA. 2µl of cDNA was then used for further RT-PCR reactions.

2.2.8. RT-PCR

Primers were designed using the open source website Primer3 (http://primer3.ut.ee/) to amplify a 600-800 base pair fragment of cDNA for *in situ* hybridisation probe generation (Table 2.1). Primers were designed to cover the coding sequence and include the start codon and essential amino acids so they could be cloned for use in expression vectors and would allow us to evaluate for the presence of alternative transcripts. HACD1, HACD2 and HACD4 coding sequences are 729, 735 and 669bp respectively therefore the same primer pair was

suitable for both these applications. The coding sequence of HACD3 is 1080bp, therefore separate primers were designed for probe generation and cloning. Due to the sequence similarity between HACD1 and HACD2 an additional set of primers was designed to generate a probe in the 3' UTR of HACD2 for evaluation.

RT-PCR was performed using Amplitaq Gold DNA polymerase (Applied Biosciences). Each 50µl reaction contained: 4% cDNA, 0.25µM forward and reverse primers, 0.25mM dNTPs (Fisher Scientific), 1 x PCR buffer II, 2.5mM MgCl2 and 0.025U/µl Taq DNA polymerase (Applied Biosciences). Reactions were run for 35 cycles of: 95ºC for five minutes (initial denaturing) followed by 40 cycles of 94ºC for 30s (denaturing), 55ºC for 30s annealing (unless otherwise stated as this is primer dependent and reactions were optimised via temperature gradients to determine annealing temperature) and 72ºC for 50s extension (unless otherwise stated) and a final extension step of 72ºC for seven minutes. PCR products were visualised after gel agarose electrophoresis on a 1.5-2% gel with GelRed nucleic stain (Cambridge Biosciences). Products were run against either a 100bp or 1kbp ladder (Invitrogen) and all samples were mixed with BlueJuice loading dye to aid visualisation and loading (Invitrogen).

PCR products were then purified prior to cloning or sequencing using a QIAquick PCR purification kit (Qiagen, catalogue number 28104) or, where multiple bands were detected, bands were cut out of the agarose gel under UV light and extracted using a gel extraction kit (Qiagen, catalogue number 28704). Sequencing was carried out by commercial company (GATC Biotech) and analysed in CLC workbench.

Table 2.1: List of RT-PCR primers used to amplify up cDNA for RNA probe synthesis and cloning, annotated with red arrows in Figure 2.5.

Primer	Product	Product Length (bp)	Primers (5'-3')
hacd1	Transcript including start and essential amino acid codons. Exons 1-7.	730	**F:**GTTTTTGTGACTTTCGCAGT **R:**AAGTACCCTCCTCCTTTGAC
hacd2	Transcript including start and essential amino acid codons. Exons 1-7.	777	**F:**GCTGGATTCATAAGCAGCTT **R:**CATGTGGAAGTAGAGCTGAG
hacd2 3' UTR	Transcript including stop codon. Exons 6-3'UTR	712	**F:**ACTACCACACGTTCCTCATC **R:** TTCTTTTGTTTTGTGCTGTG
hacd3	Transcript including essential amino acids and stop codon. Exons 5-11/3'UTR as reverse primer binds across stop codon.	706	**F:**TTGAGTCAAGGGTTCGTAAG **R**: CTTGCTCTTTCCTCAGCGTT
hacd4	Transcript including start, essential amino acids and stop codons. Exons 1-7.	776	**F:**TGTAATCAGAACTTCCTCACA **R:**ACCTGTTCATCATCGTCTTT

Several primer pairs were initially designed and tested for each assay. Reaction conditions were optimised including the annealing temperature was determined by applying a gradient to different reactions in the thermocycler; a range of magnesium concentrations was also trialled for certain reactions to improve product yield or reduce any non-specific binding that might have occurred.

2.2.9. Cloning of *hacd* transcripts

Purified products from RT-PCR assays were cloned for sequencing, to allow for future sub-cloning into an expression vector and for synthesis of RNA probes for *in situ* hybridisation.

Transcripts were ligated into the pGEM-T plasmid vector (Promega) (Figure 2.1) (50ng) containing both the T7 and SP6 promoter sites using the T4 ligase enzyme (Promega) overnight at 4ºC. Reaction contained 3µl transcript, 5µl 1X reaction buffer, 1µl vector (50ng) and 1µl T4 ligase (3 Units/µl).

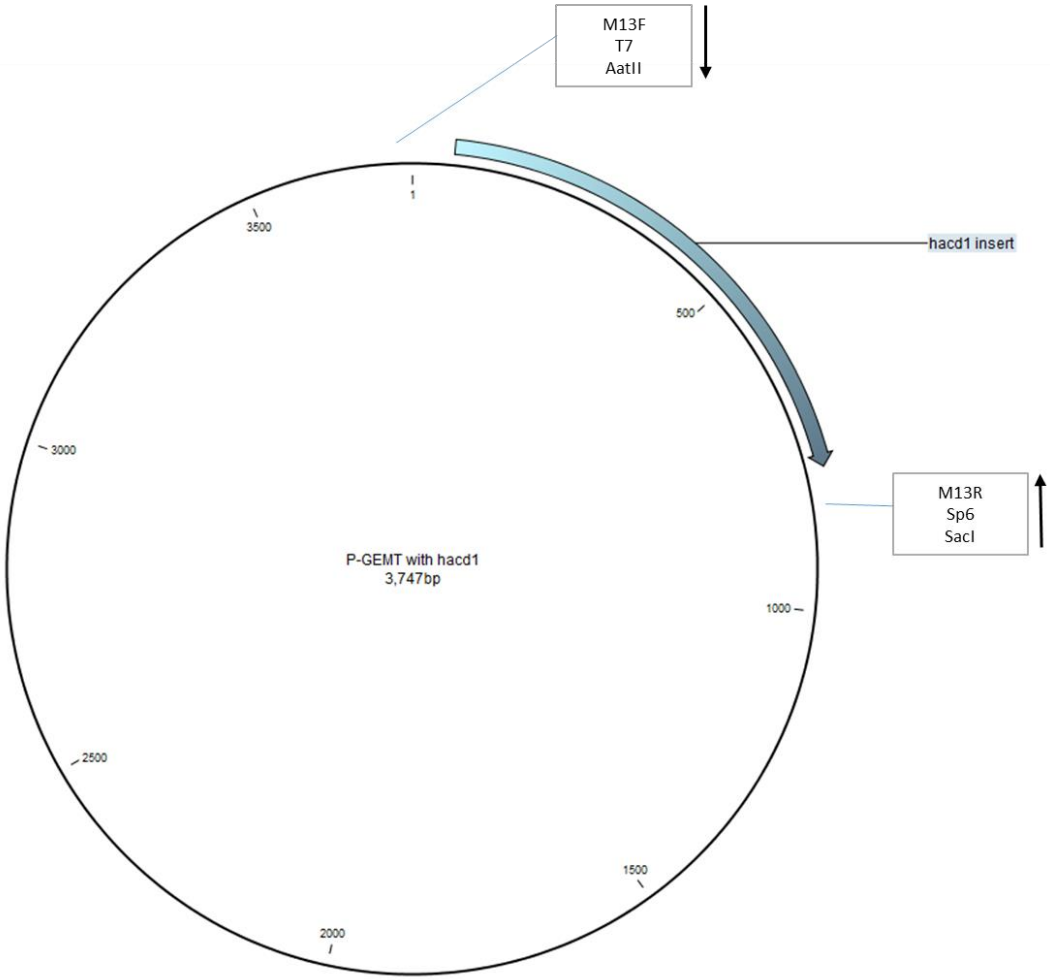

Figure 2.1: pGEM-T plasmid with *hacd1* transcript inserted as an example.
Universal M13 primer binding sites and polymerase sites Sp6 and T7 (used for probe synthesis) are annotated.

Plasmids were used to transform chemically competent E.coli (TOP10, Invitrogen) using heat shock. The entire ligation mixture was added to 50µl of competent cells and incubated on ice for 30 minutes. This mixture was heat shocked at 42ºC for 30 seconds before placing on ice again for two minutes. 250µl SOC medium (Super Optimal broth with Catabolite repression, Sigma Aldrich) (preheated to 37ºC) was added and shook for one hour at 225rpm. This was then plated and colonies were allowed to grow overnight at 37ºC on LB agar plates containing 100µg/mL ampicillin (Sigma Aldrich).

Individual colonies were selected and seeded into LB broth containing 100μg/mL ampicillin (Sigma Aldrich) and grown overnight again at 37ºC in in an orbital shaker. To confirm successful transformation with ligated vector, RT-PCR reactions were performed either directly on selected colonies or from the broth after overnight incubation. To simplify probe synthesis, we required ligation of *hacd1-4* in the correct orientation for antisense probe synthesis from SP6 promoter and sense (control) probe synthesis from the T7 promoter. To select for this, the M13 reverse primer found within the plasmid sequence was used alongside the forward primer for the transcript to produce the desired product if cloning was successful (Figure 2.2). Plasmid DNA was then extracted by Miniprep spin columns (Qiagen, catalogue number 27104) and sent for sequencing using the universal primer binding site (M13R) and a primer from inside the *hacd* insert (GATC). Purified plasmid from several colonies for each of *hacd1-4* were sent for sequencing to evaluate the sequence of cloned transcripts. Plasmids confirmed by sequencing to contain full length *hacd* transcript in the desired alignment and with the correct sequence with no errors were used to synthesise *in situ* hybridisation probes.

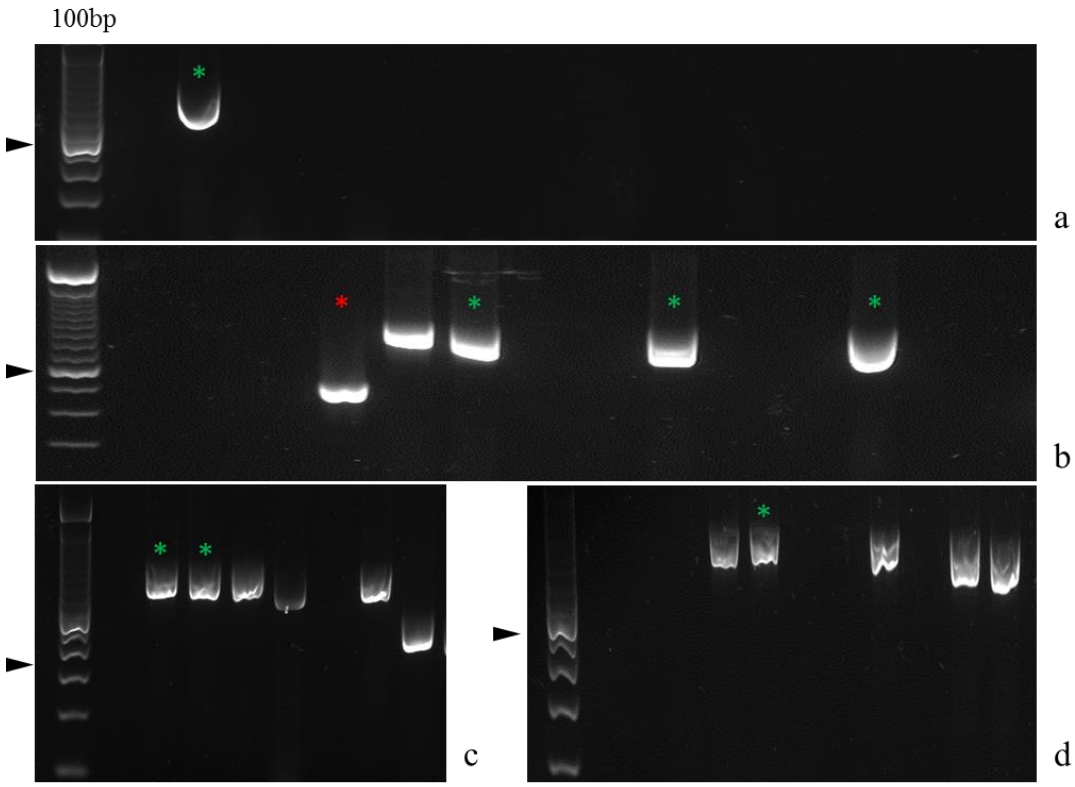

Figure 2.2: RT-PCR evaluation of cloning for full length *hacd* transcripts.
Selective RT-PCR for (a) *hacd1*, (b) *hacd2*, (c) *hacd3* and (d) for *hacd4* ligated into pGEM-T performed on transformed bacterial colonies, green asterisk indicates colonies subsequently confirmed by sequencing to have the correct sequence for the full length transcript inserted in the desired orientation. The red aterisk indicates a novel isoform of *hacd2* encoding exons 1, 2 and 7. All gels were run against the 100bp ladder, black arrow indicating the 600bp reference band.

2.2.10. *In situ* hybridisation

2.2.10.1. RNA probe synthesis

pGEM-T plasmids containing the *hacd* sequences were purified by Midiprep (Qiagen, catalogue number 12125) and approximately 1µg/µl plasmid was linearised using either AatII or SacI in 50µl reactions at 37ºC overnight (16 hours) before a 20-minute heat inactivation step (80ºC for AatII and 65ºC for SacI). Efficiency of restriction enzyme activity was assessed by performing single and double digests of each plasmid to check for complete digestion. Figure 2.3 shows the restriction digests performed on the pGEM-t plasmids containing a *hacd* transcript after digest via either AatII, SacI, cut with both and the uncut plasmid. When cut by either AatII or SacI the linearised plasmid was ~3000bp in length, and when plasmid was digested successfully with both enzymes this produced a larger fragment of DNA at ~2500bp and a smaller fragment of ~500bp. The uncut plasmid ran at several levels due to the nature of circular DNA running through agarose: bands were produced from the circular structure, supercoiled and with single strand nicks in its structure. This verified that other plasmids were

completely linearised before moving onto the probe synthesis, as without completely linear plasmid DNA the reaction efficiency is impaired.

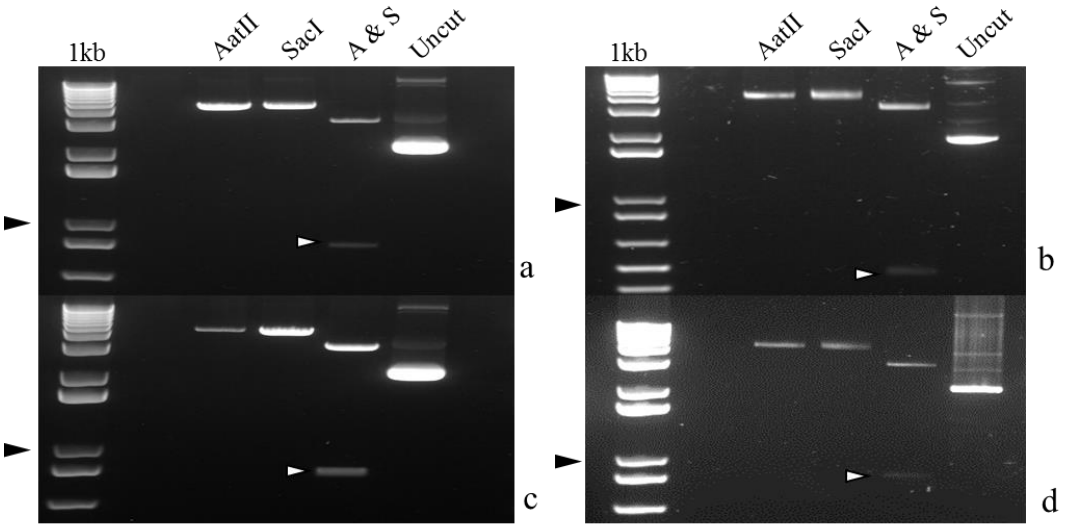

Figure 2.3: Restriction digest of pGEM-T plasmid containing *hacd1-4* inserts (panels a-d respectively).
Plasmids were cut with either AatII, SacI or a double digest was performed with both enzymes. Samples were run against uncut plasmids as a control and a 1kb plus ladder, black arrow indicates 1kb reference band. For all single digests the results show single bands of the linearised plasmid which was approximately 3.5-4kb in size. The double digests all produced two bands of the expected length of approximately 3kb and a smaller band containing the *hacd* transcript at 600-800bp (white arrows).

Linearised plasmids were cleaned using sodium acetate and ice-cold ethanol and concentration assessed on the Nanodrop. Then 1µg of purified DNA template was used to synthesise digoxigenin-labelled (Roche) RNA probes using the SP6 (antisense probes) and T7 (sense probes) polymerases within the pGEM-T sequence. Alongside the DNA the reaction included 1X NTP labelling mixture (containing 10mM ATP, 10mM CTP, 10mM GTP, 6.5mM UTP and 3.5mM DIG-11-UTP), 1X transcription buffer, RNase inhibitor (20U/µl) and either the SP6 or T7 RNA polymerases (20U/µl). The reaction was run for two hours at 37ºC before RNase free DNase was added (10U/µl) to the reaction and run for a further 15 minutes to remove any leftover DNA template. RNA probes were also subject to a cleaning protocol, this time using 1X TE buffer (Sigma Aldrich), LiCl (Sigma Aldrich) and ice-cold ethanol. Probes were frozen in 5µl aliquots and stored at -80ºC to prevent degradation. Probes were visualised and checked via agarose gel electrophoresis at various stages after DNase treatment and purification steps. Figure 2.4 shows successful clean-up of all probes (lanes 2 and 4 display a few clear bands, indicative of running RNA on an agarose gel). One lane 1 is missing bands, due to the sample not being saved to run on the gel, however the cleaned probe in lane 2 depicts a successful reaction and clean-up process (Figure 2.4d).

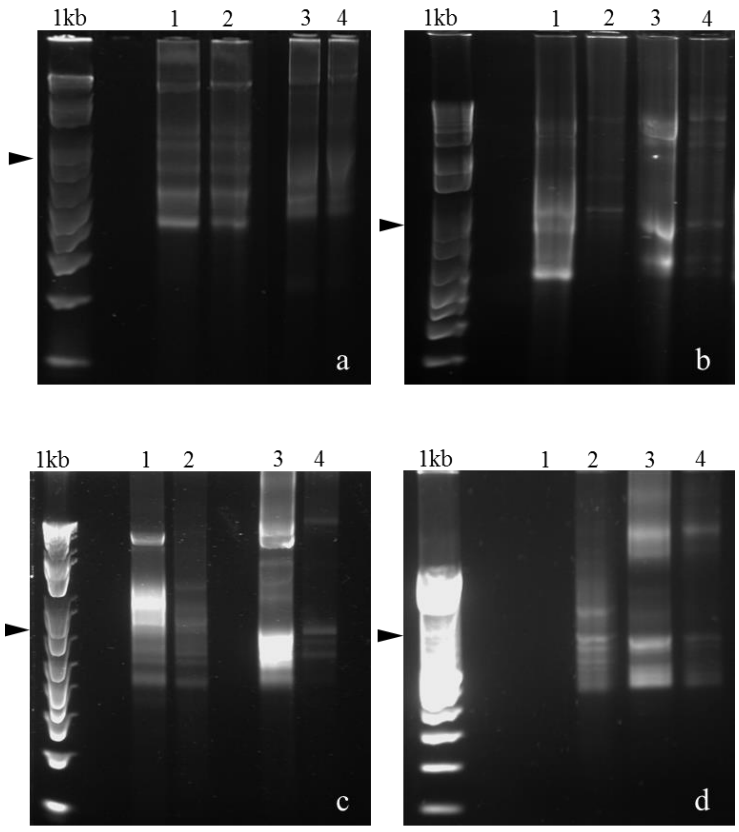

Figure 2.4: DIG-labelled RNA probe clean up for *in situ* hybridisation, run on 1% agarose gel. Figures a-d represent RNA probes for *hacd1-4* respectively. Lanes numbered 1 represent the unclean antisense RNA probe and lane 2 the cleaned probe. Lanes 3 indicate the unclean sense probe with 4 representing the final cleaned product. All cleaned up products show a number of clearly defined bands indicative of RNA gels.

2.2.10.2. *In situ* hybridisation protocol

Embryos from different developmental stages were collected and fixed in 4% paraformaldehyde (PFA) before dehydration through graded concentrations of methanol and storage at -20ºC. They were then rehydrated with PBS (Sigma Aldrich) and 0.1% Tween-20 (Sigma Aldrich) before the experiment and prepared for experiment dependent upon age (Table 2.2). Embryos over 48hpf were first de-pigmented via a bleaching solution (0.5x SSC (Sigma Aldrich), 1% H_2O_2 (Sigma Aldrich), 5% formamide (Sigma Aldrich) and 0.1% Tween-20 in PBS) and then permeabilised with proteinase K (Table 2.2), any embryos under 48hpf had not developed enough pigment to require this step.

Table 2.2: Proteinase K (10µg/ml) digestion times of zebrafish embryos prior to *in situ* hybridisation.

Embryos were digested in various concentrations for differing lengths of time according to their age as hours post fertilisation (hpf).

Age of Embryo (hpf)	Permeabilisation in Proteinase K
10-12	2.5 mins in 1X
16-22	3 mins in 1X
24	10 mins in 1X
36-48	10 mins in 1X
48	10 mins in 1X
72	20 mins in 2X
96	20 mins in 3X

Embryos were then incubated in a prehybridisation solution (50% formamide, 5x SSC and 0.1% Tween-20, pH 6) for two hours at 68ºC before changing the solution to a hybridisation solution (50% formamide, 5x SSC, 0.1% Tween-20, 5mg/ml torula RNA (Sigma Aldrich), 50µg/ml heparin (Sigma Aldrich), pH 6 and preheated to 70ºC) and incubated for one hour at 68ºC. Solution was then changed to fresh hybridisation solution (again preheated to 70ºC) and digoxigenin-labelled RNA probes (antisense or sense) added before incubating overnight.

After overnight incubation embryos were put through a series of wash steps (with solutions all preheated to 70ºC and washes carried out at 68ºC. The first wash was five minutes in prehybridisation solution before five minutes with 25% prehybridisation solution and 75% 2x SSC. Embryos were then washed in 2x SSC for 10 minutes, twice, before three washes of 0.2x SSC for 30 minutes. MABT buffer (150mM NaCl (Sigma Aldrich), 100mM malic acid (Sigma Aldrich) and 0.1% Tween-20) was then used to wash embryos twice for five minutes before embryos were blocked with 2% Blocking Agent (Roche) in MAB buffer (MABT without Tween-20) for 2.5 hours at room temperature on a rocker to aid prevention of non-specific staining before incubating in the 2% blocking solution with a 1:6000 dilution of anti-DIG (conjugated with an alkaline phosphatase) overnight at 4ºC. Colour was then developed with Nitro Blue Tetrazolium (NBT) and 5-bromo-4-chloro-3-indolyl phosphate (BCIP) (Sigma Aldrich) through detection of the alkaline phosphatase conjugated to the antibody. BCIP is a substrate to the alkaline phosphatase which was oxidised by the NBT to form the blue dye 5,5′-dibromo-4,4′-dichloro-indigo.

Bright field images were taken with an Olympus SZX12 camera and embryos then fixed in 4% PFA and stored at 4ºC prior to processing and sectioning.

2.2.11. Whole embryo processing & sectioning

Embryos were processed by hand as, having been previously permeabilised and bleached, auto-processing proved too harsh and embryos fragmented. Embryos were first washed twice in Diethyl pyrocarbonate (DEPC, Sigma Aldrich) treated water for 10 minutes to remove any PFA. Embryos were then dehydrated with increasing ethanol washes (10 minutes in 30%, 50%, 70%, 95% and two x 100% ethanol) before the infiltration stage using increasing concentrations of xylene (Sigma Aldrich) in ethanol to aid the paraffin later infiltrate the tissue (10 minutes in 50% xylene, 75% xylene and 100% xylene). Embryos were then immersed in melted paraffin for two x 20 minutes to allow time for complete infiltration.

Embryos were then embedded in fresh paraffin to allow for either transverse or longitudinal sectioning. Sectioning was performed using a Leica Microtome and sections were cut at a thickness of 4 microns. Sections were left overnight at 37^{o}C to dry on the coverslips and then dewaxed with two x 100% xylene washes for five minutes before cover slipping with DPX mountant (Sigma Aldrich) to protect samples and ensure their longevity. Sections were then imaged with the Zeiss BX60 microscope using bright field microscopy.

2.2.12. cDNA synthesis for qRT-PCR

From RNA isolated as described in section 2.2.5, 1µg was converted to cDNA by reverse transcriptase (iScript, BioRad). RNA was combined with nuclease free water to give a volume of 13µl then added to 1x Reaction Mix (4µl) and iScript reverse transcriptase (1µl). Reaction was run at 25^{o}C for five minutes, 46^{o}C for 20 minutes and 95^{o}C for one minute. cDNA was then stored at -20^{o}C until use.

2.2.12.1. qRT-PCR geNorm

As this study involved zebrafish embryos developing from a single cell to an organism capable of self-feeding at 5dpf (days post fertilisation) many genes will be up and down regulated within this time frame. Housekeeping genes for embryonic zebrafish have been previously published (Cooper *et al*., 2006; McCurley *et al*., 2008), however these did not work or were highly inefficient when tested. Thus, a housekeeping test was conducted with a 14-primer assay to determine the most stable genes between 12-96hpf. This qRT-PCR reaction was set up as described in Section 2.2.13 and analysis was done via the qBase+ software (Biogazelle). Genes tested for stability were: *gapdh, actb2, 18s, actb1, sdha, top2a, usp5, ef1a, eif1b, ywhaz, slc25a5, rlp13, nadh* and *atpsynth*.

2.2.12.2. qRT-PCR primer and assay optimisation

Primers were self-designed initially but found to have poor efficiencies and so the final primers used in this thesis were designed by Primer Design based on information provided about different transcripts in zebrafish embryos. Cloned *hacd1-4* transcripts were provided as positive control for initial validation by Primer Design. All primers crossed one exon-exon boundary, except the primer set for *hacd3* (Figure 2.5). Primers for both *hacd1* and *hacd2* were designed to have two sets: one to amplify up total amount and one set designed to amplify just the full-length isoforms that contain the essential amino acids for HACD activity (Kihara *et al*., 2008). Table 2.3 displays the sequences for primer sets (Primer Design) used in this study and Figure 2.5 shows annotation of these primers qRT-PCR in purple, as well as those used in RT-PCR experiments (for ISH probe synthesis, red annotations) in Section 2.2.8. Appendix figures A1.2, A1.3, A1.4 and A1.5 represent the *hacd1-4* cDNA sequences with primers annotated.

Table 2.3: List of final zebrafish qPCR primers.
Sequences of the house keeper genes from Primer Design were not provided.

Gene	Product Length (bp)	Primers (5'-3')
hacd1-total	85	**F:**GTGTCCTTTGACTATTACTACTTCTTGA **R:**GTAGCATGTGGAAGTAGAGCTGA
hacd1-fl	112	**F:**AGCATCAGACAGATTCAGAACGAG **R:**GCAGATGGTTGAGCAGGTTGAA
hacd2 - total	95	**F:** GACCATTGGATGATCCAGTCTTTC **R:** GCACAGTGAGTCCGGTCAC
hacd2-fl	114	**F:**ACCCGATGGGAGTGATGGG **R:**AGTCGAATGAGAAGTTGTACTTGTTAG
hacd3	75	**F:**GTTGGCCTGCATTGACACTG **R**:AGAGGGTACAGCGGCATCC
hacd4	120	**F:**CACCGATGTACATGTATTCTCCATA **R:**TCCAGCTCTCCAGATTCTCTTT
rlp13	N/A	Sequence not provided
nadh	N/A	Sequence not provided
ATP-synthase	N/A	Sequence not provided

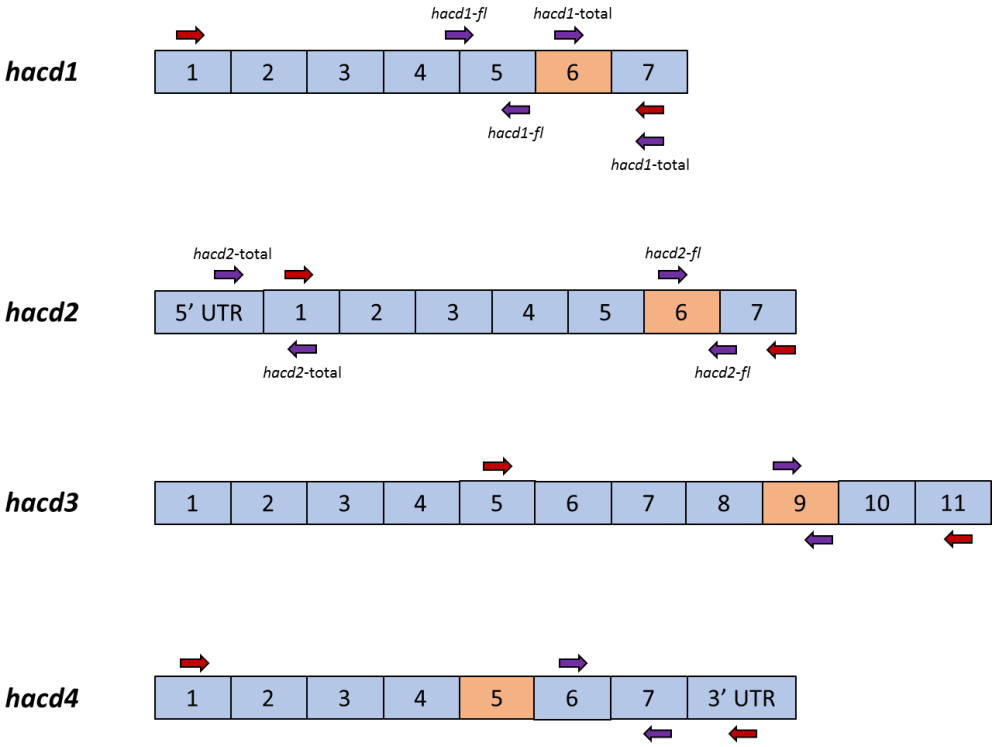

Figure 2.5: Annotation of both RT-PCR primers used for the synthesis of *in situ* hybridisation (ISH) probes and qRT-PCR primers.
Exons are numbered and in blue, with the exon containing the essential amino acids in orange. Red arrows indicate ISH primers and purple indicate qRT-PCR primers. Where two sets of qRT-PCR primers were used these have been labelled.

To confirm there was no contamination by genomic DNA, qRT-PCR assays included a well where the template was prepared without addition of reverse transcriptase for cDNA synthesis (no RT control) and to confirm no contamination of reagents of false positive results a well was run with molecular grade water instead of cDNA (no template control). Primers from Primer Design were independently validated once received and standard curve reactions were performed to evaluate assay efficiencies as a secondary validation. Standard curves were run with a pooled set of zebrafish embryo cDNA from various time points throughout development as template and the cDNA was serially diluted 1:10, 1:100, 1:1,000 and 1:10,000. A reaction efficiency of 90-110% indicates that the amount of product is being doubled every cycle (Figure 2.6a).

The standard curve (Figure 2.6c) allows calculation of the efficiency of the reaction and also a correlation coefficient (R^2) value. Efficiency is calculated using the slope of the graph (Figure 2.6c) using the following equation:

$$\mathbf{E} = \left(\mathbf{10}^{\frac{\mathbf{-1}}{\mathbf{slope}}} - \mathbf{1}\right) * \mathbf{100}$$

Equation 2.1

Melt curves and peaks were assessed to ensure they only produced one clear peak, indicating only one target was being amplified (Figure 2.6a&b) (Wienken *et al*., 2011).

All the *hacd* genes passed this validation with efficiencies of 90-110% (Table 2.4) with the exception of *hacd4* which was slightly below this. It was concluded this was likely due to the low abundance of *hacd4* due to higher Ct values within these assays.

Table 2.4: qRT-PCR primer validation results for *hacd* genes in zebrafish.

Primer	Efficiency (%)	R^2	Slope
hacd1-total	112.8	0.997	-3.049
hacd1-fl	95.5	0.995	-3.435
hacd2-total	97.1	0.989	-3.394
hacd2-fl	91.5	0.993	-3.545
hacd3	94.4	0.997	-3.464
hacd4	87.8	0.991	-3.653

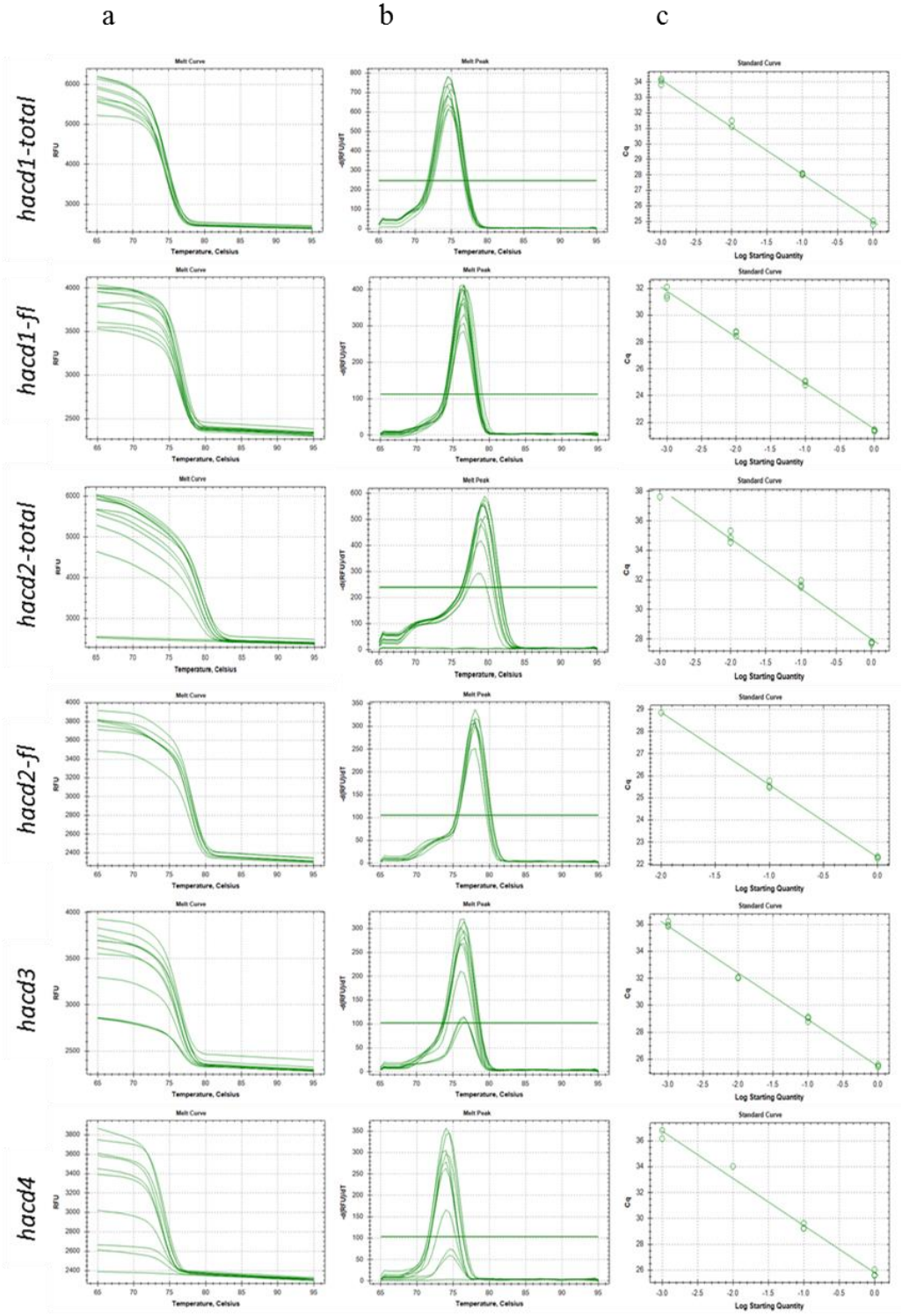

Figure 2.6: Validation of all pRT-PCR assays for *hacd1-4* expression in embryonic zebrafish.
Outputs from BioRad CFX Manager software: (a) melt curves, (b) melt peaks both indicating only single products being amplified and therefore primers sufficiently specific and (c) standard curves reporting on the efficiency of primers.

2.2.13. Quantitative RT-PCR assay

20µl reactions were run with 8µl cDNA diluted 1:100 using molecular grade water, 2µl (0.15µM) primer and 10µl (1x) SYBR green mastermix (Roche). Each reaction was run at 95ºC for 10 minutes to initially denature the cDNA before 40 cycles of: 95ºC for 15 seconds followed by a combined annealing and extension step at 58ºC or 60ºC (primer dependent) for one minute. Reactions were run on the BioRad CFX Connect Real Time PCR System (BioRad).

Zebrafish embryo cDNA was tested at 12, 24, 48 and 72hpf in triplicate to assess levels of each gene over development including both full length isoforms of *hacd1* and *hacd2*. Expression levels were calculated via the ΔΔCt method (Livak & Schmittgen, 2001) and normalised against three housekeeping genes: *rlp13*, *nadh* and *atp-synthase*, selected after stability analysis.

2.2.14. Statistical analysis

Analysis of variance (ANOVAs) were conducted for qRT-PCR data in GraphPad Prism (GraphPad Software Inc.) and represented as mean values with error bars indicating standard error of the mean (SEM). Significance annotated on graphs as follows: * indicates $p \leq 0.05$, ** indicates $p \leq 0.01$, *** indicates $p \leq 0.001$ and **** indicates $p \leq 0.0001$.

2.3. Results

2.3.1. Using bioinformatics to identify the zebrafish orthologues of the HACD enzymes

To identify HACD enzymes in zebrafish the ENSEMBL database was consulted to identify genes most likely to be orthologues of mammalian HACD1-4 and evaluate for other potential paralogues (particularly important in zebrafish due to their genome duplication). Transcript data was also evaluated and compared, particularly those likely to have functional HACD activity and the potential to compensate for HACD1-deficiency (Kihara *et al*., 2008; Sawai *et al*., 2017). Exon arrangements and synteny were compared with human and murine databases as transcriptomic annotation of zebrafish genes was comparatively poor.

2.3.1.1. HACD1

The ENSEMBL genome database reported one orthologue for human HACD1 in zebrafish (Danio rerio) ENSDARG00000103744. This gene was previously suggested as the zebrafish homologue of HACD1 (Walmsley, 2013) based on sequence similarity, exon arrangements and transcript expression in muscle, and this sequence was annotated as *hacd1* in the ENSEMBL database. Some synteny was apparent on comparison of the region surrounding *hacd1* with corresponding area in humans and mice (Figure 2.7). Only one transcript was listed on ENSEMBL for *hacd1* (NCBI Reference Sequence NM_014241.3, ENSDART00000157873, which is the full 7 exon length isoform *hacd1-fl*) in zebrafish, however two main transcripts have been listed previously (*HACD1-fl* and *HACD1-d5*) in canine (Pelé *et al*., 2005) mouse tissues (Blondelle *et al*., 2015) and were also found in zebrafish embryos (Walmsley, 2013).

On the ENSEMBL database, the human HACD1 had the full length transcript listed (ENST00000361271.8) and two other listed transcripts that were said to be protein coding (ENST00000326961.6 and ENST00000466335.1) though neither encoded exon 6 with the essential amino acids, therefore suggesting no HACD activity. The canine HACD1 had four listed transcripts that were protein coding on ENSEMBL: the full length *HACD1-fl* (ENSCAFT00000049354.2), a second transcript with an extra exon, a third with 10 exons that were mostly a few base pairs long, suggesting this transcript required further characterising (ENSCAFT00000045812.1) and finally the *Hacd1-d5* transcript (ENSCAFT00000037117.3). The mouse HACD1 gene had three protein coding transcripts, the full length *Hacd1* (ENSMUST00000114753.7), one transcript with eight exons (ENSMUST00000074854.8) and the *Hacd1-d5* transcript (ENSMUST00000091429.11).

The zebrafish *hacd1* gene had three paralogues listed in the genome browser: *hacd2* (ENSDARG00000014806), *hacd3* (ENSDARG00000016038) and *hacd4* (ENSDARG00000102221) as expected and had conserved amino acid sequences among the paralogues (Appendix Figure A1.1). Sequence identity between human *HACD1-fl* and zebrafish *hacd1-fl* was 74%. BLAST search of Hacd1 amino acid sequence in ENSEMBL against the zebrafish protein database returned only Hacd1-4.

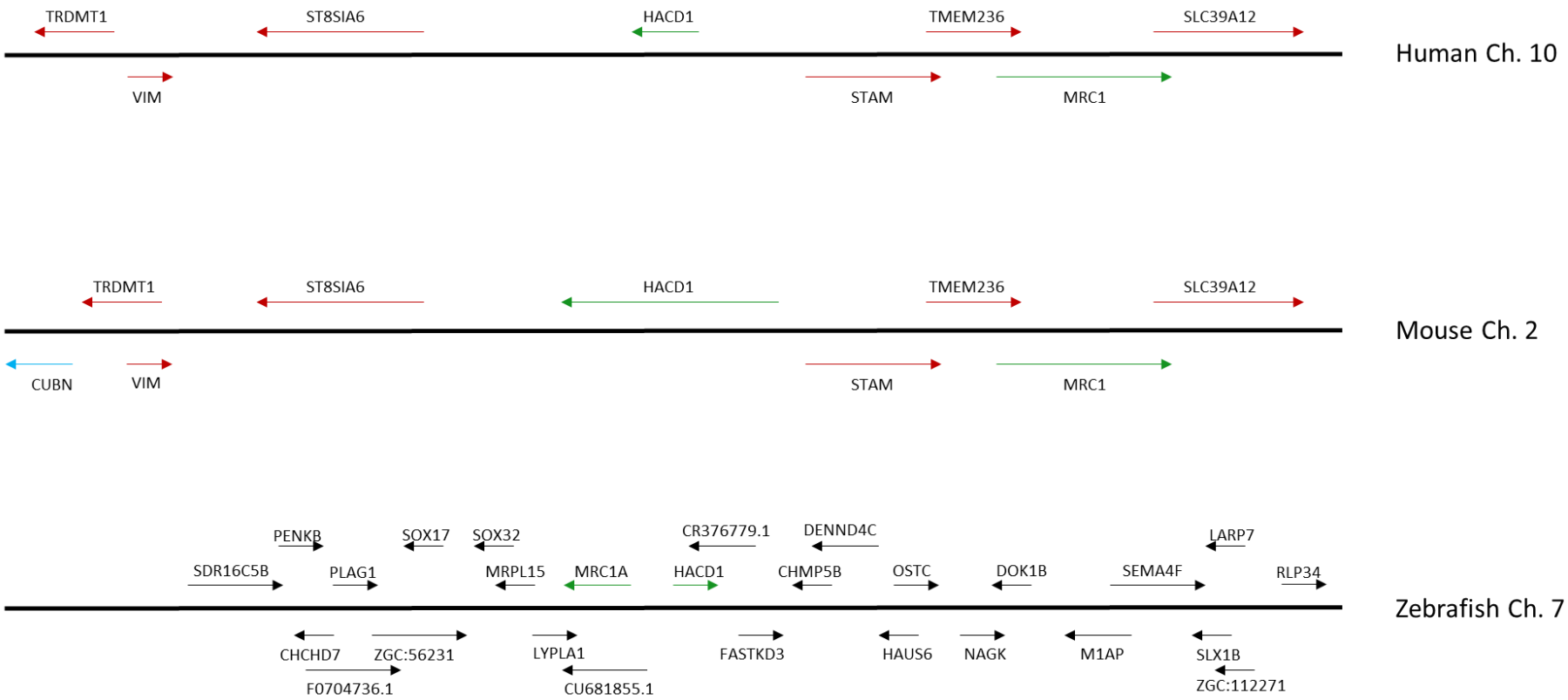

Figure 2.7: Synteny of the HACD1 gene over human, mouse and zebrafish species over a 1MB region.
Genes found in all three species are annotated in green, genes found in human and mice annotated as red, those only in mouse annotated as blue and genes only in the zebrafish sequence in black.

2.3.1.2. HACD2

ENSEMBL identified one zebrafish orthologue for HACD2 gene (ENSDARG00000014806). Analysis of synteny reported the gene to be in a syntenic block of four other genes across human and mouse genomes (Figure 2.8). ENSEMBL genome browser identified three transcripts for *hacd2* for zebrafish gene, five for the human and one for the mouse gene. One transcript (ENSDART00000133998), likely to be the orthologue of the protein encoding human HACD2 (due to comparison of exon arrangement) had a 78% sequence identity with the human *HACD2*. A BLAST search of Hacd2 amino acid sequence in ENSEMBL against the zebrafish protein database returned only Hacd1-4. The zebrafish *hacd2* gene had a target ID with *hacd1* of 60%.

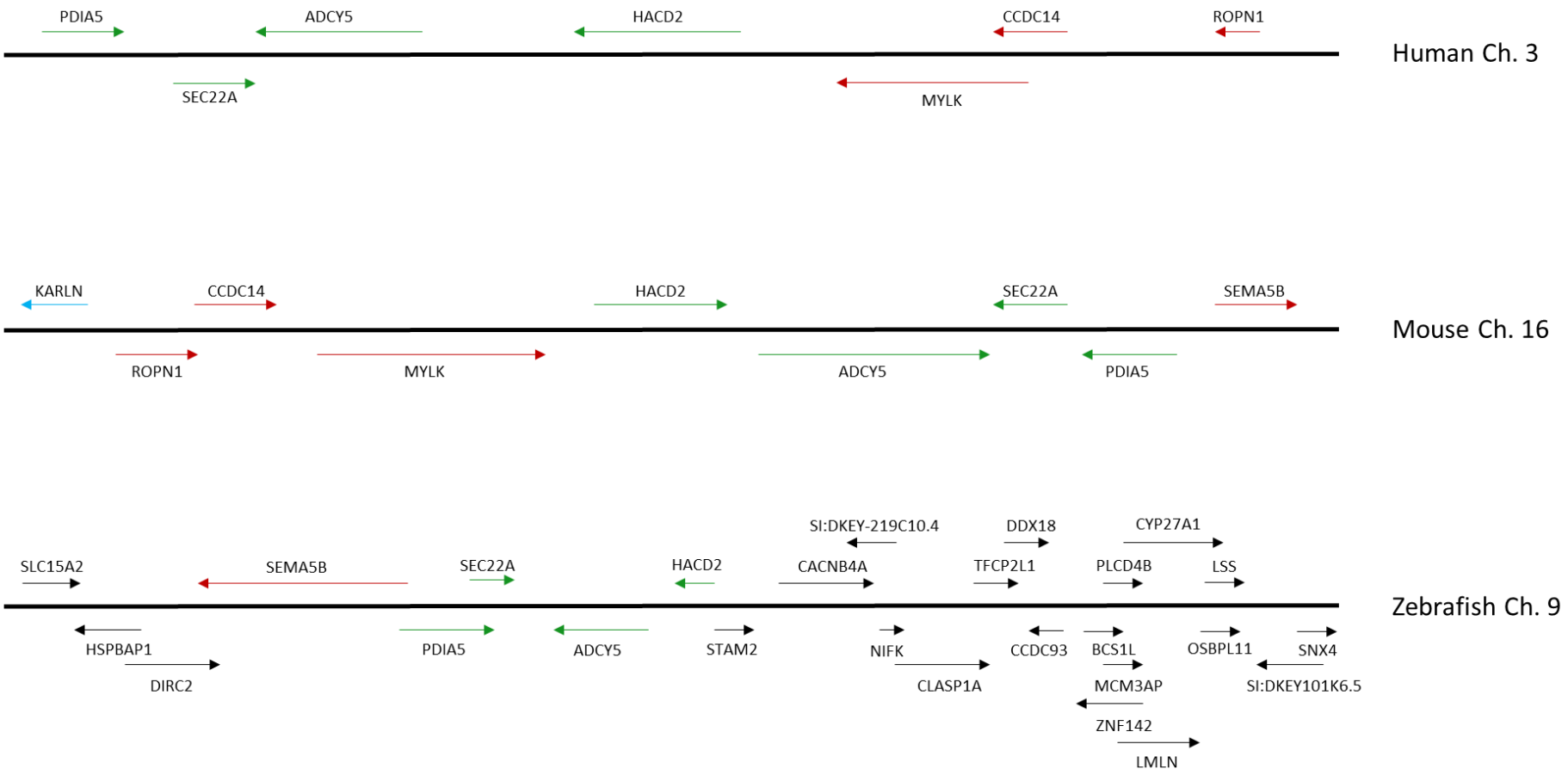

Figure 2.8: Synteny of the HACD2 gene over human, mouse and zebrafish species over a 1MB region.

Genes found in all three species are annotated in green, genes found in human and mice annotated as red, those only in mouse annotated as blue and genes only in the zebrafish sequence in black.

2.3.1.3. HACD3

ENSEMBL identifies one zebrafish orthologue for HACD3 and this zebrafish *hacd3* gene (ENSDARG00000016038) and this was found in a block of six genes that had conserved synteny across human and murine genomes (Figure 2.9). There was one transcript (ENSDART00000006300) listed for the zebrafish *hacd3* gene, 12 transcripts for human and one transcript listed for the murine genome. The zebrafish transcript (ENSDART00000006300.7) and what was likely to be the full length HACD3 human transcript (ENST00000261875.10), due to its high annotation and exon arrangement shared a 70% sequence identity. BLAST search of Hacd3 amino acid sequence in ENSEMBL against the zebrafish protein database identified Hacd1-4 as the top hits with a family of prostaglandin synthase proteins also returned; however, these had shorter alignments of lower identity which did not match with the conserved region and essential amino acids in exon 9. The zebrafish *hacd3* gene had a target ID of 18% with the *hacd1* gene.

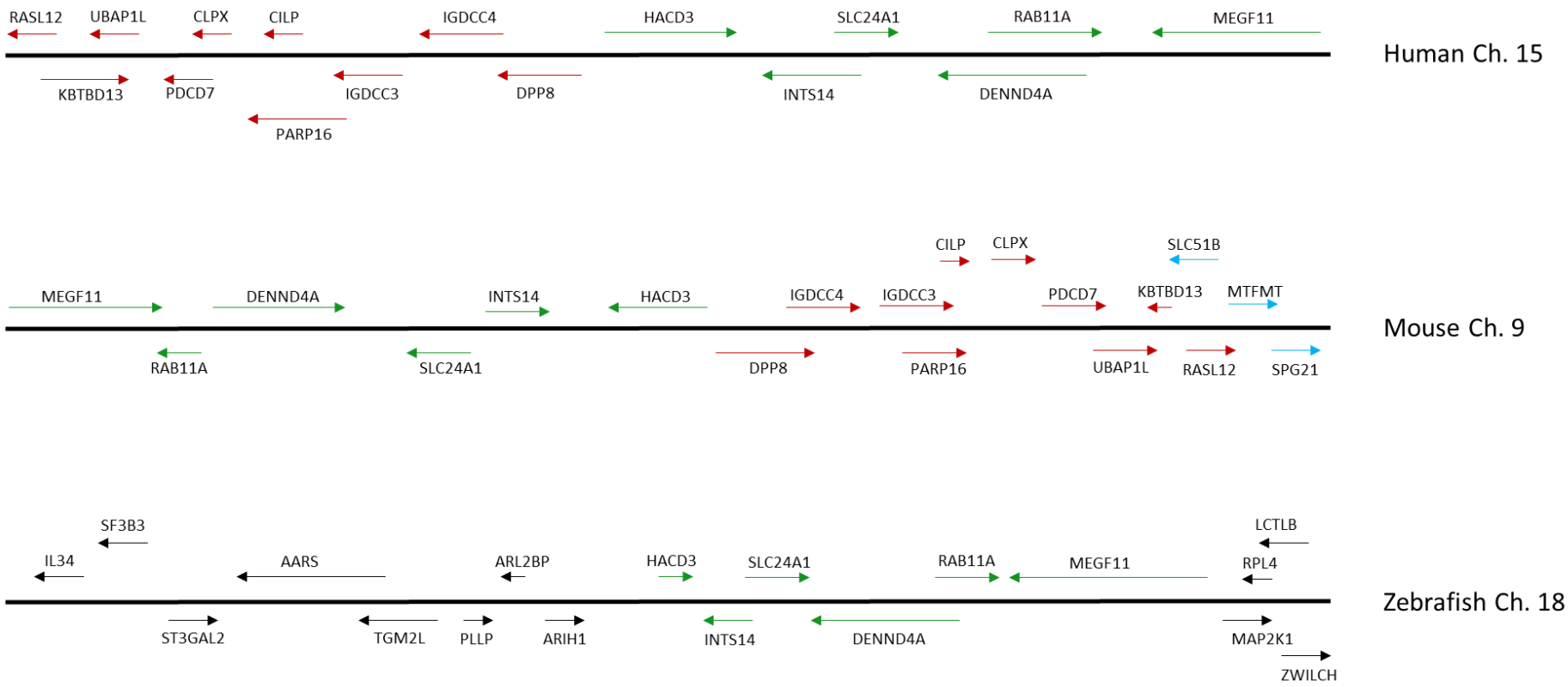

Figure 2.9: Synteny of the HACD3 gene over human, mouse and zebrafish species over a 1MB region.
Genes found in all three species are annotated in green, genes found in human and mice annotated as red, those only in mouse annotated as blue and genes only in the zebrafish sequence in black.

2.3.1.4. HACD4

ENSEMBL identified one zebrafish orthologue for HACD4 and this zebrafish *hacd4* gene (ENSDARG00000102221) and was found in a block of six genes with synteny across human and murine genome sequences (Figure 2.10). There was only one transcript listed for *hacd4* (ENSDART00000157618) for zebrafish, two for human (with only one annotated as protein coding) and three for mouse. This zebrafish transcript had a 76% sequence identity with the protein coding human *HACD4* transcript (ENST00000495827.3). BLAST search of Hacd4 amino acid sequence in ENSEMBL against the zebrafish protein database returned only Hacd1-4 and the *hacd4* gene had a target ID of 18% with *hacd1*.

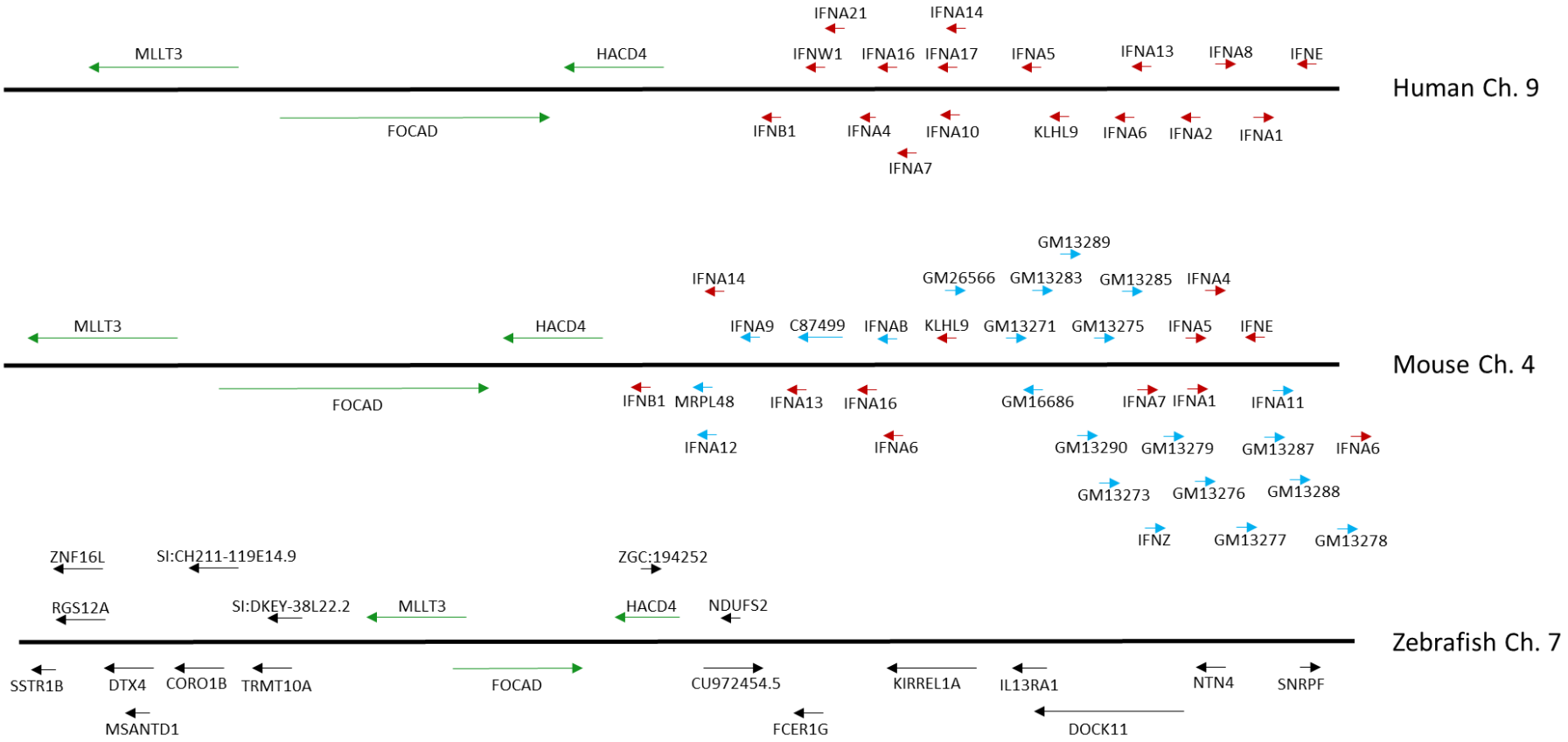

Figure 2.10: Synteny of the HACD4 gene over human, mouse and zebrafish species over a 1MB region.

Genes found in all three species are annotated in green, genes found in human and mice annotated as red, those only in mouse annotated as blue and genes only in the zebrafish sequence in black.

Bioinformatics analysis identified four genes, likely to be the only orthologues for HACD1-4 in zebrafish. This was based on sequence similarity with mammalian counterparts, exon structure, full length transcripts producing proteins and the synteny of the genes on surrounding chromosome regions.

2.3.2. *hacd1* is expressed in developing and mature muscle in embryonic and adult zebrafish

Expression of *hacd1* in embryonic zebrafish was evaluated by conventional RT-PCR using primers designed to amplify the full-length coding sequence (Figure 2.11). Products at each time point were of a size consistent with both the *hacd1-fl* and *hacd1-d5* isoforms (expected product lengths of 730 and 608bp respectively). Relative expression of *hacd1-fl* in comparison with *hacd1-d5* appeared to increase in later embryonic developmental stages (48 and 72hpf). Sequencing subsequently confirmed the *hacd1-fl* within the embryos.

The same RT-PCR evaluation for *hacd1* was performed on a variety of adult zebrafish tissues and the same the products were identified (Figure 2.12). The larger of the products thought to be *hacd1-fl* was detected exclusively in striated muscles (skeletal muscle and heart samples), whereas the smaller band, thought to be *hacd1-d5* was detected in heart, spleen & kidney and the swim bladder samples.

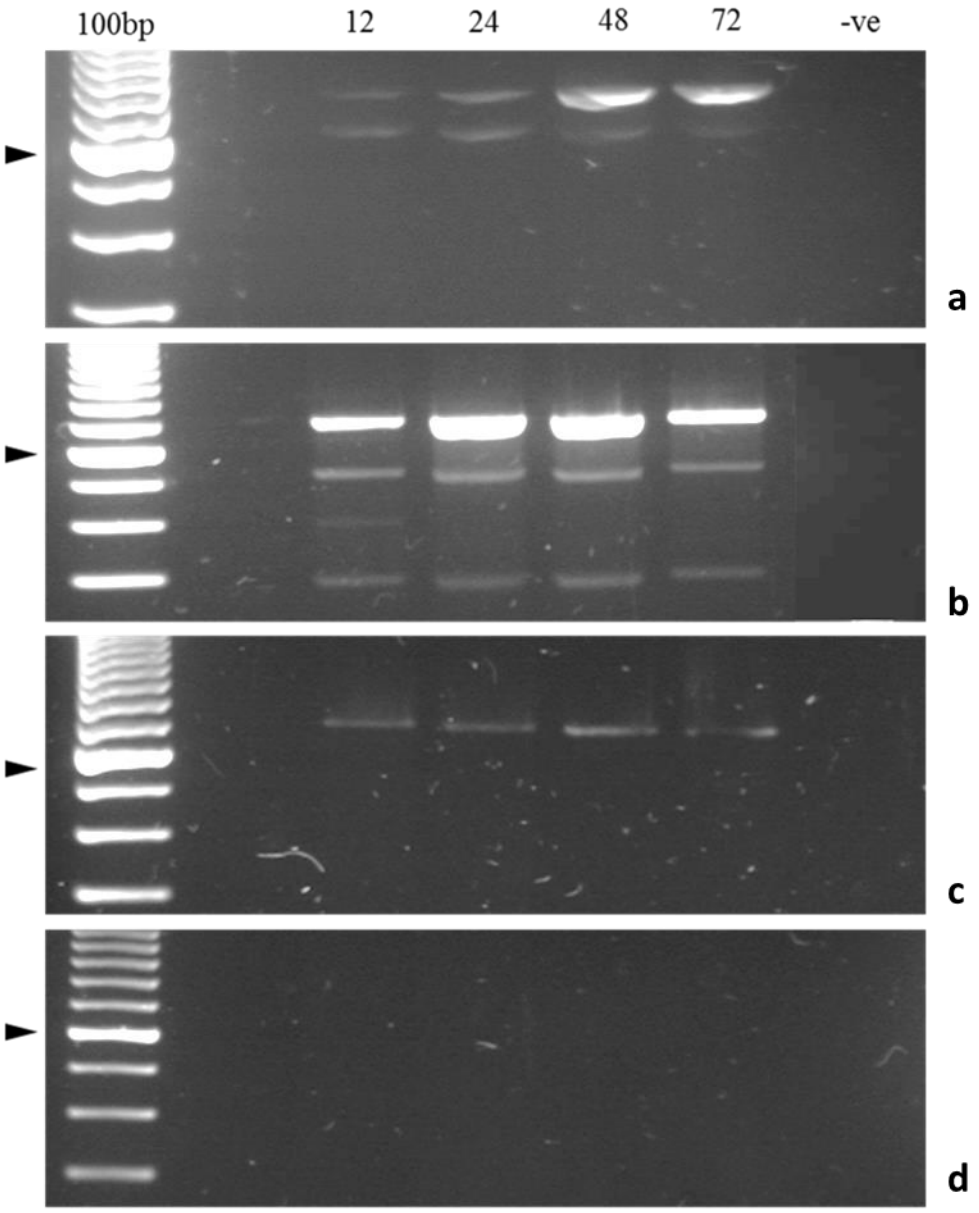

Figure 2.11: Expression of *hacd* transcripts in developing zebrafish embryos.

Agarose gel analysis of RT-PCR products from embryonic ages 12-72 hours post fertilisation (hpf) including a no template control (molecular grade water) run in the far-right lane (labelled as "-ve"). Products were run against a 100bp ladder, black arrow indicates the 600bp band for reference. (a) RT-PCR for *hacd1* detected two products of approximately 800 and 700bp lengths consistent with the *hacd1-fl* (expected at 730bp) and *hacd1-d5* (expected at 608bp) transcripts label them: the full-length transcript was subsequently confirmed via sequencing. (b) RT-PCR for *hacd2* revealed products of approximately 750 (full length product expected at 777bp), 550, 400 and 300bp length 12hpf with only bands at 750, 550 and 300bp in later time points. (c) RT-PCR for *hacd3* RT-PCR detected a single product from embryos at all time points of approximately 700bp (expected product was 706bp). (d) RT-PCR for *hacd4* on mRNA from embryos at all time points detected no transcripts by agarose gel electrophoresis and the expected product length was 776bp.

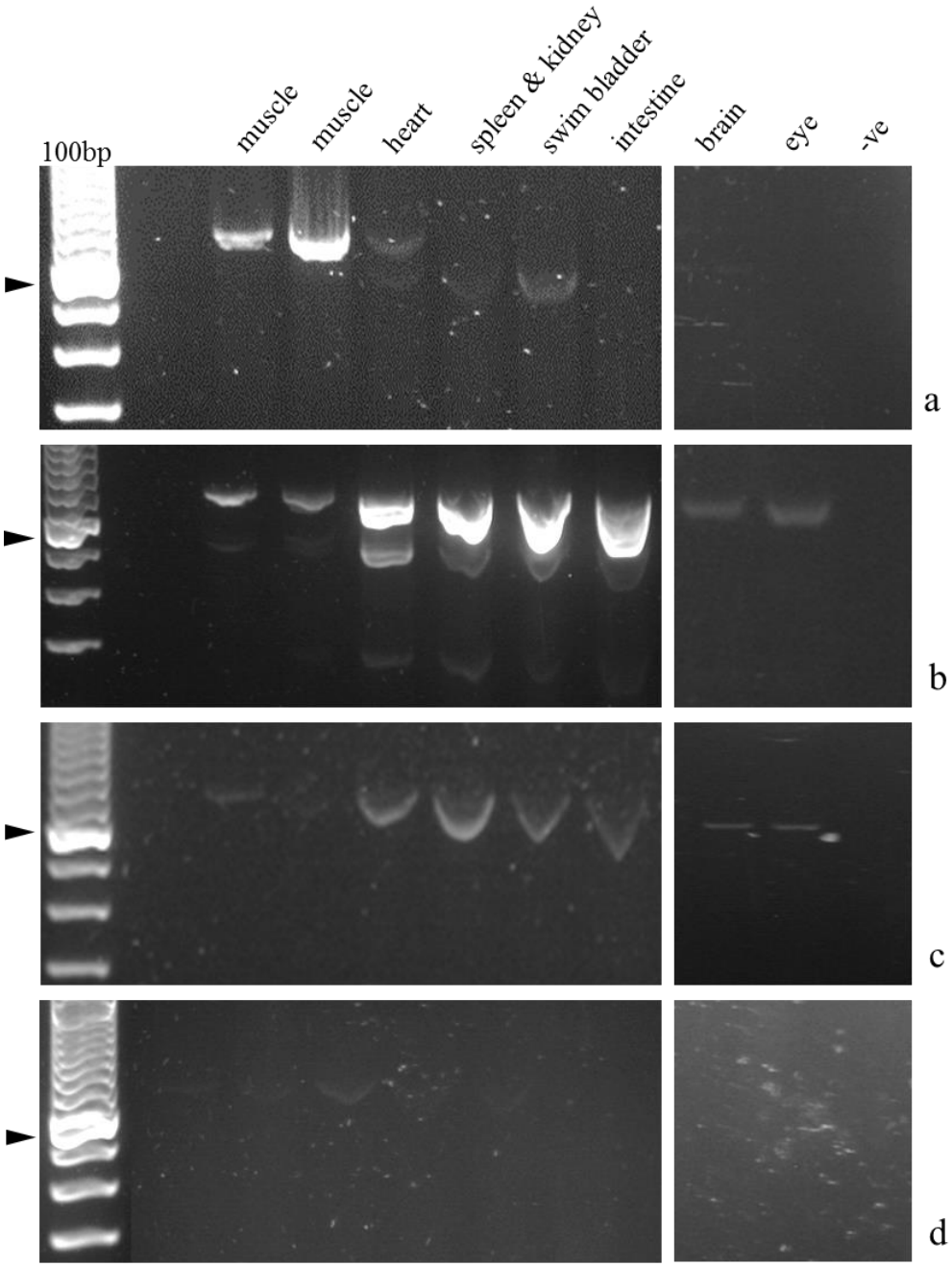

Figure 2.12: Expression of *hacd* transcripts in adult zebrafish tissues by RT-PCR on cDNA from tissue RNA extraction.

Samples analysed by agarose gel electrophoresis and run against 100bp ladder with a black arrow indicating 600bp reference band and a negative control in the far-right lane (molecular grade water in the place of cDNA template, labelled "-ve"). (a) RT-PCR for *hacd1* displaying products that corresponded to the *hacd1-fl* and *hacd1-d5* transcripts; with the corresponding product for *hacd1-fl* present in muscle and heart samples and products corresponding to *hacd1-d5* in heart spleen and swim bladder samples (*hacd1-fl* product expected at 730bp and *hacd1-d5* at 608bp). (b) RT-PCR for *hacd2* with products identified at approximately 750, 550 and 300bp with the largest product (expected to be 777bp) seen in all tissues and the smaller products in heart, spleen & kidney, swim bladder and intestine. (c) RT-PCR for *hacd3* showing a single product at approximately 700bp (expected product was 706bp) in all tissues but only very faint bands in muscle and heart cDNA samples. (d) RT-PCR gel for *hacd4* products with a very faint band seen at approximately 800bp (expected product was 777bp) in the heart tissue sample and another in the spleen & kidney cDNA sample.

2.3.3. *hacd2-fl* is ubiquitously expressed in zebrafish embryos from 12 to 72hpf and adult zebrafish tissues

Embryonic RT-PCR reactions amplified four products at 12hpf (approximately 750, 550, 400 and 300bp) and three products at 24, 48 and 72hpf (approximately 750, 550 and 300bp) (Figure 2.11). The largest and most intense product of approximately 750bp (expected product was 777bp) corresponded to the full length *hacd2* transcript (*hacd2-fl*) which was the only listed transcript and was subsequently confirmed by sequencing. The other products were approximately 550, 400 and 300bp: the largest and smallest of these were subsequently cloned and sequenced (Section 2.3.3.1).

In adult zebrafish tissues; the largest product corresponding to the listed transcript of *hacd2* (referred to as *hacd2-fl* in this thesis) was present in all tissues. This was the only product identified in eye and brain tissues, these samples were extracted and analysed separately therefore relative intensity cannot be compared. The product of ~550bp was amplified in all tissues expect eye and brain and also lower intensity in muscle samples compared to other tissues (heart, spleen & kidney, swim bladder and intestine). A 400bp produce was not detected in adult tissues. The smallest product of 300bp had only faint bands seen in heart, spleen & kidney, swim bladder and intestine tissues.

2.3.3.1. Two novel *hacd2* isoforms were identified

RT-PCR for *hacd2* performed on both adult tissues and embryos detected additional smaller products of low relative abundance to *hacd2-fl*. To determine if these were previously unlisted transcripts, products were isolated and extracted from the gel, cloned and sequenced. The largest product was confirmed to be the full length *hacd2* transcript (expected product was 777bp). The product of around 550bp was identified as an alternative transcript without exon 6 (598bp). The shortest product of around 300bp was identified as a transcript containing only exons 1, 2 and 7 (368bp) (depicted in Figure 2.13). These isoforms, like *hacd1-d5*, do not encode for the essential amino acids that are required for HACD activity.

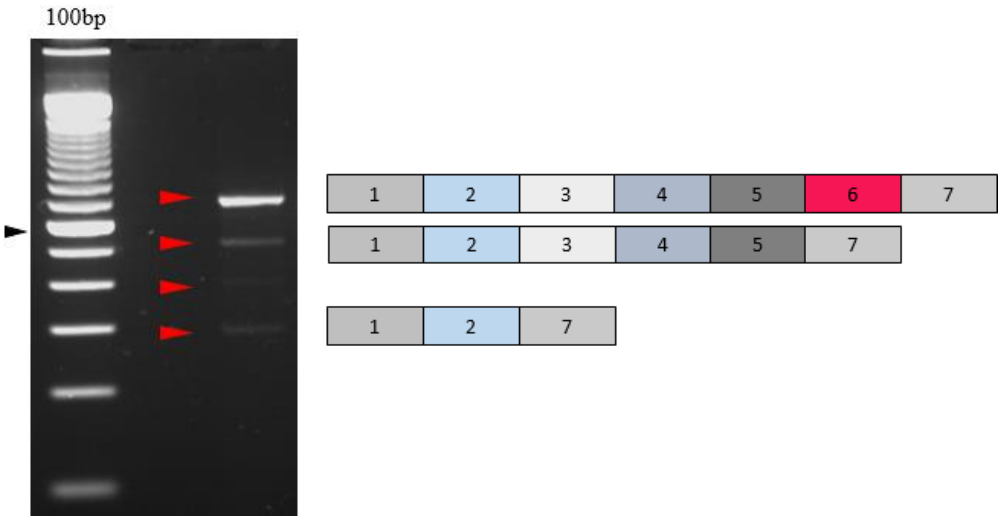

Figure 2.13: Novel isoforms of *hacd2*.
(a) RT-PCR for *hacd2* run against 100bp ladder, black arrow indicates reference 600bp. Four bands are present and annotated by the red arrows. (b) Three out of four isoforms were then successfully isolated and sequenced and these have displayed here as blocks of exons, with the active site containing exon highlighted in pink.

2.3.4. RT-PCR expression data for *hacd3* in embryonic and adult zebrafish tissues found it to be ubiquitously expressed

RT-PCR for *hacd3* in embryonic zebrafish detected one product at approximately 700bp which was present at all time points across development (Figure 2.11), this was subsequently cloned and sequenced to be the full length *hacd3* transcript previously listed (expected product was 706bp). The same product of approximately 700bp was found in all adult tissues except the skeletal muscle samples (Figure 2.12). A primer set designed from exons 1-11 was designed also to amplify any other possible isoforms, but the RT-PCR reactions with this primer set were unsuccessful.

2.3.5. RT-PCR expression data for *hacd4* was inconclusive

Standard 35-cycle RT-PCR for *hacd4* in embryonic zebrafish samples detected no products at any time point, even once assays were optimised, expected product length would have been expected at 776bp. A 40-cycle RT-PCR reaction was run including cDNA from both 96 and 120hpf embryos (Figure 2.14). When reaction products were run on a gel it displayed two products at all time points of approximately 1kb and 800bp and fainter bands under 600bp, seen from 24hpf onwards (expected product from primers was 776bp). It was unclear from the RT-PCR gel if these products are *hacd4*, or if they are due to artefacts from running a longer than conventional reaction.

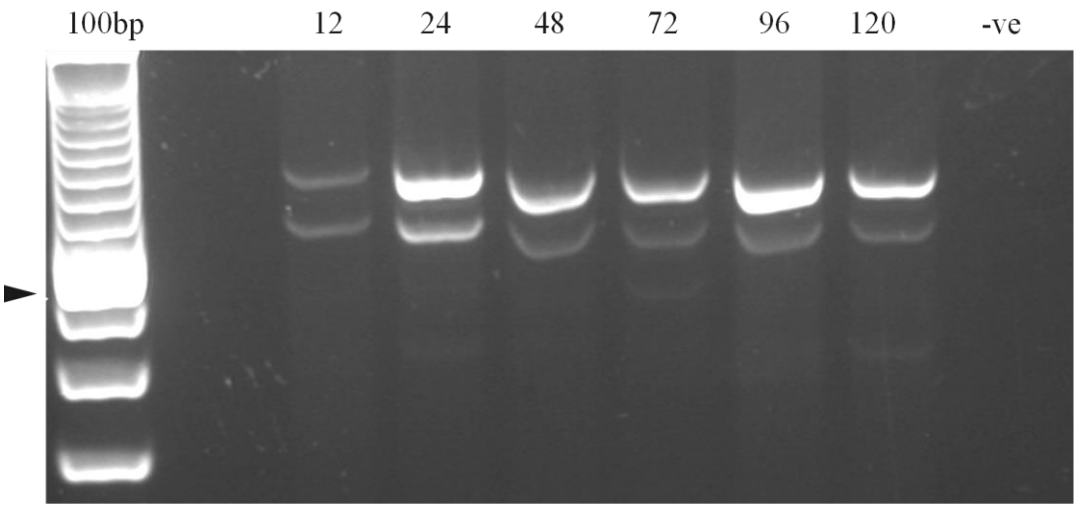

Figure 2.14: Products from a 40 cycle RT-PCR reaction for *hacd4* over embryogenesis, 12-120 hours post fertilisation (hpf) with a negative control run on the far right.
PCR was run against a 100bp ladder with a black arrow indicating the 600bp position. Products appeared at approximately 1kb and 800bp with fainter bands at approximately 600 and 400bp and expected full length product was expected to be 776bp.

When adult tissue samples were run through RT-PCR with primers to amplify *hacd4*, there were faint bands of approximately 800bp seen for *hacd4* in muscle, heart, spleen and kidney (Figure 2.12).

2.3.6. Localisation of *hacd* enzymes throughout embryogenesis

The presence of the *hacd* enzymes throughout embryogenesis and the tissue specificity in adult fish was initially assessed via RT-PCR. To determine what tissues and stages of developing embryos expressed the various HACD enzymes whole mount ISH was performed on the embryos at a variety of ages.

2.3.6.1. *hacd1* is localised in the striated muscle of zebrafish embryos

As HACD1 is expressed throughout myogenesis in mammals (Blondelle *et al*., 2015; Lin *et al*., 2012; Walmsley, 2013) and preliminary work (Walmsley, 2013) had detected *hacd1-fl* expression in somites of embryos by the Prim-5 stage/24hpf, time points were selected for before, during and after the onset of myogenesis (Figure 2.15). *hacd1* expression (shown by dark purple staining) could not be detected in early embryos of the early segmentation period (around 5 somites)/12hpf but the colour began to develop with the development of somites by the segmentation period of 20-somites (18hpf). Functional muscle is present in the embryo at 17hpf (Saint-Amant & Drapeua, 1998) and by 21hpf a clear line along the developing tail had developed colour demonstrating *hacd1* expression (Kimmel *et al*., 1995). By 72hpf (protruding-mouth stage) the expression of *hacd1* was seen unmistakably in the myotomes of the tail where myoblasts had developed into mature myofibres.

Embryos imaged from the dorsal plane showed the two separate myotomes on either side of the developing notochord. For all stages control experiments were run with sense probes and representative control samples are shown: these control experiments exhibit trapping of the probes which tends to occur in both the head and the yolk sac due to presence of unbound probe. Importantly the controls show no staining within the muscle of the embryos.

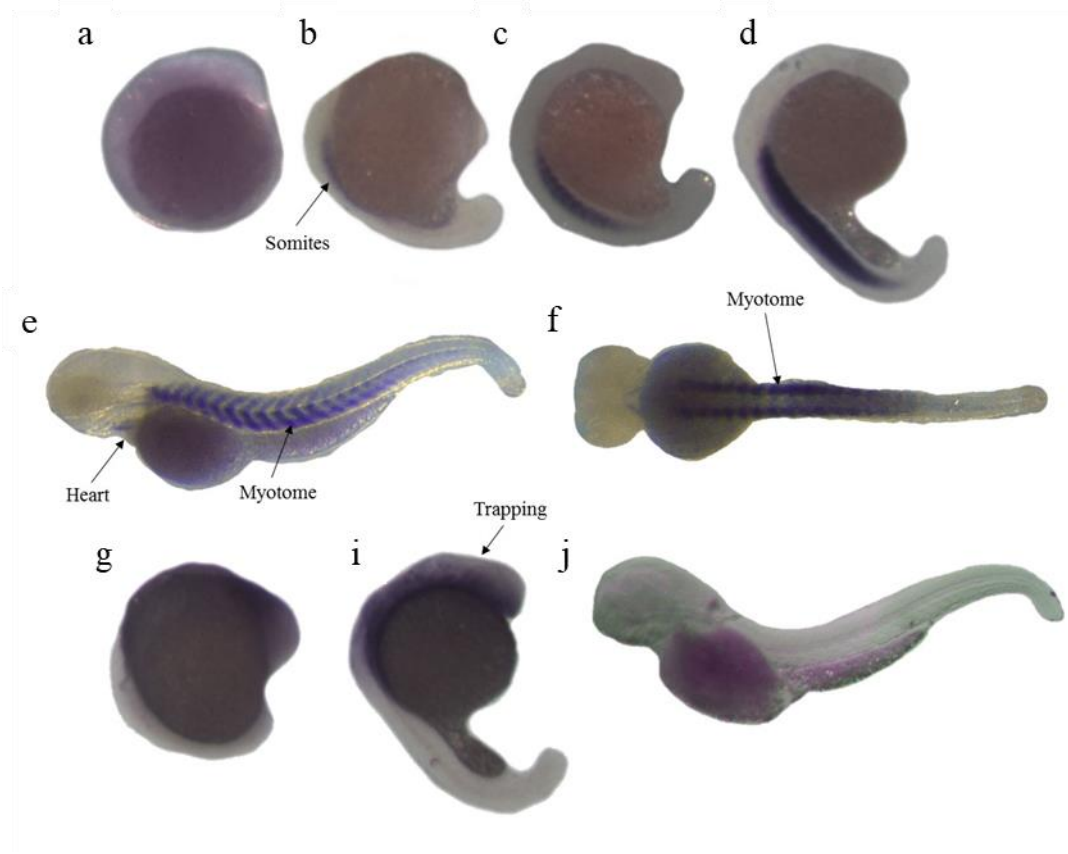

Figure 2.15: Localisation of *hacd1* throughout zebrafish embryogenesis.
Experimental embryos with anti-sense probe are shown in a-f and control (sense probe) embryos in g-i. Stages are as follows: 12 hours post fertilisation (hpf) (a), 14hpf (g) 18hpf (b), 21hpf (c, h), 24hpf (d) and 72hpf (e, f, i). In the experimental embryos from 18hpf onwards the dark purple stain indicating *hacd1* expression can be seen along the tail of the embryos where the mature muscle develops. In the control embryos there was varying levels of non-specific binding seen in both the head area and yolk sac.

2.3.6.2. *hacd2* is ubiquitously expressed in developing zebrafish embryos

Previous conventional RT-PCR experiments had shown *hacd2* to be ubiquitously expressed in all adult zebrafish tissues tested (Figure 2.12). Whole-mount ISH of embryos detected *hacd2* predominantly in the head and eye areas of developing embryos. The *hacd2* transcript could be detected as early as the segmentation period/12hpf predominantly located around the developing head of the embryo. A similar pattern was observed at the Prim-5 stage/24 hpf with well circumscribed areas of intense staining associated with brain and eye regions. At the

protruding-mouth stage/72hpf brain and ocular structures are again strongly stained and there was also staining in the body cavity and potential staining along the notochord (this was subsequently discounted on sectioning, see Figure 2.21). There was no staining for *hacd2* observed within the developing or mature striated muscles of the embryos at any stage. The control embryos all showed some degree of trapping in and around the yolk sac but importantly no staining where the *hacd2* expression was detected in the head.

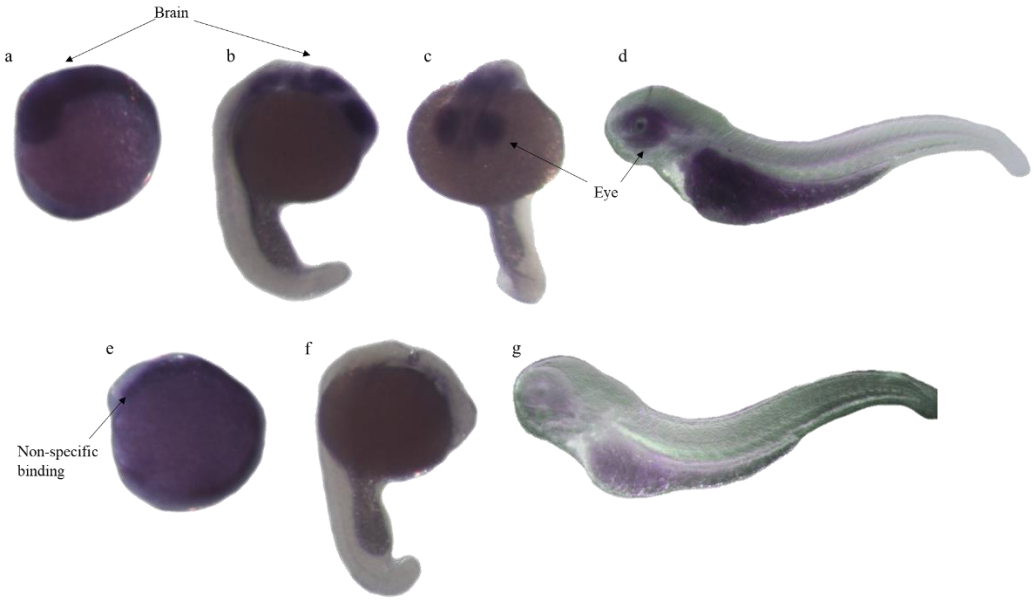

Figure 2.16: Localisation of *hacd2* throughout zebrafish embryogenesis.
Top row (a-d) displays the experimental embryos (anti-sense probe) and bottom row (e-g) displays the control experiments (sense probe). Developmental stages are as follows: 12 hours post fertilisation (hpf) (a, e), 24hpf (b, c, f) and 72hpf (d, g). Experimental embryos had staining in the brain and eye areas and none in the muscle and this staining of head and eye regions was not present in the control embryos, which display some level of non-specific binding in and around the yolk sac.

One set of *hacd2* ISH was conducted using a probe designed to bind to the 3'UTR of the *hacd2* gene. These probes were designed for this area as the main *hacd2* sequence shared a high homology with *hacd1* and therefore a second probe was designed in case the *hacd2* probe bound to *hacd1* mRNA also. Figure 2.16 and Figure 2.17 both show comparable expression patterns within the experimental embryos indicating the main *hacd2* probe from Figure 2.16 was specific only to *hacd2* and was therefore used for experiments. The control for the 3' UTR probe also had staining within the head and so this probe was not used for further experiments.

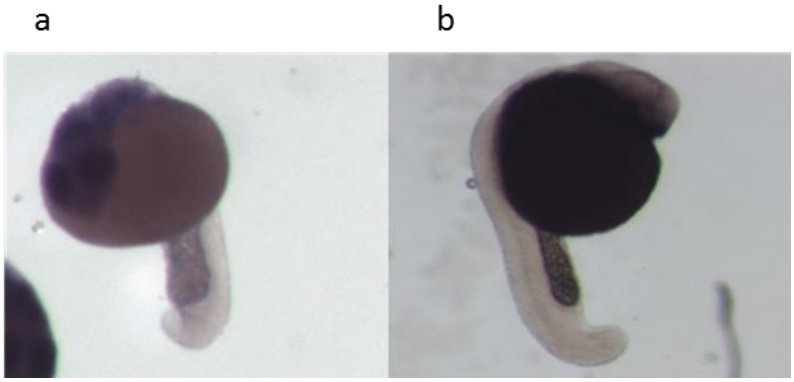

Figure 2.17: *In situ* hybridisation (ISH) of *hacd2* in zebrafish embryos using a probe against the 3' UTR of *hacd2*.

(a) 24hpf (hours post fertilisation) embryo incubated with the antisense 3'UTR *hacd2* probe. (b) Control embryo incubated with sense probe. Staining was comparable to the staining seen when using the main *hacd2* probe: within the head and eye areas of the embryo. Control probe shows stain also within the head.

2.3.6.3. *hacd3* localisation is centred in the eyes of zebrafish embryos

Results from RT-PCR found *hacd3* to be ubiquitously expressed in all adult organs (Figure 2.12). ISH found staining for *hacd3* expression in the eyes and brain, and also perhaps the notochord at 72hpf. Importantly, as with *hacd2*, there was no staining for *hacd3* expression within somites or myotomes.

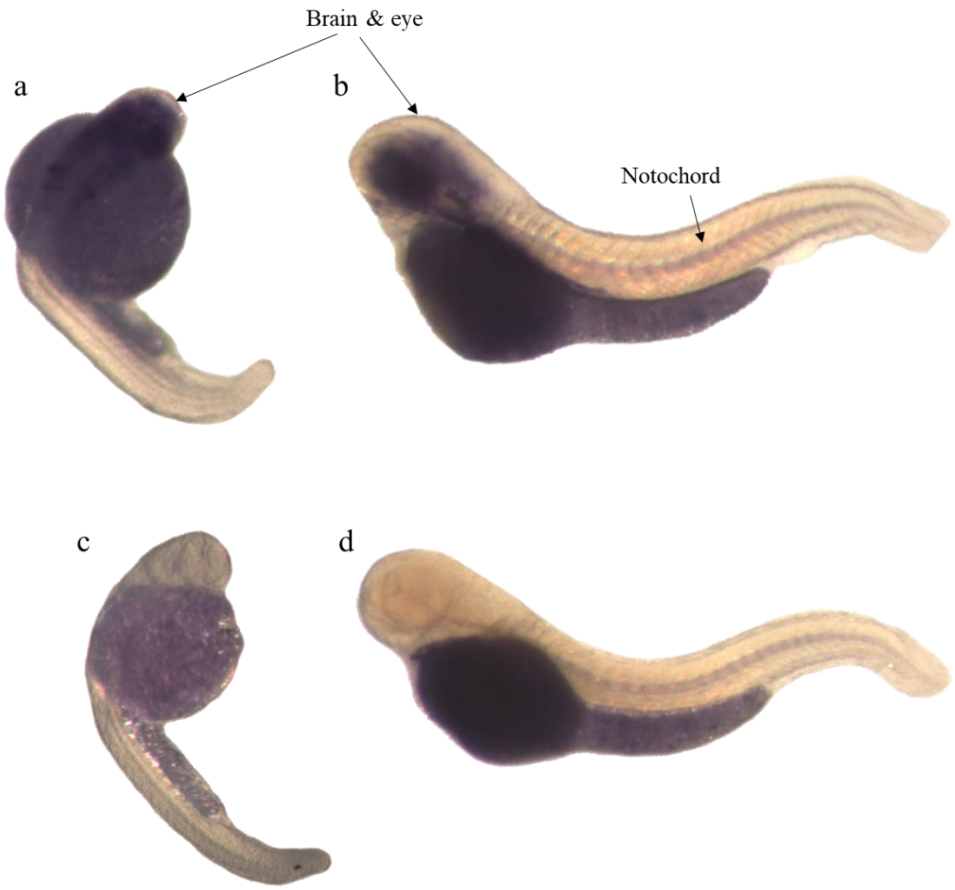

Figure 2.18: Localisation of *hacd3* through zebrafish embryogenesis.
Embryos a&b represent experimental embryos with anti-sense probe hybridised and c&d represent the control embryos hybridised with the sense probe. Ages of embryos are as follows: 30 hours post fertilisation (hpf) (a&c) and 72hpf (b&d). Experimental embryos showed staining at both developmental stages, within the developing brain and eyes and no staining within the muscle. Control embryos displayed some trapping of unbound probe within the yolk sacs.

2.3.6.4. *hacd4* could not be detected by *in situ* hybridisation

In situ hybridisation was performed in embryos of 48 and 72hpf and no staining for *hacd4* expression could be detected. Sense control embryos also had no staining apart from some non-specific staining in the head of embryos.

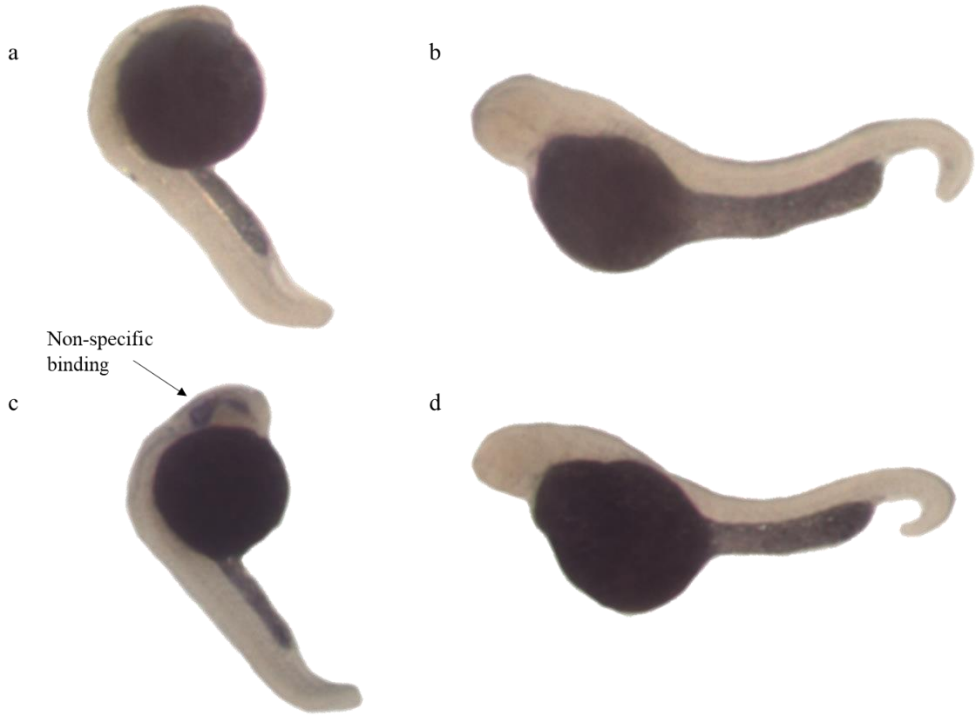

Figure 2.19: Localisation of *hacd4* throughout zebrafish embryogenesis.
Embryos a&b represent experimental embryos with anti-sense probe hybridised and c&d represent the control embryos incubated with the sense probe. Ages of embryos are as follows: 48 hours post fertilisation (hpf) (a&c) and 72hpf (b&d). There was no visible staining in the experimental embryos and a small amount of trapping in the heads of control embryos.

2.3.6.5. *Hacd1* is the major *hacd* enzyme expressed in zebrafish embryo muscle

Whole-mount stained embryos were sectioned for more precise localisation of expression. Consistent expression of *hacd1* was detected within the muscle at 24 and 72hpf symmetrically within the four developing myotomes (Figure 2.20). Importantly no staining for transcripts from the other three genes was seen in developing muscle (Figure 2.21).

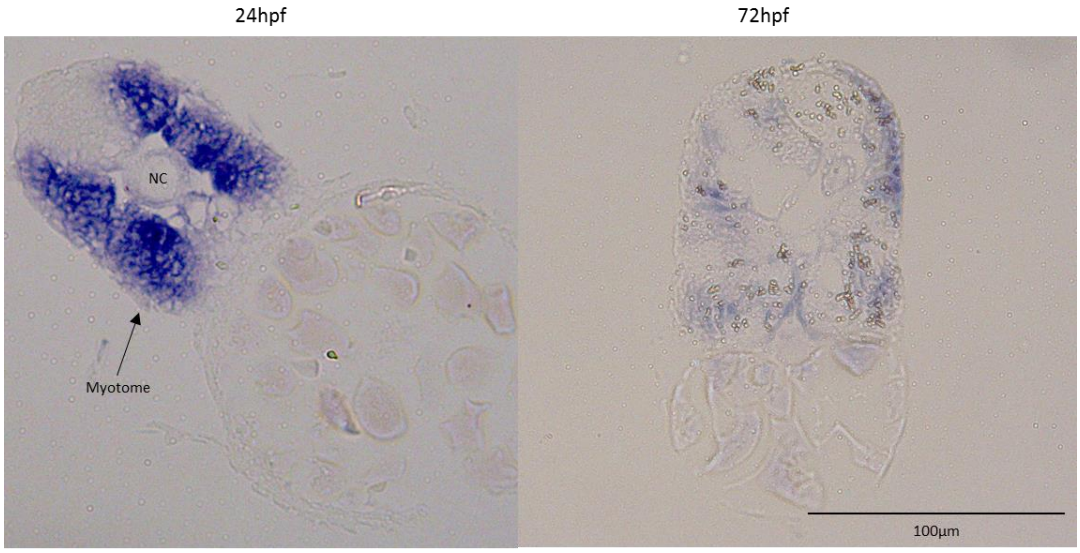

Figure 2.20: Expression of *hacd1* in the developing muscle of embryonic zebrafish.
Expression of *hacd1* can be detected in both 24hpf (hours post fertilisation) (left) and at 72hpf (right) within the myotomes of the tail muscle. There was no *hacd1* expression in others sections of the tail cross sections including the notochord (NC) (Zebrafish Bio-Atlas, Penn State University).

Figure 2.21 shows 72hpf muscle cross sections for all four *hacd* genes to allow for comparison between them. There was no staining for *hacd2* in the myotomes, and specific staining in developing abdominal organs between the muscle and yolk sac could be detected. There was no staining for *hacd3* expression within the muscles but there was staining within the notochord. As seen in the whole mount images there was no *hacd4* staining within the muscle or elsewhere (Zebrafish Bio-Atlas, Penn State University).

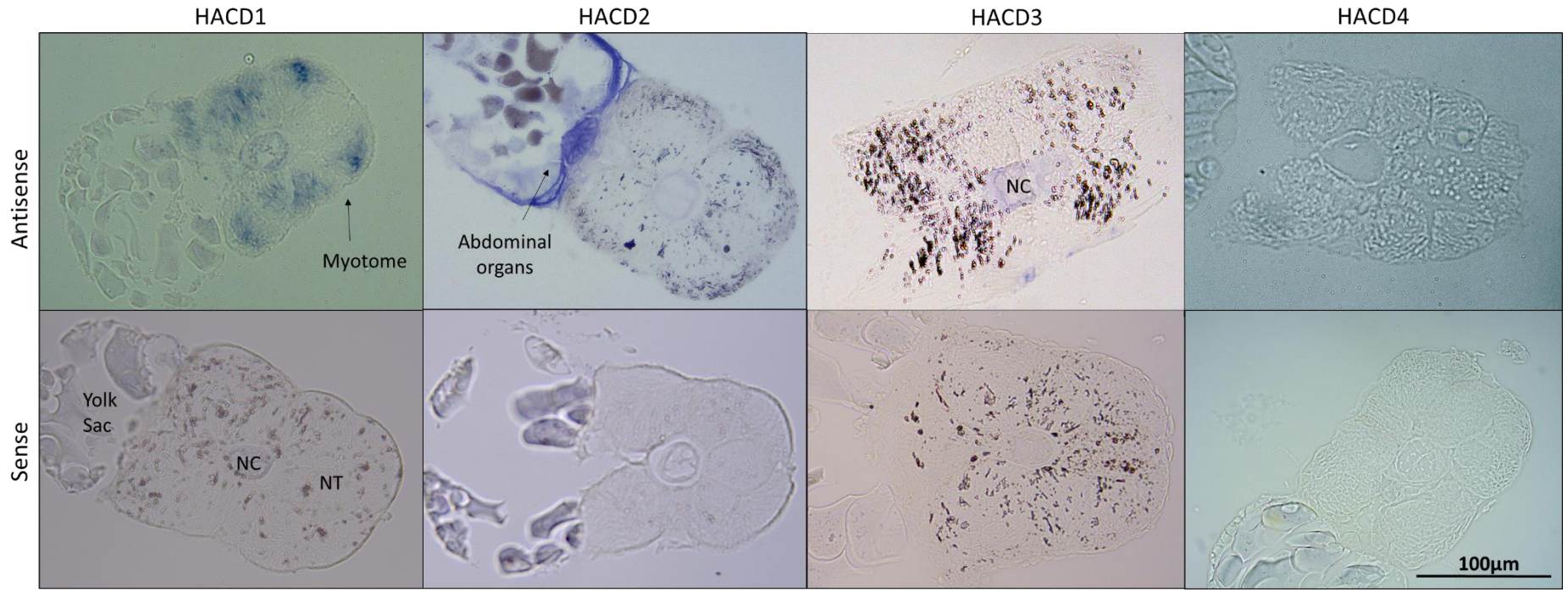

Figure 2.21: Localisation of *hacd* genes within 72 hours post fertilisation (hpf) zebrafish embryo tail muscle.

Figure shows both the antisense and sense (control) transverse sections for all four *hacd* genes, two embryos per sample set were sectioned. Expression of *hacd1* could be seen uniquely in the muscle of the embryos, specifically in the myotomes and was absent from the notochord (NC) and neural tube (NT) labelled on the *hacd1* sense embryo: whilst *hacd2-4* are all absent from the muscle. Staining for *hacd2* was present between the muscle and yolk sac, in the area which the majority of organs, including the abdominal organs, grow that will form the main body cavity of the fish. Staining for *hacd3* was strong in the notochord (NC) of the embryos. *Hacd4* showed no staining in the tail of the embryo (Zebrafish Bio-Atlas, Penn State University).

Sections through the head (Figure 2.22) found *hacd1* staining was not present in the majority of the anatomy. There was one line of staining in line with where the developing oesophagus would be. As reported for whole-mount stained embryos, *hacd2* and h*acd3* expression was found within the head and eyes of protruding-mouth stage/72hpf embryos: *hacd2* had a more intense staining within the photoreceptors of the eye and less intense staining across the most parts of the eye and brain and *hacd3* had an even spread of staining including the developing fore, mid and hindbrain (telencephalon, diencephalon and myelencephalon respectively). Unexpectedly, *hacd4* stained embryos had small areas of focal and symmetrical staining within the brain (labelled with red asterisks) indicating *hacd4* expression within the myelenchephalon of developing embryos at 72hpf (Zebrafish Bio-Atlas, Penn State University).

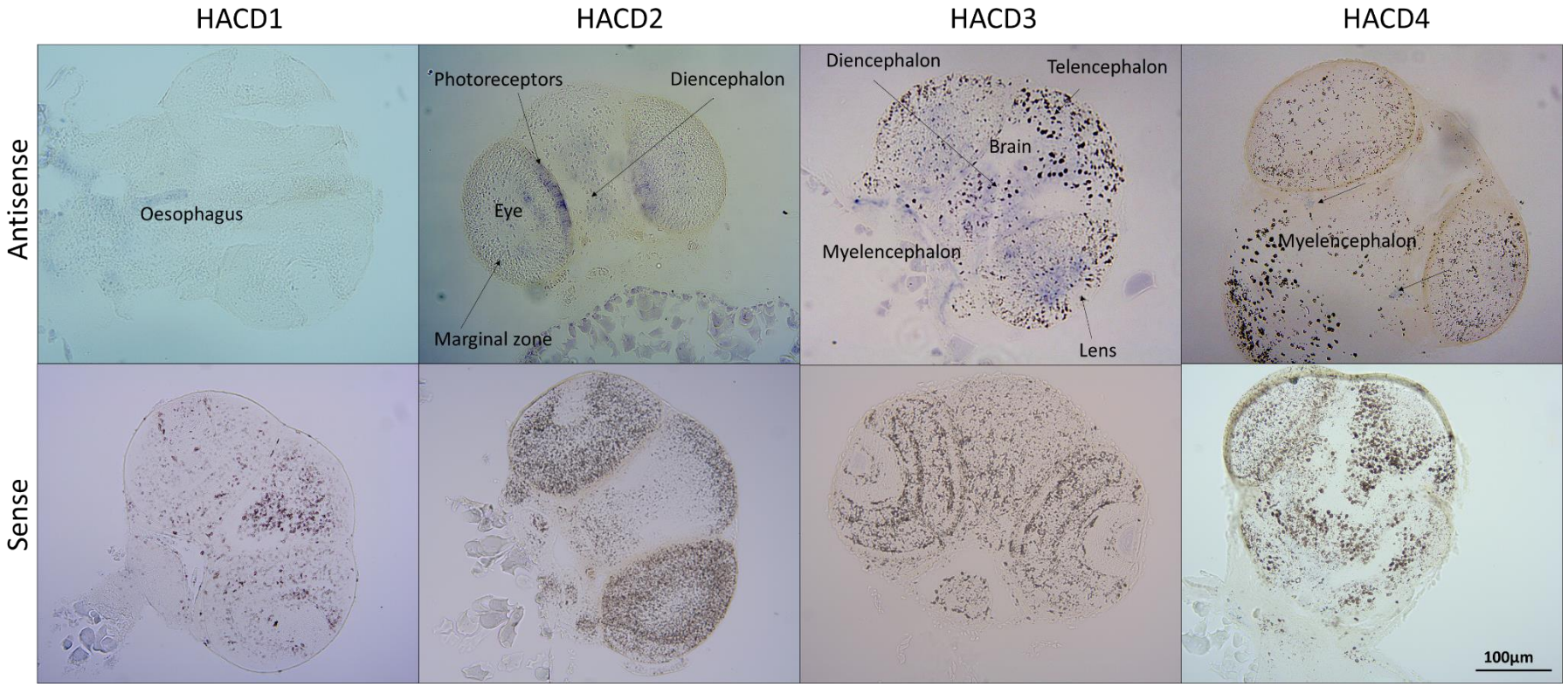

Figure 2.22: Localisation of *hacd* genes within 72 hours post fertilisation (hpf) embryo heads.

Figure shows both the antisense and sense (control) transverse sections for all four enzymes and two embryos per sample set were sectioned. Figure shows that *hacd1* staining was not present in the majority of the head apart from a line of staining which corresponded to the positioning of oesophagus. Staining for *hacd2* was seen in the eye with intense staining in the photoreceptors and also the diencephalon area of the brain. As with *hacd2*, *hacd3* was also seen within the eyes and brain, but in all areas of the myelencephalon, diencephalon and telencephalon areas which develop into the fore, mid and hindbrain. Staining of *hacd4* had two bilaterally symmetrical spots of staining (annotated by black arrows) just ventromedial to the eyes (within the myelencephalon area of the brain) (Zebrafish Bio-Atlas, Penn State University).

2.3.7. Identification of appropriate housekeeping genes for RT-PCR assays

Before qRT-PCR assays could be performed and analysed accurately, housekeeping genes that were stably expressed over embryonic development had to be identified and validated.

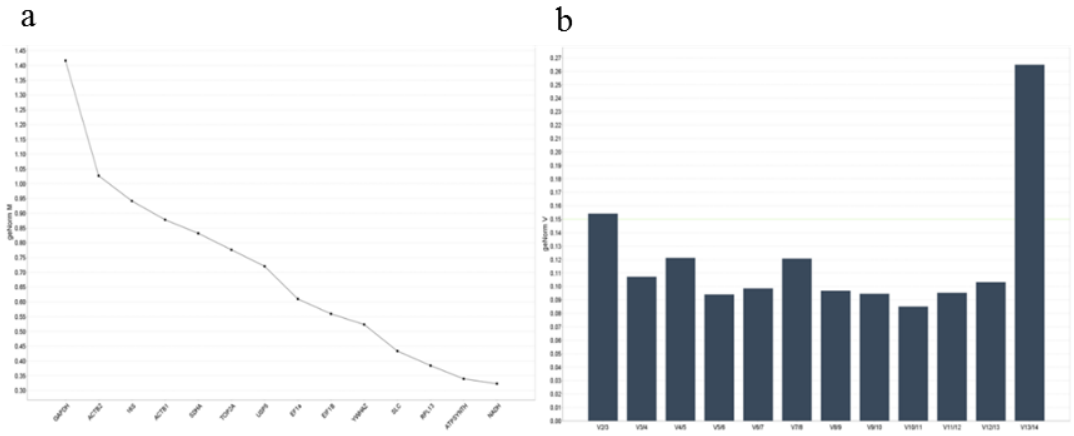

Figure 2.23: Identification of appropriate house keeper genes for embryonic zebrafish qRT-PCR assays.
Figure shows the outputs from qbase+ software (Biogazelle). (a) Stability of each housekeeping gene with most stable toward the right-hand side of X axis. (b) Displays the V value indicating the number of housekeeping genes to use as references.

Using the qbase+ algorithm the most stable housekeeping genes were found to be *nadh*, *atpsynth* and *rlp13* and the optimal number of reference targets was 3 due to the V,0.15 number generated (Figure 2.23). Figure 2.24 shows the raw Ct values for all three selected house-keeping genes, these values were stable across development, with deviations of approximately four Ct values. These three genes were then taken forward to use in all future embryonic zebrafish qRT-PCR reactions to normalise data.

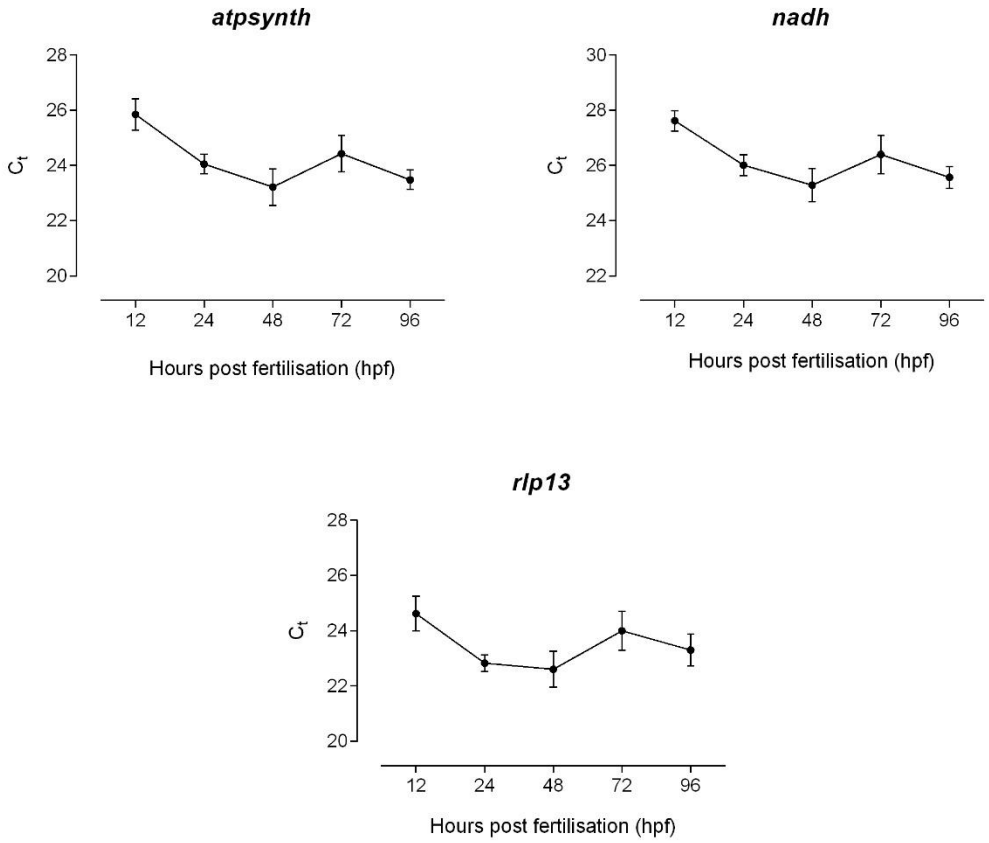

Figure 2.24: Stability of chosen housekeeping genes over zebrafish development, from 12 hours post fertilisation (hpf) till 96hpf.
Graphs display the Ct values for the three selected housekeeping genes for zebrafish embryo qRT-PCR: *nadh*, *atpsynth* and *rlp13*.

2.3.8. Expression of *hacd* genes throughout embryogenesis

Quantitative (q) RT-PCR analysis found that only the full-length isoforms of *hacd1* and *hacd2* significantly increased over embryonic development (p=0.0063 and p=0.0015 respectively). Whereas *hacd2-fl* exhibited a gradual 2-fold increase over development, *hacd1-fl* underwent a 6-fold increase between 12 and 48hpf and 7-fold between 12 and 72hpf. Expression of both *hacd3* and *hacd4* was unchanged over development of the embryos.

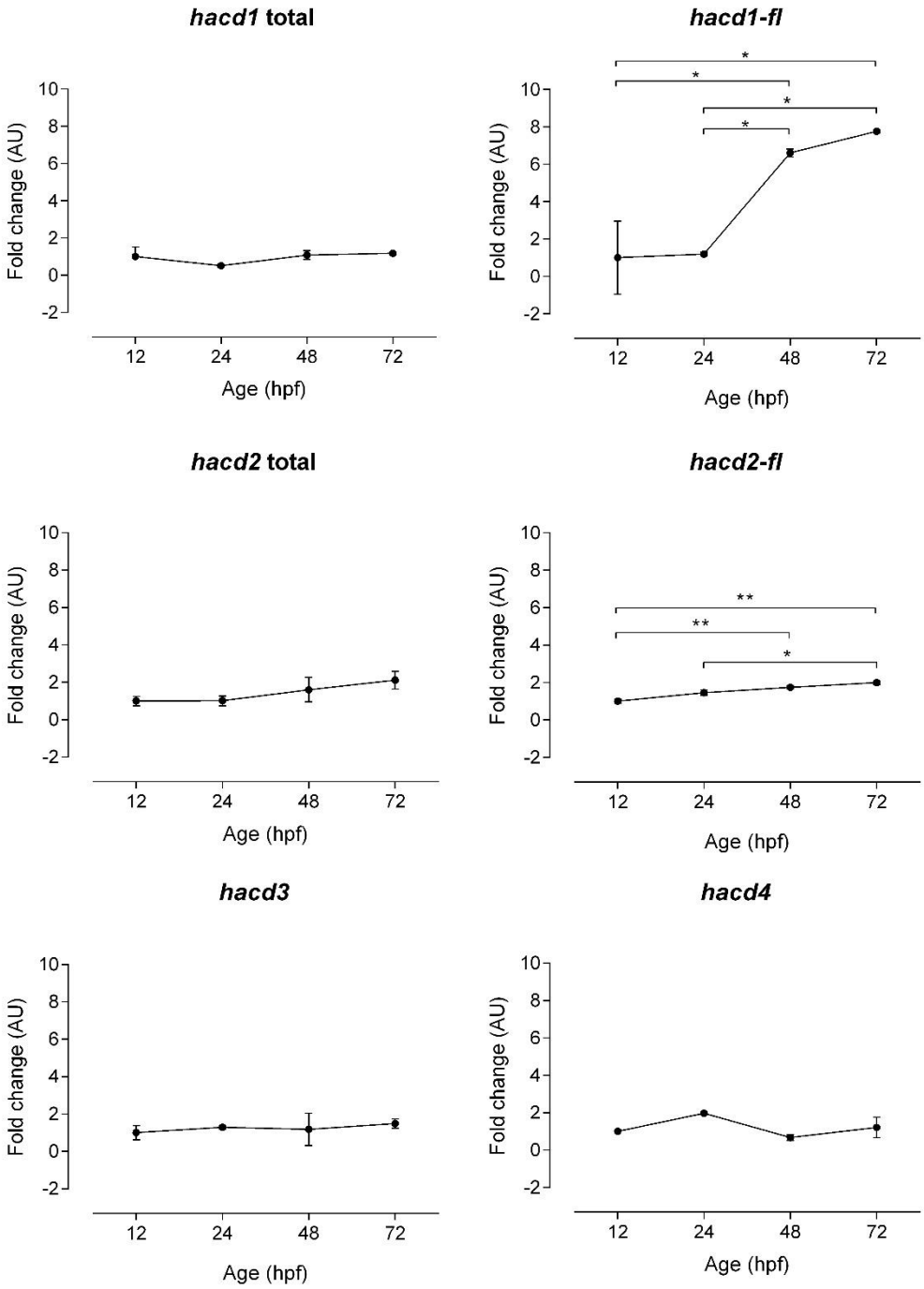

Figure 2.25: Expression of *hacd1-4* genes throughout zebrafish embryogenesis by qRT-PCR assays, including full length transcripts of *hacd1* and *hacd2*.

One-way ANOVA tests reported that total *hacd1*, total *hacd2*, *hacd3* and *hacd4* expression levels were not significantly altered over embryonic development (p=0.4316, p=0.2913, p=0.9099 and p=0.0682 respectively). Expression levels of *hacd1-fl* and *hacd2-fl* were significantly increased over development (p=0.0063 and p=0.0015 respectively). Tukey's multiple comparisons were performed and annotated on graph as indicated in Section 2.2.14.

2.4. Discussion

Mutations in *HACD1* have been implicated in both canine and human myopathies, with the mutation in canines contributing to the most commonly inherited neuromuscular disorder in Labrador retrievers; CNM (Maurer *et al*., 2012; Muhammed *et al*., 2013; Pelé *et al*., 2005; Toscano *et al*., 2017). Mammalian *HACD1* has been documented to encode a VLCFA dehydratase alongside three other VLCFA dehydratase genes, *HACD2-4*, all of which are localised to specific mammalian tissues to carry out this function (Ikeda *et al*., 2008; Kihara *et al*., 2008). As well as a requirement for tissue specific genes, *HACD1* is prone to a high level of splicing creating a number of different isoforms, some of which exclude the essential amino acids for HACD activity when translated to protein (Valdés de Hoyos *et al*., 2011; Tondeur *et al*., 2010; Walmsley, 2013).

The work documented in this chapter has characterised these four enzymes and their isoforms both within developing zebrafish embryos and adult zebrafish tissues. Different techniques were utilised to gain a global picture of the four enzymes and demonstrate that the zebrafish is a very suitable model for studying both HACD1 and CNM. We were able to easily detect three of the four *hacd* genes from zebrafish embryos, reporting a number of novel isoforms for zebrafish *hacd2* and corroborating previous work on the isoforms for *hacd1*. We have successfully shown that zebrafish embryos, as well as adult fish, have a comparable *hacd* expression pattern to that of mammals with *hacd1* specific only to striated and cardiac muscle, *hacd2* and *hacd3* were both found in most tissues and *hacd4* was found at very low levels and so data on this gene was inconclusive. Work undertaken in this thesis was also able to validate a number of appropriate housekeeping genes for expression work in zebrafish embryos.

2.4.1. Zebrafish *hacd1* is the true orthologue of mammalian *HACD1*

Analysis of zebrafish *hacd1* expression identified products corresponding to both the full length, *hacd1-fl* and the *hacd1-d5* isoform (the latter does not code for essential amino acids for HACD activity) (Kihara *et al*., 2008; Maurer *et al*., 2010). Both of these isoforms were present during 12-72hpf with the larger *hacd1-fl* product increasing in intensity from 48hpf onwards, corroborating previous expression data by Walmsley, (2013). In adult tissue the product corresponding to *hacd1-fl* was present at high intensity in both muscles tissue samples and the heart sample, with products corresponding to *hacd1-d5* found in the heart, spleen & kidney and swim bladder tissues. This corresponds to this isoform having more ubiquitous expression (Maurer *et al*., 2010). Embryonic ISH verified results seen in the conventional RT-PCR. The expression of *hacd1* supported results seen previously by Walmsley, (2013), which was then explored in greater detail in this study with a more extensive set of embryonic stages:

to determine exactly when expression of *hacd1* was visible through ISH. At ~18hpf (around the developmental stage of 20-somites present) somites with staining could be seen and by 24hpf (Prim-5 stage) a large amount of staining was seen down the tail of the embryos. No other *hacd* gene expression was seen in the muscles through ISH, and sectioned embryos also confirmed this. The tail staining of *hacd1* was seen in a clear chevron pattern with the stain absent in between myotome boundaries – where extracellular proteins are found (Henry *et al*., 2005). These ISH results correspond to those seen in embryonic mice where *Hacd1* expression was seen to be within the skeletal muscle through X-Gal staining (Blondelle *et al*., 2015; Uwanogho *et al*., 1999).

qRT-PCR data from this study reported significant *hacd1-fl* upregulation between both 12-48hpf (6-fold) and 12-72hpf (7-fold) but this was not reflected in expression levels of total *hacd1* transcripts. Walmsley, (2013) discovered a number of isoforms for *hacd1* in early embryos of 9-22hpf: one missing exons 5 & 6 and another containing intron 4, both of which would not produce the functional Hacd1 protein in the embryos, like that of the previously characterised *hacd1-d5* isoform. As these are expressed in early embryos and not specific to striated muscle (Walmsley, 2013) we speculate that the presence of these early on in development dampens the increase that was seen from *hacd1-fl* in the later embryos and therefore overall *hacd1* transcripts are not unregulated. This thus suggests that expression levels of the other three isoforms may be down regulated over development (Walmsley, 2013). Unfortunately, the 12hpf time point for *hacd1-fl* had large error bars, which we suggest is because this time point is highly dynamic with respect to gene expression. Pooled embryos were used collected from embryo batches collected from marbles placed in tanks over several hours from morning (lights on). Therefore, there would have been some variability in embryo development in the pools incorporated. This error could have been reduced by collecting embryos from single male female pairs with a more precisely known time of lay and fertilisation and collecting embryos at further time points over the first 36 hours to more precisely characterise the upregulation of *hacd1*.

Expression and localisation data of *hacd1* in zebrafish supports previous findings from Walmsley, (2013) as well as allowing me to conclude that *hacd1* is also muscle specific like its mammalian orthologue (Ikeda *et al*., 2008). During the time of this study a detailed transcriptomic time course evaluating mRNA expression by RNA sequencing (RNA-seq) over zerbrafish development was published by the Vertebrate Genetics and Genomics Group at the Wellcome Trust Sanger Institute and displayed in an online expression atlas [https://www.ebi.ac.uk/gxa/experiments/E-ERAD-475/Results] (White *et al*., 2017). This database published RNA-seq data on all four *hacd* genes: reporting *hacd1* to first be expressed

from the 1-4 somite stage, ~10hpf (White *et al*., 2017) (Figure 2.26). This is earlier than evaluated in this study but is in line with assumption that *hacd1* upregulating with the development of somites.

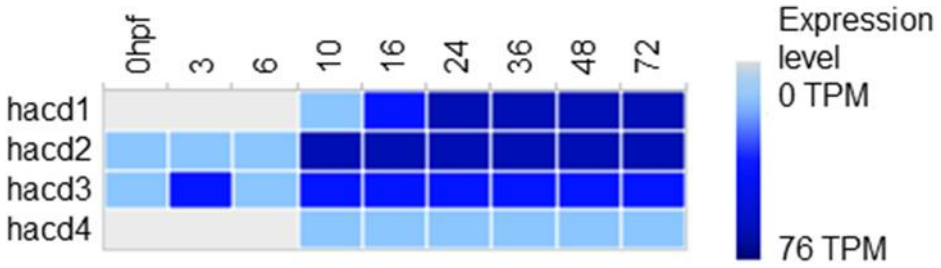

Figure 2.26: Expression levels of the *hacd* genes from RNA-seq data within developing zebrafish embryos from fertilised eggs: 0 hours post fertilisation (hpf) through to 72hpf.
Expression level is represented by transcripts per million (TPM) (Adapted from White *et al*., 2017).

2.4.2. Zebrafish *hacd2* expression is comparable to *HACD2* in mammals and is prone to multiple splicing in a similar manner to that of *hacd1*

RT-PCR expression data for *hacd2* in embryonic zebrafish and adult tissues showed it to also be ubiquitously expressed like its mammalian orthologue. Products for *hacd2* were found at all ages of development and in all tissues of adult zebrafish including the muscle samples which were likely to contain intramuscular bone, therefore the presence of *hacd2* within the muscle could not be concluded at this point (Danos & Ward, 2012). The most likely candidate for a compensatory mechanism resulting from HACD1-deficiency was *hacd2*, due to its high conservation with *hacd1*, and so the time was taken to characterise this gene in particular. We evaluated for the presence of alternative isoforms particularly those encoding essential amino acids which might have HACD activity. Two novel *hacd2* transcripts were characterised through cloning and sequencing of RT-PCR products from zebrafish embryo cDNA. There was a fourth product detected in early embryos unfortunately cloning was unsuccessful so a fourth novel transcript was not confirmed. To understand if this band was a PCR product amplified from another novel transcript, RT-PCR with shorter extension times could be used in order to favour amplification of shorter products in order to produce proportionally more of the product of interest compared to the highly abundant *hacd2-fl* band: this would allow for easier isolation of the PCR product. Additional isoforms present in early development are present for other genes (Tonduer *et al*., 2010) and described previously in C2C12 cells and zebrafish for HACD1. Walmsley, (2013) documented a number of isoforms for *hacd1* in early embryogenesis which were then not present again at later time points.

The *hacd2* ISH staining was seen in the head and developing organs of the embryos at all time points studied. When sectioned these reported some intense staining in the photoreceptors of the eye as well as less intense staining in other areas of the eye and brain.

Previous ISH has been undertaken for *hacd2* in developing embryos and it was documented to have no spatial restriction, which might have been due to a lack of specificity for their probe as this study has reported no muscle staining from ISH experiments with minimal levels found in RT-PCR as discussed for the *hacd2* in adult muscle (Thisse & Thisse, 2004, [http://zfin.org/ZDB-GENE-030131-6053]). Expression levels of *hacd2* have also been reported in mice in which *hacd2* found to be in the cardiac tissue; this is in line with our findings from adult tissue RT-PCR in which *hacd2* produced bright visible bands for the heart tissue samples (Tiret, personal communications).

Quantitative RT-PCR expression data for *hacd2*-total was reported to increase slightly over development (though this was not found to be significant) and the full length *hacd2* transcript, *hacd2-fl*, did increase significantly over embryonic development (2-fold). This was in line with results from the ISH, where *hacd2* was present from the earliest embryos of the 5-9 somite stage/12hpf right through to protruding-mouth stage/72hpf and we therefore hypothesis that *hacd2* is a ubiquitous gene present throughout embryogenesis. The RNA-seq data published during this study found *hacd2* to be expressed from the 128 cell stage/~2hpf (Figure 2.26) which corroborates *hacd2* as a ubiquitous gene expressed over embryogenesis (White *et al*., 2017).

2.4.3. Zebrafish *hacd3* is expressed comparable to mammalian expression

RT-PCR products corresponding to the *hacd3* zebrafish gene were detected at all embryonic time points and in all adult tissues tested. These primers bound exon 5 and exon 11 and those designed to amplify the whole coding sequence were unsuccessful and so even though no isoforms were detected, it cannot be concluded that there are no other *hacd3* isoforms. Results for *hacd3* ISH displayed similar expression localisation to *hacd2* with the majority of staining in head and eyes. Upon sectioning only *hacd3* could be seen within the notochord of the embryos, suggesting possible, novel spatial expression for *hacd3* within zebrafish. Published ISH on *hacd3* in zebrafish embryos is in line with our findings with the expression seen mostly in the head of embryos (Thisse & Thisse, 2004). Quantitative RT-PCR expression data for *hacd3* reported a slight increase over development (although this was insignificant) which corresponds to the results from the ISH, where *hacd3* was present from 48-72hpf. As *hacd3* levels did not increase over expression this suggests it may be present at all embryonic stages. RNA-seq data by White *et al.*, (2017) found *hacd3* expression from the 2-cell stage/<1hpf

(Figure 2.26) which is in line with the hypothesis that *hacd3* is present all throughout embryogenesis (White *et al*., 2017).

2.4.4. Zebrafish *hacd4* results were inconclusive

No products for *hacd4* were amplified in the initial RT-PCR reactions, although a 40-cycle RT-PCR for *hacd4* did present with numerous bands which might have been novel transcripts of the gene but due to these only being present in the high cycle RT-PCR reactions these products may not have been amplified from the gene and may be artefacts. The presence of *hacd4* RT-PCR products in all tissues of the adult tissue RT-PCR could be explained as mammalian *hacd4* is present in leukocytes which could be present in all tissues due to the presence of blood vessels/capillaries running through all tissues (Ikeda *et al*., 2008). ISH of adult tissues would verify this localisation. ISH of *hacd4* within embryonic zebrafish was unsuccessful as no staining could be seen, this provided me with inconclusive results for the expression of *hacd4* in embryonic zebrafish as it is possible embryos were not left for long enough for the development of pigment in leukocytes, if *hacd4* is indeed localised to the leukocytes. Another possibility was that the wrong transcript published on ENSEMBL was an error due to the genome duplication in ancestral zebrafish species. Upon sectioning these embryos, one embryo had unexpected staining indicating *hacd4 expression* in the brain, this staining was bilaterally symmetrical indicating that it was not an artefact yet it was only seen in one embryo section therefore inconclusive and may well corroborate the idea that the *hacd4* transcript on ENSEMBL may be an error. There was no change seen in *hacd4* expression levels which corresponds to the ISH where no *hacd4* expression was detected as well as the RNA-seq data in which very small levels (1-9/78 TPM (transcripts per million) comparatively to 78 TPM for *hacd1* expression) to of *hacd4* were found from 128-cell stage/2hpf onwards (Figure 2.26) (White *et al*., 2017).

2.4.5. Limitations and future work

A potential limitation of this study was the focus on gene expression without assessing protein expression. This is not a linear relationship and therefore important to not only look at RNA expression but synthesised proteins. Both *hacd1* and *hacd2* have been reported to have multiple splice variants however it is unknown if all of these variants are synthesised into proteins and if so, what their functions are as none of their isoforms apart from the full-length isoforms contain the essential amino acids thought to be required for HACD activity. We were unable to study protein expression easily due to the novelty of HACD: there are no available antibodies. Future work here could involve self-design of HACD antibodies (Tiller & Tessier, 2015).

To completely characterise novel transcripts for all four of the *hacd* genes; a technique such as 3' RACE could be performed, on all four *hacd* genes for completeness, to conclusively state the isoforms of *hacd* present in zebrafish (Chen *et al*., 2000). This was not done for this study as two novel transcripts were discovered for *hacd2*, neither of which contained the essential amino acids for HACD activity and were therefore unlikely to compensate for Hacd1 function: and *hacd3* and *hacd4* share so little homology that it was decided any transcripts for these were unlikely to compensate for Hacd1 function.

For completeness, ISH could be performed on sections of adult tissues, specifically muscle to verify the localisation of the genes in adult zebrafish; particularly for *hacd4* in which results from this study were inconclusive.

2.4.6. Chapter conclusions

In conclusion the work in this chapter has characterised the fundamentals of *hacd* expression within developing zebrafish embryos, as well as touching on expression within adult zebrafish. It has been found that *hacd1* is the major *hacd* gene within embryonic and adult zebrafish muscle and that the other *hacd* genes are localised elsewhere, in a comparable manner to mammalian *hacd* expression. The expression of *hacd1* was shown to be in time with the development of somites within the embryo and increase as myoblasts differentiated into mature myofibers found within zebrafish embryos at 3dpf.

Zebrafish embryos have been previously used to study other genes implicated in the centronuclear myopathies, including *DNM2*, *MTM* and *BIN1*. These genes have high synteny and similar expression patterns to the mammalian orthologues. (Dowling *et al*., 2009; Dowling *et al*., 2010; Gibbs *et al*., 2013; Sabha *et al*., 2016; Smith *et al*., 2014). As zebrafish are emerging as a good model to study CNM; characterising the expression of the *hacd* genes within wildtype zebrafish adults and embryos was an essential first step in the generation of a HACD1-CNM zebrafish model. This model was generated alongside the work done for later chapters in this thesis via CRISPR/Cas9 genome editing and was available for the work in Chapter 5. Having reported that *hacd1* is the major *hacd* gene within the muscle of developing zebrafish embryos strengthen the foundations for work in mutating the gene and assessing the effects of these mutations upon the embryos and their muscle structure. The *hacd* expression data in this thesis provides a model for comparing *hacd* expression in mutant embryos: as we suspect *hacd1* expression should significantly decrease in successful *hacd1*-mutant embryos. The conservation between *hacd1* and *hacd2* will be important as there could be a compensatory mechanism that is activated upon *hacd1* mutation with zebrafish.

3 Evaluating the effect of *Hacd1* deficiency on the membrane properties of a myogenic cell line

3.1. Introduction

Tubuloreticular membrane abnormalities are a central feature of centronuclear myopathies (CNMs) which result from a number of different genetic mutations (Al-Qusairi & Laporte, 2011; Nance *et al*., 2012). Disruption of excitation contraction coupling (ECC), more specifically abnormal triad formation and calcium homeostasis, leads to functional abnormalities and profound neuromuscular weakness (Al-Qusairi & Laporte, 2011). Defects in ECC and/or the membranes involved have been reported in myotubular myopathy (Al-Qusairi *et al*., 2009; Dowling *et al*., 2009; Laporte *et al*., 1996), BIN1-CNM (Nicot *et al*., 2007; Smith *et al*., 2014), DNM2-CNM (Bitoun *et al*., 2005; Gibbs *et al*., 2013a; Jungbluth *et al*., 2010) and RYR1-CNM (Jungbluth *et al*., 2007). Altered calcium homeostasis has been hypothesised to result from the morphological membrane abnormalities seen within the triads in CNM and high cytosolic Ca^{2+} concentration as a secondary pathology has been historically correlated with muscle weakness (Al-Qusairi & Laporte, 2011; Fraysse *et al*., 2016; Jungbluth & Gautel, 2014; Nance *et al*., 2012). The interaction between both the voltage-gated dihydropyridine (DHPR) and the ryanodine receptor 1 (RYR1) calcium release channel may be involved in the pathologies seen within CNM pathology (Jungbluth & Gautel, 2014). Mutations in the *DHPR* gene have been reported to cause congenital myopathies with internalised myonuclei (Schartner *et al*., 2017) further corroborating its importance within ECC and myopathies.

Due to the implication that, alongside tubuloreticular membrane disorganisation seen in CNM (Al-Qusairi & Laporte, 2011), ECC and the function of DHPR and RYR1 calcium channels may be highly involved in CNM pathogenesis: this chapter aimed to further evaluate the impact of *Hacd1*-deficiency on cell membranes and calcium responses of the C2C12 murine muscle cell line. The murine muscle cell line, C2C12 has been well studied and found to develop basic and functioning forms of SR and t-tubules (Carozzi *et al*., 2000; Lee *et al*., 2002; Parton *et al*., 1997; Nori *et al*., 2006; Wang *et al*., 2009). Functionally, C2C12 myotubes exhibit calcium transport from internal and external environments via a number of calcium channels including DHPR and RYR1 (Gutierrez-Martin *et al*., 2005) and express ion channel activity that imitates activity seen in skeletal muscle fibres (Kurth *et al*., 2015). They have also been used extensively to study altered calcium homeostasis and disruptions within the

ECC apparatus (Araya *et al*., 2003; Wang *et al*., 2006; Wang *et al*., 2009; Vega *et al*., 2011). Here a transfected clonal C2C12 cell lines were used with short hairpin RNA (shRNA)-mediated *Hacd1* knockdown and a control with an empty vector that were originally a gift from Prof L. Tiret (Blondelle *et al*., 2015) and previously validated in our laboratory (Walmsley, 2013; Walmsley *et al*., 2017). shRNA knockdown is a method of post translational gene silencing using RNA interference, in this case directed against exon 4 of the *Hacd1* transcript (Blondelle *et al*., 2015; Walmsley, 2013; Walmsley *et al*., 2017).

Previous work on this *Hacd1*-kd cell line conducted by Blondelle *et al*., (2015) reported impaired differentiation within the clones investigated. They reported that upregulation of *Hacd1-fl* during early myogenesis was associated with a reduction in membrane fluidity in myotubes at 3dpd (days post differentiation). They concluded that *Hacd1*-deficiency lead to impaired myoblast fusion, which was then successfully restored by re-expression of *Hacd1-fl*, and therefore further concluded HACD1 activity was responsible for the increase in membrane fluidity myoblasts prior to fusion (Blondelle *et al*., 2015). Lin *et al*., (2012) also conducted research on the C2C12 line transfected with an shRNA targeting *Hacd1*. Their results were in line with Blondelle *et al*., (2015) and reported *Hacd1* to be important for myoblast growth and differentiation (Lin *et al*., 2012). Recent cell work was done in a human haploid cell line which confirmed the redundancy of HACD1 and HACD2 (Sawai *et al*., 2017), but this was not a muscle cell line and membrane properties affected by either HACD1 or HACD2 were not evaluated.

Walmsley, (2013) and Walmsley *et al*., (2017) tested several of the clones used by Blondelle *et al*., (2015) and used a clone which differentiated under certain conditions (hydrophilic polymer coated dishes and a particular batch of horse serum in the differentiation media). This allowed the cells to differentiate into myotubes and therefore develop the internal membrane structures for excitation evoked calcium response (Walmsley, 2013). Work was also undertaken to investigate into the localisation of RYR1 in these cells; unusual clusters of nuclei within the *Hacd1*-kd cells at 12dpd were reported that often formed complete or partial rings of nuclei and these correlated with focal areas of intense RYR1 and BIN1 immunostaining (Walmsley, 2013; Walmsley *et al*., 2017). Walmsley, (2013) found RYR1 function, through the stimulation of SR calcium release via caffeine, to be impaired as they reported slower responses in *Hacd1*-kd cells that tended to oscillate: which is an uncommon response for mature myotubes and seen more frequently in early differentiation (Lorenzon *et al*., 1997). This suggested numerous calcium releases via the RYR1 channel from just one stimulation: an abnormal response. Excitation-evoked calcium release was similar between control and knockdown cells and this was thought to be due to limitations of the techniques

used including the lack of a perfusion system to apply different reagents onto the cells and the low temporal resolution of the confocal imaging technique – quick responses would not have been recorded. Therefore patch-clamp techniques would be an appropriate way in which to study calcium release through the assessment of calcium-activated channels, providing fast kinetic information on calcium homeostasis and ECC within the cells (Leech & Holz, 1994). This approach allows analysis with the "cell-attached" mode of patch clamp (Hamill *et al*., 1981). This approach has a number of strengths such as the applicability to both small and large cells (there is no limit to the size of the target cell) and the fact that cells are "intact" there is no need to rupture the membrane, or introduce chemical dyes or expose to high power light sources (Hamill *et al*., 1981). A limitation of the cell-attached mode of recording is that analysis generally requires knowledge of the underlying resting membrane potential (see Chapter 3 methods).

Electrophysiology has long been used to study calcium responses (Sperelakis, 1987) and the patch-clamp technique, studying the ionic currents through cells, is a common way to do so (Leech & Holz, 1994). Numerous patch-clamp based techniques have been developed including: using classical patch-clamp methods to hold membranes at different voltages and measuring the calcium responses via fluorescence in a technique that combines both patch-clamp and calcium imaging protocols (Jacquemond, 1997). Previous electrophysiological work on CNM includes Al-Qusairi *et al.,* (2009) findings: in *Mtm1*-deficient myofibres RYR1 protein expression was decreased 3-fold and a dampened calcium release in response to voltage-clamp depolarisations was reported. *Bin1*-deficient myofibres presented with swollen t-tubules, and Tjondrokoesoemo *et al.,* (2011) reported this phenotype to be linked with a reduced voltage-induced intracellular calcium release suggesting disruption in the coupling between the voltage sensitive DHPR and the SR Ca^{2+} channel RYR1.

Work in this chapter was undertaken to investigate the effect of HACD1-deficiency on calcium homeostasis and electrophysiology properties of a myogenic cell line including characterising any distinct channel phenotypes observed between the control and *Hacd1*-kd cells. Several ion channels are activated by intracellular calcium and could potentially be useful surrogates for intracellular calcium release. One of the most well-established families are calcium activated potassium channels (Vergara *et al*., 1998). Calcium-activated potassium channels are essential regulators of cell excitability (Vergara *et al*., 1998) and therefore will be assessed between the control and *Hacd1*-kd cells among all other channels recorded. The calcium-activated potassium channels may be of small (SK channels), intermediate (IK channels) or large conductance (BK channels) (Kim *et al*., 2014; Vergara *et al*., 1998). It is

plausible that sarcolemmal ion channels are affected as a secondary pathology seen in CNM after membranes are disrupted (Jungbluth & Gautel, 2014). Congenital myopathies have been associated with loss-of-function mutations in *SCN4A* that presented with neonatal-onset hypotonia (Zaharieva *et al*., 2016). Thus, using cell-attached patch clamp to both assess ion channels profiles within cells and characterising the ion channels present on the cells sarcolemma will provide insight into the membrane systems of these cells.

3.1.1. Chapter aims and hypotheses

The work conducted in this chapter aimed to further characterise the phenotype and function of *Hacd1*-deficient C2C12 myoblasts and myotubes. We hypothesised that a change in calcium handling will result in measurable differences in electrophysiological properties of *Hacd1*-kd myotubes in comparison with control myotubes. Aims were specifically to:

1) Assess the comparative differentiation of control and *Hacd1*-kd myotubes;
2) Quantify the expression of *Hacd* genes over differentiaionm including the effect of *Hacd1* knockdown upon this expression
3) Measure the resting membrane potential in control and *Hacd1*-kd cells both at myoblast and myotube stages;
4) Investigate the differential functional expression of ion channels in control and *Hacd1*-kd cells, in both single cell myoblasts and also multinucleated myotubes at 8dpd, ahead of studying the response to depolarisation in the cells.

3.2. Methods

3.2.1. C2C12 cell culture

The *Hacd1*-kd C2C12 cell line used in this chapter, selected because it retained myogenic capacity under the conditions described here, is a clonal cell line stably transfected with the pGIPZ shRNA construct (Figure 3.1) (V2LHS_5923 (GCTCATTACTCACAGTATA) against exon 4 of *Hacd1* (Thermo Scientific) (Walmsley *et al*., 2017). An additional clone, developed in the same fashion, expressed an empty vector for use as a control (RHS4349). The C2C12 murine cell line has been well characterised previously and cells were cultured under standard conditions (37ºC and 5% CO_2) and aseptic technique (Yaffe & Saxel, 1977). C2C12 myoblasts were cultured in Dulbecco's Modified Eagle's Medium (DMEM) (Sigma Aldrich) containing: 10% foetal calf serum (FCS) (Gibco), 2mM L-Glutamine (Sigma Aldrich), 0.1mg/ml penicillin and streptomycin (Sigma Aldrich) and 2µg/ml of puromycin (Invitrogen) within the media to select for only the cells containing the pGIPZ plasmid and therefore the shRNA to knockdown *Hacd1* expression. Wildtype C2C12 were grown under the same conditions, but without the puromycin added to media.

To stimulate differentiation and the fusion of myoblasts into myotubes, cell media was swapped to media containing 2% horse serum (HS) (Gibco) in the place of 10% FCS for up to 12 days and differentiation of cells was visually inspected over this time by phase contrast microscopy using a Nikon Diaphot microscope (Nikon) and ToupView software (ToupTek). *Hacd1*-kd and control cells were grown and differentiated in the selective media containing puromycin and expression of turboGFP (tGFP) (which was linked to shRNA expression via the IRES) was confirmed periodically using a Nikon Eclipse TiE live cell fluorescent microscope (Nikon) and the NIS-elements software (Nikon).

Cell culture was carried out in T75 tissue culture flasks (Costar) and passaged once confluency reached 70-80% using 1x trypsin (Sigma Aldrich) to remove cells from flasks and spinning at 1000rpm for five minutes at room temperate to pellet and cells resuspended in fresh DMEM media before plating at a seeding density of 5000 cells per cm^2, cells were counted using an automatic cell counter (BioRad).

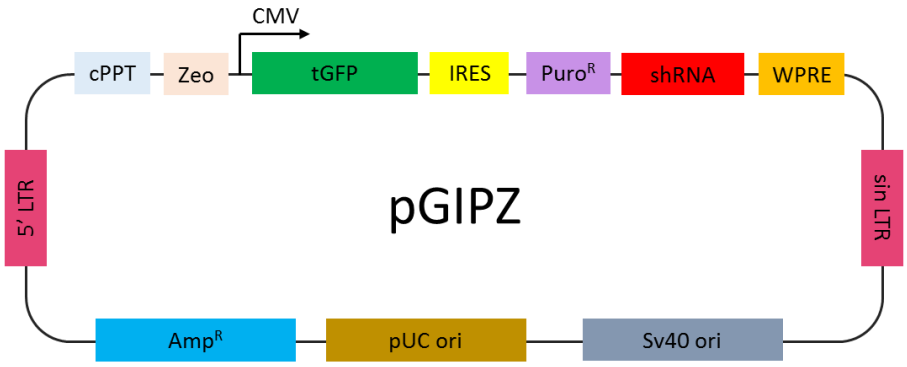

Figure 3.1: The pGIPZ plasmid within C2C12 *Hacd1*-kd cells.
Control cells included plasmid with empty vector. cPPT = central polypurine tract, Zeo = zeocin bacterial selection marker, CMV = cytomegalovirus promoter, tGFP = turbo green fluorescent protein, IRES = internal ribosome entry site, PuroR = puromycin resistance, shRNA = short hairpin RNA, WRE = woodchuck hepatitis virus posttranscriptional regulatory element, sin LTR = self-inactivating long terminal repeat, sv40 Ori = origin of replication, pUC ori = origin of replication, AmpR = ampicillin resistance.

Myoblasts were seeded into 6-well tissue culture plates (Costar) for molecular studies and for immunocytochemistry cells were seeded onto hydrophilic polymer coated, optical-bottomed Ibidi dishes or slides (35mm dishes or 8-welled slides) (Thistle Scientific). For electrophysiological experiments undertaken on myoblasts cells, cells were resuspended in serum free DMEM media while passaging and pipetted into a chamber within the electrophysiology rig. Cells were then allowed to settle for an hour to lightly adhere to the bottom. When using myotubes for patch-clamping: the cells were seeded onto broken sections of treated polymer coverslips (Ibidi, Thistle Scientific) and differentiated into myotubes on a surface that would then fit into the rig for experiments.

Cells were seeded at time zero and, to stimulate differentiation, media was changed to differentiation media 8 hours later. Day 0 was defined to be 24 hours post seeding and day 1 defined as 24 hours after the change to differentiation media. This was done for both consistency and to eliminate the different media as a variable that could show up in ^{1}H-NMR lipidomic analysis (Chapter 4).

3.2.2. RNA extraction and cDNA synthesis from C2C12 cell lines

C2C12 myoblasts and myotubes were cultured as described in Section 3.2.1, and were harvested using a cell scraper (Corning) into 1ml of TRIzol reagent (Life Technologies) before storing at -80^{o}C until RNA extraction. Scraping of cells was visually checked to ensure cells were not left behind on the tissue culture plastic.

Once thawed, samples were incubated at room temperature for five minutes. 200µl chloroform (Sigma Aldrich) was added to sample, agitated for 15 seconds and allowed to stand at room

temperature for a further 15 minutes. Samples were then centrifuged at 12,000g for 15 minutes at 4ºC. This separated the cell lysates into several layers: an upper aqueous phase (containing RNA), an interphase containing DNA and a lower organic protein containing phase. The upper phase was transferred into a new tube and combined with 500µl isopropanol (Sigma Aldrich), vortexed briefly and incubated at room temperature for 10 minutes before a 10 minute centrifugation at 12,000g and 4ºC. Supernatants were discarded and RNA pellets washed with 75% ethanol (Sigma Aldrich) and centrifuged again at 12,000g and 4ºC for five minutes. Supernatants again discarded and pellet allowed to air dry for 10 minutes.

RNA pellets were then re-suspended into 30µl RNase and DNase free water. Re-suspension was aided by a heating step of 55ºC for 15 minutes. Samples were then analysed on a Nanodrop (Nanodrop 2000, Thermo Scientific) to test concentration (ng/µl) and purity, with respect to protein or phenol (260/280) and phenol contaminants (260/230). 1µg of RNA was then reverse transcribed into cDNA by a reverse transcriptase (iScript, BioRad). RNA was combined with nuclease free water to give a volume of 13µl RNA and combined with a 1x Reaction Mix and iScript reverse transcriptase. The reaction was run at 25ºC for five minutes, 46ºC for 20 minutes and 95ºC for 1 minute. The cDNA was stored at -20ºC until use.

3.2.3. Quantitative RT-PCR assay

Both control and *Hacd1*-kd C2C12 cells were grown in triplicate in 6 well plates and differentiated to 10 days. Cells were collected at 0, 1, 2, 4, 8 & 10 dpd (days post differentiation) and RNA was isolated and cDNA synthesised as described in sections 3.2.2. qRT-PCR assays were used to quantify levels of all four *Hacd* genes and the full-length isoform of *Hacd1* across these time points. Three technical replicates were performed for each of the three biological replicates cultured. 20µl reactions were run with 8µl cDNA diluted 1:100 using molecular grade water, 2µl (0.15µM) primer and 10µl (1x) SYBR green mastermix (Roche). The reaction was run at 95ºC for 10 minutes to initially denature the cDNA before 40 cycles of: 95ºC for 15 seconds followed by a combined annealing and extension step at 60ºC for one minute. Relative gene expression was calculated against the house keeping gene *Gapdh* (Walmsley, 2013) by the ΔΔCt method (Livak & Schmittgen, 2001).

Primer sequences were obtained from Walmsley, (2013) (*Hacd1* and *Gapdh* primers) and Blondelle *et al.,* (2015) (*Hacd2-4* primers) and standard curves were performed using 1:10 serial dilutions of a pooled set of C2C12 control cDNA. Plotting a standard curve allowed the efficiency (E) of the reaction to be calculated using the slope, which should be between 90-110% indicating doubling of target DNA each cycle.

$$E = \left(10^{\left(\frac{-1}{slope}\right)} - 1\right) * 100$$

Equation 2

Table 3.1: List of primers used in C2C12 qRT-PCR assays

Gene	Product Length (bp)	Primers (5'-3')
Hacd1-total	212	**F:** ATATCCCGTTGGAGTTGCTG **R:** CGTGGAGCACCTTTCTTCTC
Hacd1-fl	184	**F:** ATGAAGAGAGCGTGGTGCTT **R:** AAGGCGGCGTATATTGTGAG
Hacd2	160	**F:** TGCTATAGGGATTGTGCCATC **R:** ACGGATAATTTCCGTGATTGTCC
Hacd3	174	**F:** GACGTGCAGAACCCTGCTATC **R**: CTTCTGGACTGTGATGTTCACC
Hacd4	186	**F:** CAGCTCACAGAGAGAGTGATC **R:** GAGTGTTTGACTGAGCCATGTC
Gapdh	283	**F:** TTGTGATGGGTGTGAACCAC **R:** TTCAGCTCTGGGATGACCTT

3.2.4. qRT-PCR primer validation

Primer sequences (Table 3.1) were used from Blondelle *et al*., (2015) and Walmsley, (2013) and were validated by assessing melt curves and peaks, and standard curves to evaluate efficiencies. *Hacd1-4* sequences with primers annotated can be seen in Appendix Figures A2.2, A2.3, A2.4 and A2.5.

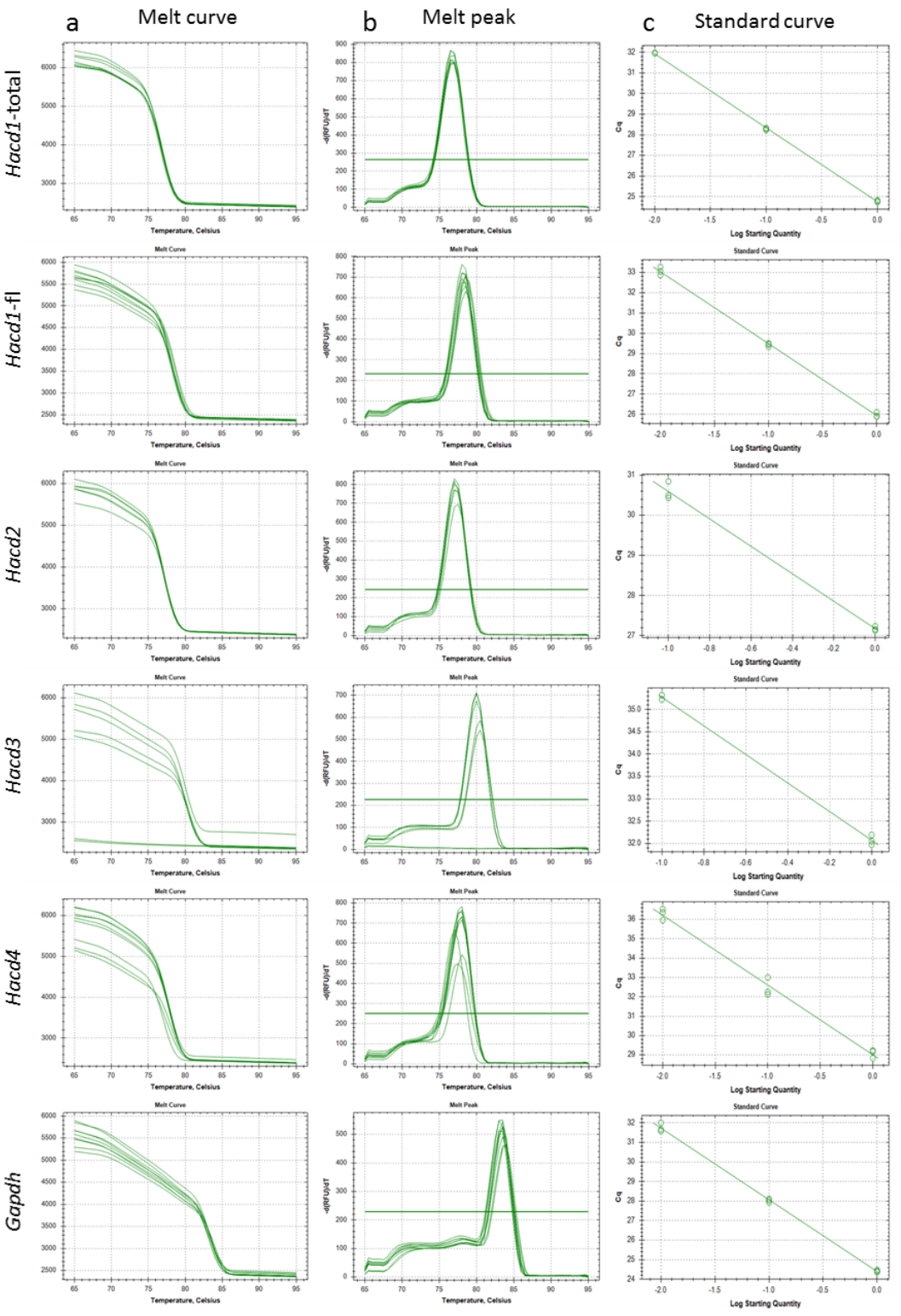

Figure 3.2: Validation of *Hacd* and *Gapdh* primers for C2C12 qRT-PCR assays.

Outputs from BioRad CFX Manager software: (a) melt curves, (b) melt peaks both indicating only single products being amplified and therefore primers sufficiently specific and (c) standard curves reporting on the efficiency of primers. Values from c are displayed in Table 3.2.

Table 3.2: Efficiency of primers used in C2C12 qRT-PCR reactions in this chapter.

Primer	Efficiency (%)	R^2	Slope
Hacd1-total	90.2	1.00	-3.583
Hacd1-fl	91.5	0.998	-3.544
Hacd2	96.3	0.994	-3.415
Hacd3	105.4	0.998	-3.198
Hacd4	88.2	0.989	-3.643
Gapdh	87.4	0.998	-3.665

3.2.5. Immunocytochemistry

Cells were seeded onto coated hydrophilic polymer coated, optical-bottomed Ibidi dishes or slides (35mm dishes or 8-welled slides) and fixed at day 0 as myoblasts or myotubes at 8dpd. Cells were fixed and permeabilised using ice cold methanol: acetone (Fisher Scientific) at a ratio of 1:1 before air drying and storing at -20^{o}C till use. On day of experiment cells were brought back up to room temperature and blocked in 1% goat serum (Sigma Aldrich) in phosphate buffered solution (PBS, Sigma Aldrich) before incubating with the primary antibody overnight on a rocker at 4^{o}C. After primary incubation cells were washed with PBS before incubating for an hour at room temperature on a rocker with the secondary antibody, from this stage onwards cells were protected from light due to the fluorescent nature of secondary antibodies used. Cells were then washed again and incubated with Hoechst at a concentration of 1mg/ml (Sigma Aldrich) for 10 minutes at room temperature to stain the nuclei of the cells. Cells were then covered with a coverslip using Hydromount (National Diagnostics) for imaging.

Samples were imaged using a Hamamatsu camera (Hamamatsu), a Nikon TE2000 microscope (Nikon) and IP Lab software (BD Biosciences). Exposure times were decided upon using control cells and the auto-exposure tool. Once an appropriate exposure time was decided upon for each antibody, this was kept consistent across all experiments. Images were taken at the top and both sides of dishes to obtain three images.

Table 3.3: Table of antibodies used in this chapter.

Primary Antibody	Type	Concentration	Secondary Antibody	Source
RYR1	Mouse monoclonal IgG1	1:100	Anti-mouse Alexa Flour 488	Abcam, ab2868
DHPR	Rabbit polyclonal IgG	1:100	Anti-rabbit Alexa Flour 594	Abcam, ab2864
MF20	Mouse monoclonal IgG2b (Supernatent)	1:2	Anti-mouse Alexa Flour 488	DSHB, ab2147781

3.2.5.1. Assessment of myotube differentiation

To assess the differentiation of myoblasts into multinucleated myotubes both the control and *Hacd1*-kd cells were stained at 8 days post differentiation (dpd) with an antibody against sarcomeric myosin (MF20) which is used as a marker for differentiation (Wallace *et al*., 2016) as described in Section 3.2.5. Into the 8-well Ibidi dis hes, control and *Hacd1*-kd cells were seeded into four/eight wells each - three were incubated with the primary antibodies and one well for each cell type used for negative controls with no MF20 primary antibody incubation step. This was repeated twice creating an n=6 for analyses. Three images were taken from each well creating a total of 18 images which were analysed and averaged per well to create the n=6.

Differentiation index was obtained by manually counting nuclei and calculated as the percentage of all DAPI stained nuclei counted within the MF20 positive myotubes (containing at least two nuclei) (Blondelle *et al*., 2015) and fusion index as the average number of nuclei per myotubes using the same criteria (Blondelle *et al*., 2015; Wallace *et al*., 2016). Myotube density was calculated using Image J (National Institute of Health) to analyse the percentage of image area that was positive for MF20; images were converted into binary images where the fluorescence of the image was converted to black pixels. These black pixels then represented MF20 stain and therefore myotube differentiation (Velica *et al*., 2011). Clusters of abnormal myonuclei were classified as four or more myonuclei in contact with another or those forming ring-like shapes.

3.2.6. Electrophysiology

Patch pipettes were prepared using 1.5mm thick walled borosilicate glass capillary tubes (Intracel) using a Narishige two-step pipette puller (Narishige). When filled, whole-cell pipettes had a 3-8MΩ/Ohm resistance and pipettes for cell-attached patch configuration had 8-12MΩ/Ohm resistance. Solutions used in these experiments are detailed in Table 3.4.

For all experiments patch pipettes were filled with the appropriate solution and lowered down the cell chamber via a micromanipulator to reach a single myoblast or myotube. Once the pipette was just touching the top of the cell negative pressure was applied to form a giga-seal with the cell. Cell-attached patch requires this seal and whole-cell requires high pressure being applied in order to perforate the membrane (Hamill *et al*., 1981). The establishment of a giga-seal ensures that any current activity recorded is from channel gating on the cell membrane (Hamill *et al*., 1981). Recordings were collected into the WinEDR software (John Dempster) using an Axopatch 200b amplifier (Axon Instruments) with a sampling interval of 0.1ms and filtered at 2 kHz.

Table 3.4: Table of reagent concentrations (mM) used in solutions for electrophysiological experiments, all pH adjusted to 7.35 using NaOH.

	HEPES bath solution	Intracellular
NaCl	156	-
KCl	3	26
$MgSO_4$	2	-
KH_2PO_4	1.25	-
$CaCl_2$	2	-
Glucose	10	-
HEPES	10	10
EGTA	-	5
KG	-	115
$MgCl_2$	-	1

RMPs were adjusted by +3.5mV (Table 3.5) to offset the junction potential created by the use of two solutions of different concentrations.

Table 3.5: Solutions used in each experiment and the junction potentials for these conditions, calculated using JPcalc software (Axon Instruments).

Experiment configuration	Bath Solution	Pipette solution	V_j (mV)
Cell-attached (single channel)	HEPES bath solution	HEPES bath solution	0
Whole cell (RMP)	HEPES bath solution	Intracellular solution	+3.5

3.2.6.1. Resting membrane potential (RMP) recording and analysis

Whole-cell configuration was used to record the RMP, for whole-cell configuration once the giga-seal was obtained, increased negative pressure was then applied to perforate the cell membrane and create a whole-cell seal. The amplifier settings were then adjusted so that there

was no current being applied to the cells to record the cells natural RMP (I=0). RMP was then recorded for ~200 seconds. Gain used in recordings was 10x.

The most stable 100 seconds of recording was (mode) averaged to calculate the RMP for each cell. Ten recordings were collected for each cell type and age (dpd) and all recordings are plotted alongside median of recordings and standard error of the mean (SEM).

3.2.6.2. Single channel recording and analysis

Following on from obtaining a giga-seal, recordings were made in the voltage-clamp mode to record changes in current, with a high gain of 200x. Holding potential of the cell was then changed (between -100mV and 100mV) in increments of 10mV to record any changes in amplitude due to channels gating (opening or closing).

Holding voltage was subtracted from the RMP of cells to calculate the real cell voltage during recordings. These were plotted against currents (pA) measured at different holding voltages from the raw data traces to create current-voltage (IV) curves from which reversal potential (V_{rev}) (the membrane voltage at which there is no net flow of ions) and slope conductance (pS) (rate of ion travel through channels) were calculated from the curve.

QuB software (QuB, State University of New York) was used to create all-points histograms by selecting areas of the trace that represented the channel at 'open and 'closed' gating. These provided information on the time in the traces the channels spent at either 'open' or 'closed' states.

3.2.6.3. K-means clustering

K-means clustering is a form of unsupervised machine learning that groups ("clusters") multi-dimensional data by similarity. Scripts were written in python (Python) by another researcher, Dr. Barrett-Jolley, using the open source library sklearn (Scikit-learn package). These were used to identify patterns of ion channel phenotype using two dimensions; channel reversal potential and single channel conductance. These were first calculated for each patch using linear fits to current-voltage relationships.

3.2.6.4. Equilibrium potentials

The equilibrium potential (Eq_x) was calculated from the Nernst equation (Equation 2).

$$Eq_x = \frac{RT}{zF} \ln\left(\frac{[X]_{out}}{[X]_{in}}\right)$$

Equation 3

Where, [X] is the concentration of ion X, R is the universal gas constant (8.314 Joules per Kelvin per mole), F is the Faraday's constant (96485 Coulombs per mole) and *z* is the valence of ion X. Ion channels are often selective for a single ionic species and their equilibrium potential value therefore approaches the value for the reversal potential of the channel (V_{rev}). This is useful since the *Vrev* itself can be measured directly using the IV (current-voltage) curve; the point where the line crosses the X axis (current = 0).

Table 3.6: The theoretical equilibrium potentials, of the major monovalent ions.
As discussed in the text, the reversal potential of a selective ion will approach the ion's equilibrium potential under normal conditions. Note that for a non-specific ion channel, one would expect a reversal potential near to 0mV. Values calculated using Equation 3 for the solutions used in these studies. (Values for cellular concentration of ions within muscle obtained from McKenna *et al*., 2008).

Ion selectivity	Equilibrium potentials (mV)
Na^+	+61
K^+	-93
Cl^-	-66

3.2.6.5. Statistics

With the exception of the k-means clustering, all statistics were performed with GraphPad Prism (GraphPad Software Inc.).

Two-way ANOVAs (analysis of variance) were conducted for qRT-PCR data and represented as mean values with error bars indicating standard error of the mean (SEM). Student's t-tests were performed to analyse any significance between control and *Hacd1*-kd RMPs. For k-means clustering, statistical differences between numbers of clusters and between cell populations were determined by F-tests computed within the Python code (Scipy package). Significance was annotated on graphs as follows: * indicates $p \leq 0.05$, ** indicates $p \leq 0.01$, *** indicates $p \leq 0.001$ and **** indicates $p \leq 0.0001$.

3.3. Results

3.3.1. Control and *Hacd1*-kd C2C12 cell morphology over differentiation is comparable

Figure 3.3 shows the morphology of both control and *Hacd1*-kd cells over eight days of differentiation, which was comparable between both cell types. At Day 0 single myoblasts were present for both cell types and by 4dpd (days post differentiation) the myoblasts had begun to fuse and elongate. At 4dpd the control cells covered more of the dish compared to the *Hacd1*-kd cells – this was likely due to the control cells observably proliferating at a faster rate, reported also by Blondelle *et al.,* (2015). By 8dpd both control and *Hacd1*-kd cells had formed multinucleated myotubes.

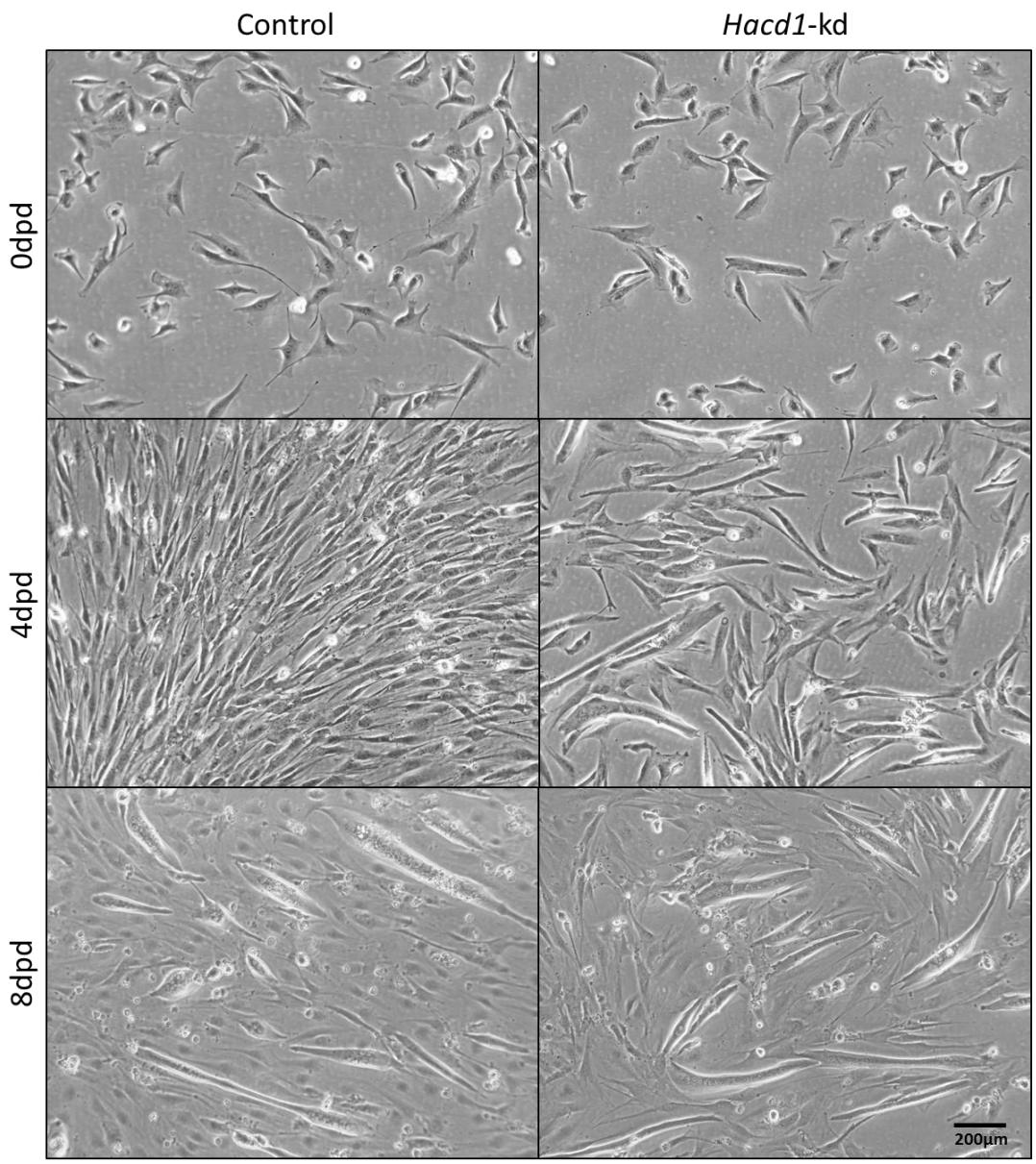

Figure 3.3: Morphology of both control and *Hacd1*-kd C2C12 cells over differentiation.
Both control and *Hacd1*-kd cells were single myoblasts at 0dpd (days post differentiation), by 4dpd both control and *Hacd1*-kd cells began to elongate as they started to fuse with nearby cells and by 8dpd there were distinct myotubes with multiple nuclei. Scale bar represents 200µm.

Both control and *Hacd1*-kd cells expressed the tGFP (Figure 3.4) due to the pGIPZ plasmid (Figure 3.1) (not present in wildtype C2C12 cells).

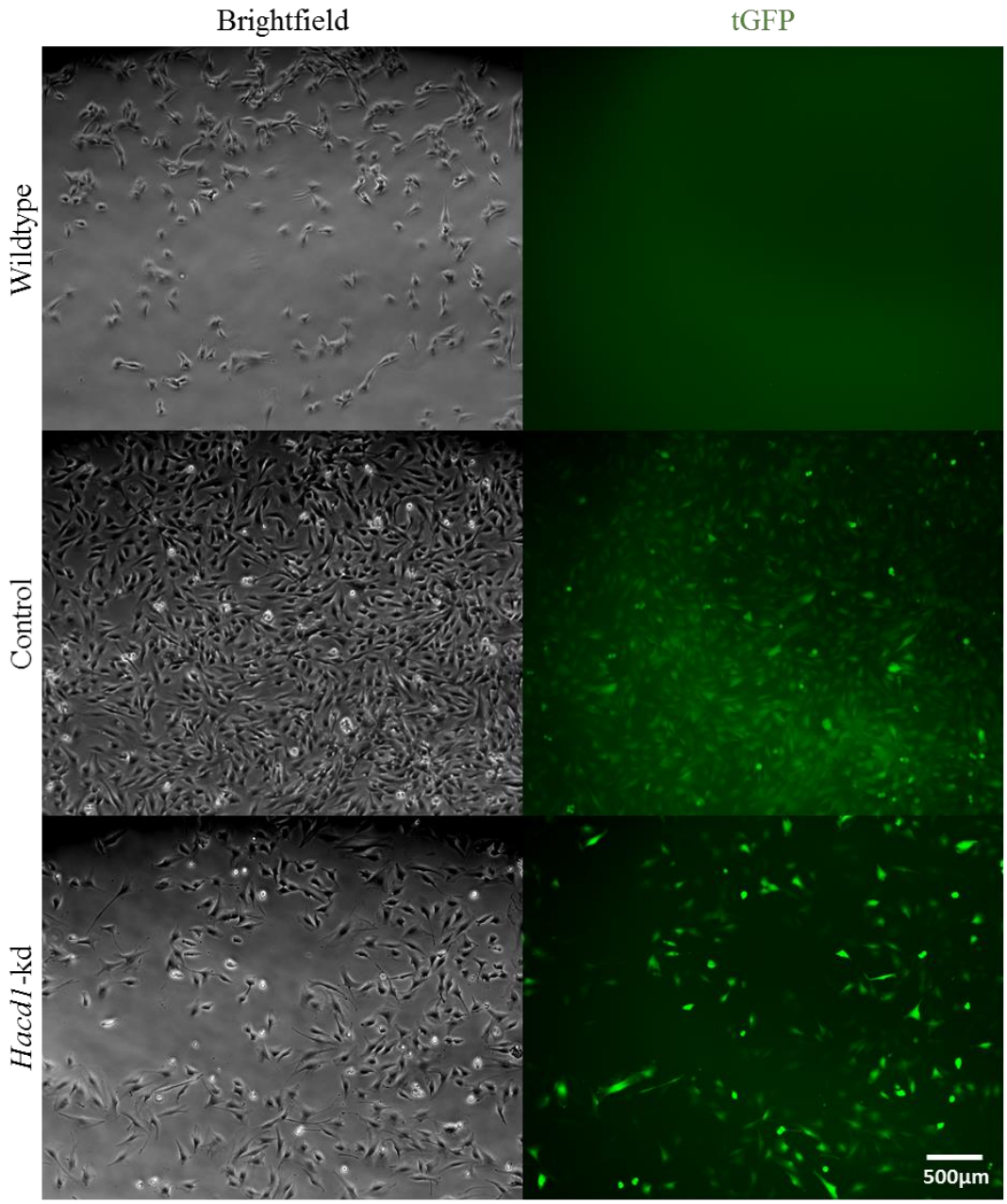

Figure 3.4: tGFP expression in pGIPZ transfected cells.
Myoblasts of wildtype cells did not express tGFP and both control and *Hacd1*-kd cells transfected with pGIPZ plasmid did express the tGFP. Scale bar represents 500µm.

3.3.2. *Hacd1* expression was significantly knocked down in the later stages of differentiation in this *Hacd1*-kd cell line

Cells were collected for qRT-PCR analysis to evaluate levels of all four *Hacd* genes in the context of *Hacd1* knockdown and to independently validate the cell lines used. Previous work had demonstrated consistent knockdown of *Hacd1* of at least 80% at all time points in this particular clonal cell line (Walmsley, 2013).

In control cells, expression levels of *Hacd1*-total (which detects all *Hacd1* isoforms), increased significantly from 4 days post differentiation (dpd) by ~1.5-fold and after - up till 10dpd where the increase was 3.5-fold (Two-way ANOVA, $p<0.01$). In the *Hacd1*-kd cell line the *Hacd1*-total expression did not increase up until 8dpd where there was a small, insignificant, increase. By 10dpd the knockdown was a 3.5-fold knockdown (35%, Sidak's multiple comparisons, $p<0.01$).

Expression of the *Hacd1-fl* isoform increased by 5-fold between 2 and 4dpd and then by 10dpd had increased by 20-fold (Two-way ANOVA, $p<0.0001$). In comparison, the *Hacd1*-kd cell line did not have this increase and the knockdown was significant from 4dpd onwards. At 10dpd there was a 15-fold increase (75%, Sidak's multiple comparisons, $p<0.0001$).

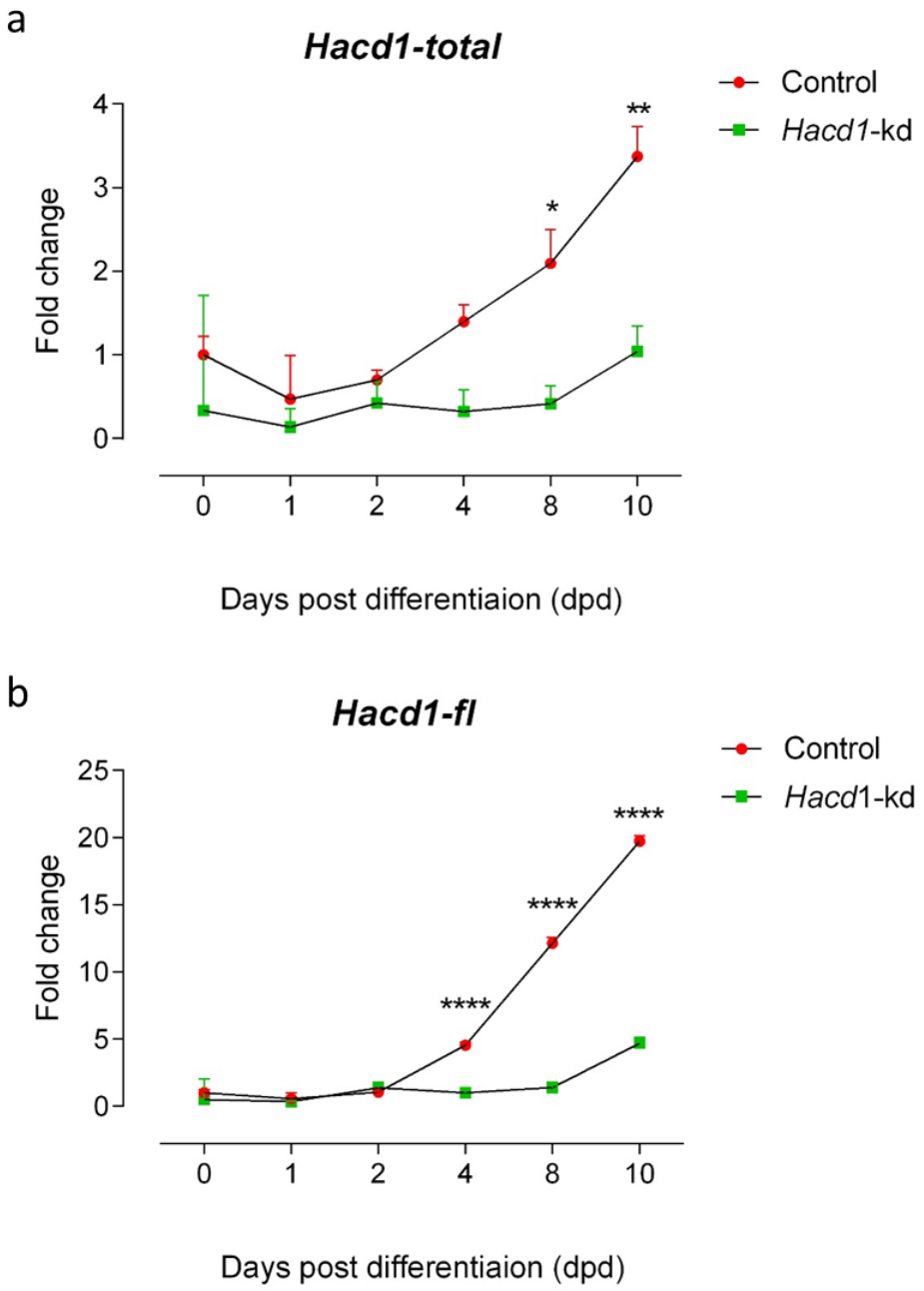

Figure 3.5: Expression levels of *Hacd1-total* and *Hacd1-fl* over 10 days of differentiation in C2C12 cells presented as fold change from control cells at 0dpd (days post differentiation) (n=3).
(a) Two-way ANOVA reported *Hacd1*-total expression increased significantly by 3.5-fold ($p<0.01$) in control cells over differentiation and was significantly lower in *Hacd1*-kd cells over the time course ($p<0.001$). (b) *Hacd1-fl* expression levels were unchanged in control cells up until 2dpd when it began to be upregulated 20-fold ($p<0.0001$). This upregulation after 2dpd was not present within the *Hacd1*-kd cells and the difference between *Hacd1-fl* expression within control and *Hacd1*-kd cells was significant ($p<0.0001$). Sidak's post-hoc tests assessing significance between control and *Hacd1*-kd cells at each timepoint are annotated on the graphs as follows: * indicates $p\leq0.05$, ** indicates $p\leq0.01$, *** indicates $p\leq0.001$ and **** indicates $p\leq0.0001$ and error bars represent the standard error of the mean (SEM).

3.3.3. Reduction in *Hacd1* expression is not associated with a compensatory change in *Hacd2-4* expression in C2C12 myotubes

Expression levels of *Hacd2* were significantly affected (Two-way ANOVA) by differentiation ($p<0.05$) in control cells where they increased by 2-fold over differentiation. Expression levels of *Hacd2* in *Hacd1*-kd cells decreased by 2-fold over differentiation ($p<0.05$). Despite these changes over differentiation, there was no significant difference in *Hacd2* expression at any time point between control and *Hacd1*-kd cells. *Hacd3* expression in control cells was unchanged over differentiation yet in *Hacd1*-kd cells *Hacd3* expression was 3.5-fold upregulated at 0dpd (days post differentiation) ($p<0.0001$) but by 4dpd onwards expression was not significantly different between control and *Hacd1*-kd cells. Overall two-way ANOVA analysis found the *Hacd1* knockdown to have a significant effect upon *Hacd3* expression. *Hacd4* expression was also unchanged over differentiation in control cells, but significantly affected in *Hacd1*-kd myoblasts ($p<0.0001$). At 0dpd there was 5-fold more *Hacd4* expression in *Hacd1*-kd cells than in control ($p<0.0001$) and at 1dpd there was 4 times more expression ($p\leq0.01$). From 2dpd onwards there was no significant difference between control and *Hacd1*-kd cells. Overall there was a significant difference in *Hacd1*-kd cells ($p<0.001$).

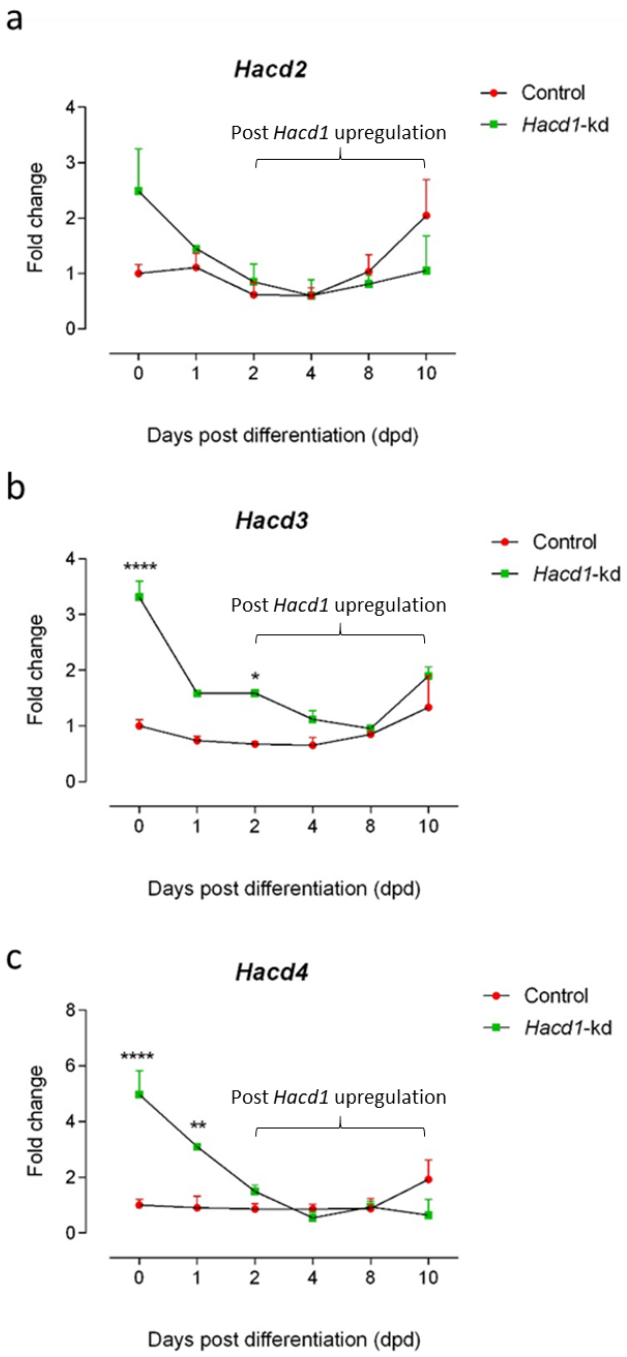

Figure 3.6: Expression levels of *Hacd2*, *Hacd3* and *Hacd4* over 10 days of differentiation in C2C12 cells presented as fold change from control cells at 0dpd (days post differentiation) (n=3).

Hacd2 expression increased 2-fold over differentiation in control cells, and this was seen to decrease in *Hacd1*-kd cells by 1.5-fold. Two-way ANOVA results reported differentiation to have a significant effect on *Hacd2* expression ($p<0.05$) and that there was no significant difference overall between control and *Hacd1*-kd group ($p=0.5020$). *Hacd3* expression levels were significantly different over differentiation in *Hacd1*-kd cells ($p<0.0001$) and there was a significant difference between expression in control and *Hacd1*-kd cells ($p<0.0001$). *Hacd4* expression was significantly different over differentiation ($p<0.0001$) and also between control and *Hacd1*-kd cells ($p<0.001$). Sidak's post-hoc tests to test for significance between control and *Hacd1*-kd cells at different time points are annotated on the graphs as follows: * indicates $p\leq0.05$, ** indicates $p\leq0.01$, *** indicates $p\leq0.001$ and **** indicates $p\leq0.0001$ and error bars represent the standard error of the mean (SEM).

3.3.4. Myogenic differentiation analysis

To quantify aspects of myogenic differentiation, both control and *Hacd1*-kd myotubes aged 8dpd were used to perform immunocytochemistry (ICC) for MF20 (a marker of myogenic differentiation). MF20 antibody was first validated as seen in Figure 3.7, where it was not present in 0dpd but was present in differentiated myotubes at 8dpd. Both cell lines expressed sarcomeric myosin confirming myogenic differentiation at 8dpd. Figure 3.8 shows fairly uniformed myotubes formed by control cells and myotube formed by *Hacd1*-kd cells that includes a large cluster of nuclei at the end.

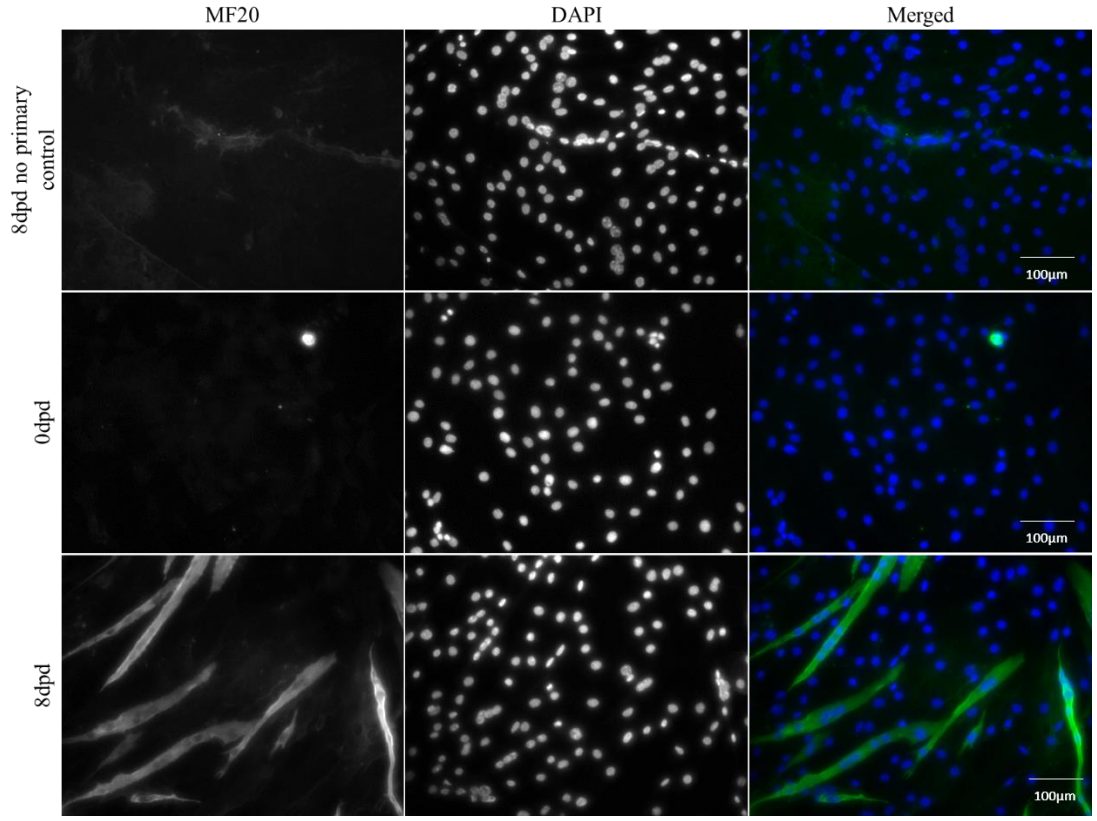

Figure 3.7: Validation of MF20 immunocytochemistry within control day 8 myotubes.
Left column shows MF20 stain, the middle column shows the DAPI stain and a merged image of both stains in shown in the right column. Only the DAPI stain was present at 0dpd (days post differentiation) or when no primary antibody was tested, which confirmed specificity of MF20 antibody to that of differentiated myotubes (8dpd).

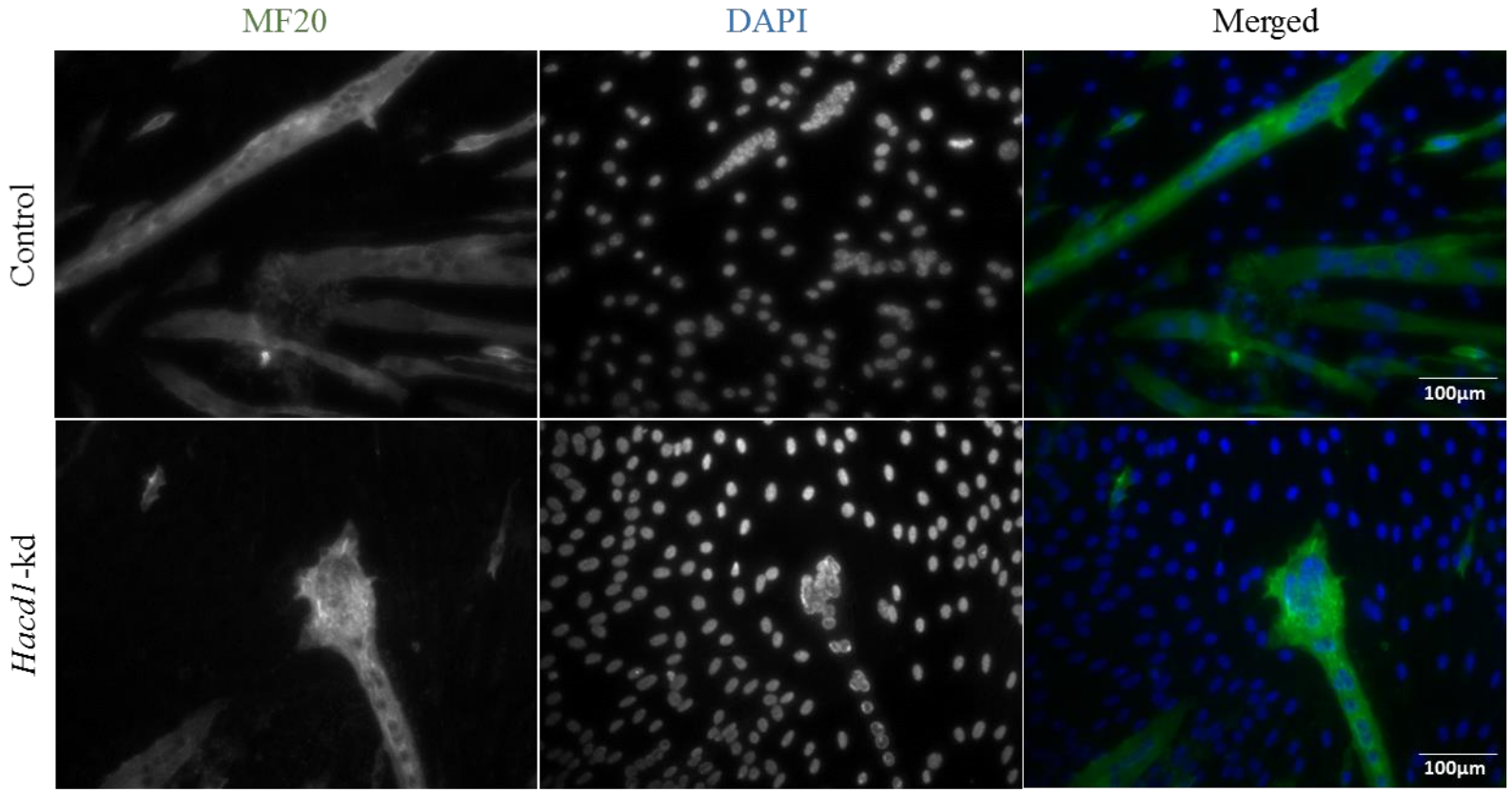

Figure 3.8: MF20 (sarcomeric myosin) stained C2C12 myotubes at 8dpd (days post differentiation).
Analysis of myogenic differentiation was performed as an n=6, and representative images are shown above.

Abnormal nuclei clusters were counted in both control and *Hacd1*-kd myotubes to assess the frequency of these in both cell lines. There were twice as many myotubes with these abnormal clusters in the *Hacd1*-kd populations (10% in control and 20% in *Hacd1*-kd cells) although this was not a significant result (t-test, p=0.26).

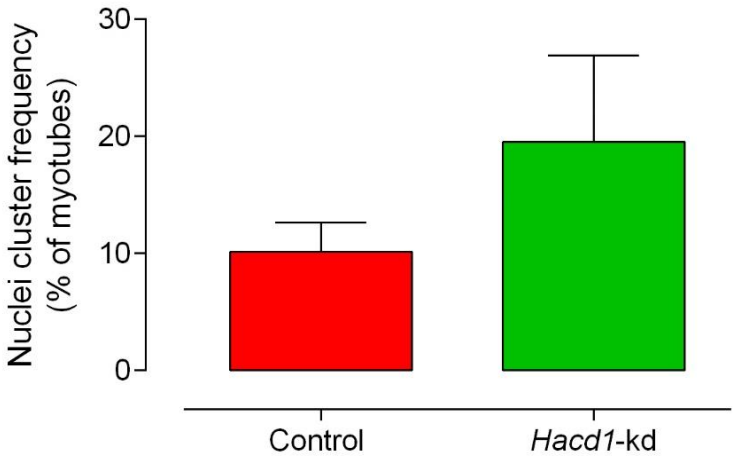

Figure 3.9: Quantification of abnormal nuclei clustering in control and *Hacd1*-kd myotubes at 8 days post differentiation (dpd).
Clustering of nuclei was considered abnormal if there were four or more nuclei in contact that was not linear. There was no significant difference between the amount of control and *Hacd1*-kd myotubes with abnormal clusters (10% control myotubes, 20% *Hacd1*-kd myotubes) (p=0.26, n=6). Coloured bars represent the mean and error bars represent the standard error of the mean (SEM).

The MF20 ICC images were also used to quantify myogenic differentiation. Figure 3.10a displays the quantified differentiation index results, which were not significantly different between control and *Hacd1*-kd cells (28.5% and 26.9% of nuclei within myotubes respectively, p=0.812). Figure 3.10b shows results from the fusion index, which was also not significantly different between control and *Hacd1*-kd cells (6.9 and 6.8 nuclei per myotube respectively, p=0.926). Figure 3.10c shows results from the myotube density quantification - no significant difference was found between myotube density in control and *Hacd1*-kd cells (10.1% and 8.4% of the dish respectively, p=0.566).

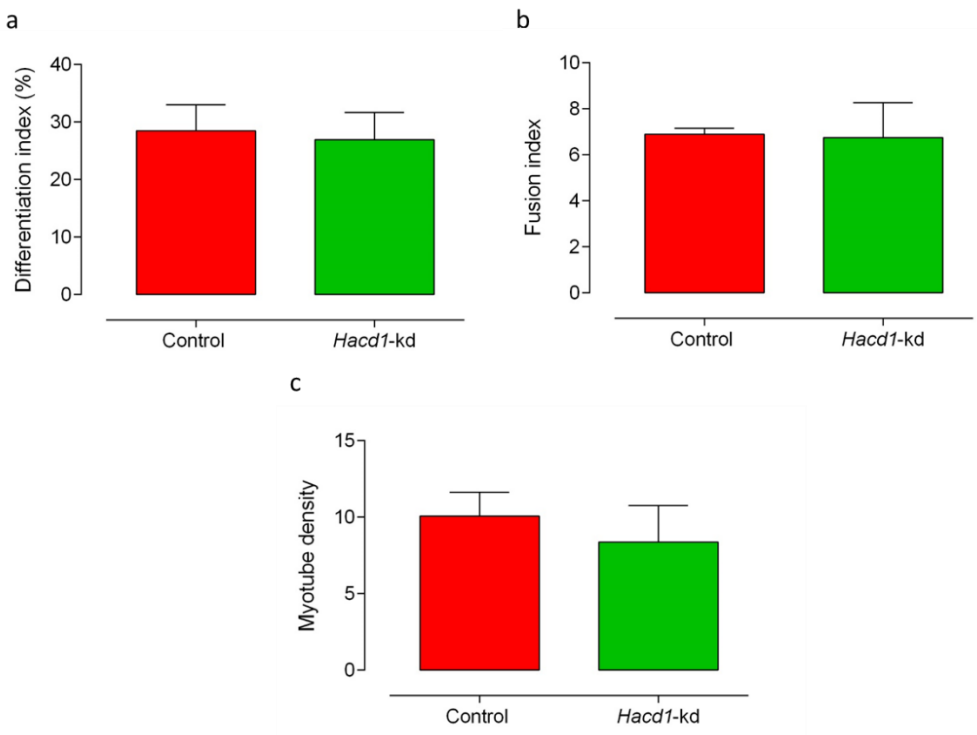

Figure 3.10: Assessment of myotube differentiation in both control and *Hacd1*-kd myotubes at 8dpd (days post differentiation).

(a) Differentiation index in control and *Hacd1*-kd cells was reported to be 28.5% and 26.9% respectively (% of nuclei within MF20 positive cells). Unpaired t-test reported no significant difference between the two groups, p=0.812. (b) Fusion index (average nuclei per MF20 positive myotube) of control cells was reported to be 6.9, and 6.8 in *Hacd1*-kd cells. Unpaired t-test reported no significant difference between the two groups, p=0.926. (c) Control cells had a myotube density of 10.1% compared to 8.4% in *Hacd1*-kd cells, this was not significantly different (t-test, p=0.566). All experiments were n=6. Coloured bars represent the mean and error bars represent the standard error of the mean (SEM).

3.3.5. RYR1 & DHPR calcium channels are both present in myotubes at 8dpd

Immunocytochemistry was performed to confirm the presence of both DHPR and RYR1 channels in mature myotubes. Figure 3.11 shows the validation of the co-staining of RYR1 and DHPR which was confirmed to be specific due to the absence of either red or green fluorescence when neither primary antibody was incubated on the cells.

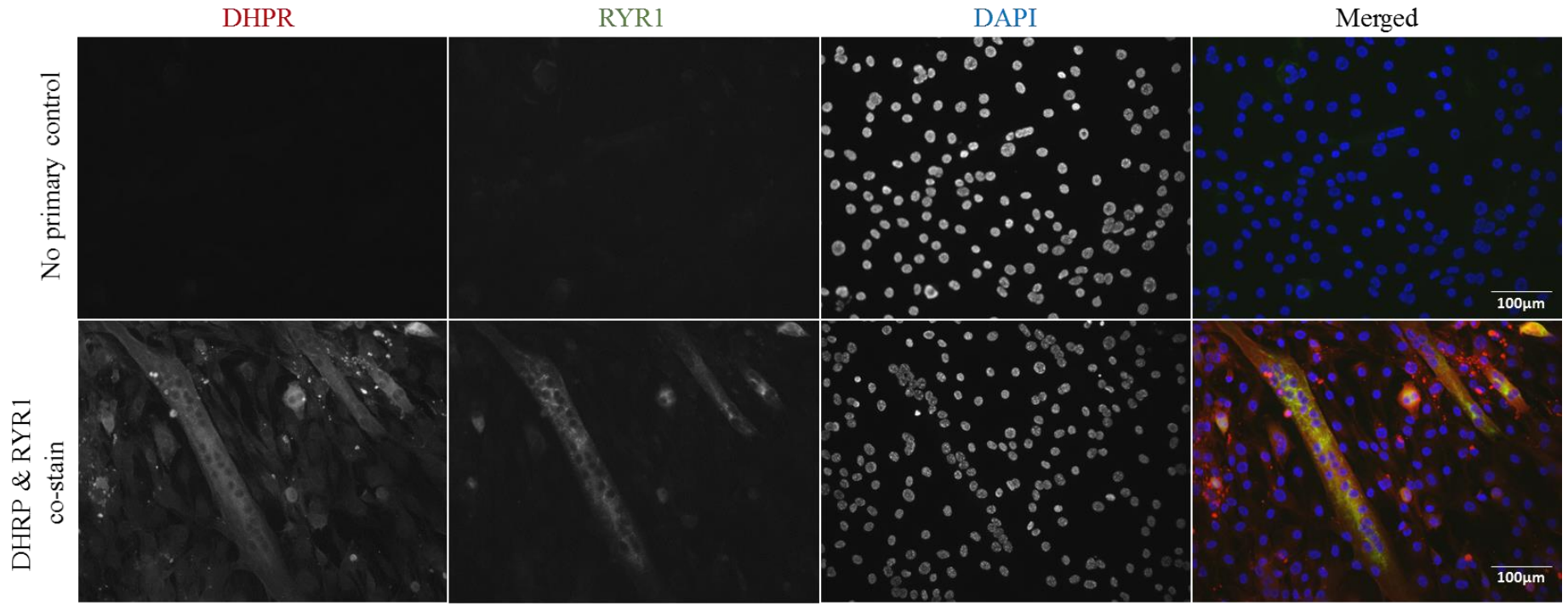

Figure 3.11: Validation of RYR1 and DHPR co-stain within control day 8 myotubes.
Far left image shows DHPR channel, then next along the RYR1 channel, the DAPI channel and finally on the far left a merge of all 3. Only the DAPI stain was present when no primary controls were tested, confirmed specificity of stain visualised.

Figure 3.12 shows the co-staining of both DHPR and RYR1 calcium channels. Whereas RYR1 was only present within the myotubes, DHPR was also present within the myoblasts that had not differentiated in the dishes. RYR1 staining was stronger with consistent imaging technique within the control than the *Hacd1*-kd myotubes and the *Hacd1*-kd myotube annotated by a red arrow indicates an area of intense RYR1 stain alongside an abnormal nuclear cluster. Some of the areas of high staining appear to be extracellular therefore this was thought to be non-specific staining of debris. Importantly, the ICC confirmed the presence of the two channels before this time point was taken forward to use for electrophysiological experiments.

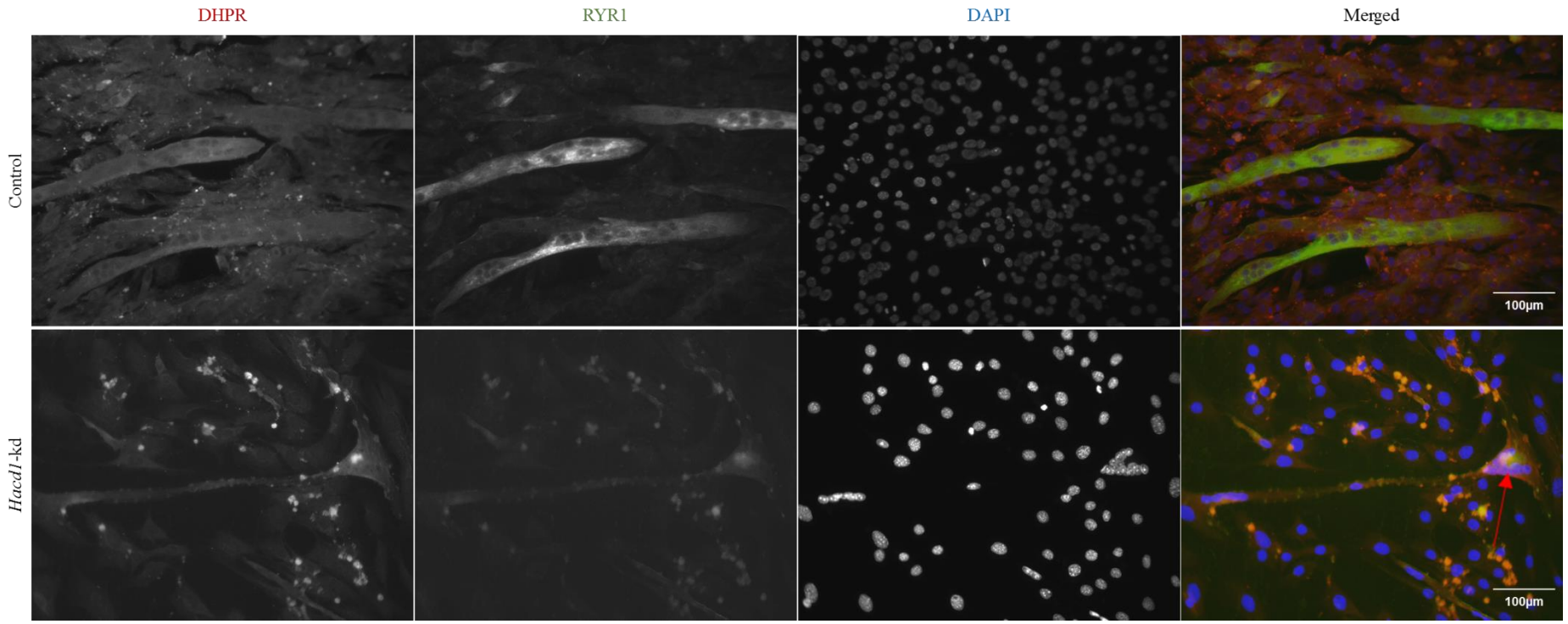

Figure 3.12: Immunocytochemistry of both RYR1 and DHPR calcium channels in myotubes aged 8 days post differentiation (dpd).
DHPR staining is shown in the far left column, followed by RYR1 in the second left hand column, DAPI staining in the third and a merge of all 3 channels in the far-right column. Scale bar represents 100µm and the red arrow in the *Hacd1*-kd merged figure indicates an area of the myotube with an abnormal nuclear cluster with an area of intense RYR1 stain.

3.3.6. Electrophysiological analysis of a *Hacd1* deficient myogenic cell line

3.3.6.1. Resting membrane potential of control and *Hacd1*-kd myoblasts was not significantly different

For accurate single ion channel analysis, the resting membrane potential (RMP) of cells was required to calculate the true cell voltage from the holding voltage used during recordings. RMPs were therefore recorded for both myoblasts and myotubes in both control and *Hacd1*-kd cells: this also allowed assessment of any differences in RMP as a result of *Hacd1* knockdown.

After recording RMP for both control and *Hacd1*-kd myoblasts, and using a student t-test, there was no significant difference (p=0.88, n=10) in the RMP for control cells (-7mV ± 2.1mV) and for *Hacd1*-kd cells (-4mV ± 4.8mV). An F test of variance found there to be significantly more variance within the *Hacd1*-kd myoblast RMPs (F= 5.6, p=0.01).

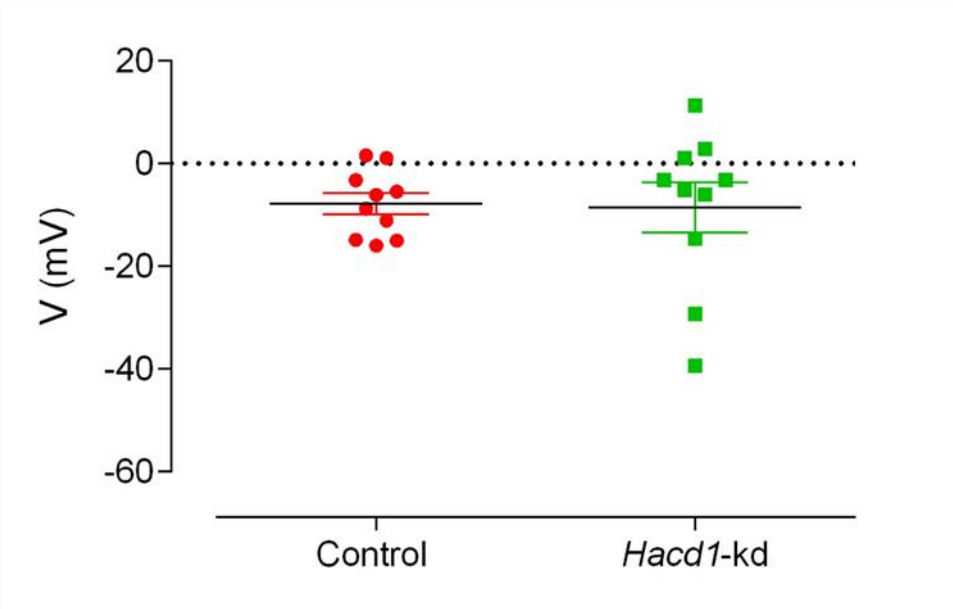

Figure 3.13: Resting membrane potential (RMP) of control and *Hacd1*-kd C2C12 myoblasts.
There was no significant difference (p=0.89) between the RMP of control (-7mV) and of *Hacd1*-kd (-4mV) cells by unpaired t-test analysis, n=10. F test of variance found *Hacd1*-kd RMPs to be significantly more varied (F=5.6, p=0.01).

3.3.6.2. K-mean clustering reveals differences in ion channel profile between control and *Hacd1*-kd myoblasts

Patch-clamp recordings of control and *Hacd1*-kd myoblasts provided data on a number of different ion channels. It was observed that the *Hacd1*-kd cells were easier to achieve a seal with and for that reason there were a higher number of recordings achieved for the *Hacd1*-kd cells. After all ion channel openings seen in recordings had been analysed (conductance in pS, and reversal potential in mV), channels from both control and *Hacd1*-kd myoblasts were run

through a k-means clustering script in Python. Clustering analysis was carried out to evaluate which myoblast channels were similar in regards to the conductance and reversal potential. Six clusters were determined to be appropriate for cluster analysis after running the analysis on control cells as six clusters were a significantly better fit for grouping similar channels than using five clusters to group the channels ($p<0.0001$). This was also the case for *Hacd1*-kd myoblasts with six clusters providing a significantly better fit ($p<0.0001$). Further analysis reported clusters seen in control and *Hacd1*-kd myoblasts were significantly different ($p<0.0001$). If calcium-activated potassium channels were present within these recordings we would have expected them to reverse at approximately -93mV (Lee & Cui, 2010): a few channels in the *Hacd1*-kd myoblasts reversed at negative reversal potentials close to -93mV.

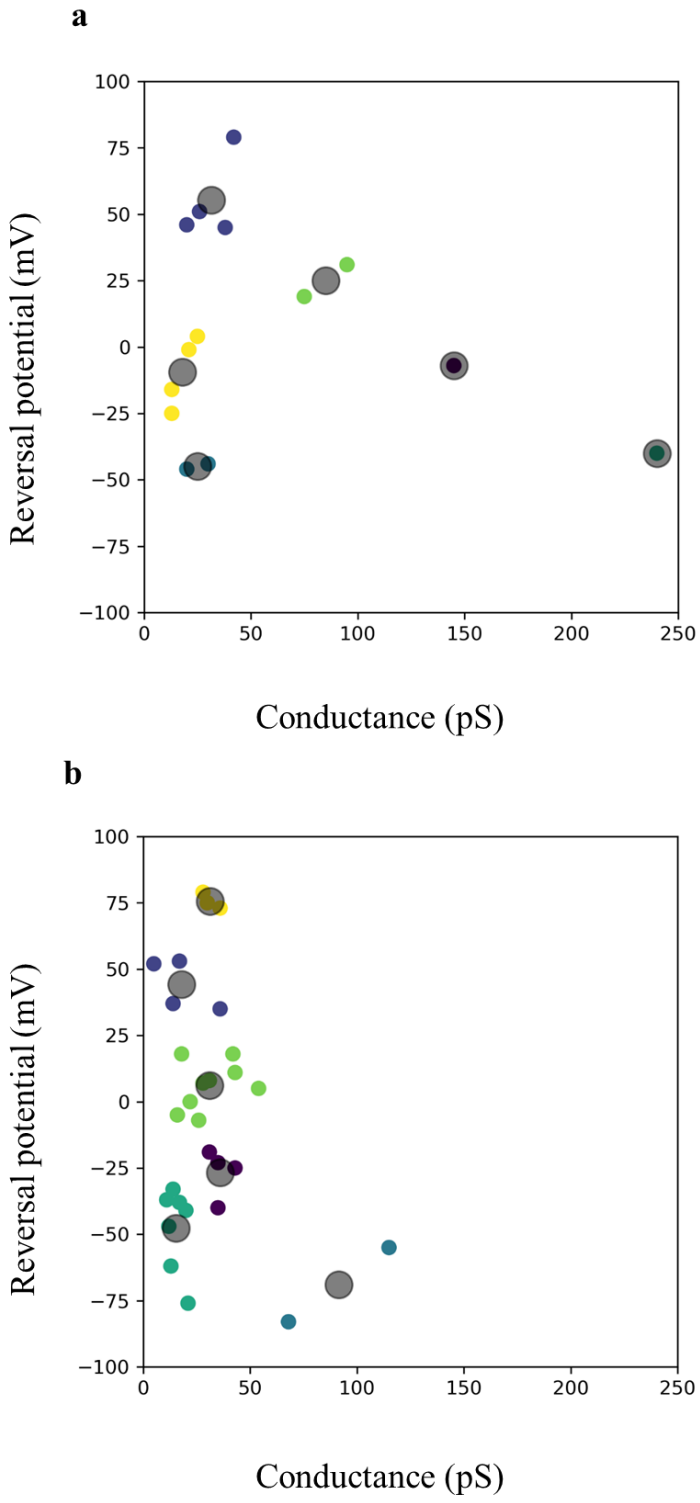

Figure 3.14: Clustering of ion channels seen during patch-clamp single channel analysis of control (a, n=14) and *Hacd1*-kd (b, n=29) myoblasts.

For both control and *Hacd1*-kd myoblasts, clustering channels into six clusters provided a significantly better fit than five clusters ($p<0.0001$ for both). Comparison of clusters between the two groups reported that the channels in control and *Hacd1*-kd myoblasts were significantly different ($p<0.001$).

3.3.6.3. Non-selective channels were predominantly seen in both control and *Hacd1*-kd myoblasts

The predominant channels for both control and *Hacd1*-kd myoblasts did not appear to be calcium-activated potassium channels and were analysed in more depth in order to characterise their properties. In control myoblasts, this unknown channel in Figure 3.15 was seen in 28% of channel recordings (4/14). Figure 3.15a shows raw data from a representative trace at three different holding voltages, dashed lines represent channel gating (O=open, C=closed) and this channel opened at a negative amplitude with clear openings. Figure 3.15b shows the all-points amplitude histogram from a holding voltage of -80mV displaying the channel as closed (0pA) and open (~1.4pA). Current-voltage (IV) analysis on the data were plotted (Figure 3.15c); this channel was found to have a slope conductance of 18pS ± 1.3pS and the current reversed at a reversal potential of -1mV ± 8mV. This channel was therefore most likely to be a non-selective channel.

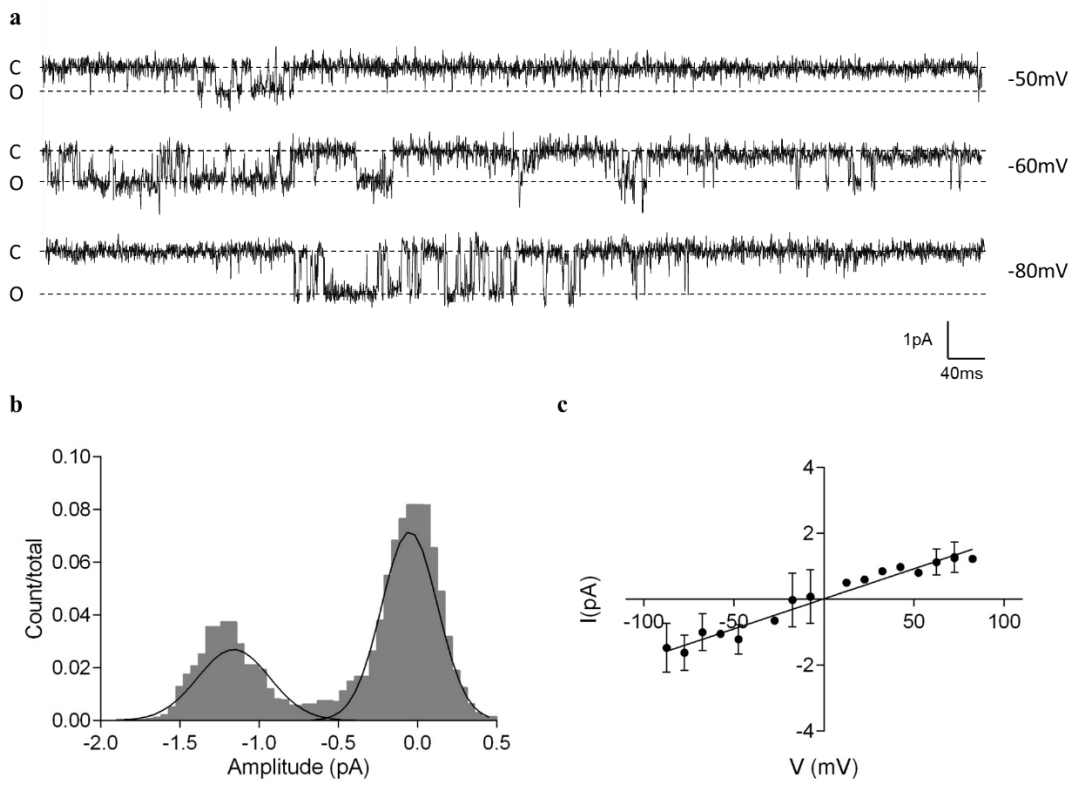

Figure 3.15: Patch-clamp recordings of control myoblasts revealed the predominant channel was a non-selective channel.

(a) Raw traces of cell-attached patch single channel activity at -50mV, -60mV and -80mV from a representative recording. (b) All-points amplitude histogram at -80mV from the same recording in (a). (c) Single channel current-voltage (IV) curve for the channel from all recordings of the channel reporting the channel to have a conductance of 18pS and a reversal potential of -1mV. IV curve plotted with the calculated cell membrane potential using the cells RMP (resting membrane potential) minus the holding potential (n=4).

The predominant channel seen in *Hacd1*-kd myoblasts was also one that could be a non-selective channel. This unknown channel, as shown in Figure 3.15, was seen in 28% of channel recordings (8/29). Figure 3.16 shows raw data from a representative trace at three different holding voltages, dashed lines represent channel gating (O=open, C=closed) and this channel opened clearly at a negative amplitude. Figure 3.16b shows the all-points amplitude histogram from a holding voltage of -60mV displaying two peaks, the closed peak at 0pA and then the open at around -1.5pA indicating this was the amplitude of the channel at -60mV. IV analysis on the data were plotted (Figure 3.16c) and the channel was found to have a slope conductance of 22pS ± 12.9pS and the current reversed at a reversal potential of 0mV ± 6mV. Figure 3.16c for this channel shows a plateau of currents with very positive and negative potentials, which indicates that has both inwardly and outwardly rectifying properties at positive and negative potentials respectively. Rectification in channels is often seen due to channel blockage via ions (Nishida & MacKinnon, 2002).

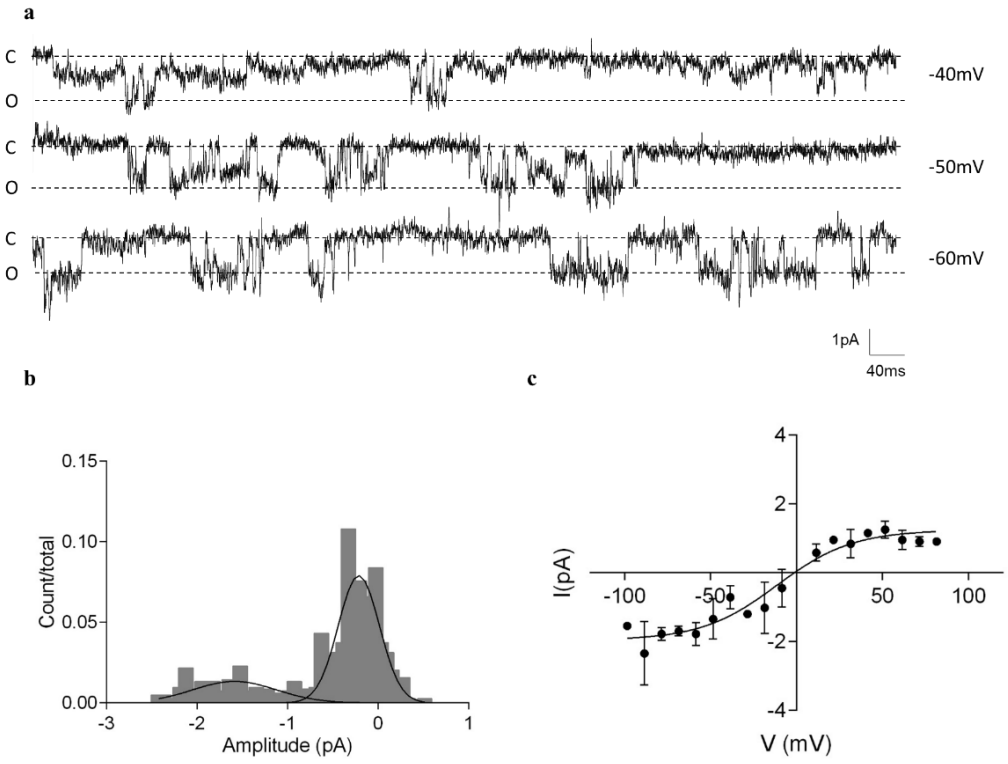

Figure 3.16: Patch-clamp recordings of *Hacd1*-kd myoblasts revealed the presence of a non-selective channel.

(a) Raw traces of cell-attached patch single channel activity at holding voltages of -40mV, -50mV and -60mV from a representative recording. (b) All-points amplitude histogram at -60mV from the same recording in (a). (c) Single channel current-voltage (IV) curve for the channel from all recordings of the channel reporting the channel to have a conductance of 22pS ±12.9pS and a reversal potential of 0mV ± 6mV. IV curve plotted with the calculated cell membrane potential using the cells RMP (resting membrane potential) minus the holding potential. This channel has been fitted with a Boltzmann sigmoidal line due to the nature of the data points (n=8).

3.3.6.4. Resting membrane potential of control and *Hacd1*-kd myotubes was not significantly different

Resting membrane potentials for the myotubes at 8dpd were more negative than those for the myoblasts (p<0.0001 for both control and *Hacd1*-kd cells). There was no significant difference in the RMP when *Hacd1*-kd was knocked down (p=0.13, n=10). The RMP for control cells (-33mV ± 3.9mV) and for *Hacd1*-kd cells (-41mV ± 4.7mV). An F test for variance did not find any significant difference between the two populations (F=1.45, p=0.58).

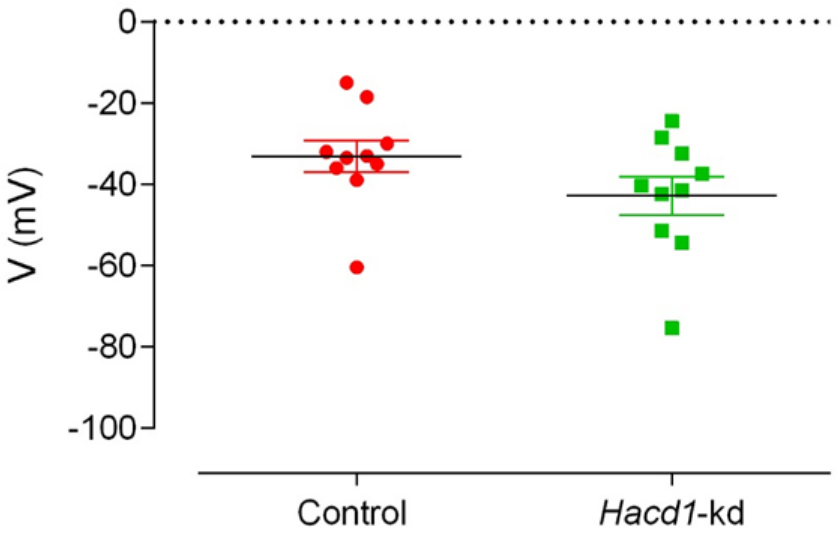

Figure 3.17: Resting membrane potential (RMP) of control and *Hacd1*-kd C2C12 myotubes at 8 days post differentiation (dpd).
There was no significant difference (p=0.13) between the RMP of control (-33 mV) and of *Hacd1*-kd (-41 mV) cells by unpaired t-test analysis, n=10. Variance in cell populations was not significantly different (F=1,45, p=0.58).

3.3.6.5. K-mean clustering found no differences in channels seen between control and *Hacd1*-kd myotubes

Patch-clamp recordings of control and *Hacd1*-kd myotubes were performed and analysed in an identical manner to the myoblasts. The myotubes were harder to work with and so recording numbers were fewer. For this reason, four clusters were used for myotubes to evaluate which channels might be similar. Four clusters was determined to be a significantly better fit for clustering data, when comparing to three clusters; this was determined by running the analysis on control cell channels (p<0.0001). This was also the case for *Hacd1*-kd myoblasts with four clusters providing significantly better grouping than three clusters (p<0.01). When analysing the difference in clustering between the control and *Hacd1*-kd myotubes this was not found to be significantly different (p=0.18). There were a few channels in each cell type that reversed at very negative reversal potentials which could have been calcium-activated potassium channels.

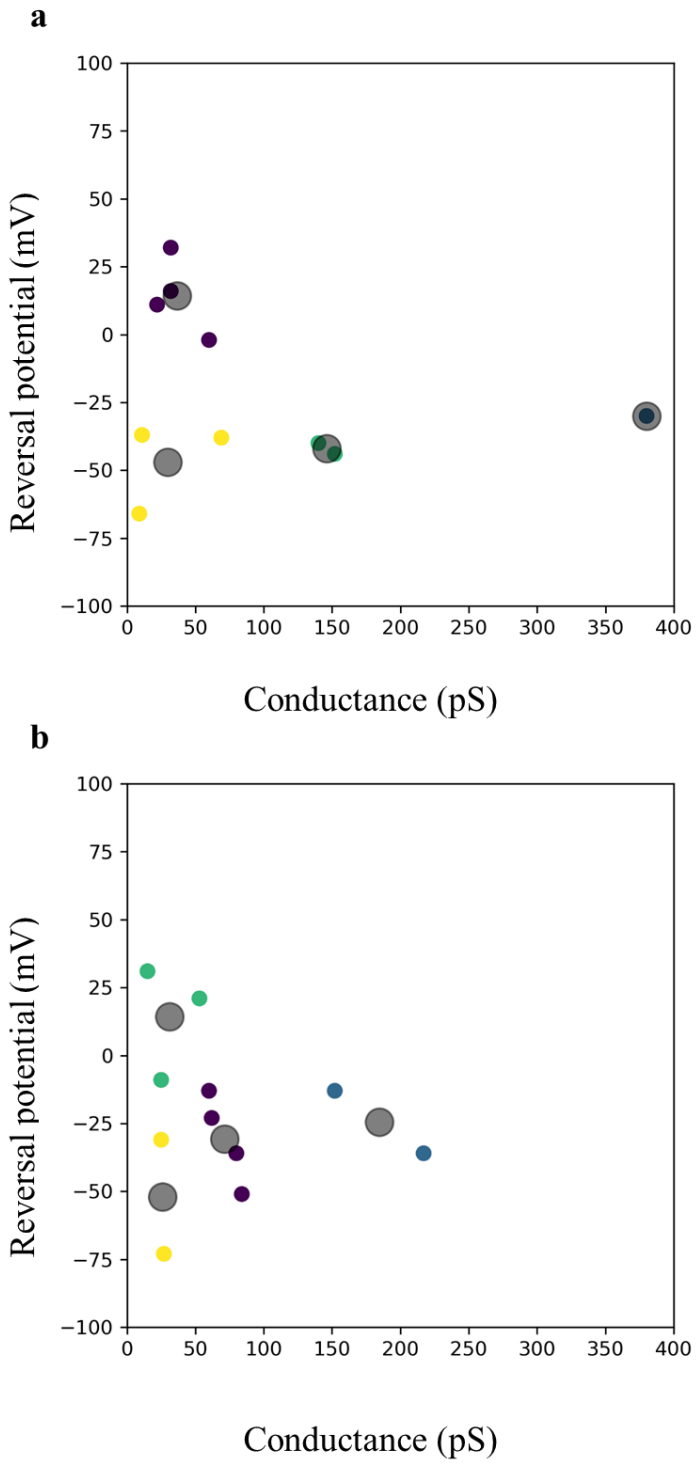

Figure 3.18: Clustering of ion channels seen during patch-clamp single channel analysis of control (a, n=10) and *Hacd1*-kd (b, n=11) myotubes at 8 days post differentiation (dpd).
It was found that for both control and *Hacd1*-kd myotubes that clustering channels into four clusters was a significantly better fit than three clusters ($p<0.0001$ and $p<0.01$ respectively). Comparison of clusters between the two groups reported that the channels in control and *Hacd1*-kd were not significantly different ($p=0.18$).

3.3.6.6. Predominant channel seen in myotube patch-clamp analysis were likely to be either non-selective or Cl^- channels

The predominant channel seen in both control and *Hacd1*-kd myotubes was then analysed in more depth in order to characterise its properties, as done for myoblasts also.

The unknown channel in Figure 3.19 was seen in 50% of channel recordings (5/10). Figure 3.19a shows raw data from a representative recording at three different holding voltages. The dashed lines represent the channel gating (O=open, C=closed) and this channel opened clearly at a positive amplitude at these holding voltages. Figure 3.19b shows the all-points amplitude histogram from a holding voltage of -60mV displaying the channel as closed (0pA) and open (~3pA). Current-voltage analysis on the data were plotted (Figure 3.19c) the channel was found to have a slope conductance of 65pS ± 10.3pS and the current reversed at a reversal potential of -44mV ± 14mV. From the Nernst equations in Table 3.6 this channel had a reversal potential between that expected for a non-specific channel (which always reverse at 0mV) and that of a pure Cl^- channel (-66mV) therefore it is possible that this channel was either non-selective or selective for Cl^- ions.

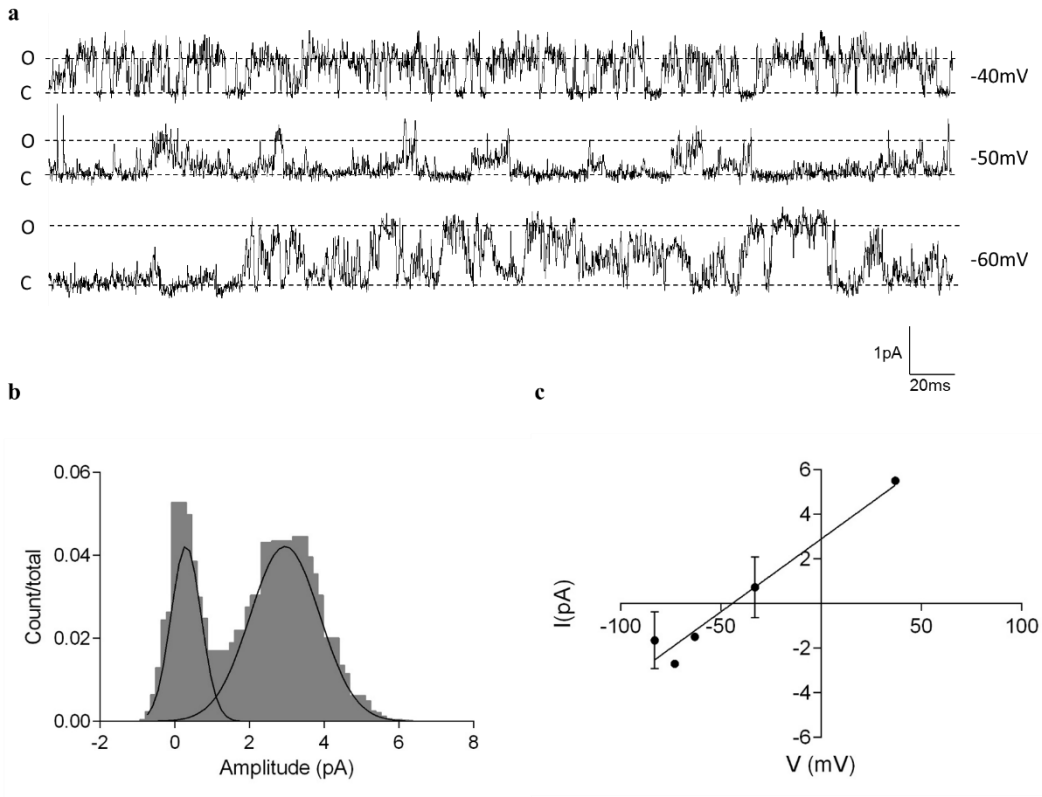

Figure 3.19: Patch-clamp recordings of the predominant channel observed in control myotubes at 8 days post differentiation (dpd).

(a) Raw traces of cell-attached patch single channel activity at holding voltages of -40mV, -50mV and -60mV from a representative recording. (b) All-points amplitude histogram at -60mV from the same recording in (a). (c) Single channel current-voltage (IV) curve for the channel from all recordings of the channel reporting the channel to have a conductance of 65pS ± 10.3pS and have a reversal potential of -44mV ± 14mV. IV curve plotted with the calculated cell membrane potential using the cells RMP (resting membrane potential) minus the holding potential (n=5).

One of the predominant channels seen in *Hacd1*-kd myotubes that was similar in properties to the one seen in control myotubes is presented in Figure 3.20. This unknown channel, was seen in 45% of channel recordings (5/11). Figure 3.20a shows raw data from a representative trace at three different holding voltages, dashed lines represent channel gating (O=open, C=closed) and this channel like that seen in control myotubes opened clearly at positive amplitudes at holding voltages shown. Figure 3.20b shows the all-points amplitude histogram from a holding voltage of 60mV displaying the channel as open (0pA) and open (~2.5pA). This histogram is less clear than previous due to few openings and less consistent channel gating. Current-voltage analysis on the data were plotted (Figure 3.20c) and the channel was found to have a slope conductance of 39pS ± 10.1pS and the current reversed at a reversal potential of -35mV ± 15mV. Similarly, to the channel seen in control myotubes this channels selectivity was more difficult to determine as the channel has a reversal potential that fell between Cl^- channels and non-selective channels.

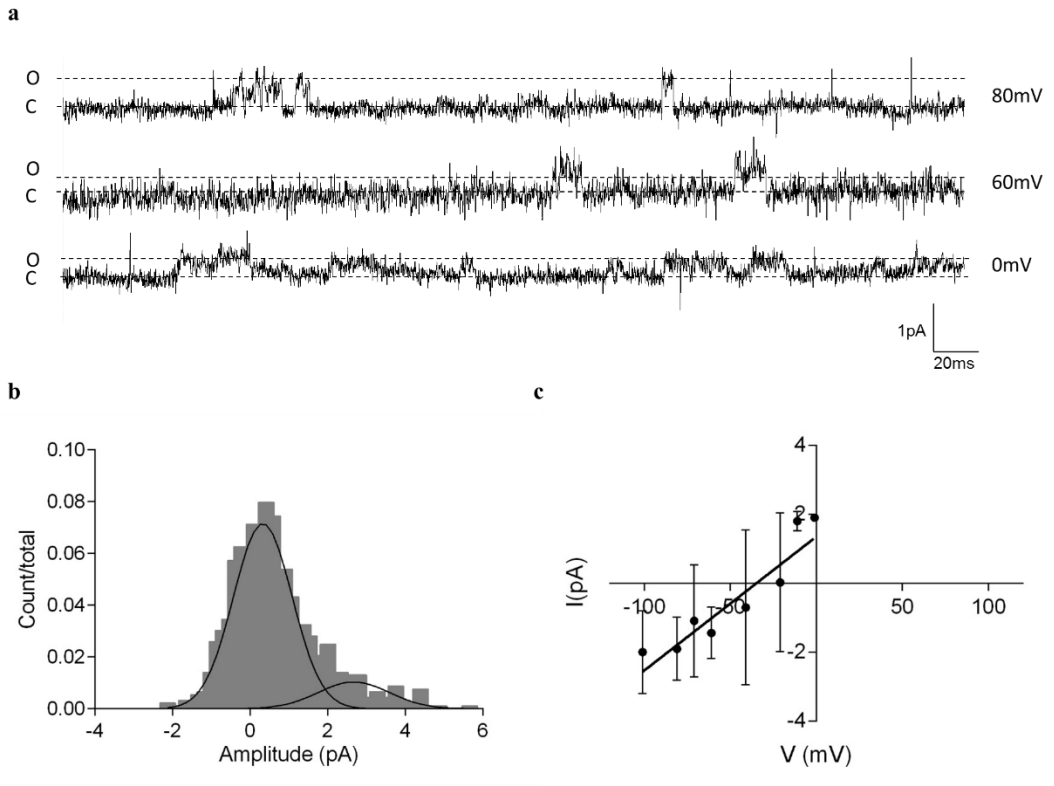

Figure 3.20: Patch-clamp recordings of *Hacd1*-kd myotubes at 8 days post differentiation (dpd) revealed the presence of a predominant channel with unknown selectivity.

(a) Raw traces of cell-attached patch single channel activity at holding potentials of 80mV, 60mV and 0mV from a representative recording. (b) All-points amplitude histogram at 60mV from the same recording in (a). (c) Single channel current-voltage (IV) curve for the channel from all recordings of the channel reporting the channel to be 39pS ± 10.1p and have a reversal potential of -35mV ± 15mV. IV curve plotted with the calculated cell membrane potential using the cells RMP (resting membrane potential) minus the holding potential (n=5).

3.4. Discussion

Expression of HACD1 mRNA is reduced to less than 1% in canine HACD1-CNM (Pelé *et al*., 2005) and this has been reported to lead to tubuloreticular membrane abnormalities (Walmsley *et al*., 2017). These membrane disruptions are also a common feature in other CNMs (Jungbluth *et al*., 2018; Nance *et al*., 2012). Very long chain fatty acids (VLCFAs) are thought to promote curvature within membranes (Schneiter *et al*., 2004) and although little is known about the role of VLCFAs and HACD1 that elongates them in muscle, it could be hypothesised that HACD1 deficiency causes a disruption in the function as well as the structure of muscle membranes, resulting from the lack of VLCFAs, which in turn affects ion channel gating and calcium homeostasis (Jungbluth & Gautel, 2014). We have shown this particular *Hacd1*-kd cell line to have significant knockdown of both total and full length *hacd1* transcripts (the latter of which encodes the catalytically active isoform), after cells begin to fuse at 4dpd. This chapter reports similar myogenic differentiation seen in both the control and *Hacd1*-kd cell lines. The electrophysiological properties between the *Hacd1*-kd and control cell lines were found to be significantly different in the myoblasts, though this could not be demonstrated in myotubes and no significant amount of calcium-activated potassium channel activity was recorded in any of the cells.

3.4.1. A knockdown of *Hacd1* does not associate with a compensatory increase in *Hacd2-4* expression in myotubes

Quantitative RT-PCR was used to evaluate expression of all four *Hacd* genes over C2C12 differentiation in both control and *Hacd1*-kd cells: these cells had been previously shown to have 80% knockdown of both total *Hacd* and *Hacd1-fl* at all time points (Walmsley, 2013). Stable transfection with the pGIPz plasmid was assumed based on survival in selective media and direct visualisation of tGFP expression. Therefore, the qRT-PCR was not performed as an initial assessment to confirm *Hacd1* knockdown, but undertaken at a later time to assess any compensation via upregulation of genes *Hacd2-4*.

The results from control cells here show both total *Hacd1* transcripts and *Hacd1-fl* are upregulated from 4dpd, which differs slightly from all previous studies of *Hacd1* expression in C2C12 which saw earlier upregulation (Blondelle *et al*., 2015; Lin *et al*., 2012; Walmsley, 2013). Specifically, Lin *et al.*, (2012) found *Hacd1-fl* expression upregulated after 1dpd and was upregulated by approximately 6-fold when expression peaked at 3dpd. Expression then decreased to a 3-fold upregulation by 7dpd (Lin *et al*., 2012). Blondelle *et al*., (2015) also reported an upregulation of *Hacd1-fl* in differentiating C2C12 cells that peaked at a 6-fold upregulation at 3dpd before decreasing again by 5dpd. Walmsley, (2013) similarly conducted

qRT-PCR assays and found *Hacd1* total and *Hacd1-fl* to increase significantly by 2dpd with upregulation sustained throughout myogenesis up until 14dpd.

In the *Hacd1*-kd cells used in this study, *Hacd1*-total significantly reduced in comparison with controls after 8dpd and *Hacd1-fl* was significantly knocked down from 4dpd onwards. Lin *et al*., (2012) reported the upregulation of *Hacd1* seen in control cells to be completely absent in their *Hacd1*-kd cells. Blondelle *et al*., (2015) also saw no increase in the *Hacd1* expression in *Hacd1*-kd cells and Walmsley, 2013 found an 80% knockdown at all time points studied in the *Hacd1*-kd cells.

The differences seen between Blondelle *et al*., (2015), Walmsley, (2013) and Lin *et al.*, (2012) and the results here in regards to knockdown may be due to the cell clones used although this would not explain the variation seen between this thesis and the results from Walmsley, (2013). Knockdowns using transfected plasmids are sensitive to efficiency loss: methylation of CMV promoters have been associated with this (Moritz *et al*., 2015). Differences in cell culture are likely to have affected the rate of differentiation and myotube fusion seen within the cells (Blondelle *et al*., 2015; Lin *et al*., 2012). Since this has been linked with *Hacd1* expression (Blondelle *et al*., 2015) this could also explain the differences seen in *Hacd1* expression across laboratory groups. Importantly, the knockdown was present after 8dpd in the more mature myotubes which this chapter aimed to study.

Quantitative RT-PCR assays of the other three *Hacd* genes demonstrated no significant difference between control and *Hacd1*-kd cells from 4dpd onwards, after the upregulation of *Hacd1*. Therefore, we could not detect a significant compensatory upregulation of these genes in the *Hacd1*-kd cells over the time points where they were deficient in *Hacd1* vs controls. This was particularly important for *Hacd2* which has high sequence homology to *Hacd1*, *Hacd2* elongates the same classes of lipids and it has been hypothesised that *Hacd2* could have been responsible for compensating in a *Hacd1*-knock out mouse model (Sawai *et al*., 2017). The results confirmed that this was not the case in these cells and we would suggest therefore that expression of other *Hacd* genes would not have contributed to any differences seen between cell types in later stages of differentiation. Surprisingly *Hacd3* and *Hacd4* expression were both higher in the *Hacd1*-kd myoblasts in early myogenesis in comparison with controls (cells from 0-2dpd and 0-1dpd respectively). This may be due to the dynamic process of cellular fusion which could be further investigated using membrane fluidity studies such as in Blondelle *et al*., (2015). Nevertheless, these differences are unlikely to affect any results seen when looking at later stages of differentiation as there was no significant upregulation at those time points. It is also possible that HACD3 and HACD4 have functional differences to HACD1 (Sawai *et al*., 2017), and so cannot elongate VLCFA in a compensatory

manner. Hence the early expression changes seen for *Hacd3* and *Hacd4* are less important for understanding HACD1-deficiency. Blondelle *et al*., (2015) evaluated *Hacd2* and *Hacd3* in their *Hacd1*-kd cell model (but not *Hacd4*) and found no upregulation. The work in this thesis confirmed these findings for *Hacd2* and *Hacd3*, obtained expression data for *Hacd4* and in addition evaluated all hacd enzymes over a much longer time course and at later stages of differentiation. Thus, it can be concluded that *Hacd2-4* are unlikely to be acting in a compensatory manner here.

3.4.2. *Hacd1*-kd cells differentiate comparably to control C2C12 cells

Cells in this chapter differentiated into mature, multinucleated myotubes independent of *Hacd1* expression, yet the *Hacd1*-kd myotubes did appear to have an increase in the aberrant cluster of nuclei in the *Hacd1*-kd myotubes, though this was not found to be significant. We would hypothesise that the current dataset lacked power and so if it was increased the number of abnormal nuclear clusters in *Hacd1*-kd cells might become significant. Previous literature on abnormal nuclear clustering was performed at 12dpd and found to be significantly increased with *Hacd1*-deficiency (Walmsley, 2013; Walmsley *et al*., 2017). This suggests that the abnormal nuclear clustering could be progressive within the cells, as is seen in the canine CNM phenotype (Blot *et al*., 2002; Tiret *et al*., 2003). 8dpd was chosen in this thesis due to the temperamental nature of cell differentiation once taken past this time point. We speculate these abnormal nuclei clusters develop with the cells due to a disruption in internal membrane systems that are known to occur in HACD1-CNM (Walmsley *et al*., 2017) and it is possible that these clusters represent the centralised nuclei seen *in vivo* (Blot *et al*., 2002; Roman & Gomes, 2018; Spiro *et al*., 1966).

Myogenic differentiation has been assessed in C2C12 cells and *Hacd1*-kd C2C12 cells in a number of papers. Blondelle *et al*., (2015) and Lin *et al*., (2012) reported that in their cell clone *Hacd1*-kd cells did not differentiate well, indicated by a significantly decreased fusion index. However, different sera (e.g. canine instead of equine serum) and different growth surfaces have been observed to rescue the fusion-defect in *Hacd1*-deficient myoblasts by this group (Tiret, personal communication). This may be the mechanism by which embryonic canine myofibres fuse: via VLCFAs provided to developing canine embryos by the placenta (Duttaroy, 2009).

Using the same cell clone as in this thesis, Walmsley, (2013) reported their *Hacd1*-kd cells to fuse and form myotubes: this was hypothesised due to a partial phenotype rescue by fatty acids in the differentiation media or the particular serum used, or the surfaces cells were cultured on however objective measures of differentiation were not evaluated. Differentiation of control and *Hacd1*-kd myotubes at 8dpd was quantified by scoring the fusion index,

differentiation index and myotube density – of which there was found to be no significant difference between control and *Hacd1*-cells. Thus these cells were capable of differentiation independent of *Hacd1* expression in these experiments. The cells appeared to have some areas of intense RYR1 staining with an area of high stain surrounded by an abnormal nuclear cluster, which indicated a potential inconsistency in sarcoplasmic reticulum development, and that this coincided with aberrant clustering of myonuclei. Quantification of RYR1 and DHPR within myotubes by western blotting would be the logical next step to confirm any altered protein expression. There were a number of stained areas within Figure 3.12 that did not appear to be within cells – possibly on a higher focal plane than the cells themselves. The cells were temperamental and often hard to differentiate to later time points and so we speculate that these areas are most likely cell debris which is increased in kd cultures, for example from cells that have apoptosed and peeled away from the surface. Confocal microscopy would provide higher resolution images to confirm this.

3.4.3. Characterising electrophysiological properties affected by *Hacd1* knockdown in undifferentiated myoblasts

Hacd1-kd cells were found to differentiate comparably to the control cells and *Hacd1* deficiency was confirmed in the differentiated myotubes in *Hacd1*-kd cultures compared with controls. Myoblasts and myotubes of 8dpd were used to evaluate the electrophysiological properties of the cells with the focus on single ion channel analysis. This part of the study aimed to work towards characterising a basic phenotype of ion channels present in the cells since there is strong evidence to suggest that the predicted changes in free calcium handling would result in changed activity in calcium activated potassium channels. We therefore characterised a number of electrophysiological parameters from C2C12 with and without *Hacd1* expression.

Accurate determination of the RMP was essential before undertaking single channel recording because the RMP was used in the calculation of channel reversal potentials (Equation 3). Furthermore, increase in intracellular calcium would be expected to lead to depolarisation of cells, via activation of constituently expressed BK channels (Vergara *et al*., 1998), and also an altered RMP would be expected to, in turn, alter the calcium handling. The cells RMPs were recorded and were found to be significantly more polarised in 8dpd myotubes for both control and *Hacd1*-kd cells, which was expected as by 8dpd C2C12 have differentiated into excitable cells (Cárdenas *et al*., 2004). Membrane potential is an important control mechanism for cellular differentiation and maturation (Abdul Kadir *et al*., 2018). RMP was not significantly different when *Hacd1* was knocked down in either myoblasts (although it was significantly more variable within *Hacd1*-kd myoblasts) or myotubes. As *Hacd1* expression

levels are comparable in myoblasts (and *Hacd1-fl* levels are very low prior to differentiation) in both cell types it could be conjectured that there may not yet be any significant changes within the cell populations. However, the RMP was also found to be similar within control and *Hacd1*-kd myotubes suggesting that *Hacd1*-deficiency does not lead to insufficiently negative RMP within CNM muscle fibres. This is an important finding as ECC relies upon a negative basal RMP within the myofibres prior to the depolarisation of the membranes, which in turn triggers ECC through the opening of the DHPR and activates the SR calcium release (Robin & Allard, 2012). Therefore, we conclude that an increasingly positive RMP does not contribute to altered calcium homeostasis in *Hacd1*-kd C2C12 cells.

Previous electrophysiological studies on the C2C12 myoblasts and myotubes, have reported similar RMPs to that seen in the control cells in this study. Yet these studies only looked at myoblasts or myotubes and not both. Tanaka *et al*., (2017) found myoblasts to have an average RMP of -15mV and Asano *et al*., (2015) found C2C12 myotubes to have a RMP of -32mV which was only 1mV different from our average RMP recordings for control myotubes. These values for RMP correspond well with control cells from this study.

The ideal way to monitor ion channels in large cells such as muscle or myoblasts is cell-attached patch. This technique does not require the experimenter to control the membrane potential of the entire cell and also keeps the target cell intact (it does not alter intracellular calcium for example). During single channel recordings it was noticeably easier to seal *Hacd1*-kd myoblasts than the controls and therefore a larger dataset was collected for *Hacd1*-kd myoblasts. A review by Suchyna *et al*., (2009) discusses five forces involved in biological patch-clamp seals: membrane tension, stresses from cytoskeleton, electroosmotic forces, membrane viscosity and adhesion energy of the membrane. Differences in any of these membrane properties could factor into *Hacd1*-kd cells forming seals easier: such as membrane fluidity, or viscosity, which has been reported to be reduced in *Hacd1*-kd cells at 3dpd (Blondelle *et al*., 2015) and this could provide a reason as to why the *Hacd1*-kd cells were easier to seal. Analysis through k-means clustering found there to be significantly different channels recorded between control and *Hacd1*-kd cells. This was unexpected as we hypothesised there to be no quantifiable differences between the cells; as *Hacd1* expression levels are the same at this stage in differentiation and *Hacd1-fl* was not highly expressed at this stage in either control or *Hacd1*-kd cells. *Hacd3* and *Hacd4* were seen to have a significantly increased expression in early time points however so there may well be other early differences in the cells, independent of HACD1, leading to this difference in ion channel profile seen between control and *Hacd1*-kd myoblasts. One visible difference in the clusters of channels which may have contributed to the significant difference in clustering was the

presence of larger channels with conductances of 140pS and 240pS in the control myoblasts. Future patch-clamp of these cells could provide enough data to conclude that there is a higher frequency of larger channels in these cells but the limited data set means this conclusion cannot be made at this time.

The predominant channels seen in both control and *Hacd1*-kd myoblasts were apparently not the anticipated calcium activated potassium channels, widely expressed in muscle, but non-selective cation channels according to the IV (current-voltage) curves. Coupled with their single channel conductance and their high abundance this makes TRP channels (transient receptor potential) the primary candidates. TRP channels are non-selective channels made up of six transmembrane segments and are a highly diverse category of ion channel with varying levels of permeability towards different ions: often with permeability for calcium (Brinkmeier *et al*., 2011). The TRP channels can be segregated into seven subfamilies: TRPC, TRPV, TRPM, TRPN, TRPA, TRPP and TRPML (Venkatachalam *et al*., 2014). TRP channels have been studied in skeletal muscle, and gene expression data from rodent muscle has shown TRPC channels to be present, with TRPC1, C4 and C6 protein expression confirmed on the sarcolemma (Kruger *et al*., 2008; Sabourin *et al*., 2009) and TRPC3 has been reported to have a functional interaction with RYR1 (Lee *et al*., 2006). TRPC1 expression has been reported at all time points during muscle cell culture and differentiation whereas TRPC3 was found to upregulate with differentiation (Formigli *et al*., 2009; Louis *et al*., 2008). A study by Zanou *et al.,* (2010) concluded that TRPC1 channels regulate the entry of Ca^{2+} during repeat contractions and is important for muscles to maintain their force throughout these contractions. They reported their TRPC1 channels from murine fibres to have a conductance of 13pS (Zanou *et al*., 2010). Whilst blockers of TRP channels do exist and could theoretically be used to provide confirmation of phenotype, few of these inhibitors are very selective and so further work in this area may require si-RNA knock-down experiments.

The channels seen in the myoblasts in this study, and hypothesised to be TRP channels, had conductance's of 18 and 22pS (control and *Hacd1*-kd myoblasts respectively) which are only a little bigger than the previously reported conductance of the TRPC1 channel (13pS) (Zanou *et al*., 2010). As TRPC1 has been reported to be localised to the sarcolemma and reported of similar size we hypothesise that the TRCP1 is a likely candidate for the channel reported in this study. Conversely; a study by Berbey *et al.,* (2009) found opposing results for TRPC1 and stated that it is actually localised to the SR where it acts as an SR Ca^{2+} leak channel as opposed to aiding influx of Ca^{2+} into the cell via the plasma membrane. This study would require pharmacological interventions in order to fully establish the channel seen in the myoblasts.

As well as TRPC1-like channel, the predominant channel seen in the *Hacd1*-kd cells appeared to have unusual rectifying properties, this can be distinguished by the sigmoidal fit of the line and so this channel may be different to the one in the control cells. TRPC5 has been reported to have rectifying properties (Obukhov & Nowycky, 2004); but there is little data on TRPC5 within skeletal muscle suggesting it may not have significant expression there. TRPC3 has inward and outward rectification (Alexander *et al*., 2011) and although it has not been reported to be expressed on the sarcolemma, TRPC3 could be the channel seen in the *Hacd1*-kd myoblasts and due to its functional coupling with RYR1 would be an interesting channel to study further in this cell line (Lee *et al*., 2006). Of the TRPV family, an ion channel array on C2C12 myoblasts found TRPV2 and TRPV4 to be present in the cells (Morgan *et al*., 2018). TRPV4 channels tend to be larger than the channels seen in these recordings so it was unlikely to be a TRPV4 channel – TRPV2 is a possible candidate for this channel (Alexander *et al*., 2011). TRPV2 has roles in accelerating membrane depolarisation and therefore triggering ECC, this would therefore be an interesting channel to investigate further (Zanou *et al*., 2015).

3.4.4. Characterising electrophysiological properties affected by *Hacd1* knockdown in differentiated myotubes

As myotubes were more difficult to get sufficient seals and clear traces from, the number of channels recorded in both control and *Hacd1*-kd was fewer than in myoblasts, and for this reason only four clusters were used to cluster data. As with myoblasts one of the visible differences between channels in control and *Hacd1*-kd myotubes was the presence of large channels. In control myotubes there was one large channel of just below 400pS, however it was only one channel and the number of channels detected in the myotubes was low. This lack of channel data could be the reason there was no significant difference seen between control and *Hacd1*-kd channel phenotype clustering. Predominant channels seen in both the control and *Hacd1*-kd myotubes were harder to identify than those seen in myoblasts. The reversal potentials for the channels seen in myotubes was -44mV ± 14mV for the control and -35mV ± 15mV for the *Hacd1*-kd myotubes. These fall quite close to that of Cl^- ions (-66mV). It is worth bearing in mind though that there was an error of 14/15mV therefore the reversal potential could be higher or lower than calculated.

Chloride channels are involved in regulating the excitability of myofibres, and a major chloride channel of muscle is the voltage-gated C1C-1 channel (Alexander *et al*., 2001; Fahlke, 2011). C1C-1 channels are found along the t-tubule membrane systems and mutations cause myotonia, highlighting their importance for skeletal muscle function (DiFranco *et al*., 2011; Koch *et al*., 1992). The channel seen in the cells was unlikely to be a Cl^- channel as these are not often seen in patch-clamp experiments due to their small conductance (often

around 2pS) which means they are often hidden by other larger conductance channels (Alexander *et al*., 2011). Chloride channels are also thought to only activate at high or low voltages (±~100mV) (Syeda *et al*., 2016). Therefore, it is unlikely that the channels seen were chloride, and further pharmacological/molecular intervention experiments should be conducted to help with identification.

The other candidate for these unknown channels could also be a TRP channel like those seen in the myoblasts. Kruger *et al*., (2008) reported the most abundant TRP channels in murine skeletal muscle to be: TRPC3, TRPC6, TRPV4, TRPM4 and TRPM7. Some of these channels are of similar conductance to the channels seen in the myoblasts in this study (65pS in control and 39pS in the *Hacd1*-kd myotubes).TRPM7 has been reported to have a conductance that varies from 40-105pS, TRPC6 has a conductance of around 28-37pS and TRPC3 is approximately 66pS in conductance (Alexander *et al*., 2011). Further patch-clamping and the use of channel blockers would be the next step in this research to define the channels seen.

Further work in this cell culture model would involve not only an increased n number of single channel recordings in myotubes but measuring calcium responses by using HEPES buffer containing high KCl concentration perfusion to depolarise control myotubes and assessing changes in gating or channels present – particularly for the calcium-activated potassium channels we speculate would be activated during this protocol. Channel inhibitors would be advantageous to truly determine which channels were seen to be present in the cells. This was not done during this study as the focus was the global ion channel phenotype initially. Ion channel qRT-PCR would also allow us to determine changes in channel expression associated with *Hacd1* knockdown and this would help with identification of channels seen in recordings. The rectifying channel seen in *Hacd1*-kd myoblasts is an uncommon channel phenotype to detect and this therefore would be interesting to explore further using the suggested methods.

3.4.5. Conclusions

From the work done in this chapter it can be concluded that *Hacd1* is upregulated during myogenic differentiation in C2C12; this upregulation was abolished in the *Hacd1*-kd cells where *Hacd1* expression remained consistently low and was not associated with a compensatory upregulation of *Hacd2-4* expression. Differentiation was comparable in both control and *Hacd1*-kd myotubes suggesting that in these cells the HACD1-deficiency did not affect differentiation. *Hacd1* may still be implicated in cell fusion as previously described (Blondelle *et al*., 2015), we have excluded compensation from *Hacd2-3*, therefore the cells in this study may have partial rescue due to lipids and fatty acids from the serum. Differences were apparent between our findings and those of previous studies in these cells and their phenotype appears to vary dependent upon culture conditions – perhaps most likely relating

to presence of lipids particularly VLCFA in differentiation media. Electrophysiological profiles, including the variance of myoblast RMP, were shown to be significantly different between control and *Hacd1*-kd myoblasts however this is unlikely to be related to HACD1 as the time point is prior to *Hacd1* upregulation and *Hacd1-fl* and total *Hacd1* expression were similar between control and kd myoblasts. There was no difference demonstrated in the myotubes, however a more extensive study with a larger data set might have been able to detect more differences. There was little evidence for differential activity of calcium-activated potassium channel activity during these experiments, therefore continuing on from this work to depolarise cell membranes would be an appropriate next step. The predominant ion channels recorded in both myoblasts and myotubes could instead be TRP channels however this is inconclusive since no pharmacological/siRNA interventions were used to confirm it. As TRP channels are involved in calcium movement these channels may provide a novel angle for studying altered calcium homeostasis, as seen in CNM, research (Alexander *et al*., 2011; Brinkmeier *et al*., 2011; Jungbluth & Gautel, 2014). Overall this study has provided ground work to continue study calcium responses and ECC within this cell model. These cells are far less complex in their internal structures than myofibres however and so more complex models should be examined also in future work.

4 Lipidomic effects of *Hacd1* deficiency in a myogenic cell line

4.1. Introduction

The HACD enzymes (HACD1-4) catalyse the dehydration stage in the four-step cyclical process of VLCFA elongation (>20 carbons). The other elongase complex enzymes are: fatty acid elongase1-7 (ELOVL1-7), 3-ketoacyl-CoA reductase (KAR) and trans-2-enoyl-CoA reductase. The dehydration step catalysed by the HACD enzymes is rate-limiting, as seen by the accumulation of 3-hydroxyacyl-CoAs seen in *in vitro* FA elongation assays (Ikeda *et al*., 2008; Sassa & Kihara, 2014).

The active full-length isoform of HACD1 is specifically expressed in striated muscles where fatty acids with longer chain lengths are stored within more complex lipids such as sphingolipids and glycerophospholipids (Kihara, 2014; Morales *et al*., 2017; Watt & Hoy, 2011). VLCFA-containing molecules are of importance within biological membranes and used as 'structural' lipids (Baur *et al*., 1998); in particular, the phospholipids with VLCFA constituents provide strength and curvature to membranes (Guillou *et al*., 2010; Molino *et al*., 2014; Schneiter *et al*., 2004). Glycerophospholipids (GPL), glycerol based phospholipids, are the most abundant phospholipid found in cell membranes and the most important mammalian GPL's include phosphatidylcholine (PC) phospholipids incorporating a choline head group (Blanco 2017). GPL's vary in chain length and very long chain GPL's have been reported at lengths of 20-24 and PC has been reported at lengths of up to 36 carbons (Maier *et al*., 2016; Sigruener *et al*., 2014). In the L6 muscle line GPLs in total membranes represented more than 50% of total lipids with PC contributing highly (Briolay *et al*., 2013).

Lipid membranes are dynamic and within muscle cells are redistributed and recruited during myoblast fusion and myotube formation. Membrane composition changes during early differentiation to allow fusion to occur in sections of cholesterol free membrane (Mukai *et al*., 2009). Cholesterol composition is associated with membrane fluidity and decreases in relation to GPL's over myogenic differentiation (Briolay *et al*., 2013; Mukai *et al*., 2009). Relative saturation of fatty acids also decreases during differentiation and influences membrane fluidity, PUFA (polyunsaturated fatty acid) supplementation has been reported to increase myogenic differentiation in L6 cells (Briolay *et al*., 2013).

Membrane abnormalities within skeletal muscle of HACD1-CNM affected dogs are progressive, including both sarcolemmal and t-tubule system membrane disorganisation and mislocalisation of the triads. The roles of VLCFA in developing and mature muscle are poorly understood. Although the pathological changes in CNM-affected dogs, high lipid content within cellular membranes and the role of HACD1 in lipid biosynthesis would suggest a function in tubuloreticular membrane development and maintenance (Al-Qusairi & Laporte, 2011; Blanco, 2017). Blondelle *et al.,* (2015) researched the effects of *Hacd1* deficiency in C2C12 cells using a knockdown which resulted in abnormal early myogenesis – the cells were unable to fuse. A decrease in lysophosphatidylcholine (LPC) was observed in differentiating controls at 3 days post differentiation (dpd) (Blondelle *et al*., 2015). Previous work by Leikina *et al*., (2013) showed LPC levels reduced to allow cell membrane fusion and inhibited myoblast fusion when added to cell culture media. (Leikina *et al*., 2013). The decrease in LPC did not occur in *Hacd1*-kd cells but was restored, rescuing the phenotype and allowing myoblast fusion to proceed by re-expression of *Hacd1-fl*. This suggests the drop in LPC during differentiation was dependent upon HACD1 activity. At 3 days of differentiation, *Hacd1*-kd cells had higher SFA (saturated fatty acid) and lower MUFA (monounsaturated fatty acid) content than control cells at this stage of differentiation and these differences were also rescued with *Hacd1-fl* expression. Higher levels of unsaturated phospholipids are associated with an increase in fluidity of lipid bilayers and it is believed that PUFAs provide a less packed membrane (Briolay *et al*., 2013; Maxfield & Tabas, 2005). Blondelle *et al*., (2015) reported a 9% decrease in membrane fluidity in *Hacd1*-kd myotubes which corresponded to previous literature as the *Hacd1*-kd cells had reduced MUFA content (Blondelle *et al*., 2015). Blondelle *et al*., (2015) also reported that proportions of VLCFA increased within control cells between myoblasts and myotubes (3dpd) and that *Hacd1*-kd did not show this increase and in fact had significantly lower levels of VLCFA in both myoblasts and myotubes. This work by Blondelle *et al.,* (2015) has provided us with knowledge of lipid changes within early differentiating C2C12 cells as evaluated by GC- and LC-MS and the effects of *Hacd1*-kd on early myogenesis and myotube fusion. Their work also correlates with that seen in yeast when knocking down levels of the HACD1 homologue, Phs1. When Phs1 levels were decreased, an accumulation of long chain bases was reported alongside an accumulation of ceramide and decrease in more complex sphingolipids (Kihara *et al*., 2008).

Walmsley, (2013) used similar cells to those used by Blondelle *et al*., (2015) (cells contained the same plasmid and shRNA sequence but were a different clonal population in which cells retained the ability to fuse and differentiate) and found 80% knock down of *Hacd1* expression levels throughout differentiation. These cells were used to obtain more detailed information

on HACD enzyme expression during development and intracellular membrane structure and function. We have concluded from the previous experiments, as described in Chapter 3 that both the control and *Hacd1*-kd cell differentiate in to mature myotubes. In addition, that when *Hacd1* is knocked down in later stages of differentiation, there is no upregulation of the other *Hacd* genes to compensate for this loss. Differences in ion channel presence between the control and *Hacd1*-kd cells were identified, suggesting sarcolemmal membrane differences. In this chapter these cells were used to evaluate changes of the C2C12 lipidome by proton nuclear magnetic resonance (^{1}H-NMR) lipidomics in control cells and *Hacd1*-kd cells for comparison.

^{1}H-NMR provides detailed information on molecular structure through analysis of spectra produced via the principal of nuclear spin. Different lipids provide the spectra with unique peaks produced by the environment of specific hydrogen atoms within the molecule allowing the detection of certain lipids. These can also be quantified due to properties of NMR as signal intensity is directly proportional to the number of hydrogens present in that environment. (Li *et al*., 2017). NMR is a cost effective, robust method to analyse lipids and was therefore chosen for this study as an initial step in characterising the cells lipidomes (Emwas *et al*., 2015).

4.1.1. Chapter aims & hypotheses

Due to the role of HACD1 in the elongation of VLCFA, we hypothesised there would be a significant difference in the lipidome of C2C12 cells once *Hacd1* was knocked down. The work of this chapter sought to:

1) Evaluate the lipidome of differentiating C2C12 myoblasts and myotubes up to 12 days post differentiation to evaluate early and late changes during differentiation;
2) Evaluate the lipidome of differentiating *Hacd1*-kd C2C12 cells to identify and quantify functional changes following a reduction in *Hacd1* transcript levels.

4.2. Methods

4.2.1. Cell culture and collection

Control and *Hacd1*-kd C2C12 myoblasts (0 dpd) and myotubes (1, 2, 4, 6, 8, 10- and 12- dpd) were grown and differentiated in T25 flasks (Corning) as described previously (Section 3.2.1) and harvested using a cell-scraper and ice-cold Dulbecco's phosphate buffered saline (DPBS) (Sigma Aldrich). Efficient scraping was verified visually before centrifuging at 13,000g for one minute. Pellets were then snap frozen before storing at -80°C.

4.2.2. Lipid Extraction

Ice cold solvents were required for this work, and to the frozen cell pellets 500µl chloroform ($CHCl_3$) (Sigma Aldrich) was added. Samples were then sonicated in two x 30 second intervals including a 30 second pause in between. Samples were vortexed briefly before incubating at 4°C for 10 minutes. Then samples were centrifuged for 10 minutes at 21,500g and 4°C. The supernatant was snap frozen in liquid nitrogen and lyophilised to remove any solvent and solidify samples.

4.2.3. Lipid Extract Preparation

As proton NMR (^{1}H-NMR) detects H^+ ions, 200µl of deuterated chloroform ($CDCl_3$, Sigma Aldrich) was added to lyophilised material before vortexing briefly and centrifugation at full speed for one minute. Supernatant was transferred to a new tube and spun again if high levels of debris were present. Clean diluted samples were then transferred to 3mm (outer diameter) NMR tubes.

4.2.4. NMR spectrophotometer runs

All samples were run on a Bruker Avance III HD spectrometer with a TCI cryoprobe and chilled SampleJet autosampler with a field strength of 700.17MHz. Software for acquisition and processing was carried out using Topspin 3.1. Spectra were acquired and pre-processed according to standard metabolomics practices (Beckonert *et al*., 2007) by an NMR spectroscopist at the Shared Research Facility for NMR metabolomics. Briefly 1D ^{1}H-NMR NOESY standard vendor pulse sequence (all parameters constant between samples) was used to acquire with a 25ppm spectral width and 32 scans (four minute experiment) at 15°C to offset the volatility of the chloroform. Pre-processing of spectra proceeded using automated standard vendor routines (Fourier transform, phasing and window function) and spectra was aligned using the residual $CHCl_3$ peak at 7.26ppm due to the impurity of $CDCl_3$ (99.8%).

4.2.5. Peak QC and analysis

Stringent quality control was performed on all samples. Any samples failing these limits were re-run up to three times, at which point the sample was discarded from analysis. Phasing of lines was checked by eye to ensure a straight baseline and manually corrected where required. The $CHCl_3$ reference peak was checked to ensure it was a clear single peak, consistent between samples and that the half height peak width was < 1.1MHz.

4.2.6. Pattern file assembly

Using a collection of spectra from a variety of samples, all peak positions were noted down in a file with their spectral position (parts per million, ppm). Where possible peaks were identified and annotated, unfortunately lipid extracts had many unknown peaks due to the novel nature of the technology. The pattern file was checked using the Tame NMR Galaxy software which overlaid the pattern file with provided spectra to check all peaks within the spectra were accounted for and pattern file was amended accordingly (See Figure 4.1). This file was then used to 'bucket' or 'bin' the data into numerous blocks for analysis.

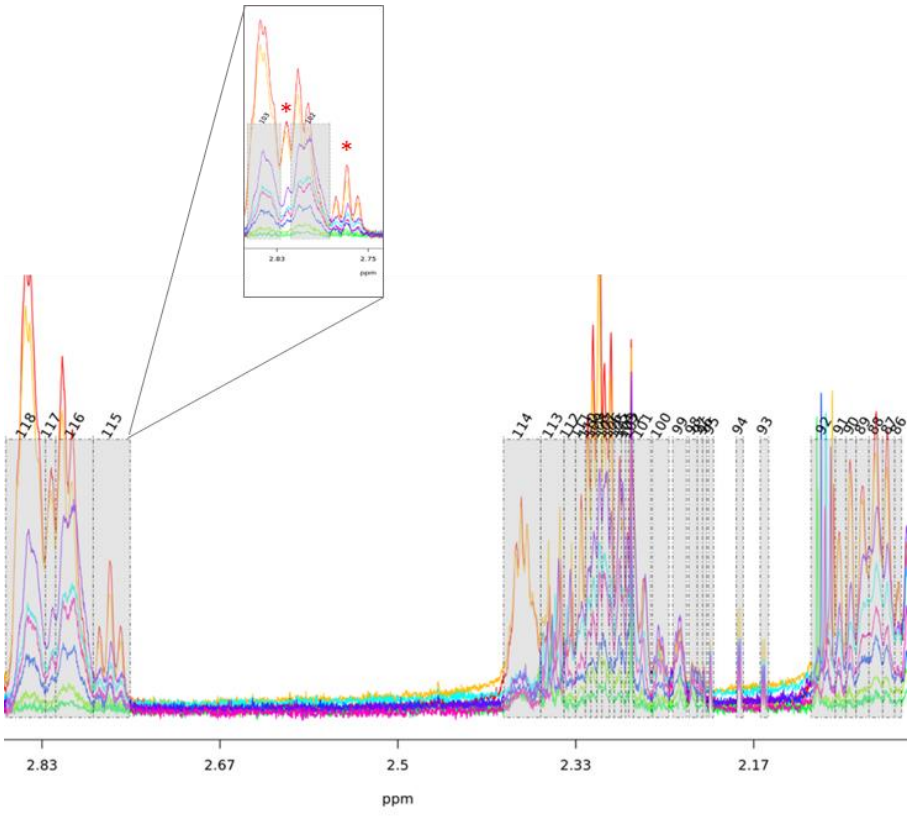

Figure 4.1: Tame NMR outputs.
Figure shows a selection of spectra run against the final pattern file created (grey boxes), with no peaks unaccounted for. Inset displays a previous Tame NMR run with an incomplete pattern file, which when run in Tame NMR highlighted missing sections (annotated with asterisks).

4.2.7. Spectra annotation

To quantify specific hydrogens or head groups of lipids the pattern file and spectra were annotated where possible. Figure 4.2 shows the peaks used to quantify proportions of saturated fatty acids (SFA) represented by a single carbon bond (HC-CH), poly unsaturated fatty acids (PUFAs) represented by the hydrogens between two double bonds (-CH=CH-CH2-CH=CH-) and also for unsaturated fatty acids (MUFA/PUFA) represented by hydrogens either side of one double bond (HC=CH). These peaks at ~1.3ppm, ~2.8ppm and ~5.4ppm were assigned respectively. Figure 4.3 shows lipid head groups annotated on to the same sample spectra. Head groups from lipids can be identified by numerous peaks but for quantification only one peak was used. The PC peak used for annotation was the characteristic peak for the PC lipid class found at ~3.3ppm, representing the hydrogens from the three methyl groups in the choline head. The peak used to quantify GPL was found at ~4.1-4.2ppm and was produced from the glycerol backbone of the GPLs.

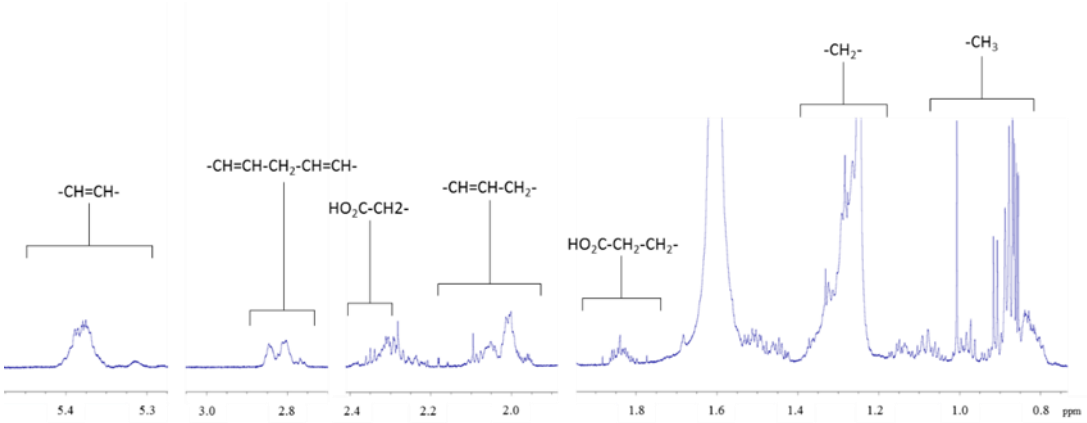

Figure 4.2: C2C12 sample spectra with positional hydrogens annotated.
Annotations includes hydrogens on either side of a carbon double bond (~5.4ppm), hydrogens between two double bonds (~2.8ppm) and hydrogens on either side of a carbon single bond (~1.3ppm).

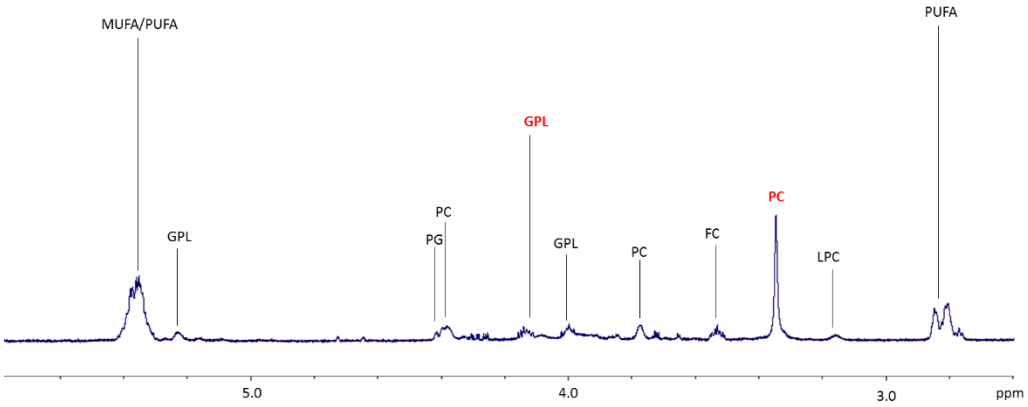

Figure 4.3: C2C12 samples with lipid head groups annotated.
Annotations include: monounsaturated/polyunsaturated fatty acids (MUFA/PUFA), glycerophospholipids (GPL) phosphatidylcholines (PC), free cholesterol (FC) and lysophosphatidylcholine (LPC). For lipid classes with more than one peak, the respective peak used for quantification is shown in bold red font.

4.2.8. Outlier analysis

The sensitivity of ^{1}H-NMR detects confounding variables within samples, including those down to human error, sample degradation, or experimental conditions (Xia *et al*., 2011). Samples with great variability causing them to lie outside the 95% confidence interval in a PCA scores plot, were initially identified as outliers and put through preliminary statistical testing. Peak intensities for each biological population were averaged and those that were identified by the PCA plots as being outside the confidence intervals, such as 'ct_d00_r12' and 'kd_d00_r14' in Figure 4.4 were tested. If over 30% of a sample's peaks lay outside one standard deviation of the peak mean average then the sample was removed as an outlier.

The initial sample size for each population was 15, but after peak quality control and outlier analysis and removal numbers were as follows: control 0 dpd n = 11, 1 dpd n = 12, 2 dpd = 13, 4 dpd = 9, 6 dpd = 11, 8 dpd = 11, 10 dpd = 12, 12 dpd = 14. Knockdown 0 dpd = 10, 1 dpd = 14, 2 dpd = 14, 4 dpd = 11, 6 dpd = 13, 8 dpd = 13, 10 dpd = 12 and 12 dpd = 14.

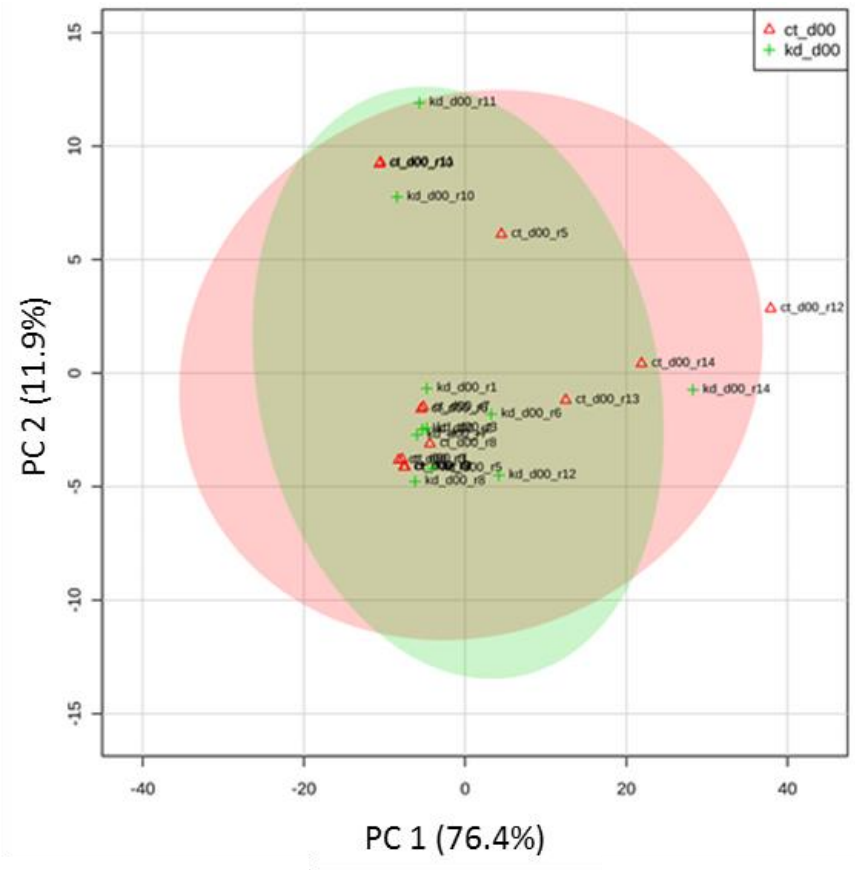

Figure 4.4: Lipidomic profile for control and *Hacd1*-kd C2C12 cells at 0 days post differentiation (dpd) displaying outlying samples.
Samples ct_d00_r12 and kd_d00_r14 lay outside the 95% confidence region for their group (red and green shaded areas respectively).

4.2.9. Reproducibility analyses

Three technical replicates were seeded simultaneously for both control and *Hacd1*-kd cell lines, and repeated five times to create a total n=15. Days 1 and 12 were chosen to represent both early and late stages of the experiment. Metaboanalyst software requires a minimum group size of n=3 and so reproducibility analysis was undertaken on spectra that had passed quality control before outlier removal, as all 15 samples were required to provide the software with five groups of three.

4.2.10. Statistical analysis

Data was normalised by median peak intensity and pareto scaled. Pareto scaling scales larger fold changes more heavily than small changes allowing smaller changes to be more easily identified. It uses the square root of the standard deviation as a scaling factor (van den Berg *et al*., 2006). Multivariate lipidomic analysis, including heat maps and PCA or PLS-DA (partial least squares-discriminant analysis) scores plots were performed using Metaboanalyst (Xia *et al*., 2011), an open source online software. The multivariate analyses were used to show any

clustering between samples: PCA or PLS-DA score plots. PLS-DA test outputs are in the form of two values, R^2: degree of fit to data, and Q^2: predictive power. Q^2 values >0.4 were thought to be acceptable for a biological model (Worley & Powers, 2013).

ANOVA and student t-test results were conducted in GraphPad (GraphPad Software Inc) are shown as mean results with error bars indicating the standard error of the mean (SEM). Significance scores were as follows: * indicates $p \leq 0.05$, ** indicates $p \leq 0.01$, *** indicates $p \leq 0.001$ and **** indicates $p \leq 0.0001$. Or in the case of graphs with high numbers of significant comparisons: black dash line indicates $p \leq 0.05$, black solid line indicates $p \leq 0.01$, red dash line indicates $p \leq 0.001$ and red solid line indicates $p \leq 0.0001$.

4.3. Results

4.3.1. Lipid extraction and analysis reproducibility

To provide confidence in the sample sizes chosen and in the consistency of experimental procedure, the reproducibility of control and *Hacd1*-kd samples at 1dpd and 12dpd were assessed qualitatively by use of PCA scores plots. Between control myotubes (12dpd) and both *Hacd1*-kd myoblasts (1dpd) and myotubes (12dpd) there was little separation between clusters. Control 1dpd samples were the most variable between the cell seeding groups with two clusters ("ct_d01_4" and "ct_d01_5") separated out entirely on their own. Groups in control 1dpd may be separated out further due to outliers which were subsequently removed. The variation between control 1dpd samples can be seen in the context of all four groups in Figure 4.6. Samples within group "ct_d01_4" continued to cluster separately and were therefore removed from further analysis.

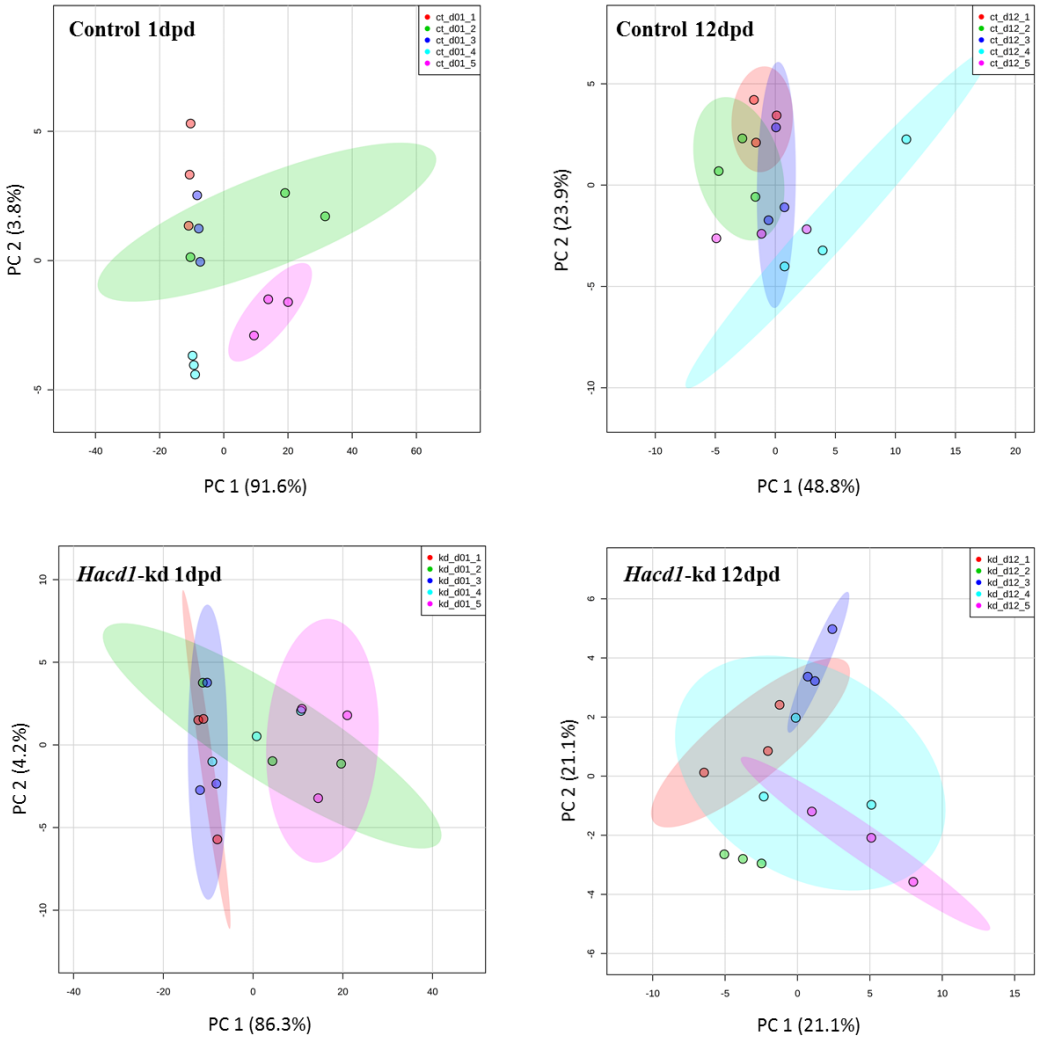

Figure 4.5: Reproducibility of C2C12 biological replicates.
Unsupervised PCA scores plots for control and *Hacd1*-kd C2C12 myoblasts at 1-day post differentiation (dpd) and myotubes at 12dpd. Shading represents the 95% confidence region.

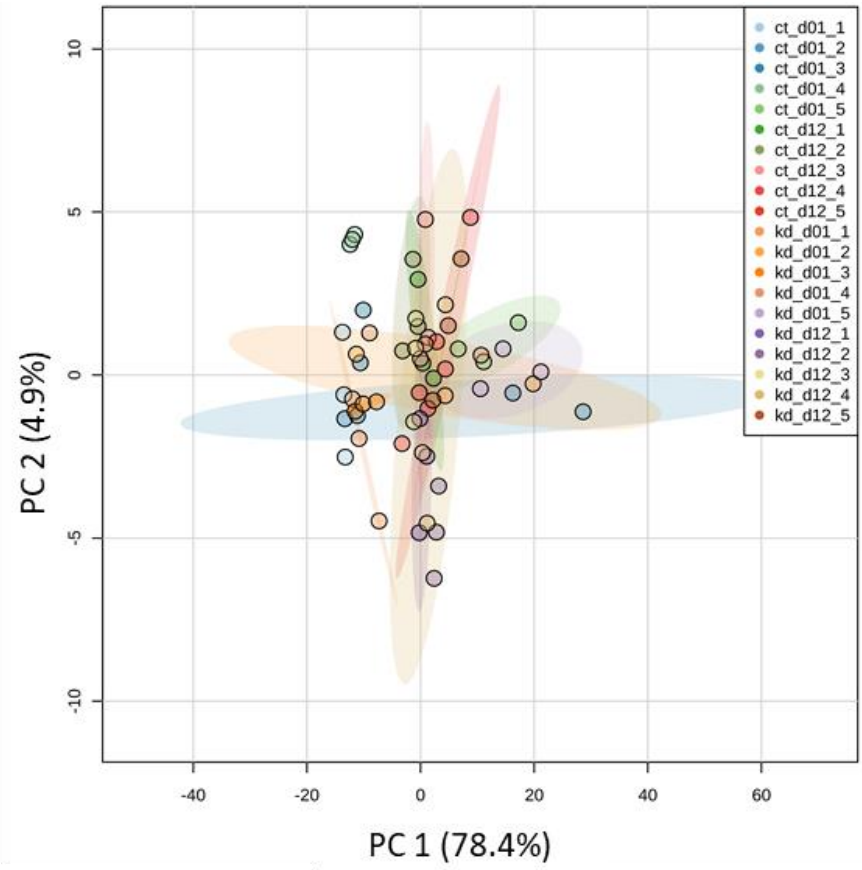

Figure 4.6: In-group and between-group variation of control and *Hacd1*-kd at 1 day post differentiation (dpd) and 12dpd.
PCA scores plot for the 20 groups assessed for reproducibility. Shading represents the 95% confidence region.

4.3.2. Lipidome changes over differentiation C2C12 cells

Before comparing lipidomic profiles after *Hacd1* knock-down in a C2C12 cell line (and therefore HACD1 activity reduced), the lipidomic profile in control cells was established. Figure 4.7 shows PCA scores plot used to identify major differences in lipids between cells as they fused together from single myoblasts, 0dpd, into multinucleated, mature myotubes at 12dpd. Figure 4.7 shows control cells grouped by time point (days post differentiation, dpd). Here there was no distinct clustering with any time point although there was slight variation in cluster shapes, represented by the cluster's shaded areas.

Figure 4.8 shows a supervised multivariate partial least squares-discriminant analysis (PLS-DA) plot of control cells both before and after the upregulation of *Hacd1*. The clusters of both groups overlap and the PLS-DA values: R^2 and Q^2 show the model of separation between the two populations and therefore the model's predictive power to be poor (0.17 and 0.044 respectively).

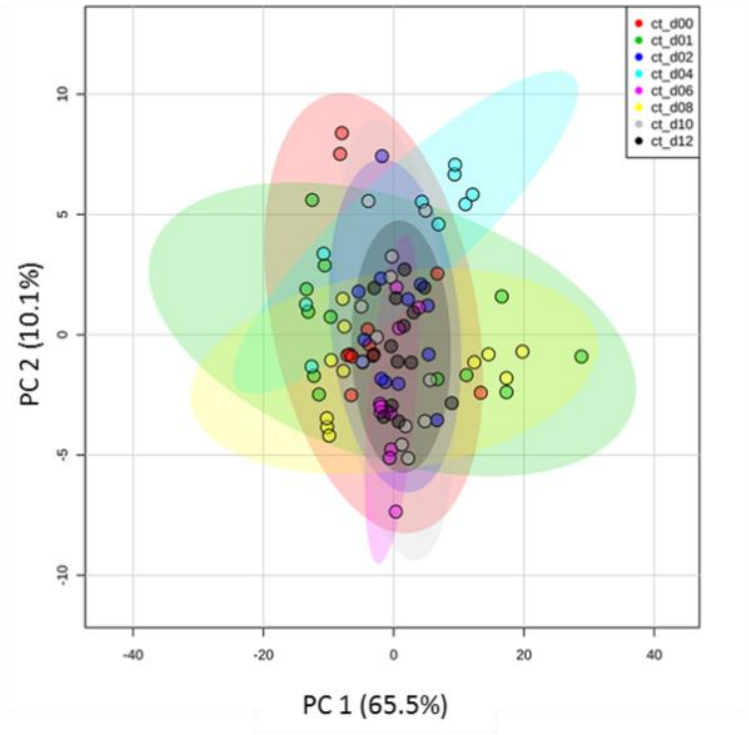

Figure 4.7: Lipidomic profile for control C2C12 cells over 12 days of differentiation.
Unsupervised PCA scores plot showing no distinct clustering with samples grouped into individual time points (days post differentiation, dpd). All data was normalised by median peak intensity and shading represents the 95% confidence regions.

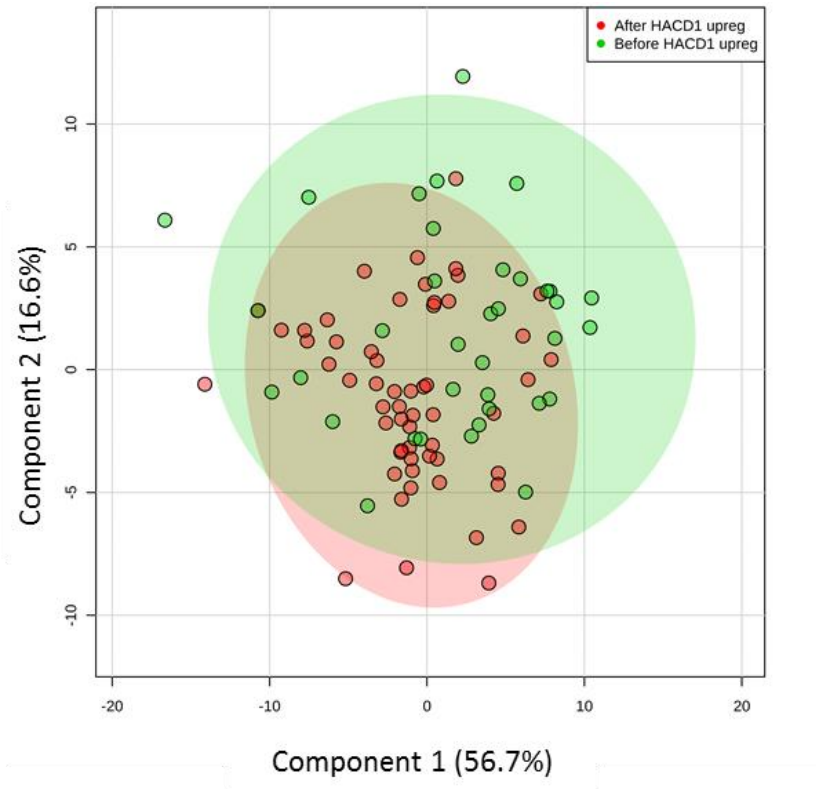

Figure 4.8: Lipidomic profile for control C2C12 cells over differentiation; before and after upregulation of *Hacd1*.
Supervised multivariate analysis by a two component PLS-DA (partial least squares-discriminant analysis) plot of samples grouped into those before (0, 1 and 2 dpd) and those after (4, 6, 8, 10 and 12 dpd) the upregulation of *Hacd1*. No distinct clustering was seen and the R^2 and Q^2 values (0.17 and 0.044 respectively) indicated a poor ability in the model to distinguish between the two sets of samples. All data was normalised by median peak intensity and shading represents the 95% confidence regions.

After examining the control cells lipidomes, we examined individual lipid phenotypes to quantify changes over differentiation namely, the structure of the lipid hydrocarbon chains. It had been documented previously that the ratio of saturated: unsaturated fatty acids decreases over earlier C2C12 differentiation (up to 3dpd). Therefore, peaks were tested that represented this to assess if our cells were conforming to this ratio change over a longer time scale than previously reported (Blondelle *et al*., 2015). The peaks chosen for this represented the double carbon bond (HC=CH) seen in MUFAs and PUFAs and the peak that was produced by hydrogens in a single carbon bond (HC-CH). The peak from a hydrogen between two double bonds was also quantified to represent PUFAs. Figure 4.9a shows raw values for these peaks and shows how the C-C peaks were more abundant due to their presence within all hydrocarbon chains, whether they were saturated or not. As it was incomparable as such (b) shows the normalised data and displays the relative saturation levels (C-C) decreasing over differentiation whilst the unsaturation (C=C) increases in relation. The decrease in relative saturated bonds was significant at 6, 10 and 12dpd (t-test, $p<0.0001$).

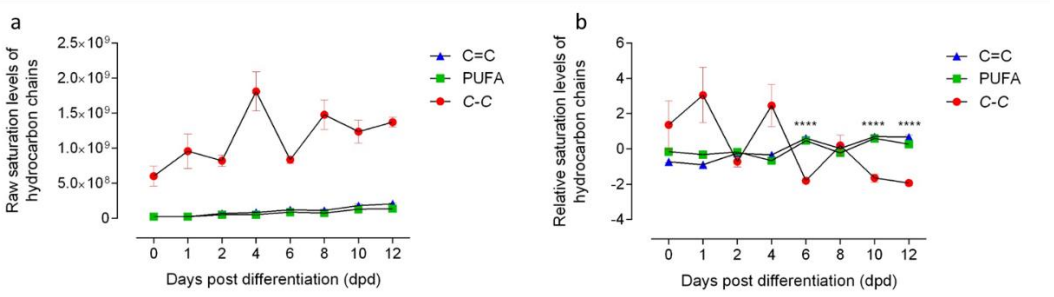

Figure 4.9: Relative saturation levels of hydrocarbon chains in differentiating control C2C12 cells.

Measured by peak intensity of single bonds (C-C) double bonds (C=C) carbon bonds and PUFA as measured by the PUFA peak annotated in Figure 4.2 from ^{1}H-NMR spectra. (a) Displays raw peak intensities showing the larger abundance of C-C bonds due to their presence in unsaturated fats also. All saturation levels increased over differentiation. (b) shows median normalised values in which saturation levels (C-C bonds) decreases relative to the double bonds (C=C and PUFA) over differentiation. Student t-tests between C-C and C=C bonds indicate the relative levels of hydrocarbon saturation were significantly decreased in 6dpd, 1-dpd and 12dpd ($p<0.0001$ for all significant results). Significance scores were as follows: * indicates $p\leq0.05$, ** indicates $p\leq0.01$, *** indicates $p\leq0.001$ and **** indicates $p\leq0.0001$ All data was normalised by median peak intensity.

Lipid classes, by analysis of peaks produced by characteristics of lipid head groups were also analysed (Figure 4.10). A significant decrease in LPC was observed over myotube differentiation (ANOVA, $p=0.0087$) with post-hoc Tukey multiple comparisons indicating significance between 0-4dpd and 0-8dpd. GPL abundance were found to significantly decrease over differentiation (ANOVA, $p<0.0001$). Post-hoc tests indicated the most significance was between early and late time points. PC abundance significantly increased over differentiation (ANOVA, $p<0.0001$) with post-hoc analysis showing most significant increases were between early-late and middle-late differentiation, with little significant changes occurring between the early-middle time points. FC abundance also decreased over differentiation (ANOVA, $p=0.0224$) with the significance coming from the 0-6dpd multiple comparison.

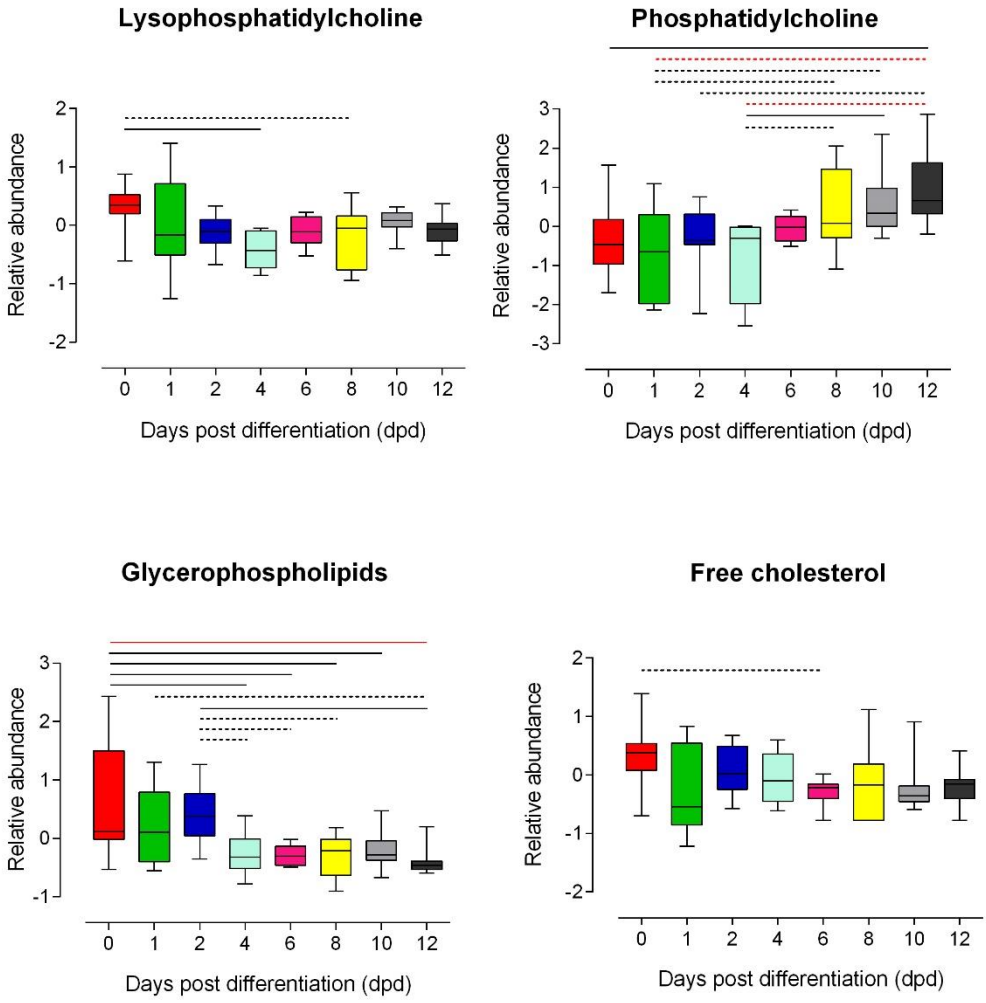

Figure 4.10: Relative abundance of lipid head groups during C2C12 myotube differentiation.
LPC = Lysophosphatidylcholine, PC = phosphatidylcholine, GPL - glycerophospholipids, FC = free cholesterol. Statistical testing done via one way ANOVA with Tukey post-hoc testing annotated on graph via lines. LPC, GPL & FC relative abundances decreased significantly over C2C12 differentiation (p=0.0087, p<0.0001 and p=0.0224 respectively). PC relative abundance significantly increased over differentiation (p<0.0001). All data was normalised by median peak intensity. Black dash line indicates $p \leq 0.05$, black solid line indicates $p \leq 0.01$, the red dash line indicates $p \leq 0.001$ and red solid line indicates $p \leq 0.0001$.

4.3.3. Lipidome comparisons between control vs *Hacd1*-kd C2C12 cells

After gaining insight into the lipidomic profile of control C2C12 cells over differentiation, analysis was then performed between control and *Hacd1*-kd samples to identify any differences seen by ^{1}H-NMR. As an initial look, all control and all *Hacd1*-kd samples over differentiation were grouped in order to perform a supervised PLS-DA. Figure 4.11 shows, overlap between the populations, yet there appeared to be a clear difference in population spreading. The PLS-DA results showed this to have some predictive power (R^2=0.51 and Q^2=0.36).

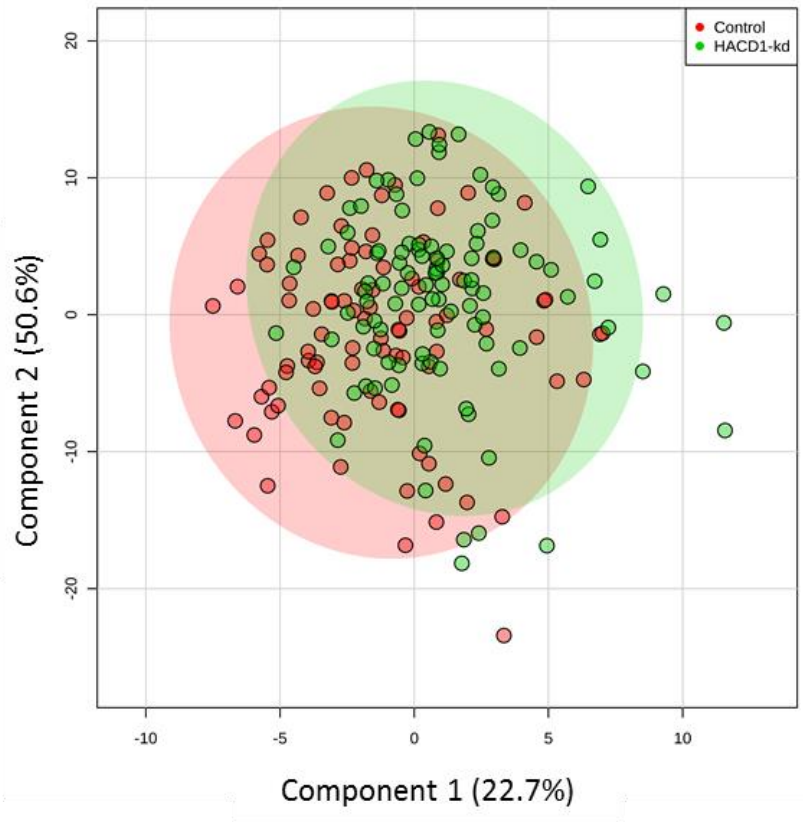

Figure 4.11: Lipidomic profile of *Hacd1*-kd C2C12 cells was moderately different to that of control cells.

Multivariate supervised PLS-DA shows overlap between control and *Hacd1*-kd clusters but was moderately predictive of which samples belong in which group, R^2=0.51 and Q^2=0.36. All data was normalised by median peak intensity, shading represents the 95% confidence regions and for clarity only first two components of a five-component model are shown.

4.3.3.1. Lipidome changes between control and *Hacd1*-kd at time points

To separate out differences between the control and *Hacd1*-kd cell population's PLS-DA were performed at each time point. Figure 4.12 shows these plots along with Table 4.1 displaying PLS-DA scores. All time points had R^2 values over 0.7 which indicates substantial model structure and Q^2 over 0.4 suggesting predictive power within the model; with the exception of early time points, 0dpd, 1dpd and 2dpd.

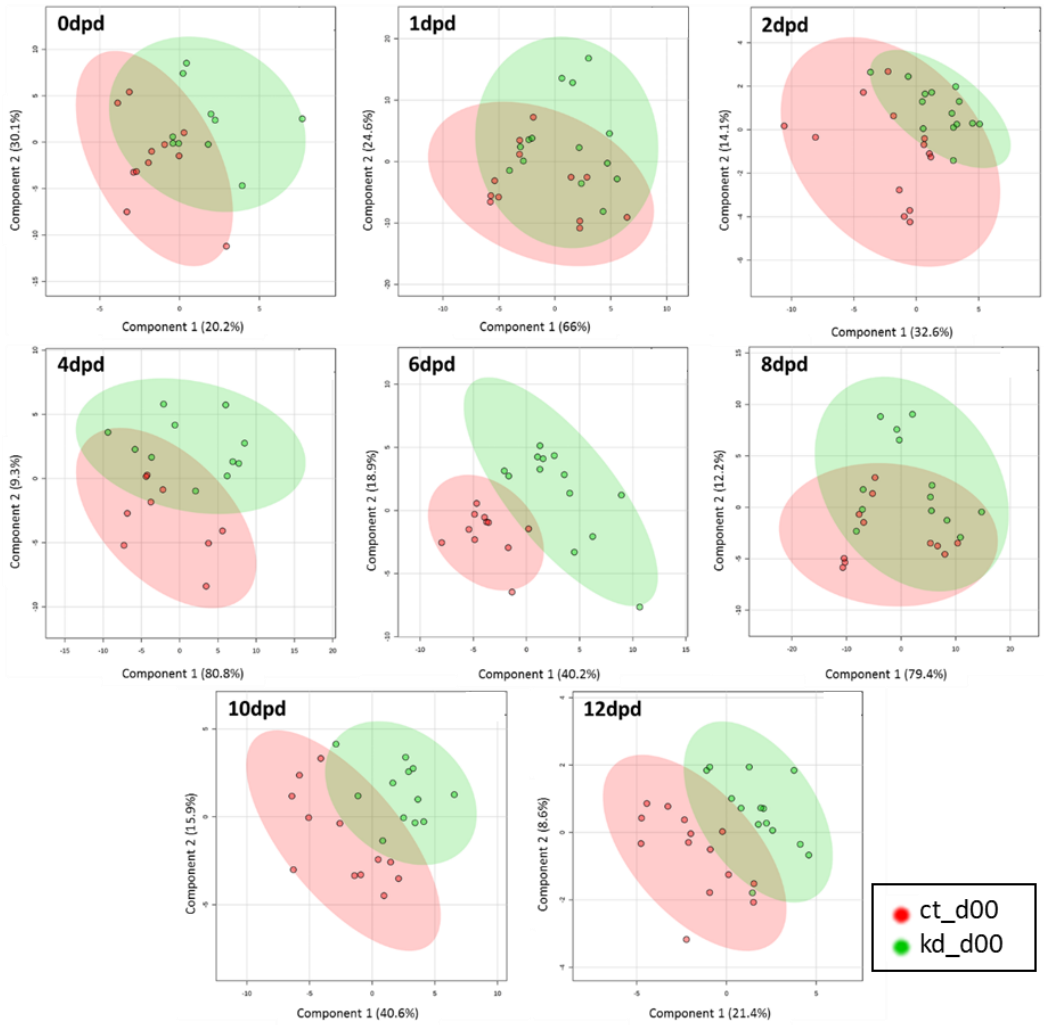

Figure 4.12: Control vs *Hacd1*-kd C2C12 cells at different time points during myotube differentiation.

Panel of figures shows supervised, multivariate PLS-DA plots of control and *Hacd1*-kd cells at different days during differentiation (scores from tests shown in Table 4.1). Comparison at 1dpd has no predictive power, comparisons of 0, 2 and 12dpd shows weak predictive power between the day-wise comparisons, 4dpd and 8dpd show moderate predictive power and comparisons between 6dpd and 10dpd show strong predictive power of the models. All data was normalised by median peak intensity, shading represents the 95% confidence regions and for clarity only first two components models are shown.

Table 4.1: PLS-DA scores for analysis shown in Figure 4.12.

Days post differentiation (dpd)	R^2	Q^2	Number of components
0	0.72	0.23	3
1	0.76	0.0203	5
2	0.86	0.31	4
4	0.95	0.58	5
6	0.91	0.75	5
8	0.88	0.51	5
10	0.92	0.75	5
12	0.88	0.43	5

4.3.3.2. Specific lipid phenotypes compared in control and *Hacd1*-kd cells throughout differentiation

The same analysis to quantify saturation levels within control samples was then performed on the *Hacd1*-kd samples (Figure 4.13) and compared to the data from the control cells (Figure 4.14). The saturation levels in *Hacd1*-kd cells followed the same trend as in the control cells.

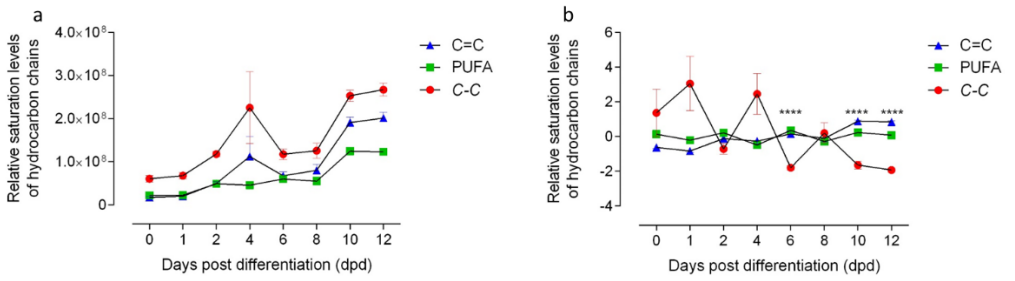

Figure 4.13: Relative saturation levels of hydrocarbon chains in differentiating *Hacd1*-kd C2C12 cells.

Measured by peak intensity of single bonds (C-C) double bonds (C=C) carbon bonds and PUFA as measured by the PUFA peak annotated in Figure 4.2 from ^{1}H-NMR spectra. (a) Displays raw peak intensities showing slightly larger abundance of C-C bonds due to their presence in unsaturated fats also. All saturation levels increased over differentiation. (b) shows median normalised values in which saturation levels (C-C bonds) decreased relative to the double bonds (C=C and PUFA) over differentiation. Student t-tests between C-C and C=C bonds indicated the relative levels of hydrocarbon saturation were significantly decreased in 6dpd, 1-dpd and 12dpd (p<0.0001 for all significant results). Significance scores were as follows: * indicates $p\leq0.05$, ** indicates $p\leq0.01$, *** indicates $p\leq0.001$ and **** indicates $p\leq0.0001$ All data was normalised by median peak intensity.

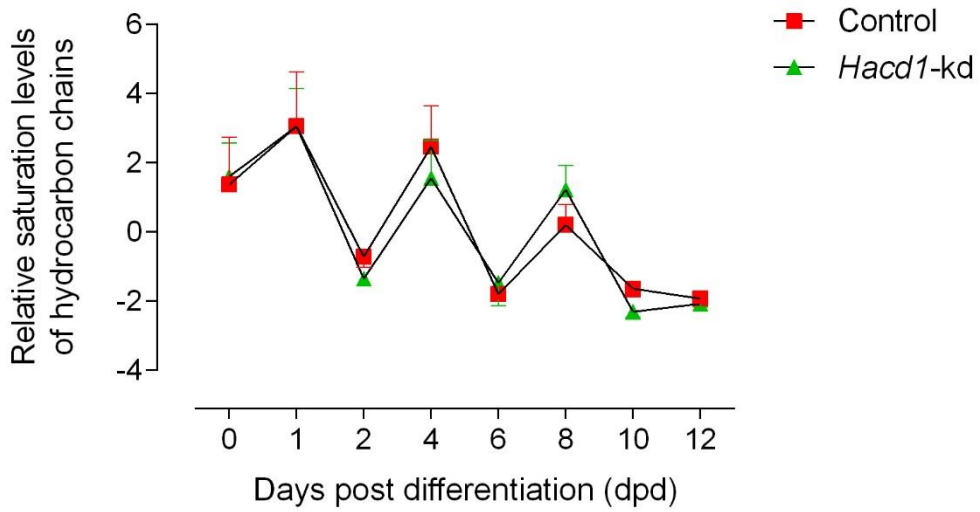

Figure 4.14: Saturation levels of control and *Hacd1*-kd C2C12 cells over differentiation represented by relative abundance of C-C bonds in hydrocarbon chains.
Both cell types followed an identical trend over differentiation and two-way ANOVA reported that the decrease in saturation levels over differentiation for both cell types was significant ($p<0.0001$) but there was no significant difference between control and *Hacd1*-kd saturation levels ($p=0.8$). All data was normalised by median peak intensity.

Figure 4.15 shows lipid class abundance in both control and *Hacd1*-kd cells over differentiation. Relative abundances of LPC and FC were significantly different between control and *Hacd1*-kd samples by a two-way ANOVA ($p=0.02$ and $p=0.04$ respectively) over differentiation whereas PC and GPL were not significantly changed in *Hacd1*-kd cells ($p=0.9$ and $p=0.5$ respectively).

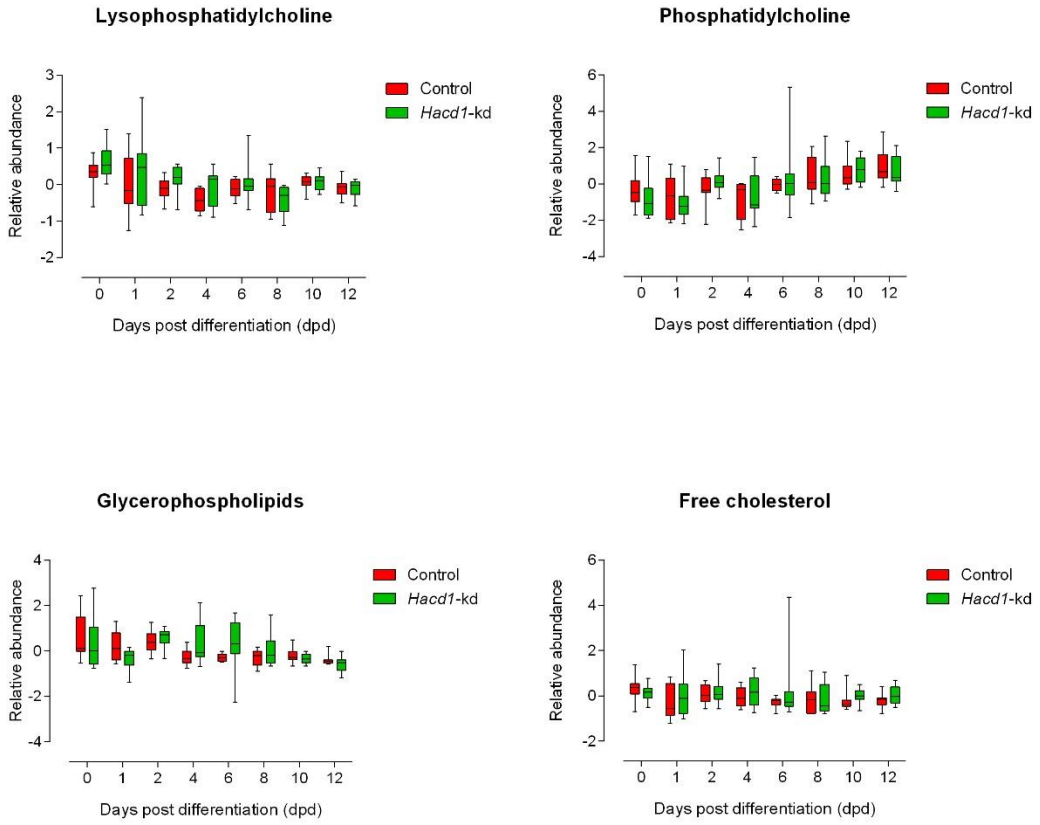

Figure 4.15: Relative abundance of lipid classes in both control and *Hacd1*-kd C2C12 cells over differentiation.

LPC = lysophosphatidylcholine, PC = phosphatidylcholine, GPL = glycerophospholipid, FC = free cholesterol. Two-way ANOVAs were performed and found that *Hacd1*-kd cells had significantly different LPC and FC abundances compared with control cells (p=0.0210 and p=0.0480 respectively). PC and GPL abundances were not significantly changed in the *Hacd1*-kd cells. Sidak's multiple comparison tests were performed on control vs *Hacd1*-kd at each time point and there was no significance indicated in the multiple comparison tests. All data was normalised by median peak intensity.

4.4. Discussion

HACD1 is required for elongating very long chain fatty acids (VLCFAs) within striated muscle (Ikeda *et al*., 2008). When the *HACD1* gene is mutated, such as in the canine neuromuscular disorder CNM, the enzyme activity is severely reduced (Blondelle *et al*., 2015; Muhammed *et al*., 2013; Pelé *et al*., 2005). Utilising a cell culture model with shRNA knockdown of *Hacd1*, this work describes changes seen in lipid phenotype through myogenic differentiation and the effect of *Hacd1* deficiency. By understanding the effect that *Hacd1* deficiency has upon lipid content in cells it provides us with a deeper understanding of HACD1 function and which lipids are likely to be most affected in HACD1-CNM.

4.4.1. Establishing the lipid phenotype for control C2C12 cells over differentiation

Work by Blondelle *et al*., (2015) provided initial insight into the lipid profile of C2C12 myotubes as they began to differentiate over early time points within myotube fusion and differentiation up to 3 days post differentiation (dpd). We aimed to expand this further in the C2C12 cell line and identify later lipidomic changes associated with *Hacd1*-deficiency that might be related with abnormalities in intracellular membranes that occur later after fusion (Walmsley *et al*., 2017). When differentiating control C2C12 cells up to 12 days subtle changes were observed within the lipidome of the differentiating sample set using ^{1}H-NMR. Samples were initially separated out by time point (dpd) and there was high overlap of group clusters within the PCA scores plot. Cluster size appeared reduced in later time points over the course of differentiation (Figure 4.7) which indicated that differentiation was associated with reduced variability in the lipidome. When samples were grouped into time points pre- and post *Hacd1*-upregulation (0-2 dpd and 4-12 dpd based on qRT-PCR, Chapter 3 Figure 3.5) there were only subtle changes between the two groups, as with differentiating cells the cluster size was reduced after *Hacd1* upregulation. This could suggest that inducing cells to differentiate leads to upregulation of *Hacd1* and stimulates synthesis of specific lipids which increases the uniformity in the myotubes lipidome. Although this is a possible explanation, it has been reported that cultured cells have lipid profiles similar to the media in which they were cultivated (Briolay *et al*., 2013). In this study serum starvation was used to stimulate differentiation and the same batch of horse serum was used throughout the project for consistency (Bajaj *et al*., 2011; Jing, 2012; Walmsley, 2013). As proliferating C2C12 are easier to culture than differentiating C2C12 cells, FBS was not controlled as strictly. Therefore possible differences between batches of serum in proliferation media may have accounted for the increased variability seen in myoblasts and early stages of differentiation. Future work on lipid phenotype in these cells should ensure to use the same proliferation and differentiation

media throughout the project to assess whether the variability seen was due to culture differences or the biology involved in myotube fusion and differentiation. A study by Lee *et al*., (2009) reported fatty acid content of differentiation media for culturing C2C12 cells to be important modulators of proliferation and differentiation, providing further suggestion that FBS used in proliferating media should be consistent across lipidomic studies (Lee *et al*., 2009).

Considering more specific lipid changes during C2C12 differentiation, we looked at fatty acid chain saturation and abundance of LPC due to previous reporting in a *Hacd1*-deficient cell line (Blondelle *et al*., 2015). Ratios of fatty acid chain lengths within phospholipids in early differentiation have also been reported to favour chain lengths of 10-16 carbons over those of 18-26 carbons in length when *Hacd1* was knocked down (Blondelle *et al*., 2015). Unfortunately, this was not possible to detect by 1D ^{1}H-NMR in this study. Blondelle *et al*., (2015) who described saturation levels of fatty acid chains within phospholipids within proliferating myoblasts and differentiating cells at day three of differentiation; found saturated fatty acids (SFA) were most abundant in control myotubes, followed by monounsaturated fatty acids (MUFAs) and least of all polyunsaturated fatty acids (PUFAs). Proportions of these fatty acids were comparable in the *Hacd1*-kd cells, and MUFA was significantly decreased when *Hacd1* was knocked down. The work in this chapter demonstrates that relative amounts of fatty acid saturation decreased over differentiation with significantly lower saturation levels at 6, 10 and 12dpd after the upregulation of *Hacd1*. Our findings correspond to work by Briolay *et al*., (2013) in which they also reported a decrease in the saturated: unsaturated fatty acid ratio in differentiating L6 muscle cells from proliferation to 4-5 days differentiated. This decrease in fatty acid saturation leads to an increase in plasma membrane fluidity which has been reported to be a primary event in the fusion of myoblast membranes, before the rigidity is restored in the membranes post myoblast fusion (Prives & Shinitzky, 1977).

Lysophosphatidylcholine relative abundance was significantly reduced over differentiation with significant changes occurring from 0-4 and 0-8dpd suggesting the LPC levels decrease in early-mid differentiation which coincides with cellular fusion (Blondelle *et al*., 2015; Leikna *et al*., 2013). The addition of LPC to cell culture medium has been reported to inhibit myoblast fusion and LPC content reduced in the C2C12 cell line between proliferating myoblasts and 3dpd cells (Blondelle *et al*., 2015; Leikna *et al*., 2013). Blondelle *et al*., (2015) determined that the drop in LPC seen up to 3dpd was dependent upon *Hacd1* upregulation because it occurred in parallel with upregulation of *Hacd1*, was diminished by *Hacd1*-kd and the re-expression of *Hacd1-fl* normalised LPC levels and fusion.

Phosphatidylcholine, GPL and FC were also quantified due to their presence within muscle (Ladbrooke & Chapman, 1969; Mukai *et al*., 2009). PC relative abundance was significantly increased over differentiation and is reported to be an important plasma membrane phospholipid and one of the major phospholipids within skeletal muscle (Stefanyk *et al*., 2010). Therefore, as myoblasts begin to differentiate and membranes fuse and reorganise themselves into more complex membrane systems the increased level of PC was expected. Significant changes were documented at 2 and 4dpd (Figure 4.10) coinciding with fusion and the onset of more complex membranes developing as the myotubes differentiate. Phosphatidylcholine rich membranes are relatively fluid and this corresponds with the decrease seen in saturation levels, also linked to membrane fluidity (Ladbrooke & Chapman, 1969). GPL abundance decreased over differentiation; Briolay *et al*., (2013) reported a decrease in the concentration of long chain PUFAs as cells differentiated into myotubes and this study reported a significant decrease in LPC, a class of GPLs. We hypothesise therefore that a decrease in certain GPL's accounts for the decrease reported however it cannot be concluded which GPLs were decreasing apart from LPC.

FC abundance also decreased over differentiation, and the only significant change was between 0-6dpd. This significant decrease in cholesterol happens in time with cells beginning to fuse as LPC levels drop off. Membrane cholesterol composition is organised into discrete and dynamic areas of the cell membrane, called lipid rafts (Brown *et al*., 2000). Cholesterol has been reported to reduce along areas of the membranes that are about to fuse (Mukai *et al*., 2009) and so in my opinion this suggests the levels of cholesterol are likely to decrease in the cells during early differentiation to allow the fusion of membranes. 1dpd cells had the lowest mean relative abundance of FC, which could be explained by the membrane lipid composition shifting and preparing the membranes for fusion - however this was not found to be significantly lower any other timepoint. Briolay *et al*., (2013) described a reduction in cholesterol: phospholipid ratios that occurred alongside changes in the saturation levels associated with cell fusion. Membrane fluidity was not evaluated in this study although increased fluidity has been associated with changes in cholesterol, FA saturation and PC levels during myogenic differentiation as reported here (Blondelle *et al*., 2015; Mukai *et al*., 2009).

4.4.2. Evaluating lipidomic differences when *Hacd1* was knocked down in the C2C12 cell line

Moderate differences were observed within the overall lipidome of *Hacd1*-kd cells when compared with controls when entire data sets were grouped together (R^2=0.51 and Q^2=0.36). These differences were clearer still when control and *Hacd1*-kd groups were analysed by each time point separately. Early time points 0, 1 and 2dpd had the least difference between groups,

then after *Hacd1* upregulation at 4dpd the differences between control and *Hacd1*-kd were exaggerated with 6, 8 and 10dpd having substantial separation in clustering of groups. 12dpd had less separation and predictive power in the PLS-DA model and we hypothesise this may be due to either a developmental delay in *Hacd1* deficiency that was overcome at this later stage or the onset of senescence as the cultures become more temperamental at later differentiation stages.

In the study conducted by Blondelle *et al*., (2015) they found that *Hacd1*-kd myoblasts, prior to differentiation, had a higher proportion of saturated fatty acids and a lower proportion of MUFAs. Here no significant difference was seen between saturation levels in control and *Hacd1*-kd cells and both followed a very similar pattern of saturation decrease over differentiation. Cells exhibited a cyclical pattern of saturation levels with an overall decreasing trend; we hypothesise this may be due to culturing limitations as media was changed approximately every other day and media changes were performed at room temperature, potentially causing cells stress due to movement in and out of incubators. Therefore, both of these factors may be confounding results. The cell culture and lipidomic methods used in this study were different to that of Blondelle *et al*., (2015) as well as a different *Hacd1*-kd clone and so differences in findings were not unexpected.

Blondelle *et al*., (2015) reported that, instead of the decrease in LPC content seen in differentiating control C2C12 cells, when *Hacd1* was knocked down LPC content increased and MUFA content decreased. In this study, *Hacd1*-kd myoblasts and myotubes in early differentiation (0-6dpd) had higher levels of LPC (insignificant) compared with controls but a similar decrease in LPC was observed on differentiation. As previously discussed, a cell clone was selected for this study that differentiated under the culture conditions presented and there was no observable difference in myogenesis between this *Hacd1*-kd cell line and the control (Figure 3.10). Contrastingly *Hacd1*-kd C2C12 used by Blondelle *et al*., (2015) had reduced fusion and differentiation. This likely explains the differences between LPC levels here and in comparison with Blondelle's results as these *Hacd1*-kd cells did fuse, LPC levels should decrease, as seen in Figure 4.15. This is, however, contradictory to their conclusion that the LPC decrease was dependent on *Hacd1* - as this decrease was present in our study without *Hacd1* expression being upregulated. The difference seen here could be due to a number of factors including differences in cell culture protocols as previously mentioned. The phenotype may be somewhat rescued by the higher concentration of horse serum used in differentiation media in this study: 4% compared to 2% used by Blondelle *et al*., (2015). Levels of *Hacd1* knockdown also vary between the Blondelle study and this one: Blondelle *et*

al., (2015) observed knockdown at all time points, and undifferentiating cells, suggesting a more severe phenotype than the cells in this study.

Phosphatidylcholine and GPL levels in *Hacd1*-kd cells followed the patterns seen in control cells suggesting *Hacd1* does not act upon these lipid classes. Although as the cells in this study also did not present with increased LPC levels in *Hacd1*-kd cells compared to control it is possible the *Hacd1*-deficient phenotype was being rescued by the serum within the media and therefore alleviating potential lipidomic changes caused by *Hacd1*-deficiency. The importance of media can be seen in Figure 4.14 in which both the control and *Hacd1*-kd exhibit the same saturation pattern across differentiation: which we hypothesise as due to media changes. Significant differences between FC levels between control and *Hacd1*-kd were identified but inconsistent with FC having higher mean abundance in 1, 2, 4, 10 & 12dpd but lower in the other time points (all multiple comparisons insignificant).

4.4.3. Limitations and future work

Lipidomics can provide a great deal of information but it has limitations. Analysis produced by NMR can be directed down two main routes: a nontargeted method which was conducted for global investigation into lipid profiles within our cells and a quantitative method which was performed for saturation levels and to evaluate a selection of different lipid classes within the cells. NMR lipidomics is a developing discipline which meant we were unable to fully annotate the spectra due to a lack of validated reference data. Quantitative evaluation to determine all lipids detectable by the spectrometer and all molecules and pathways affected by *Hacd1*-deficiency was therefore incomplete and this limitation in spectra annotation created a bottleneck in the number of lipids that were quantifiable. This study therefore began by focusing on lipids associated with plasma membranes and changes previously documented in myoblast fusion, early myogenesis and *Hacd1*-deficiency (Blondelle *et al*., 2015, Walmsley *et al*., 2017). Lipids associated with intracellular organelles, membrane trafficking and involved in signalling, for example ceramides and diacylglycerol (van Meer & de Kroon, 2011), have not been deeply explored in this data set and this may be a future avenue for analysis once lipid annotation is more accessible.

Experimental design created difficulties with normalising spectral data post ^{1}H-NMR runs. Cells were counted before seeding into flasks however as cells proliferated before beginning to differentiate this may have caused some differences in cell mass when pelleted. It was observed, that the knockdown cells appeared to proliferate slower; this had also documented by Blondelle *et al*., (2015). In future weighing these pellets would be considered, although this would have to be done wet and it is technically difficult to remove all the PBS thereby

creating another potential source of inaccuracies in measurements. We chose to normalise the data by median peak intensity per bucket for a robust normalisation method, in future experiments introducing a non-native lipid peak to each sample would be an appropriate method by which to normalise samples. These could include a lipophilic compound such as trimethyl silane which is well documented within metabolomics studies as a reference peak, due to its strong signal which falls out of the range of most lipid peaks (Tiers *et al*., 1958).

The in-group variation was high which masked lipidomic differences in cluster analysis (PCA and PLS-DA analyses), this was due to the inherent uniqueness in samples, even in immortal cell lines (Rubakhin *et al*., 2011). The variation seen in early time points could be due to serum differences as previously discussed due to the sensitivity of NMR. Samples were collected and lipids extracted over a long period of time throughout the project so as experimental technique improved this will have created variation between samples.

Compared to the mass spectrometry (MS) methods, NMR-based lipidomics are less sensitive and limited by overlap of signals and poor separation of peaks that can make identification of individual peaks difficult (Yang *et al*., 2016). NMR does however offer a number of advantages including cost, sample preservation and reproducibility and so was chosen for this study as a preliminary exploratory technique. Samples are not destroyed during the NMR protocol and so can be stored for further analysis by MS in future. The high level of potential reproducibility, lipid identification and quantification make NMR an appealing technique (Li *et al*., 2017). ^{1}H-NMR cannot provide information on chain length though which is important for the study of HACD1. As determined by Blondelle *et al*., (2015) previously, we would anticipate that VLCFA in phospholipids would increase corresponding to the upregulation of *Hacd1* and that in the *Hacd1*-kd cells this would be attenuated with proportional shift and increase in less complex lipids with shorter fatty acid chain lengths. Ultimately, other methods will need to be employed as well such as MS which would provide accurate masses for lipids and fatty acids and allow any changes in chain length would be detected.

Future work should also evaluate which lipids are affected by HACD deficiency within the context of the entire elongation cycle as the ELOVL condensation step has also been reported to be a rate-limiting step (Ikeda *et al*., 2008; Sassa & Kihara, 2014). Rescue experiments would also confirm changes seen were due to *Hacd1*-deficiency - the lipidome of cells once rescued by *Hacd1* re-expression should not be different from control cells.

4.4.4. Conclusions

This study evaluated the lipidome of C2C12 cells and their changes over myogenic differentiation and with *Hacd1*-deficiency. This study describes the lipid phenotype seen in C2C12 cells as they form mature myotubes and conclude that *Hacd1*-deficiency has an impact on the lipidome at all time points studied particularly after upregulation of *Hacd1-fl*. In this evaluation we found significant differences in LPC and FC abundances when *Hacd1* was knocked down. As these are broad lipid classes, further work could be conducted to specify which individual lipid species are affected. To fully evaluate the lipids affected by *Hacd1* deficiency – rescue experiements could be conducted to determine if lipid levels can be restored by re-expression. This will be important to expand our knowledge of HACD1 function, in particular which lipids are altered in *Hacd1*-deficient membranes to help understand the high levels of tubuloreticular membrane disorganisation in HACD1-CNM affected dogs (Pelé *et al*., 2005; Walmsley *et al*., 2017). To conclude, when comparing the lipidome between control and *Hacd1*-kd cells at each time point, there were clear differences between the two lines, however these were not accounted for by the specific lipids evaluated so far. Differences seen within the cell types was prominent at later stages of differentiation, which are more representative of myofibres than the early myoblasts are and so the findings in this chapter have provided a first look in to the lipidome of the cells this late into differentiation. Despite the cells providing an initial insight into the effect of *Hacd1*-deficiency on the lipidome, cells were found to be highly influenced by their environment suggesting this model may not be the most appropriate for studying the effects of HACD1-defiency upon lipid profiles.

5 *Hacd1*-mutations in zebrafish embryos as a novel congenital myopathy model

5.1. Introduction

The embryonic zebrafish is well-established as a model for studying embryonic development (Veldman & Lin, 2008), and more recently it has found to be a good model of mammalian genetic diseases. Sequencing of the zebrafish genome first started in 2001 by the Sanger Institute (UK) and it has since been revealed that 70% of human genes have functional homologues in zebrafish (Howe *et al*., 2013). In the 1990s large-scale random mutagenic screens began and numerous mutants were created modelling a variety of genetic conditions affecting various body systems and demonstrating the capabilities zebrafish have as a model of disease (Driever *et al*., 1996; Lieschke & Currie, 2007). Zebrafish have a number of characteristics that make them a highly desirable model for genetic study and manipulation. Zebrafish reach sexual maturity quickly at around three months: this allows mutant heterozygous lines to be established rapidly (Guyon *et al*., 2007). Embryos are fertilised externally and so can be harvested, observed and manipulated throughout development without needing to sacrifice the mother (Guyon *et al*., 2007).

Genetic manipulation is typically carried out by microinjection of nucleases or RNA, for example, into the nucleus or yolk of early (ideally single cell stage) embryos, resulting in over- or under expression of genes (Hogan *et al*., 2008). Morpholinos are widely used to knock down gene expression or interfere with splicing (Heasman, 2002), though genome editing is becoming more common utilising ZFN, TALENs and more recently CRISPR/Cas9 (Carroll, 2011; Clarke, 2011; Liu *et al*., 2017). The embryo's development from outside the body of the mother also allows direct observations and manipulation of embryos to be made before the onset of external confounding variables such as diet, up until 5 days post fertilisation (dpf) when they begin to feed. (Liu *et al*., 2017). Other benefits include their small size and shoaling behaviour of adults which allows for efficient housing relative to mammals and they are optically transparent in early embryonic stages allowing for high quality imaging (Guyon *et al*., 2007). The development of the central nervous system (CNS) with zebrafish begins during the first few days of fertilisation, although higher CNS function is not present until after 5dpf whereby A(SP)A protection of the zebrafish begins (Schmidt *et al*., 2013).

Muscle disorder models using genome editing technology are becoming increasingly common in zebrafish. Some of the genes involved in human centronuclear myopathies (CNM) are

currently being investigated using zebrafish models, often using morpholinos to edit the genomes of the embryos. CNM target genes currently being studied include: *mtm1*, *mtmr14*, *bin1* and *dnm2* (Dowling *et al*., 2009; Dowling *et al*., 2010; Gibbs *et al*., 2013a; Sabha *et al*., 2016; Smith *et al*., 2014). Dowling *et al.,* (2009 & 2010) reported that *mtm1* and *mtmr14* morphant zebrafish presented with early muscle phenotype using morpholino technology. Sabha *et al*., (2016) used ZFN genome editing to mutate the *mtm1* gene within zebrafish. Gibbs *et al*., (2013a) investigated *dmn2* within zebrafish embryos through the overexpression of a mutated version *dnm2* gene via plasmid transfection. Smith *et al.,* (2014) used morpholinos to knockdown *bin1* in zebrafish: here they found a dose dependent reduction in gene expression for one of the morpholinos tested. These models were possible due to the fast-developing muscle that is readily available for experiments (Guyon *et al*., 2007) and the phenotypes seen in the models are transferable to mammalian CNM as they reflect the mammalian disorders and so represent CNM pathology (Dowling *et al*., 2009; Dowling *et al*., 2010; Gibbs *et al*., 2013a; Sabha *et al*., 2016; Smith *et al*., 2014).

Models of HACD1 deficiency are currently limited to cell line (Blondelle *et al*., 2015; Lin *et al*., 2012; Walmsley *et al*., 2017) or mammalian models: mice and Labrador models specifically (Blondelle *et al*., 2015; Sawai *et al*., 2017). Mammalian models, particularly large animals such as dogs, have limitations including: size, cost, speed of reproduction and ethical and moral implications. A mammalian muscle cell culture model was established, as used in Chapters 3 & 4, however there are also limitations here not least with the degree of differentiation that can be achieved in these cultures. A novel zebrafish embryo model would allow investigators to study HACD1-deficiency in a complex vertebrate system and bridge the gap between these existing models.

HACD1 functions alongside other proteins including the elongases (ELOVLs) to elongate the chain length of very long chain fatty acids (VLCFA). Hence, we first aimed to characterise the lipidomic changes occurring during development of normal zebrafish embryos and correlate this with changes in *hacd1* expression using ^{1}H-NMR, with the future aim of comparing results with *hacd1*-mutant embryos once the model had been developed. Previous work has shown that the yolk sac in zebrafish embryos has a highly dynamic lipid composition and the most abundant lipids within whole embryos up to 5dpf are phosphatidylcholine (PC), cholesteryl ester (CE) and triacylglyceride (TAG) (Fraher *et al*., 2016). Fraher *et al*., (2016) reported that at 1dpf embryos had little lipid content other than within the yolks sac and by 3dpf the embryos had an increased lipid content in the forebrain, around eye and the optic vesicle and also the pharyngeal areas that form the gills. Cholesteryl ester (CE) was the most abundant lipid at 0dpf/1 cell stage, accounting for 40% lipid content, and so they concluded

that CE was the most abundant lipid class within the yolk sac. PC was the next abundant at 17% in yolk sac and Fraher *et al*., (2016) reported TAG and PC increase in the yolk sac from 0-1dpf and then decrease during rest of embryogenesis and CE levels within the embryo body increased after 1dpf.

Previous work on the elongation of fatty acids, specifically in the context of the ELOVL proteins, has shown that there are similarities between mammalian and zebrafish mechanisms and expression. Two isoforms of *elovl1*: *elovl1a* and *elovl1b* were shown to be highly expressed in the swim bladder and the kidney (*elovl1b* only) and when knocked down in embryonic zebrafish long chain fatty acids (LCFA) were increased alongside a reduction in yolk lipid consumption (Bhandari *et al*., 2016). Work conducted by Monroig *et al*., (2010) also found the zebrafish orthologue of ELOVL4, *elovl4b* had comparable expression to mammals within the pineal gland of embryonic zebrafish and expressed in the eye and gonads of adult fish. They also reported an alternative elongase within zebrafish *elovl4a* which was expressed neuronally in embryonic zebrafish and then expressed ubiquitously within adult fish. Both *elovl4a* and *4b* functioned to elongate fatty acids when expressed in yeast (Monroig *et al*., 2010). ELOVL2 has also been studied within zebrafish and an increase in C22 docosahexaenoic acid (DHA) was seen alongside the upregulation of *elovl2* from approximately 12 hours post fertilisation (hpf) (Monroig *et al*., 2009).

These models have furthered our understanding of CNM mechanisms and pathogenesis. The effects of *hacd1* mutation have yet to be studied within zebrafish and currently no CRISPR knockdowns or mutants have been created either for any of the CNM genes.

5.1.1. Chapter aims & hypotheses

Due to the success of previous embryonic zebrafish CNM models we hypothesised that the newly generated CRISPR/Cas9 *hacd1*-mutant zebrafish embryos would be also be a good model for HACD1-CNM. Specifically, the work in this chapter sought to:

1) Evaluate the lipidome of wildtype AB zebrafish embryos from 1-3 days post fertilisation (dpf) and optimise ^{1}H-NMR lipidomics within this model organism;
2) Evaluate phenotypically abnormal F_0 embryos from CRISPR/Cas9 injected zebrafish embryos.

5.2. Methods

5.2.1. Sample preparation and ^{1}H-NMR experiments

AB wildtype zebrafish (Danio rerio) embryos were collected at either 1dpf, 2dpf or 3dpf. Embryos were collected in groups of 10 unless otherwise stated and placed into microcentrifuge tubes, as much water was removed as possible before snap freezing in liquid nitrogen and storing at -80^{o}C. For sample size experiments, embryos aged 3dpf were used as it was thought these would contain the most material to extract lipids from and therefore produce good quality, reproducible peaks. For experiments with dechorionated embryos (section 5.3.2.1), chorions were removed manually from live embryos using a pair of fine watchmaker forceps (Dumont Laboratories) and discarded before freezing embryos. Experiments were all performed in triplicate.

Lipid extraction and extract preparation was carried out as described in Sections 4.2.2 and 4.2.3, with the addition of an extra sonication step in order to fully disrupt and break apart samples. ^{1}H-NMR spectrometer experiments and quality controls were set up and run as described in 4.2.4.

5.2.2. Lipidomic analysis of developing wildtype embryos

Pattern files and spectra annotation for spectra 'bucketing' was undertaken as described in Sections 4.2.6 and 4.2.7. Lipid abundance was measured using both Metaboanalyst, an open source online software (Xia *et al*., 2011) and analysed in GraphPad Prism (GraphPad Software Inc.). Data was normalised to the methyl peak (CH_3) as this was considered to be the most stable reference peak (Appendix Figure A3.1): this method assumes most molecules only have one methyl group and a small proportion of lipids may be branched, so this must be considered when analysing data (Jakobsson *et al*., 2006). Data was pareto scaled to avoid large peak changes masking smaller changes within the data set (van den Berg *et al*., 2006). Multivariate analyses were used to identify clustering between samples using PCA (principal component analysis) or PLS-DA (partial least squares-discriminant analysis) score plots. PLS-DA test outputs are provided in the form of two values: R^2 which describes degree of fit to data; and Q^2 denotes predictive power. Q^2 values >0.4 are thought to be acceptable for a biological model (Worley & Powers, 2013). ANOVA tests (analysis of variance) were also used to identify any specific lipid changes between samples. ANOVA results are shown as mean with error bars indicating the standard error of the mean (SEM). Significance scores were as follows: * indicates $p \leq 0.05$, ** indicates $p \leq 0.01$, *** indicates $p \leq 0.001$ and **** indicates $p \leq 0.0001$.

5.2.3. Phenotypic evaluation of injected embryos

Embryos were injected with Cas9 protein and a previously validated guide RNA targeting exon 1 of *hacd1* (data not shown). Validation was performed by another researcher and confirmed that the guide and Cas9 together was the only combination to cut the *hacd1* sequence within the plasmid and that the guide was specific to *hacd1* (plasmid containing *hacd2* transcript was not cut). Injection mixes contained: 1µl (20µM) Cas9 protein (NEB), 2µl (350ng/µl) guide RNA (*in vitro* synthesis), 0.5µl (0.5%) phenol red solution in PBS (Sigma) and 1.5µl H_2O. The guide specifically targeted an area within exon 1 adjacent to the *hacd1* start codon (see Figure 5.1).

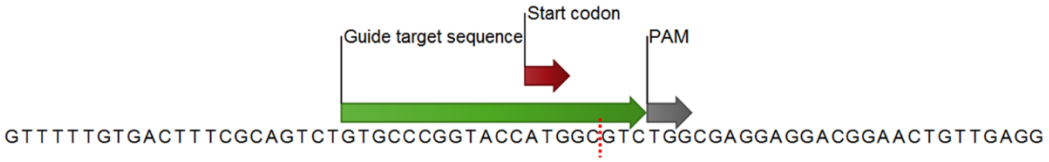

Figure 5.1: *hacd1* guide directed cut site.
hacd1 sequence for a section of exon 1 with the start codon, PAM sequence and the designed, the validated guide RNA and the expected cut site (red dashed line) annotated.

Around 75% of embryos screened by high resolution melt curve analysis (not presented in this thesis) at 72hpf had an abnormal peak in comparison with wild type and control embryos and subsequent cloning from these embryos demonstrated a 25-100% somatic lesion frequency. An abnormal live phenotype had been observed in 10-25% of F_0 Cas9/guide injected embryos at 72hpf, this correlates with the presence of mutations and are not seen in control embryos injected with Cas9 alone. Embryos were evaluated throughout development and phenotypically abnormal embryos at 72hpf selected for this work. Morphology was evaluated at 72hpf and a grading system devised for scoring. To assess swimming behaviour in embryos at 72hpf: embryos were touched on the tail by an external stimulus and their response was observed and recorded using a 5MP digital camera (Microtech) and Touplite software (ToupTek photonics). This assessed muscle function - following the tactile stimulus a rapid, strong response was seen in wild type embryos and they swam out of the view of the camera (Smith *et al*., 2013).

5.2.4. gDNA mutation screening in F_0 embryos

Mutation analysis was performed on single embryos selected based upon morphological abnormalities and frozen prior to evaluation or following immunohistochemistry (IHC). 72hpf single embryos were digested using a lysis buffer (50µl per embryo) containing: 10mM Tris-HCl pH8 (Gibco), 1mM EDTA (Ethylenediaminetetraacetic acid, Invitrogen), 80mM KCl (Sigma Aldrich), 0.3% NP40 (Sigma Aldrich), 0.3% Tween (Sigma Aldrich) and

0.5mg/ml proteinase K (Qiagen). Embryos were incubated at 55ºC with intermittent vortexing until samples were disrupted. Typically this occurred within 90 minutes in embryos already processed for IHC or up to three hours otherwise. Digestion was followed by 15 minutes at 95ºC to inactivate the reaction and digests were then stored at -20ºC.

A PCR to amplify a 440bp region around the target sequence was performed on these digests using Amplitaq Gold DNA polymerase (Applied Biosciences). The forward primer sequence targeted a sequence upstream from the *hacd1* gene: GCATAACTTAATGTGGGGGA and the reverse primer sequence targeted intron 1: AAAAGCTTCAGTACAAGCCA.

Figure 5.2: Primer binding sites around exon 1 of the zebrafish *hacd1* gene.
Forward primer bound to a section of sequence upstream from the *hacd1* gene and this section is denoted by lower case letters and the end of exon 1 is indicated by a black line: the reverse primer bound to a section within intron 1. Guide RNA sequence, start codon and PAM sequence are also annotated for context.

Each 50µl reaction contained: 2% DNA, 0.25µM forward and reverse primers (Invitrogen Custom Oligonucleotides), 0.25mM dNTPs (Fisher Scientific), 1 x PCR buffer II, 2.5mM MgCl2 and 0.025U/µl Taq DNA polymerase (Applied Biosciences). Reactions were run for 35 cycles of: 95ºC for five minutes (initial denaturing) followed by 35 cycles of 94ºC for 30s (denaturing), 55ºC for 30s annealing and 72ºC for 30s extension and a final extension step of 72ºC for 7 minutes. Products were divided and 10µl with 1X BlueJuice loading dye (Invitrogen) was run on a 1.5% agarose gels with GelRed nucleic stain (Cambridge Biosciences) to visualise the *hacd1* gene and confirm DNA was present to clone.

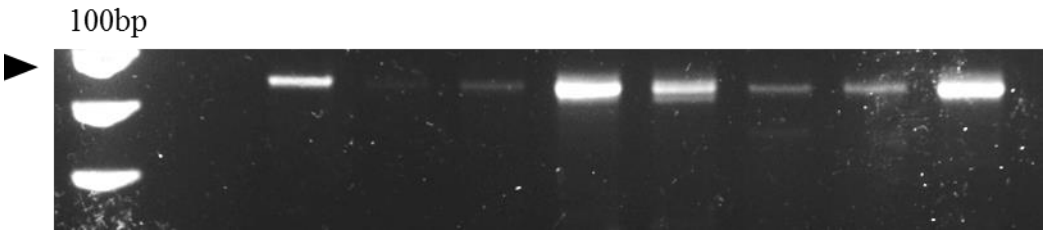

Figure 5.3: Example agarose gel from PCR on Cas9 guide injected embryos, digested using lysis buffer.
Left hand lane shows the 100bp ladder with the 500bp band annotated by a black arrow. All bands in other lanes represent *hacd1* DNA that has been successfully amplified by the PCR – with some lanes representing more successful PCRs than others.

The remainder of the PCR product was purified for cloning using a QIAquick PCR purification kit (Qiagen, catalogue number 28104) according to the datasheet. PCR product was then cloned into the pCR2.1-TOPO vector using a TOPO TA kit (Thermo Fisher) in accordance with the datasheet. Briefly, 4µl of the purified product was incubated with 1µl vector and 1µl salt solution for 20 minutes at room temperature before transferring to ice. Competent E.coli cells (TOP10, Invitrogen) were then thawed and ligation mixture was added before incubating again on ice for 20-30 minutes. Competent cells were then heat shocked for 30 seconds at 42°C in order to take up ligated vector then transferred back to ice before 250µl pre-warmed SOC medium (Sigma Aldrich) was added and cells were shaken for one hour at 37°C. Cell mixture was plated up on LB agar (Sigma Aldrich) plates containing 100µg/ml ampicillin (Sigma Aldrich) overnight to allow colonies to grow. Colonies formed were then selected and grown in LB broth (Sigma Aldrich) containing 100µg/ml ampicillin before plasmids were extracted via minipreparation (QIAprep Miniprep kit, Qiagen, catalogue number 27104) and submitted for external sequencing (GATC). Sequencing was analysed using CLC workbench software (Qiagen).

5.2.5. Immunohistochemistry

Phenotypically abnormal F_0 and wildtype embryos were fixed with 4% paraformaldehyde (PFA) and then dehydrated with graded methanols and stored at -20°C. Embryos for staining were thawed to room temperature and rehydrated with PBS (Sigma Aldrich) and 0.1% Tween-20 (Sigma Aldrich) (PBTw) before de-pigmentation using a bleach solution (0.5x SSC (Sigma Aldrich), 1% H_2O_2 (Sigma Aldrich), 5% formamide (Sigma Aldrich) and 0.1% Tween-20 in PBS). Bleaching was performed for 10-25 minutes until pigment was removed from the tails to avoid damaging the muscle and then embryos were transferred into PBTw before washing with PBS with 0.8% Triton X (Sigma Aldrich) (PBT), a detergent.

Following the bleaching protocol, embryos were then trypsinised on ice with 0.25% trypsin in PBT for four minutes. While still incubated on ice, embryos were washed twice for five

minutes with PBT before incubating in block solution (PBT with 1% DMSO and 10% goat serum) for one hour at room temperature. Embryos were then incubated with the primary antibody in block solution overnight at 4ºC (see Table 5.1 for concentrations). Embryos were then rinsed twice in PBT and washed for four x 30 minutes with PBT, blocked for an hour in PBT with a block solution containing a lower concentration of goat serum: 1% DMSO and 1% goat serum. Samples were then incubated again at 4ºC overnight with secondary antibody in this secondary block solution (1:200 concentration, Alexafluor 488). Following secondary antibody incubation embryos were rinsed twice in PBT before four x 15-minute PBT washes and incubated with Hoechst (Thermo Fisher) at a concentration of 1mg/ml for one hour. They were then rinsed twice and washed for two x 10 minutes in PBS before being mounted in soft set fluorescent mountant (Vectashield, Vector Laboratories) for imaging to allow embryos to then be retrieved for digestion.

Whole embryos were imaged in wide-field view using a Nikon TE2000 microscope. For fluorescent confocal microscopy a Nikon Eclipse Ti (Nikon) was used along with the Nikon EZ-CI software (Nikon). Levels for the offset and gain were chosen after imaging wild type embryos.

Table 5.1: Table of antibodies used for immunohistochemistry in this chapter.

Primary Antibody	Type	Concentration	Source & Catalogue Number
RYR1	Mouse monoclonal IgG1	1:100	Abcam, ab2868
MF20	Mouse monoclonal IgG2b (supernatant)	1:10	DSHB, ab2147781
Pax7	Mouse monoclonal IgG1 (supernatant)	1:3	DSHB, ab528428

5.3. Results

5.3.1. Evaluating the developing lipidome in wildtype embryonic zebrafish

Studies were performed to determine the optimal sample size and technique for ^{1}H-NMR lipidomic analysis of embryonic zebrafish and to establish the normal lipidomic changes in developing zebrafish.

5.3.2. Increasing sample size increases signal: noise ratio for lipidomic analysis of 72hpf zebrafish embryos by ^{1}H-NMR

To optimise the technique of extraction and lipidomic analysis from zebrafish embryos sample sizes of 1, 2, 5 and 10 embryos were evaluated at 3dpf. Figure 5.4a shows raw spectra of all experimental samples (n=3 per group) which clearly show an increase in peak intensity in the larger sized samples. Figure 5b shows signal: noise analysis from these spectra and the R^2 value (0.998) shows a highly positive correlation between this and increasing number of embryos per sample.

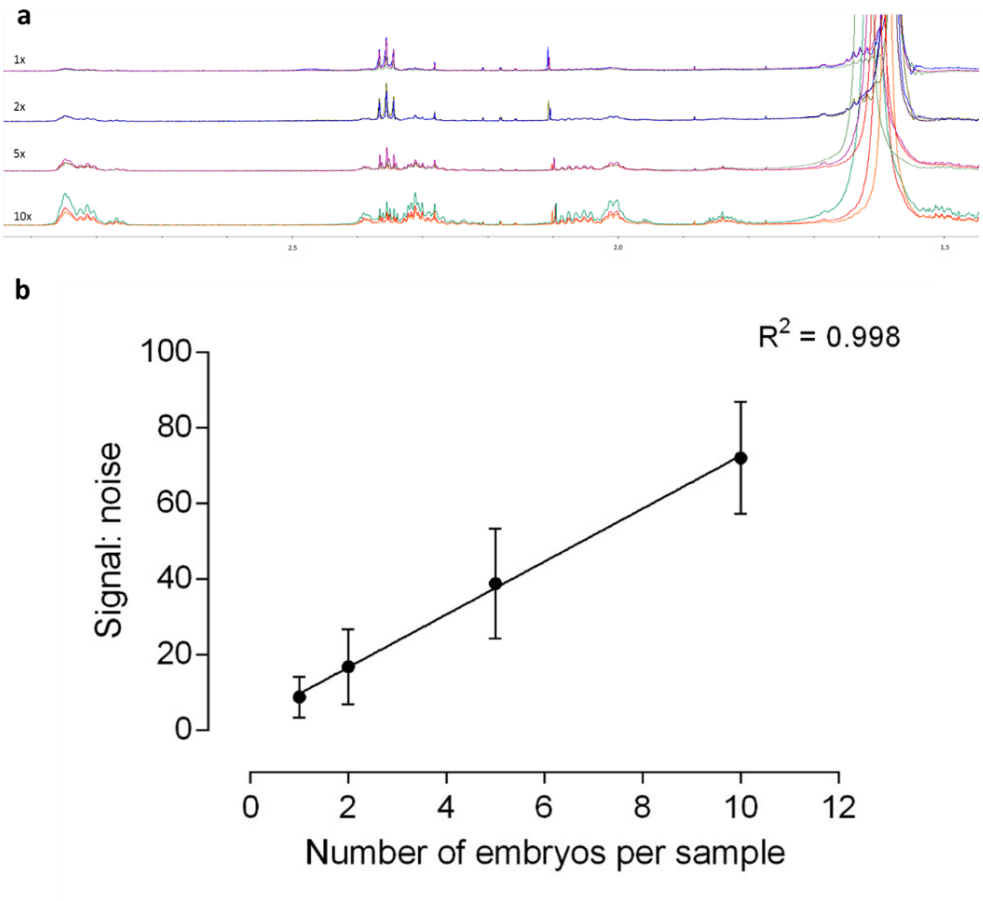

Figure 5.4: Signal intensity in samples of increasing embryo number (n=3).
(a) Output from Topspin 3.1. software displaying all signals from varying sample sizes analysed. (b) Signal: noise ratio analysis reported a positive correlation between the two variables (R^2=0.998). Samples were not normalised here in order to determine effects of sample size.

Multivariate analysis (Figure 5.5) showed that groups of different numbers of embryos per sample cluster separately almost completely from each other. Correlation using heat map analysis in Figure 5.5b shows samples from 10x embryo group clustered together whereas for smaller sizes there was more variability and they did not cluster together. These analyses determined that a sample size of 10 embryos provides more intense and therefore more informative peaks in a spectra and more consistency therefore this was used for subsequent experiments.

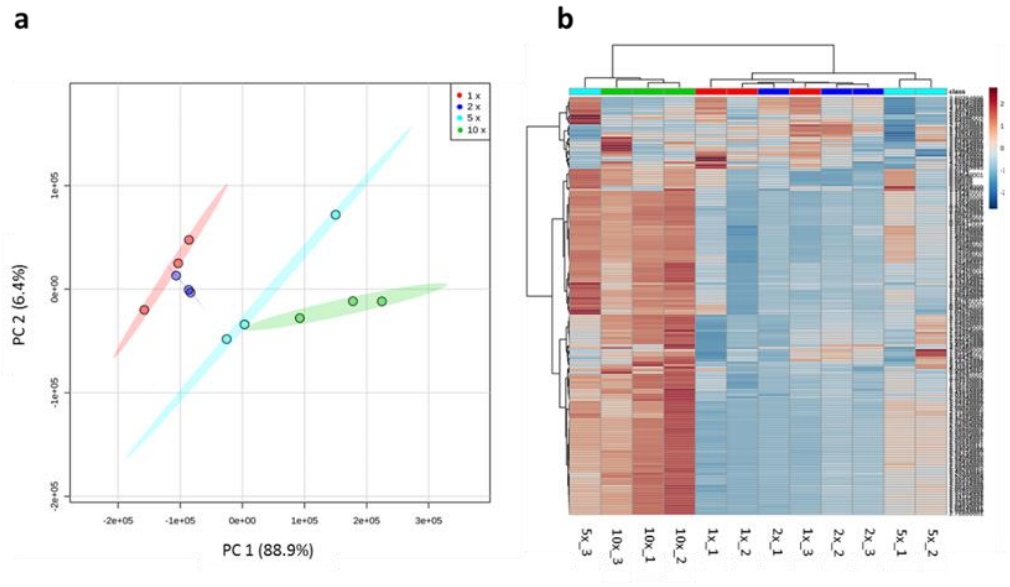

Figure 5.5: Multivariate analysis of increasing the number of embryos analysed per sample size. 1x embryo is represented by a red colour, 2x by dark blue, 5x by light blue and the 10x group by a green colour (a & b). (a) PCA scores plot of all four groups which all cluster separately, shaded region indicates 95% confidence region. (b) Heat map also showing clustering in which samples from the 10x group segregate together and samples in other groups also partially cluster. Samples were not normalised to determine effects of sample size.

5.3.2.1. Chorions do not affect the lipidome of zebrafish embryos

Embryos hatch from their chorions between 2-3 days post fertilisation (dpf) and this can be delayed in mutants with poor motility. Over the developmental time course studied chorions would have been variably present: on all embryos at 1dpf, most at 2dpf and a few at 3dpf. Therefore, to determine if chorions should be removed prior to analysis (a time consuming task manually), we conducted preliminary analyses to determine what effect the presence of chorions had upon the lipidome. Cluster analysis (Figure 5.6) of 1dpf embryos both with and without the chorions showed there was little separation between the two groups and a greater variation was seen in-between samples with chorions removed (Figure 5.6a). The heat map shown in Figure 5.6b displayed no clustering of groups and was unable to distinguish between groups. It was therefore concluded that removal of chorions was not required for this study and so these were not removed in any subsequent experiments.

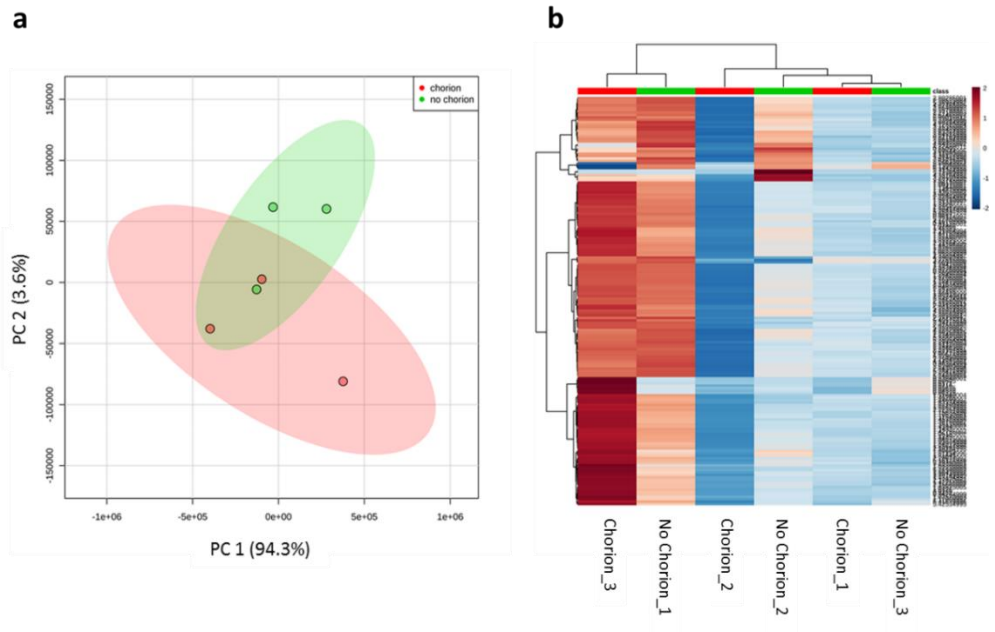

Figure 5.6: ^{1}H-NMR lipidomic profiles of 1 day post fertilisation (dpf) embryos with (red samples) and without chorions (green samples) present (n=3).
(a) Unsupervised PCA scores plot of 1dpf embryos with and without chorions present shows overlaps between groups. Shaded areas represent 95% confidence region (b) Heat map analysis of samples showed that samples within groups do not cluster together. Samples were normalised to the methyl peak (CH_3).

5.3.2.2. Lipidomic changes during embryo development

These conditions (groups of ten embryos and not dechorionated) were then applied to analyse the lipidome in zebrafish embryos from 1-3dpf. These time point were selected based on onset of HACD1 expression and myogenic differentiation from myoblasts present at 1dpf to mature myotubes seen in 3dpf embryos.

Initially the entire data set was analysed in a multivariate approach to determine, at the global level, what effect the development of the embryos had on the lipidome. Figure 5.7a displays a PCA scores plot of all three ages with 1 and 2dpf overlapping and 3dpf clustering almost separately from the earlier ages. When using a more supervised analysis; PLS-DA (Figure 5.7b) that allows for greater discrimination between groups, the groups separated out completely reporting three discrete groups. This analysis is normally used for analysis of two groups however the PLS-DA scores were very acceptable: R^2=0.98 and Q^2=0.72 suggesting this analysis appropriate and that samples dependent upon age are discrete from one another in regards to their lipidome. Figure 5.7c shows heat map analysis of all samples with the three 3dpf samples grouped together and samples from 1 and 2dpf were unable to be separated out by dpf. Blue colours within the heat map indicate relatively low intensities for peaks compared to the peak average and red indicates higher relative intensities and overall there were more blue boxes representing peaks within the samples for 3dpf suggesting lower lipid content in

these samples. There were some lipids that appeared to be more abundant in the 3dpf samples.

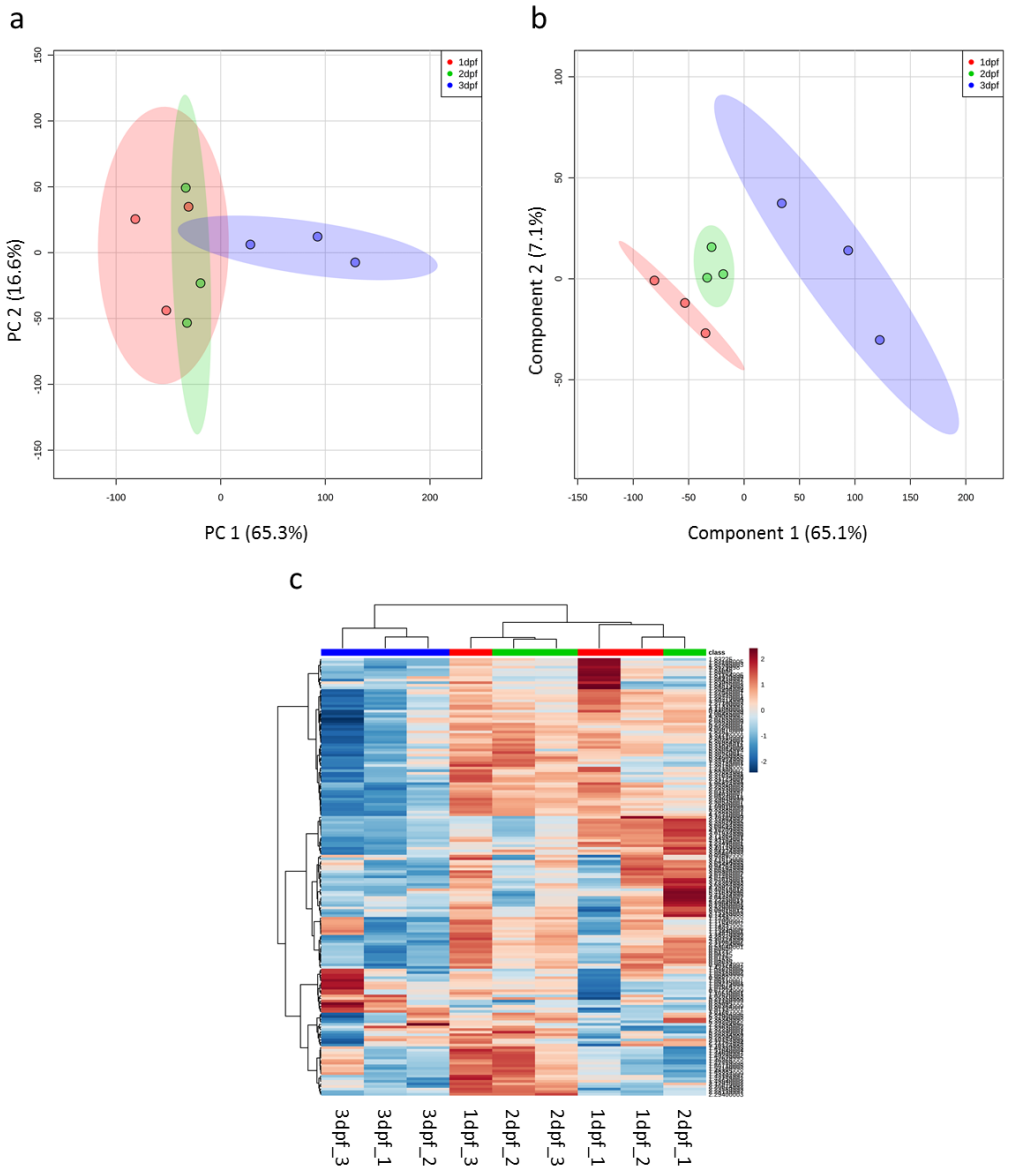

Figure 5.7: Cluster analysis of embryonic zebrafish lipidome over the developmental time course at ages 1, 2 and 3 days post fertilisation (dpf), red colours represent 1dpf.
Blue represent 2dpf and green represents 3dpf. (a) Unsupervised PCA scores plot displaying some overlap between groups. (b) Supervised multivariate PLS-DA plot displaying clear discrete groups dependent upon age of embryo (R^2=0.98 and Q^2=0.72) and for clarity only 2 components from a three component model are shown. Shaded areas represent 95% confidence regions (a & b). (c) Heat map of developing embryos; 3dpf embryos cluster together in heat map whereas the clustering was less discrete with 1 and 2dpf embryos. Samples were normalised to the methyl (CH_3) peak.

As the literature (Blondelle *et al.*, 2015; Briolay *et al.*, 2013) and previous work in Chapter 4 show the level of saturation within fatty acids should decrease during muscle cell differentiation it was hypothesised that the same change would occur in zebrafish myoblasts as they developed. Whole embryos from 1-3dpf were evaluated and saturation analysis (Figure 5.8) showed the relative abundance of different hydrocarbon saturation levels: saturated bonds

(HC-CH), unsaturated bonds (HC=CH) found in both mono- and polyunsaturated fatty acids and levels of PUFA (HC=CH-CH_2-CH=CH). At 1dpf the levels of saturated bonds were higher than unsaturated bonds in both MUFA and PUFA. At 2dpf the proportions of all carbon bond saturations were similar and then by 3dpf the relative abundance of saturated bonds decreased and became lower than the relative abundance of unsaturated bonds. Two-way ANOVA analysis reported the effect of age of embryos on levels of saturation was significant (p<0.0001) and the interaction between both age of embryo and bond saturation was also significant (p=0.0056).

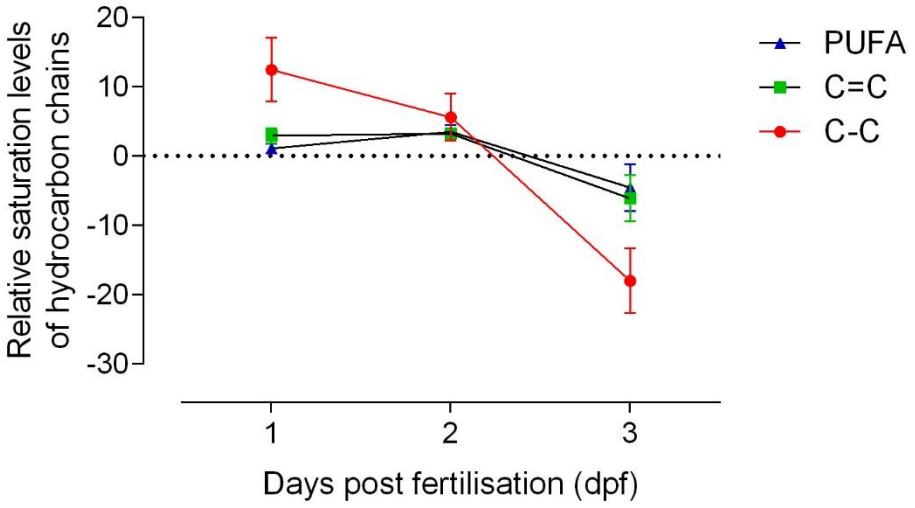

Figure 5.8: Relative abundances of hydrocarbon saturation over developing embryos from 1-3 days post fertilisation (dpf).
C-C represents single carbon bonds and therefore a saturated bond, C=C represents double bonds found in all unsaturated fatty acids and poly unsaturated fatty acids (PUFA) are those with more than one C=C double bond. All levels of saturation decrease over development with relative levels of saturated bonds being the most abundant at 1dpf and dropping to the least abundant by 3dpf. Two-way ANOVA results signify the age of embryos has a significant effect on saturation levels (p<0.0001) and the interaction between age and groups was also significant (p=0.0056). Samples were normalised to the methyl (CH_3) peak.

Lipid class head groups were then quantified over the course of embryonic development from 1-3dpf as previously investigated in muscle cells (Chapter 4).

Figure 5.9 shows the relative abundance of LPC, PC, FC, TAG, GPLs and CE. LPC decreases over myotube differentiation in murine cells (Blondelle *et al*., 2015; Briolay *et al*., 2013; and Chapter 4); the relative abundance of LPC in whole embryos had a reducing trend over development and there was no significant difference. PC levels significantly decreased (ANOVA, p=0.0230) over embryonic development. FC levels are relatively unchanged over development, levels of which were seen to decrease in C2C12 cells. TAG was not studied in C2C12 cells due to undefined roles within muscle however as they have been previously

reported to be highly abundant with embryonic zebrafish yolk sacs (Fraher *et al*., 2016) and to decrease over embryogenesis, TAG was therefore analysed within our samples and also saw its abundance decrease significantly over development (ANOVA, p=0.0406). GPL levels changed in an opposite manner and levels of GPL had a trending increase in abundance over development. CE levels were also not studied in muscle cells as cholesterol is only present in muscle as free cholesterol and not the esterified molecule (CE). CE has been reported to be the most abundant lipid within zebrafish embryo yolk sacs (Fraher *et al*., 2016) and CE was found to decrease over embryonic development (ANOVA, p=0.0362).

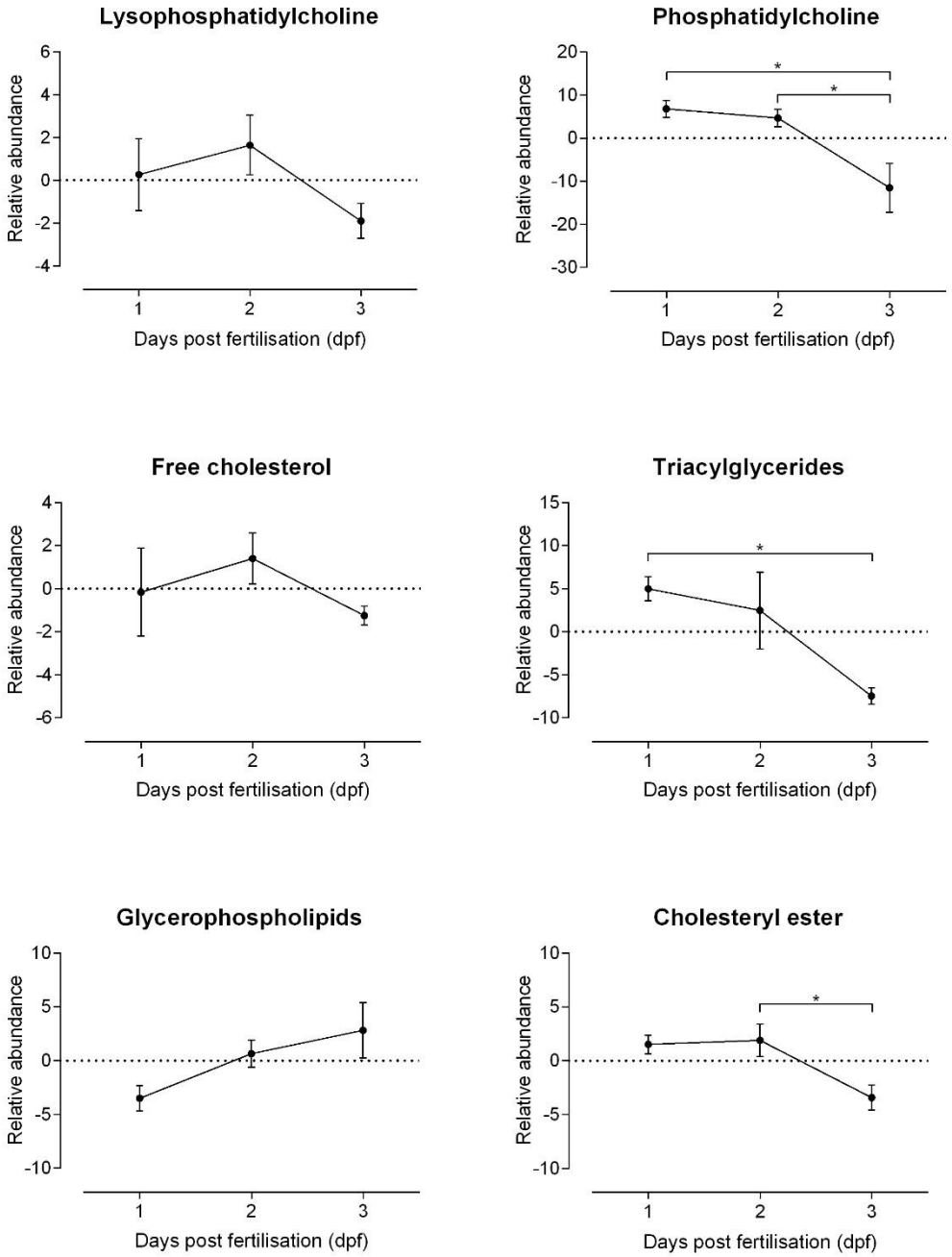

Figure 5.9: Relative abundance of lipid classes over developing embryos from the age of 1 day post fertilisation (dpf) to 3dpf.

LPC = lysophosphatidylcholine, PC = phosphatidylcholine, FC = free cholesterol, TAG = triacylglyceride, GPL = glycerophospholipids and CE = cholesteryl ester. ANOVA tests performed to assess significance of findings. LPC abundance increases at 2dpf before decreasing at 3dpf. PC abundance significantly decreases over development (p=0.0230). FC increases at 2dpf before decreasing between 2dpf and 3dpf embryos. TAG significantly decreases over development (p=0.0406). GPL abundance increases over development and CE decreases significantly overall between 1 and 3dpf (p=0.0362). Post-hoc Tukey multiple comparison tests are annotated on graphs by asterisk, defined in Section 5.2.2 and samples were normalised to the methyl (CH_3) peak.

5.3.3. Phenotypic evaluation of CRISPR/Cas9 injected zebrafish embryos

Embryos were observed during development following injection with guide RNA and Cas9 protein and evaluated at 72hpf. Injected embryos presented with a spectrum of phenotypes due to the mosaic nature of the CRISPR editing in F_0 embryos and so the classification system was created as a guide for the severity of the embryos phenotype and not a definitive classification. Phenotypic classification was evaluated as in Figure 5.10 and Figure 5.11. Embryos were categorised as phenotypically normal, mild, moderate or severe based on their live phenotype and abnormal embryos were selected for further analysis.

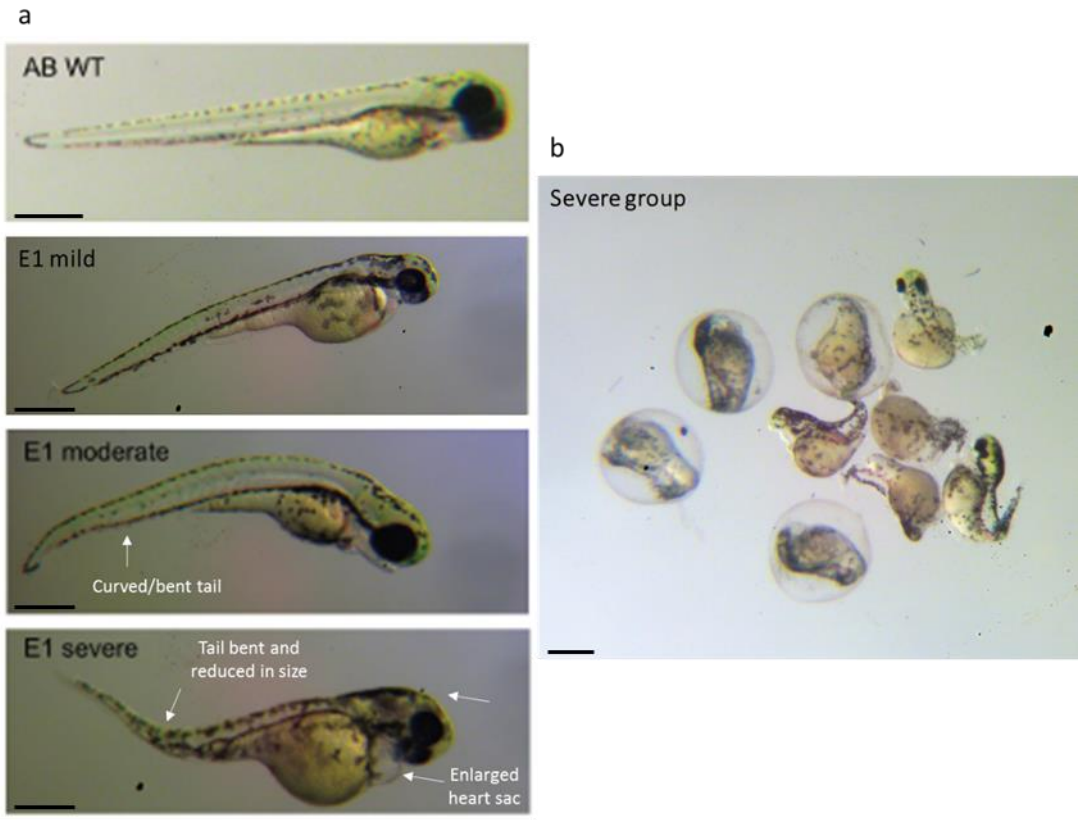

Figure 5.10: Phenotype of Cas9/guide injected embryos at 72hpf.
(a) Example embryos for wildtype, mild, moderate and severe phenotypes, 'E1' indicates the first set of embryos assessed. Mild embryos may present with either normal phenotypes as seen above, but they have no motility when assessed. Moderate embryos might exhibit a curved and bent tail/spine as seen above. Severe embryo in figure exhibits malformed head, enlarged heart sac, enlarged yolk sac and a bent tail which was visibly thinner. (b) A proportion of embryos exhibited very severe generalised defects and developmental abnormalities, including absence of normal body structure – for example the eyes, and severely underdeveloped tails. These phenotypes are unexpected and may be due to the injection toxicity or manual process damaging the yolk sac and were therefore not analysed in this thesis. Scale bars represent 0.5cm.

To assess skeletal muscle function in injected embryos a touch-evoked swim test was performed. Wild type embryos swim quickly away when they are touched by an external stimulus as they have 'normal' muscle contraction and function. Figure 5.11 shows the responses of a wild type embryo along with two injected embryos of moderate phenotype that

exhibited reduced and absent motility. The embryos with reduced motility had weak twitches of the tail and showed some movement in response to the stimulus yet they never moved out the field of view in the 10 second recording. The embryos with absent motility simply do not move at all in response to being touched. These phenotypes are both represented in Figure 5.11.

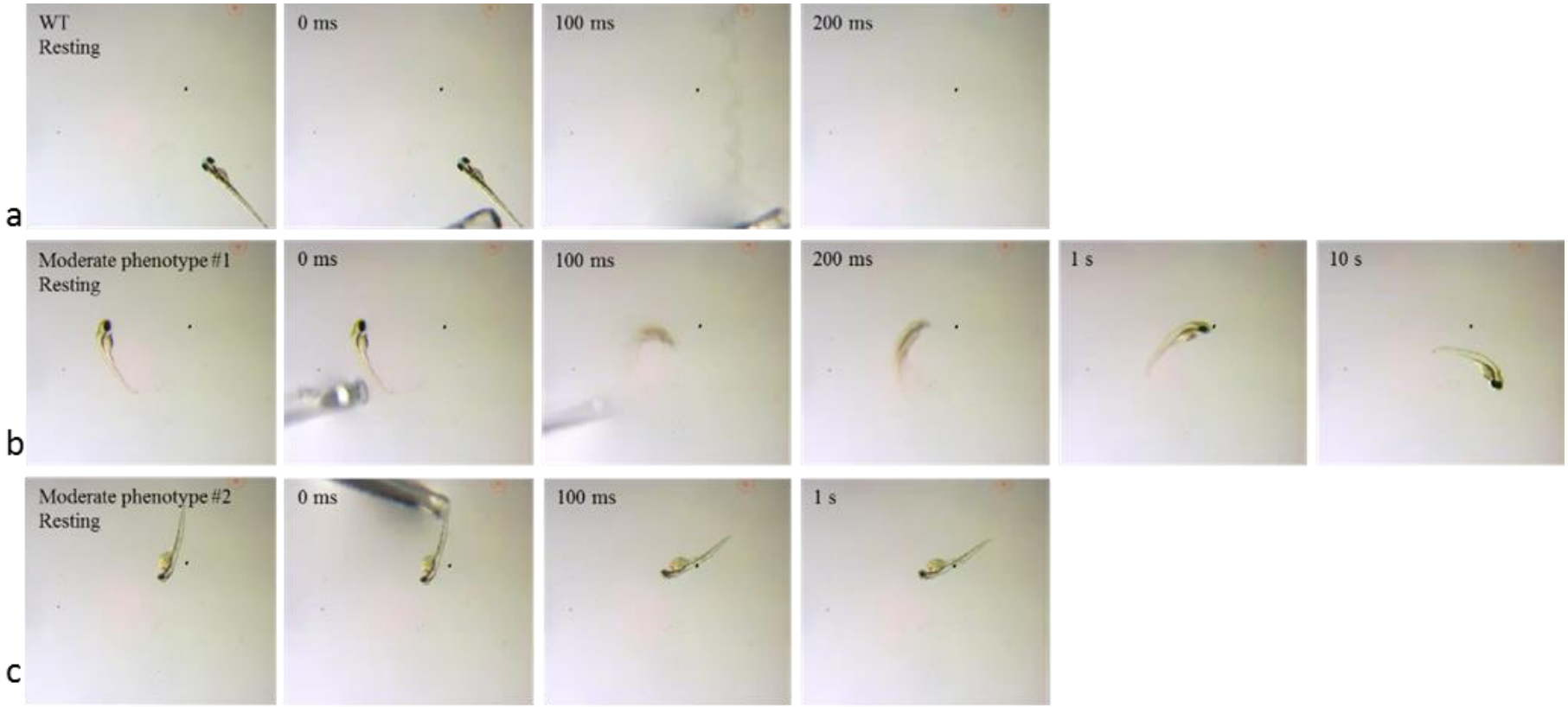

Figure 5.11: Cas9/guide injected embryos (72 hours post fertilisation, hpf) had different levels of motor function as tested by touch evoked swim responses.
(a) row shows the response from wild type embryos that immediately swam away in response to touch. (b) row shows an embryo classified as moderate CRISPR injected phenotype (#1) in which we saw poor movement of embryo. (c) row shows another moderate affected *hacd1*-mutant embryo (#2) which does not move at all in response to touch.

Two batches of injections provided 82 Cas9/guide injected embryos of which 45 (55%) were of normal phenotype, 27 (33%) were mild and moderate and 10 (12%) were severe. The mild and moderate embryos were split into two batches and fixed for IHC to examine finer muscle structure, and sequencing of the *hacd1* gene.

Table 5.2: Category classification for Cas9/guide injected zebrafish embryos.

Embryo Classification	Phenotype
Mild	• Slight/no abnormality in tail morphology • Touch evoked swim response poor/no swim response
Moderate	• Abnormal tail morphology, truncated somites, curvature • May/may not have abnormal heart or pericardial sac • May/may not have mild abnormalities of the eyes • Touch evoked swim response poor/no swim response
Severe	• Very abnormal tail morphology • Abnormal heart or pericardial sac • May/may not have mild abnormalities of the eyes • Abnormalities of other organs including eyes, head • Touch evoked swim response poor/no swim response

5.3.3.1. Muscle evaluation within phenotypically abnormal embryos

Immunohistochemistry was first trialled on wildtype embryonic zebrafish at 72hpf to evaluate efficiency and specificity of primary and secondary antibodies. Antibodies (all represented in green due to the secondary 488-Alexafluor bound) for MF20 (myosin), RYR1 and Pax7 (the transcription factor found in satellite cells) were tested alongside DAPI (seen in blue) (Figure 5.12). Pax7 was present within the nuclei of eye, brain and the myotome boundaries, with a number of Pax7 positive nuclei present within the myotomes. MF20 staining was present with the developing muscles of the head and the myofibres of the tail. RYR1 staining was also present with the tail myofibres. Green stain was absent in embryos incubated without primary antibody – therefore the staining of Pax7, MF20 and RYR1 was specific for the target proteins.

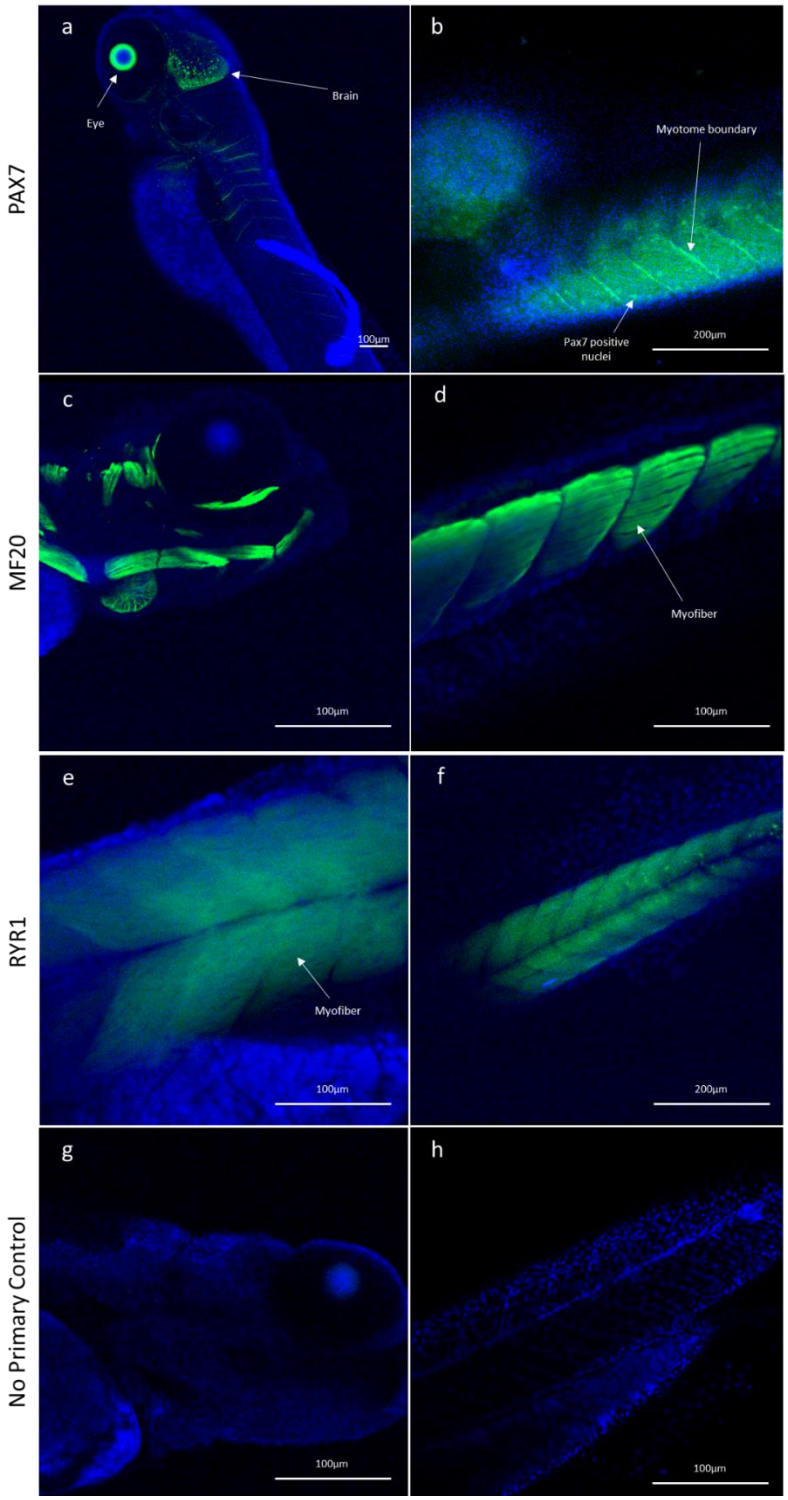

Figure 5.12: Test immunohistochemistry on 72 hours post fertilisation (hpf) wildtype embryos to assess muscle structure.

Images were taken using the same settings for all stains. (a and b) Pax7 staining within the developing eye, brain and within the satellite cells of the tail muscle and between myotome boundaries. (c) MF20 can be seen within the muscles in the head including mandibular and hyoid muscle. (d) MF20 also seen within the myofibres of the tail. (e and f) RYR1 staining was located to the myofibres within the muscle tail. (g and h) represent the no primary control for these stains showing no non-specific staining of the anti-mouse secondary antibody.

Wild type embryos have a long straight tail and clear myotome definition and sarcomeric striations visible on phase contrast imaging. MF20 staining in the wild type embryos clear and even myotome definition and striations are visible (Figure 5.13). The Cas9/guide injected embryos presented with uneven myotomes, myofibre disorganisation, shortened and irregular somites either side of the neural tube (Figure 5.13).

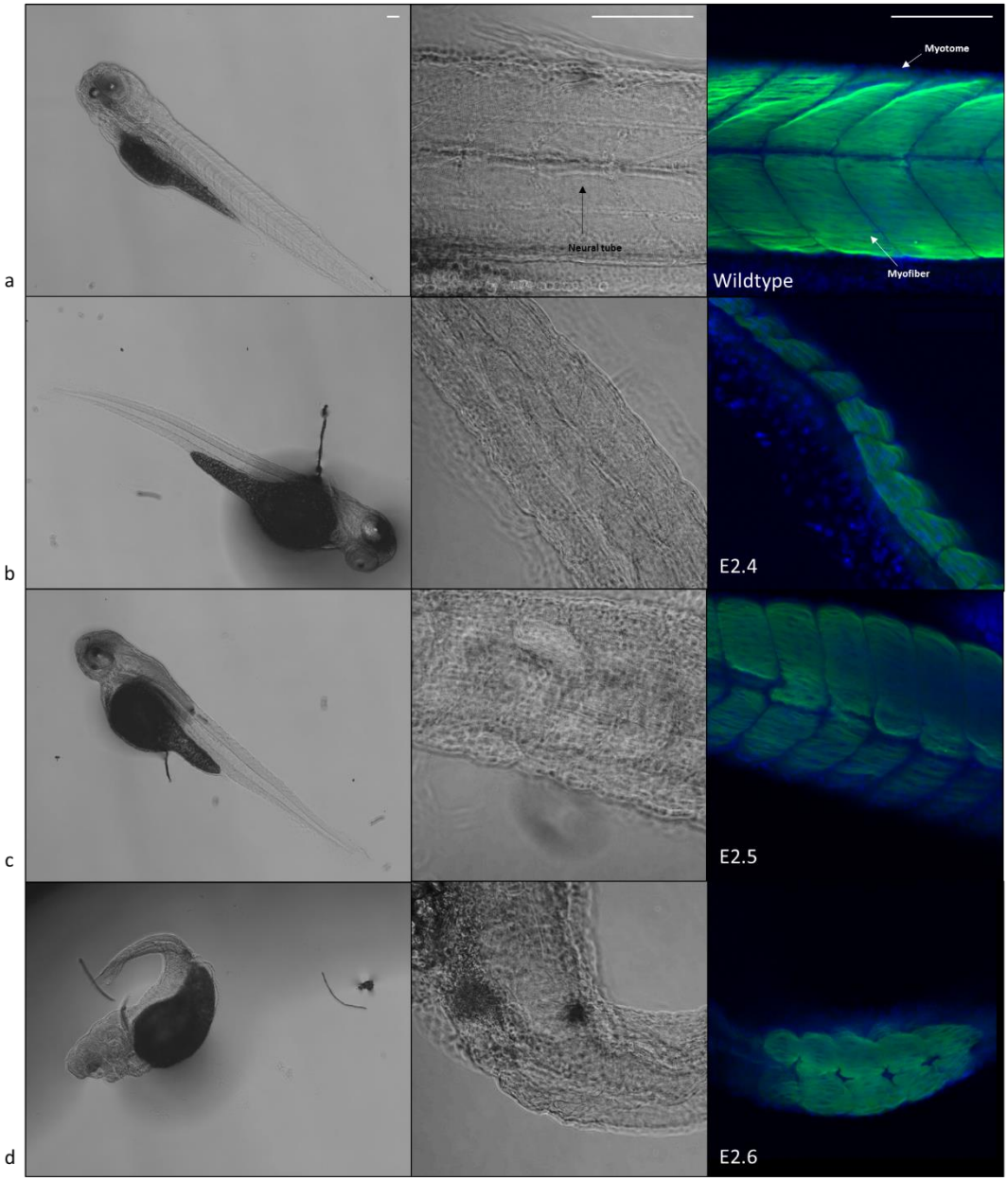

Figure 5.13: Cas9/guide injected embryos at 3 days post fertilisation (dpf) have different muscle phenotype.

Left images are phase contrast at 4x magnification and images in the middle are at 40x. Images on the right correspond to embryos to images in the same row and display sections of the tail from MF20 and dapi stained whole embryos. Top panel (a) shows a wild type embryo with normal phenotype with the three embryos below (b-d, E2.4, E2.5 and E2.6) displaying differing affected phenotypes. Scale bars on top row of panel represent 100µm.

Staining of RYR1 was performed in the phenotypically abnormal zebrafish embryos to evaluate triadic SR within the embryo muscle and assess if RYR1 staining was altered (Figure 5.14). Myofibre disorganisation was also evident from RYR1 staining and embryos presented varying levels of abnormalities in RYR1 staining particularly loss of the normal regular staining pattern. RYR1 was patchy and disorganised within all injected embryos and the normal striated pattern was lost or unclear in Cas9/guide injected embryos. Also, the gain had to be increased to image the RYR1 staining within injected embryos suggesting RYR1 protein might be also be reduced.

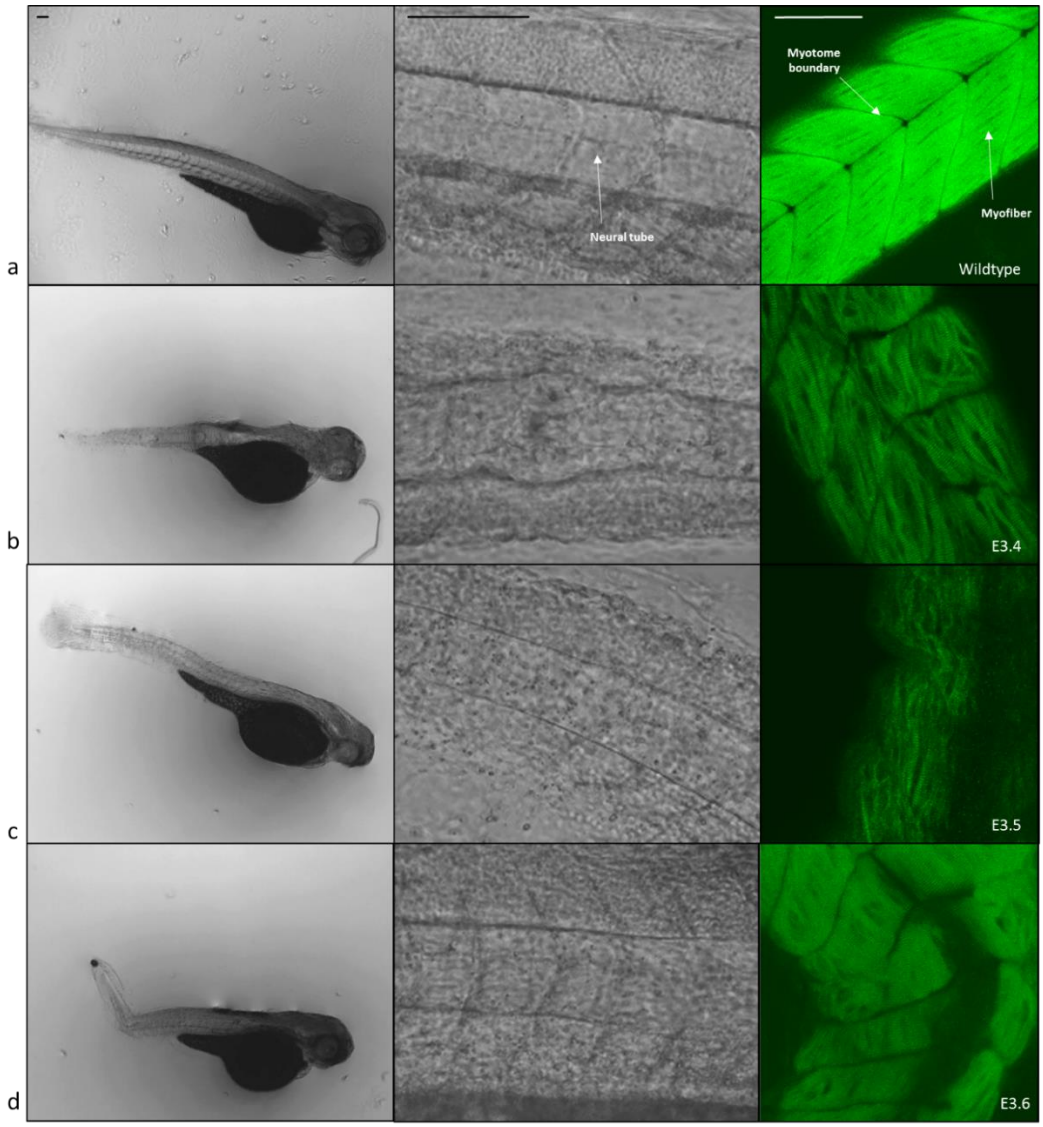

Figure 5.14: Cas9/guide injected embryos at 3 days post fertilisation (dpf) have altered phenotype and muscle structure.

Left images are phase contrast at 4x magnification with 40x images in the middle. Right images are corresponding embryos in their row and display the tail section of RYR1 stained whole embryos. Top panel shows a wild type embryo with normal phenotype with the three embryos below displaying affected phenotypes (E3.4-6). Microscope gain was turned up higher to image injected embryos and, scale bars represent 100µm.

5.3.3.2. Mutation analysis of F_0 embryos

10 phenotypically abnormal embryos (five mild, three moderate and two severe) were digested for amplification and cloning of the *hacd1* exon 1 for mutation analysis with 4 clones from each embryo sequenced. Mutations that were out of frame or affected the start codon were considered likely to affect functional transcripts and therefore designated disease causing. Of the mildly affected embryos: two had 1/4 clones, one had 3/4 and the other two had 4/4 clones with likely disease-causing mutations. For the moderate embryos one had 2/4 clones and two 4/4 clones with likely disease-causing mutations. Both severely affected embryos had 4/4 clones with likely disease-causing mutations. Most mutations were small deletions of which a 7bp deletion was the most common seen in 16 clones.

Stained embryos were digested following RYR1-IHC and it was determined as possible to perform PCR and cloning of *hacd1* after fixation and processing. After imaging, RYR1-stained phenotypically abnormal embryos were analysed to confirm the presence of *hacd1* mutations. Embryo E3.5 with markedly abnormal RYR1 staining was evaluated in more detail. All sequenced clones were abnormal and 11/12 mutations affected the reading frame and/or start codon, the most common mutation (7/12 clones) was the 7bp deletion shown in Figure 5.16.

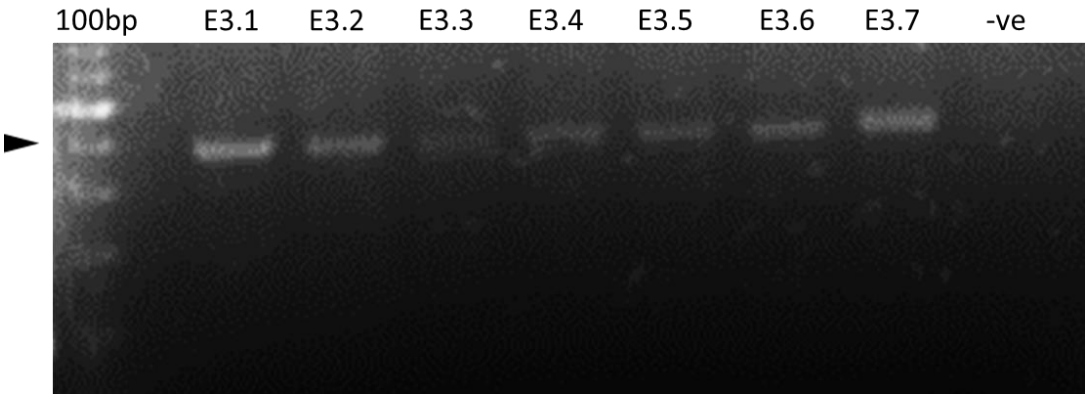

Figure 5.15: PCR of RYR1 stained Cas9/guide injected embryos from Figure 5.14.
Agarose gel displays bands for each embryo indicating successful amplification of the *hacd1* gDNA via PCR and that sequencing previously stained embryos would be possible. Samples were run against a 100bp ladder black arrow indicates the 500bp band.

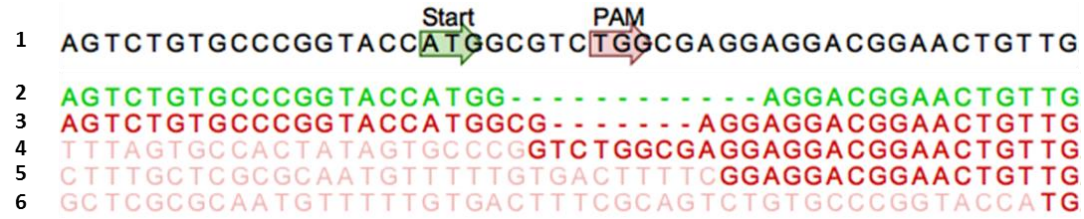

Figure 5.16: Mutations seen within the *hacd1* gene from Cas9/guide injected zebrafish embryos.
Line 1 shows the *hacd1* exon 1 sequence with the start codon and PAM sequence annotated. Line 2 shows a clone with a 12bp deletion which would not affect the reading frame and so it represented by a green coloured sequence. Line 3 shows a clone in which the common 7bp deletion has occurred which would cause a frameshift and therefore shown in red – it would likely be a disease causing mutation. Lines 4-5 show larger deletions within the sequence that has led to a removal of the start codon, the *hacd1* sequence, likely disease causing, and is therefore represented in red here also, with pre-*hacd1* sequence in pink.

5.4. Discussion

Zebrafish models targeting other CNM-associated genes have contributed immensely to our understanding of CNM pathogenesis (Dowling *et al*., 2009; Dowling *et al*., 2010; Gibbs *et al*., 2013a; Sabha *et al*., 2016; Smith *et al*., 2014). The work in this chapter has begun characterising a novel model for *hacd1*-deficiency in zebrafish embryos which could ultimately pave the way for similar advances for HACD1-CNM. Our previous work (Chapter 2) demonstrated that *hacd1* has an expression pattern in zebrafish embryos that corresponds with that of its mammalian homologue: namely that it is the major *hacd* gene expressed in the muscle of developing zebrafish embryos and is strongly upregulated during myogenesis. ^{1}H-NMR lipidomics was performed in differentiating murine myoblasts which documented changes in hydrocarbon chain saturation levels over differentiation and differences in a number of lipid classes that occurred following the onset of *hacd1* expression: there were also lipidomic differences between control and *Hacd1*-kd myoblasts (Chapters 3 and 4). Here lipidomic changes in wildtype embryos were evaluated and a protocol was optimised for future use in *hacd1*-mutant embryos. The phenotype was evaluated in F_0 Cas9/guide injected zebrafish embryos and those with abnormal phenotype were also found to have disrupted and disorganised muscle structure when examined via IHC. Sequencing found a variety of mutations present as a result of the CRISPR/Cas9 genome editing of which a 7bp deletion affecting the reading frame was the most common.

5.4.1. Embryonic zebrafish lipidome can be studied via ^{1}H-NMR, however the presence of the yolk sac may hide changes occurring elsewhere within the embryo

The first stage of optimisation was to determine the number of embryos required to obtain informative spectra. The signal: noise ratio improved linearly with increased embryo numbers within samples up to 10 (R^2=0.998) therefore further samples with larger numbers should be evaluated to see when the increase in number of embryos ceases to add value to the results. Multivariate analyses showed groups of different embryos to be discrete from one another suggesting spectra were different dependent on sample size. These results indicate that including more embryos per sample to be extracted give improved spectra from which more information can be obtained. Wild type embryos are produced in large quantities therefore larger sample sizes can be included (Guyon *et al*., 2007). Our current *hacd1*-mutant model in F_0 embryos produces a heterogeneous population with variable phenotypes and mutations therefore it may be difficult to obtain sufficient sample sizes of embryos grouped by phenotype for optimal spectra. Our ultimate aim is to generate a line of zebrafish with a germline mutation

in *hacd1* and in this case it would be feasible to collect the required numbers of embryos that are homozygous for a specific mutation and, hopefully, a more consistent phenotype. To analyse lipids from a single embryo or even specifically the muscle of the tail, a different technique such as matrix-assisted laser desorption/ionisation (MALDI) could be used (Duneas *et al*., 2017).

Wildtype embryonic zebrafish were then optimised for ^{1}H-NMR lipidomics through analysing the lipidome of 1dpf embryos with and without their protective chorions. The chorion is an extraembryonic structure, in that it will not contribute to the developing embryo (Bonsignorio *et al*., 1996). It is proteinaceous (Kim *et al*., 2004) and therefore was thought unlikely to contribute to the lipidome. Nevertheless, as embryos hatch from their chorions between 2 and 3dpf so would therefore be present in younger embryos and not older embryos, and mutations that affect development or motility can delay hatching and so it was necessary to rule the chorions out as a confounding variable. The results suggested that the chorions do not affect the lipidome as multivariate analysis could not separate out the two groups. Variation was actually greater in the sample set that had been dechorionated and this may reflect the additional handling these embryos received, more residual water leftover or the presence of leftover chorion could have contributed to the variation seen. Manual dechorionation is time consuming and the process is performed on live embryos at 1dpf which are fragile and injuries to the embryo or yolk sac could greatly affect results. Therefore, it was concluded that removing chorions from embryos would not improve lipidomic analyses and in fact contribute to more variation and potential error and so was not performed on subsequent embryos. Chorions can also be removed enzymatically using a combination of proteases (Pronase, Sigma Aldrich) (Mandrell *et al*., 2012); this was not evaluated as adding an additional treatment step to the chorionated embryos could introduce additional sources of error and variability to the highly sensitive ^{1}H-NMR technique. One lab group has developed an automatic system of chorion removal using Pronase and robotic equipment, allowing the dechorionation of 1,600 embryos simultaneously – this is a great development for studying embryonic zebrafish (Mandrell *et al*., 2012).

Through analysing the lipidome of embryos aged 1, 2 and 3dpf we were able to conclude that there were distinct differences between ages and demonstrating that the lipid content within the embryos is dynamic over the course of development. Heat map analysis showed that there was relatively less lipid content within the 3dpf embryos and we hypothesised this to be due to decrease in yolk sac size/volume over this time course. The yolk sac is high in lipids and fatty acids which are incorporated into the developing embryos and used as an energy source up to 5dpf when the embryos start to feed (Avdesh *et al*., 2012). As the contents of the yolk sac are absorbed by the embryos and lipids are hydrolysed for energy this may have

contributed to the lipid content decrease seen in this study (Quinlivan & Farber, 2017). The observed decrease in lipid content over 1-3dpf may also be due to extraction technique aswe expect lipids within membranes would be more difficult to extract than those within the yolk sac. Therefore, further work to optimise the extraction protocols for lipids in intracellular organelles may be warranted. A combination of both of these factors is plausible, as lipids incorporate into complex systems such as membranes they may be harder to attain for lipidomic analyses, therefore resulting in what appears to be a decrease in lipid content. Further optimisation of the sonication technique might be required to ensure the full break down of samples.

Saturation levels of fatty acids decreased in differentiating muscle cells (Blondelle *et al*., 2015; Briolay *et al*., 2013) and this was also evident in this thesis in Chapter 4. Therefore, we evaluated this in developing embryos and saw a decrease in both saturated and unsaturated bonds, likely due to the overall decrease in lipid content. The decrease in the saturated bonds was in fact greater, with a higher abundance of saturated bonds relative to unsaturated bonds at 1dpf and lower at 3dpf. These follow the results from this thesis seen in C2C12 cells cannot be attributed solely to muscle as lipids were extracted from whole embryos.

Lipid classes were also analysed and although LPC abundance decreased in differentiating C2C12 cells this was not seen in the zebrafish embryos. The decrease in LPC within cells was seen along with the upregulation of *Hacd1* at the onset of myogenesis (myoblast fusion) (Blondelle *et al.*, 2015) and our previous results showed that *hacd1-fl* starts to be expressed in embryos from 18 hpf and by 1dpf myoblasts fuse and *hacd1-fl* was found to be present within the muscle from ~18hpf therefore it would have been interesting to include a time point at 0 and/or 12 hpf before *hacd1-fl* expression. It is also possible LPC was decreasing in muscle but by analysing the whole embryos we were unable to detect this as changing levels of LPC elsewhere in the embryo are confounding results from muscle. LPC is low within the yolk sac (Fraher *et al*., 2016) and so the potential confounding LPC would be unlikely due to the yolk sac unlike other lipid classes: LPC may be high within other regions of the embryo.

Abundances of PC, TAG and CE were reported to be high within the embryo yolk sac (Fraher *et al*., 2016). Lipidomic results from this study show a significant decrease in PC and TAG which is in line with the study conducted by Fraher *et al*., (2016) and we suggest that since the results match up with their work on yolk sacs that this is indeed due to the yolk sac lipid dynamics and therefore not muscle related. CE is the most abundant lipid class within the yolk sac (Fraher *et al*., 2016) and they reported that CE levels increase within the embryo body after 24hpf. There was a significant decrease in CE between 2 and 3dpf embryos - which could be due to the effect of the yolk sac decreasing in size and lipid content. FC was relatively unchanged over development. FC is essential for normal functioning in cells as it plays an

important role in the biophysics of lipid membranes (Maxfield & van Meer, 2010) and therefore we hypothesise its relative abundance was unchanged over development due to its necessity for cellular functions. The GPL peak, which represents this entire class, was seen to increase within developing embryos between 1 and 3dpf. This overall increase suggests the class is increasing in abundance however of the specific members evaluated LPC was stable and PC decreases. GPLs are a major component of plasma membranes (Blanco, 2017) and as cells divide and differentiate to produce the embryo an increase in GPL would make biological sense. Overall, the results seem to be highly affected by the yolk sac and likely also other areas of the developing embryo body. Therefore for further work to compare control and mutant embryos at 72hpf their tails should be isolated from the rest of the embryo before extracting lipids for ^{1}H-NMR.

A limitation to significant results within the study was the sample size used. This work was undertaken as a pilot study to explore if lipid content in embryos could be studied and so n numbers were small (n=3). Therefore the study likely lacked power and in the case of LPC no significance was found despite the literature (Blondelle *et al*., 2015; Briolay *et al*., 2013), and our findings in Chapter 4 suggesting LPC should significantly decrease in the developing embryos. Another limitation to the developmental lipidomic study were the time points used (1-3dpf). These were selected because over this period myoblasts develop into mature muscle (Kimmel *et al*., 1995), though this provided us with no information on the lipidome of embryos prior to *hacd1* upregulation (~1dpf) and so further work would need to be done to examine the lipid profiles of earlier embryos.

A significant limitation of ^{1}H-NMR in this study was the inability to determine chain length of lipids which is important to evaluate as we would expect the proportion of VLCFA should increase in comparison with shorter FA over embryonic muscle development and that this will be disrupted with *hacd1*-mutants, due to results from Blondelle *et al*., (2015) in which this was seen in the *Hacd1*-kd C2C12 cell line. Because of this, other methods should be employed such as LC-MS or MALDI (Blondelle *et al*., 2015; Yang *et al*., 2016) to gain insight into lengths of fatty acids present over embryogenesis. As whole embryo lipidomics seems to be highly affected by the yolk sac and other anatomy, we hypothesise that the directed MALDI technique on embryo tails will be a possible approach to take forward. LC-MS on pooled embryos or embryo tails would also provide more information regarding chain length and has high sensitivity for low abundant VLCFA (Monroig *et al*., 2010; Yang *et al*., 2016).

Further work could also involve studying HACD1 in the context of the other elongation enzymes, such as ELOVL proteins which have comparable orthologues in zebrafish to that of mammals that have similar expression patterns and functions (Bhandari *et al*., 2016; Monroig *et al*., 2009; Monroig *et al*., 2010). As there is a lack of literature on any ELOVL orthologue

specific to zebrafish embryos, fatty acid assays such as those conducted by Ikeda *et al*., (2008), and utilising yeast (Monroig *et al*., 2009; Monroig *et al*., 2010) to express zebrafish Hacd and Elovl proteins may provide a greater understanding into the functional relationship between the zebrafish Hacd1 and the Elovl enzymes within zebrafish.

5.4.2. CRISPR/Cas9 genome editing produces *hacd1*-mutant F_0 zebrafish embryos with myopathic phenotype

A guide RNA targeting exon 1 had previously been generated and validated by another researcher. My work aimed to evaluate the phenotypically abnormal F_0 embryos in order to characterise their muscle abnormalities in more detail and correlate these with the presence of *hacd1* mutations.

When assessing the muscle structure though IHC, this was found to be affected within the set of Cas9/guide embryos stained for MF20 (sarcomeric myosin) as a spectrum of phenotypes. The fluorescence intensity was subjectively consistent between wildtype and Cas9/guide injected embryos. These embryos presented with myofibres that were disorganised, variable and uneven myotome shape and size and often the striated pattern of the fibres was indistinct. RYR1 stained Cas9/guide embryos as previously discussed, including: loss of visible striations, myofibre disorganisation, shortened somites, irregular myotomes and a decrease in RYR1 fluorescence (gain was increased in order to obtain informative images of muscle structure within the phenotypically abnormal embryos). This decrease in fluorescence could be due to a reduction in RYR1 from a lack of triad membrane development. Molecular quantification through qPCR and western blot could allow quantification of RYR1 in wildtype and mutant embryos to differentiate between disorganisation/mislocalisation and reduced expression and protein levels. Staining embryos with antibodies specific to the DHPR channel (Smith *et al*., 2014) may also be interesting, in that it may provide more information regarding triad formation: a co-stain of both channels would be a good way to look visually at the triad structure and development. Electron microscopy has been previously used on zebrafish embryos to visualise triads (Walmsley, 2013) and so this would also be a useful tool going forward.

Similar myofibre phenotypes were seen in the other CNM zebrafish models. The BIN1-CNM model was reported to have disorganised myofibres, along with mislocalised nuclei (Smith *et al*., 2014). The MTM1-CNM model using morpholinos was documented to have thin myofibres, also with abnormally localised myonuclei; interestingly the MTMR14-CNM zebrafish did not have altered muscle structure (Dowling *et al*., 2009; Dowling *et al*., 2010). ZFNs have also been used to generate *mtm1*-mutants (Sabha *et al*., 2016). This model was found to have triad abnormalities comparable to those seen in human XLMTM as well as

being used to perform drug screens and rescue experiments allowing for the identification of a potential therapeutic agent (Sabha *et al*., 2016). The DNM2-CNM model was documented to have severe myofibre disorganisation (Gibbs *et al*., 2013a) and so this is a common feature of all CNM models: which correlate to the disease phenotype seen in human and canine CNM (Blot *et al*., 2002; Cassandrini *et al*., 2017).

As F_0 embryos generated by CRISPR/Cas9 gene editing are mosaic this provided a spectrum of phenotypes in embryos injected (Mehravar *et al*., 2019). 45% of Cas9/guide injected embryos presented with an abnormal phenotype – categorised on the basis of both morphology and functional muscle testing. Of the current zebrafish CNM models differing levels of abnormal phenotypes were produced (Dowling *et al*., 2009; Dowling *et al*., 2010; Gibbs *et al*., 2013a; Smith *et al*., 2014). Gibbs *et al*., (2013a) used morpholino technology to create two morphants for the two dynamin isoforms discovered within zebrafish (*dnm2* and *dnm2-like*). The morphants for these isoforms produced 93 and 75% morphologically abnormal embryos respectively. Gibbs *et al*., (2013a) tested and quantified function separately using both a touch-evoked method like this study but also by assessing spontaneous twitching in 1dpf embryos; this was seen in embryos from 17-26hpf (Saint-Amant & Drapeua, 1998). They reported only the *dnm2* morphant to have significantly less coiling activity than control embryos and this morphants also presented with the most severe lack of touch-evoked swim response (Gibbs *et al*., 2013a). The XLMTM model by Dowling *et al*., 2009 found the most common phenotype in the *mtm1*-morphants was a thinning of the tail – this was also seen in our HACD1-CNM model. They also reported the spontaneous coiling to be significantly reduced in these morphants (Dowling *et al*., 2009). The *mtm1*-morphants were reported to have a delayed development which stopped them hatching from their chorions (35% hatched) by 60hpf, a time point by which 90% of the control embryos had hatched (Dowling *et al*., 2009). Dowling *et al*., (2010) then looked again at *mtm1* morphants, and also *mtmr14*-morphants. Here they found ~50% of *mtmr14*-morphants were phenotypically abnormal, which was a similar percentage to our findings with *hacd1*-mutants. Dowling *et al*., (2010) also assessed coiling and found the reduction in coiling was dependent upon the area of the gene targeted by the morpholino. The BIN1-CNM model generated by Smith *et al*., (2014) using morpholinos exhibited varying degrees of spine curvature and when measuring chorion hatching found that the amount of embryos hatched by 60hpf was halved in *bin1*-morphants and by 3dpf the morphants also had impaired motility, as tested for by touch-evoked swim response tests.

The studies mentioned quantified the gross morphology and the muscle function tests separately providing the models with clear statistics regarding abnormality of embryos. This was not done in this study as the aim was to identify broadly abnormal embryos to further

investigate with regards to muscle structure and mutations introduced. The separation of these phenotypes could be implemented in this work in the future. These models also measured the hatching of embryos and spontaneous coiling which was not done in this study but could provide a more in-depth analysis of muscle function within the HACD1-CNM model: in particular, the coiling which provides information on function at an earlier stage of development.

Other techniques used within these studies included measuring the birefringence of the embryonic muscle (Smith *et al*., 2014): whereby the ordered muscle of wildtype embryos appears bright (through passing polarised light thorough the embryo) and when muscle becomes disorganised this creates patterns specific to the disorder, in myopathies the high disorganisation is seen by a reduction in this birefringence (Smith *et al*., 2013). Myofibre length was measured (Gibbs *et al*., 2013a), electron microscopy was used to study muscle ultrastructure (Dowling *et al*., 2009; Dowling *et al*., 2010; Smith *et al*., 2014). These models have also been used to functionally assess ECC: Dowling *et al*., (2010) used electrophysiology patch-clamp methods to study the embryos ECC in response to electrical stimulation and Smith *et al*., (2014) used calcium imaging to assess if ECC was disrupted as a secondary pathology of the disrupted triads.

5.4.3. Future work

Further work in evaluating this HACD1-CNM model would include the phenotype chorion hatching to be evaluated, as having mentioned previously in this chapter the presence of the chorion is something to keep in mind with the lipidomic analysis. Calcium imaging and electrophysiological experiments would provide great functional insight. There is also potential to isolate myofibres from zebrafish embryos (Horstick *et al*., 2013) which could then also be used in ECC experiments as well as being used for IHC to assess fibre structure.

The mosaicism within genomes of Cas9/guide embryos reported within our embryos can have both advantages and disadvantages to the model. One potential pitfall of the mosaicism within the embryos is the chance of false-positive genotyping (Mehravar *et al*., 2019). In future studies the head could be removed from the tail section of the embryo to allow genetic analysis of the head and other analysis such as ^{1}H-NMR lipidomics of the tail portion. It must be considered though that these sections of the embryo are likely to have different *hacd1* genetics/mutations due to the mosaic nature of CRISPR/Cas9. Once a line has been generated this would not be of concern however as embryos would no longer no mosaic.

Future work on this study could involve continuing the evaluation of phenotypically abnormal embryos including: expression analysis by qRT-PCR and *in situ* hybridisation and also lipidomic analysis as discussed previously in this chapter. The embryos that do not present as

phenotypically abnormal can be utilised in the creation of a *hacd1*-transgenic zebrafish line: during the study no Home Office licence was in place to do this. Breeding from the phenotypically normal Cas9/guide fish will produce more consistent F_1 progeny than seen in the F_0 embryos with a varied spectrum of phenotypes. Another avenue of research could be to design and direct sgRNA towards the essential amino acids in exon 6 of the *hacd1* gene (Kihara *et al*., 2008; Toscano *et al*., 2017). By mutating these amino acids, the function of these enzymes, and importance of these conserved amino acids could be verified within zebrafish. Rescue experiments should be implemented within the future of this work: including the re-expression of *hacd1* and the addition of VLCFA to look at both genetic and functional rescues.

5.4.4. Conclusions

To conclude, work from this chapter has both optimised a lipidomic method in zebrafish embryos that can be implemented in future studies and evaluated the effects of *hacd1* deficiency in embryonic zebrafish. The ^{1}H-NMR method has proved informative as a first assessment of embryonic zebrafish lipidomics, unfortunately using whole embryos as undertaken in this chapter does not appear the optimal method to take forward and so isolating tails to assess alongside whole embryos, and the implementation of additional techniques including mass spectrometry should be undertaken in the future.

The *hacd1*-mutant model is highly promising as a relevant model of canine CNM and reproduces many of the disease features including disorganisation of triad markers (Blot *et al*., 2002; Tiret *et al*., 2003; Walmsley *et al*., 2017).

6 Discussion

The essential role of *HACD1* in mammalian muscle is becoming increasingly apparent through the characterisation of *HACD1* mutations in dogs and humans that cause HACD1 deficiency and lead to congenital myopathies (Maurer *et al*., 2012; Muhammed *et al*., 2013; Pelé *et al*., 2005; Toscano *et al*., 2017). These mutations have since been modelled in mice and cell culture models paving the way for HACD1 research (Blondelle *et al*., 2015; Sawai *et al*., 2017; Walmsley, 2013; Walmsley *et al*., 2017) and it is known now that HACD1 functions in very long chain fatty acids (VLCFA) elongation (Ikeda *et al*., 2008). The essential roles of VLCFA for functions including barrier formation and inflammation in tissues such as the skin, eye, CNS and testis have been well documented (Monroig *et al*., 2010; Sassa & Kihara, 2014; Schneiter *et al*., 1996), yet little is known regarding their specific role in muscle.

The work described here in Chapters 2 and 5 presents evidence that embryonic zebrafish are a novel and appropriate model for the study of HACD1-CNM. The *hacd1* gene in zebrafish appears to be a true homologue of mammalian HACD1. The embryos expressed *hacd1* within their skeletal muscle, and importantly, the other three genes encoding HACD enzymes were not highly expressed in developing or mature muscle. Furthermore, when *hacd1* was mutated in embryos, the phenotype was comparable to the pathology of CNM (Blot *et al*., 2002; Tiret *et al*., 2003) and to the previously studied embryonic zebrafish CNM models (Dowling *et al*., 2009; Dowling *et al*., 2010; Gibbs *et al*., 2013a; Smith *et al*., 2014). Chapters 3 and 4 further characterised a *Hacd1*-kd cell model which allowed initial studies to be conducted regarding the cell membrane function and the effects of *hacd1* expression and deficiency on the lipidome, both of which are critical to improve the understanding of CNM.

6.1. Major findings

6.1.1. Zebrafish embryos as a model for the study of HACD1-CNM

6.1.1.1. *hacd1* is the major HACD enzyme within zebrafish muscle

Mammalian expression of the HACD enzymes has a specific tissue distribution: HACD1 is expressed in skeletal and cardiac muscle, HACD2 is expressed ubiquitously, HACD3 is also expressed ubiquitously excluding the leukocytes and HACD4 is uniquely expressed within leukocytes (Ikeda *et al*., 2008). Investigations into the expression pattern of the zebrafish HACD paralogues was necessary and fundamental work in order to validate embryonic zebrafish as a potential HACD1-CNM model. For embryonic zebrafish to be an appropriate

model it was essential to determine if the putative HACD1 orthologue (*hacd1*) was strongly expressed in muscle, was upregulated during myogenesis as seen in mammals and that none of *hacd2*, *hacd3* or *hacd4* were. Quantitative RT-PCR reactions found the *hacd1* gene expression to be significantly upregulated in line with the development of myofibres which begins in developing somites before embryos are 1dpf (Devoto *et al*., 1996; Kimmel *et al*., 1995). Results from ISH documented that *hacd1* was expressed most strongly within the myotomes of the developing tail and that *hacd2* and *hacd3* were mostly localised to the head and developing abdominal cavity. Expression of *hacd4* was not detectable grossly within whole embryos and only one section found areas within the brain which appeared to express *hacd4*. These results for *hacd4* were thus inconclusive, and future work to comprehensively characterise HACD enzyme expression in zebrafish should address this – including by further ISH in embryos and adults to evaluate for presence in other areas of the CNS and leukocytes. For the purposes of this study, full length *hacd4* could be amplified from a number of adult tissues and this was cloned, expression in embryos was at a low levels and did not change over the time course of muscle development, furthermore, mammalian HACD4 cannot rescue loss of Phs1 in yeast as HACD1 and HACD2 can, and only HACD1 and HACD2 share high homology in sequence and function (Ikeda *et al*., 2008; Sawai *et al*., 2017). Therefore, there is unlikely to be any compensatory mechanisms involving *hacd4* upon the knockdown of *hacd1* however, qRT-PCR assay for *hacd4* is validated and can be performed to evaluate for this in mutants. Ensuring no compensation from any of the other *hacd* genes should be investigated thoroughly in vertebrate models including the zebrafish. Work presented in this thesis expanded on previous preliminary data reported by Walmsley, (2013) to further recognise when the *hacd1* expression first begins within the embryos and to pinpoint the onset of *hacd1-fl* upregulation in line with myogenesis. Where previous results in zebrafish were available for comparison, agreement was found with Walmsley, (2013). This is in contrast with the cell model also evaluated, in which *Hacd1* expression in control cells and the knockdown of this expression in *Hacd1*-kd cells was seen from single cell myoblasts in Walmsley, (2013) but only evident after 4dpd in this thesis. Therefore, this highlights the variability evident in cell culture between laboratories.

HACD1 is prone to multiple splicing in humans (Valdés de Hoyos *et al*., 2011; Tondeur *et al*., 2010) and dogs (Maurer *et al*., 2010; Pelé *et al*., 2005), most of which do not code for the amino acids essential for HACD activity (Kihara *et al*., 2008). Work by Walmsley, (2013) then documented was true of the zebrafish *hacd1* including the presence of a splice variant, *hacd1-d5* (Walmsley, 2013). Chapter 2 characterised two novel transcripts for the zebrafish *hacd2*, both of which do not code for the essential amino acids (Kihara *et al*., 2008), like the

HACD1 splice variants (Valdés de Hoyos *et al*., 2011; Ikeda *et al*., 2008; Maurer *et al*., 2010; Pelé *et al*., 2005; Tondeur *et al*., 2010; Walmsley, 2013).

These results on zebrafish embryos confirm that the zebrafish *hacd1* gene is the major gene expressed within developing muscle of zebrafish embryos and that they exhibit a tissue expression pattern of all four *hacd* genes in a manner that is similar to mammalian expression, with the exception, as mentioned above, of *hacd4* (Ikeda *et al*., 2008). It also provided the fundamental knowledge regarding HACD expression within developing zebrafish embryos, as well as validated assays for evaluation ahead of using them as a model of HACD1-deficient myopathies.

6.1.1.2. Use of zebrafish embryos for lipidomic studies

It was important to first evaluate the lipidome of wildtype embryos, to confirm that the protocol was achievable and to establish a lipidomic profile for wildtype embryos ahead of the generation of the *hacd1*-mutant zebrafish embryo model. ^{1}H-NMR was employed to characterise the lipidome of the wildtype embryos from 1-3dpf. Work in Chapter 5 was undertaken to first validate this technique in which it was found that an increase in sample size had a strong positive correlation with signal: noise indicating where possible, pooled embryo sets would be the most informative. The chorion did not have a significant effect upon the lipidome and therefore it was not removed in further experiments. This was expected as the chorion membranes are made up mostly of polypeptides (Bonsignorio *et al*., 1996). After the technique was validated, the experimental data provided evidence that the lipidome of the embryos changed during development. The data on abundance of lipid classes within the embryos over development corresponded to a previous report on the lipid content of the embryo yolk sac (Fraher *et al*., 2016). Therefore, it is likely that the yolk sac was contributing to the results seen here and potentially confounding changes in lipid abundances from the rest of the embryo, including the tail muscle. Therefore, in future whole embryos and the tails alone can be used for lipidomic studies. We suggest that by using both the whole embryos and just the tails, this will be an informative model for examining lipids affected by HACD1-deficiency than the *Hacd1*-kd cell model, as the embryos are an isolated system and thus variability due to serum and media changes, as shown in Chapter 4, would not be present in this model.

6.1.1.3. Validation of an embryonic zebrafish HACD1-CNM model

A zebrafish embryo model with mutations in *hacd1*, generated by another researcher using CRISPR/Cas9 genome editing, was available for study. Up to 25% of F_0 injected embryos developed abnormal live phenotypes. The embryos presented with poor motility suggesting muscle dysfunction and possible impairment of ECC (Gibbs *et al*., 2013a), and morphological

defects predominantly affecting striated muscles including bent tails and malformed hearts. These abnormal phenotypes were comparable to the other zebrafish CNM models in the literature (Dowling *et al*., 2009; Dowling *et al*., 2010; Gibbs *et al*., 2013a; Smith *et al*., 2014). Work in Chapter 5 presented evidence that *hacd1*-mutant embryos had phenotypes that corresponded to the disease and will therefore provide a good model to use in the future to study both HACD1 and VLCFA in CNM (Blot *et al*., 2002; Tiret *et al*., 2003).

Zebrafish embryos provide an isolated system for the first 5 days after fertilisation due to their development external to the mother (Guyon *et al*., 2007). Mature functioning myotubes have developed by 3dpf and can be studied without confounding variables such as the addition of media onto cells, which our results strongly suggest impacts the phenotype of cell culture models of HACD1 deficiency. C2C12 cells comparatively do not develop mature internal structures as zebrafish embryos do and require longer in culture to develop primitive forms of internal membranes (Asano *et al*., 2015). C2C12 have to be cultured for 8 days before the cells start to express RYR1, an indicator of SR development (Walmsley, 2013), unlike the zebrafish embryo which shows strong RYR1 expression and sarcomeric organisation by 48hpf and displays motor function through tail twitches by 17hpf (Saint-Amant & Drapeua, 1998). C2C12 cells have been reported to contract (Manabe *et al*., 2012) however this requires stimulation and this is inconsistent with the literature as it has also been reported that robust contraction is rare (Asano *et al*., 2015).

To summarise this section on the use of zebrafish embryos as a model for CNM, work presented here has confirmed the initial hypotheses that the embryonic zebrafish would have comparable HACD expression to mammals and that they make a good model of HACD1-CNM which may provide certain benefits over a cell culture model. By validating the model, this work will allow HACD1, VLCFA and CNM research to advance considerably in coming years because of the ready accessibility of zebrafish embryos as a disease model.

6.1.2. Further characterisation of HACD1-deficiency in a cell culture model

The C2C12 cell model allowed us to gain insight into membrane function and membrane lipid profiles in HACD1-deficiency and the work done in this thesis has laid down the groundwork for future electrophysiological and lipidomic studies. We have conducted novel work into C2C12 sarcolemmal ion channels and resting membrane potentials (RMPs) in the context of HACD1-CNM and found here was no significant difference in the RMP of the *Hacd1*-kd cells which suggests weakness of HACD1-CNM, thought to be a result of disrupted ECC (Walmsley *et al*., 2017), is not caused by an increasingly positive basal RMP of cells. We concluded that it was likely that non-selective channels were commonly recorded in the C2C12 cells regardless of HACD1 activity. There were other channels present within

recordings, including possible chloride channels and calcium-activated potassium channels, further work is required to further characterise and identify channels. As discussed in Chapter 3 a larger sample size, pharmacological interventions such as channel blockers and looking into the effects of depolarisation would be needed to truly understand how the ion channels are affected by HACD1-deficiency. Nevertheless, this was the first study to patch clamp HACD1-deficicient cells and further work on the cells would provide insight into cellular calcium and ionic homeostasis.

This work in this thesis also furthered previous work undertaken by Blondelle *et al*., (2015) to assess lipid profiles within cells, with the aim of understanding which membrane lipids might be affected by HACD1-deficiency. We documented changes within the lipidome when cellular *Hacd1* was knocked down, in particular the later stages of differentiation when the internal membrane systems begin to develop. Unfortunately, it was not possible to determine which lipids were causing these differences in the lipidomes due to limitations in the novelty of ^{1}H-NMR lipidomics. Lysophosphatidylcholine (LPC) levels were shown to significantly decrease in the cells irrespective of *Hacd1* expression and this decrease has been reported to be necessary for cells to fuse and differentiate (Blondelle *et al*., 2015; Leikina *et al*., 2013). This finding contrasted with that of earlier work in which the *Hacd1*-kd were unable to fuse together (Blondelle *et al*., 2015; Lin *et al*., 2012) and that LPC levels did not decrease in these non-fusing cells (Blondelle *et al*., 2015). It was concluded that these differences are likely down to diverse cell clones being used, and that cell media may also have affected lipid results due to the 4% serum used in this study.

LPC has also been linked to the stimulation of the non-selective TRPC5 channel, thought to either results from a phospholipid binding site on the channel or the sensitivity of the TRPC5 channel to bilayer changes by certain lipids (Flemming *et al*., 2005). The regulation of ion channels by membrane lipids has been documented previously and could therefore be a novel and interesting avenue for future research (Rosenhouse-Dantsker *et al*., 2012).

A novel and important finding was the absence of any compensatory upregulation of the *Hacd2-4* genes in response to the knockdown of *Hacd1* at later stages of differentiation. *Hacd2* and *Hacd3* and been previously reported to show no compensatory upregulation in early differentiation (5dpd) and also in the *Hacd1*-null mouse model (Blondelle *et al*., 2015). The work presented in this thesis takes the cell work from Blondelle *et al*., (2015) further in concluding at later stages of differentiation in *Hacd1*-kd cells that *Hacd2, Hacd3* and *Hacd4* do not upregulate and therefore it can be concluded that they are unlikely to compensate for the HACD1-deficiency in this model. This should be evaluated in other species – including the zebrafish *hacd1*-mutant model.

6.2. Directions for further work and potential applications

To advance our understanding of HACD1-CNM and the role(s) of HACD1 and VLCFA in muscle we must first answer a number of questions. Which VLCFA(s) does HACD1 elongate and which molecules are these incorporated into? What are the roles of these VLCFA-containing lipids in muscle during development, maintenance and disease? A structural role has been proposed in highly curved membranes therefore do these localise at the triad in muscle and is this also where HACD1 localises within the SR? Can VLCFA in muscle be manipulated, for example in the diet, and targeted for therapy?

I will discuss further work using the two models from this thesis however it is important to remember that a larger variety of biological models have been essential in forming our current understanding of HACD1-CNM. Yeast was the model in which the function of HACD1 was determined (Ikeda *et al*., 2018), and has since been used to understand more about which VLCFA HACD1 may elongate, including the overlap seen in VLCFA elongation between both HACD1 and HACD2 (Sawai *et al*., 2017). Yeast have also been used to study the elongase proteins, ELOVLs, whereby zebrafish Elovl proteins were expressed within yeast to identify the VLCFAs synthesised (Monroig *et al*., 2010). *Hacd1* null mice have also been used to report on the clinical pathology of HACD1-deficiency (Blondelle *et al*., 2015; Sawai *et al*., 2017) which was reported to be comparable to that seen in HACD1-CNM dogs (Blot *et al*., 2002; Tiret *et al*., 2003). The C2C12 cell line used in this thesis and other cell clones also discussed have reported on lipidomics and membrane properties (Blondelle *et al*., 2015; Lin *et al*., 2012), briefly on the calcium homeostasis of the cells (Walmsley, 2013) and the general morphology of the cells including staining of triad proteins (Walmsley *et al*., 2017).

6.2.1. Further work using the *Hacd1*-kd C2C12 cell line

A preliminary ion channel phenotype for the control and *Hacd1*-kd cells was identified in this thesis, however the aim of measuring calcium responses through ion channel patch-clamping was not completed due to time constraints. For that reason this work should be continued to recorded single ion channel activity whilst depolarising cells to record calcium responses in cells. This can be undertaken using high potassium solutions to trigger the DHPR channels via membrane depolarisation or caffeine to stimulate the RYR1 channels. Large-conductance calcium-activated K^+ channels (BK) (Alexander *et al*., 2011) would be informative of calcium responses and therefore should be the focus of this work. Cell morphology was briefly examined in this thesis, showing nuclear clusters to be more common (insignificant) in *Hacd1*-kd cells which had been previously reported along with high levels of RYR1 (Walmsley, 2013; Walmsley *et al*., 2017). Internal membrane structures and nuclei

ultrastructure could be examined further using electron microscopy to visualise triads formed in the cells and compare the morphology of the triads in *Hacd1*-kd myotubes.

The lipidomic analysis performed in this thesis found there to be a global difference in the lipid profile of *Hacd1*-kd cells compared to control, particularly at later stages of differentiation. Employing different lipidomic techniques will help identify which lipids are changing between cell types. Mass spectrometry (Blondelle *et al*., 2015), and 2D NMR (with the inclusion of ^{13}C-NMR) would provide information on chain length (Yang *et al*., 2016). Lipid rescue studies are another avenue for this cell work, by adding different VLCFAs into the media and examining membrane properties of the cells. The addition of fluorescently labelled VLCFAs (Schultz *et al*., 2010) would help to understand where these VLCFA are localising within the cells.

6.2.2. Further work using the novel HACD1-CNM zebrafish model

As previously discussed, the characteristics of zebrafish embryos make them an excellent model for further study of HACD1 and VLCFA. Initially techniques such as 3' RACE could be implemented to fully characterise the unconfirmed isoforms in HACD2 and potentially discover any other HACD isoforms that may, as of yet, be unidentified (Deng *et al*., 2009). This would provide a clear picture of the splicing of zebrafish *hacd* genes. To further validate the model, experiments like those described in Chapter 2 to characterise *hacd* expression in wildtype embryos should now be conducted in *hacd1*-mutant embryos. It will be important to evaluate the effect of different mutations on hacd1 expression particularly when selecting a mutation to establishing a line of zebrafish. Mutations may trigger the aberrant splicing seen in the canine CNM and so expression analysis and 3' RACE on the embryos would be required (Maurer *et al*., 2010; Pelé *et al*., 2005). This work will also provide insight into compensatory mechanisms which may occur within this model and will allow us to quantify the *hacd1* expression levels in mutant embryos.

The expression work done in this thesis concentrated on the mRNA level and ultimately it will be important to evaluate the protein expression and localisation. At the time of this thesis no antibodies were available for the HACD proteins and so going forward self-design of antibodies (Tiller & Tessier, 2015) for both zebrafish and mouse species would be appropriate.

The current guide targets exon 1 and will affect all major isoforms. An additional model targeting *hacd1-fl* only via the essential amino acids would allow us to isolate the specific roles of HACD1-fl in muscle (Kihara *et al*., 2008). The human mutation reported by Toscano *et al*., (2017) is a point mutation affecting the active site therefore we anticipate that this will result in a similar myopathic phenotype. Either of these *hacd1*-mutant models have the

potential to be grown past development and create *hacd1*-mutant zebrafish lines, which would provide consistent genotype and phenotype within embryos. This is turn would tighten up results from a highly reproducible model.

Lipidomic analysis in the *hacd1*-mutant embryos will provide some functional information on HACD1-deficiency. This can be further optimised from the work in this thesis by using isolated tails as this without doing this the lipids from the yolk sac confound the results considerably. As with the cell culture model, using more in-depth NMR to look at ^{13}C would provide more detail on chain length by separating out spectra further, however MS would possibly be the best option to take this work further and fully identify changes in chain length when *hacd1* is mutated in the embryos (Blondelle *et al*., 2015; Yang *et al*., 2016). Also similarly to future work with the cell culture model, injecting labelled lipids or VLCFA into the yolk sac of embryos (Zeituni & Farber, 2016) will help in the understanding of their role within muscle. By using zebrafish embryos this work will benefit from the knowledge of VLCFA function within working muscle (Saint-Amant & Drapeua, 1998).

Another direction to take this work in would involve using the HACD1-CNM embryonic zebrafish model currently being validated to study the electrophysiology of HACD1-deficiency. C2C12 only develop a basic internal membrane system whereas by 1dpf embryonic zebrafish have developed quantifiable motor phenotypes allowing for a more in-depth functional study into ECC (Gibbs *et al*., 2013a). Calcium homeostasis and response to contractions has been previously studied in whole zebrafish embryos through injection of ratiometric calcium dyes and stimulating contraction in embryos (Smith *et al*., 2014). Experiments to study ECC could also be done via the isolation of whole myofibres from the embryos (Horstick *et al*., 2013). These fibres should then be subjected to calcium imaging studies, patch-clamping and immunohistochemistry. Calcium imaging would allow for the selection of areas within the myofibres to assess calcium responses when ECC is triggered through membrane depolarisation, providing functional information on the workings of the calcium channels and associated membranes.

Immunohistochemistry will provide confirmation of the tubuloreticular membrane disorganisation and staining for the other CNM related proteins would provide further detail on this disorganisation: DNM2, BIN1 and MTM1 (Jungbluth *et al*., 2018). Birefringence is a common microscopy technique that is utilised to assess the uniformity of skeletal muscle, and this could be done within the embryos (Smith *et al*., 2013). Finally, electron microscopy of the embryonic muscle would provide high resolution images of the muscle ultrastructure and allow the triad structure to be compared between control and affected embryos.

6.2.3. Potential applications

By studying the rescue of the HACD1-CNM phenotype, translation from laboratory to clinical application can progress. The effects of cell media changes upon fatty acid bond saturation (Chapter 4) would suggest there is potential in the manipulation of lipid profiles via external factors. To further examine this, rescue studies on the novel HACD1-CNM zebrafish embryo model will be conducted; firstly by injecting *hacd1* mRNA into zebrafish embryos to assess effects of replacing the *hacd1* lost via genome editing. Injecting *hacd2* mRNA will provide further clarity regarding the redundancy of the two enzymes and provide evidence as to whether Hacd2 can act to elongate VLCFA in muscle. A lipid based rescue experiment should also be performed involving the injection of different VLCFA into the yolk sac of embryos in order to determine which VLFCA may ameliorate the effect of *hacd1* mutation. This would allow us to determine the interplay between diet and genetics on VLCFA in muscle and could ultimately lead to the development of a diet-based therapy for dogs with HACD1-CNM or humans with HACD1 congenital myopathies. The use of diet therapy for muscle lipid metabolic disorders has been discussed by Laforêt & Vianey-Saban, (2010) in the context of lipid storage myopathies and humans with muscle lipid metabolism disorders have shown marked improvement of symptoms after diet therapy (Roe *et al*., 2002). Gaining increased insight into the role of HACD1 and VLCFA is critical for the understanding of how the tubuloreticular membrane disorganisation seen in the canine disorder (Walmsley *et al*., 2017) comes about and how potential therapies could be implemented in the future. With knowledge of which lipids and fatty acids are decreased in CNM and can successfully rescue phenotype once reintroduced into a biological system: this can have potential medical and veterinary translation.

6.3. Final conclusions

In conclusion the embryonic zebrafish is a promising model to utilise for further research into HACD1-CNM and this studypresents work that details their suitability. The zebrafish have a comparable *hacd* expression pattern to that of mammals, embryos can be utilised for lipidomics analysis and when *hacd1* is mutated embryos present with a phenotype similar to that of previous CNM models (Dowling *et al*., 2009; Dowling *et al*., 2010; Gibbs *et al*., 2013a; Sabha *et al*., 2016; Smith *et al*., 2014) and the disease phenotype in mammals (Blot *et al*., 2002; Tiret *et al*., 2003). Work undertaken in this thesis has allowed for functional characterisation of HACD1 within C2C12 cells and has shown the lipidome of the C2C12 *Hacd1*-kd cell line to be affected by *Hacd1* deficiency. Complementing the use of the

zebrafish model with the *Hacd1*-kd cell line has aided in the characterisation of HACD expression, localisation and function, providing a solid basis for further work into HACD1-CNM.

References

Abdul Kadir, L., Stacey, M. & Barrett-Jolley, R. (2018). Emerging Roles of the Membrane Potential: Action Beyond the Action Potential. *Frontiers in Physiology*, 9(1661).

Abedi, E. & Sahari, M. A. (2014). Long-chain polyunsaturated fatty acid sources and evaluation of their nutritional and functional properties. *Food Science & Nutrition*, 2(5), 443-463.

Al-Qusairi, L. & Laporte, J. (2011). T-tubule biogenesis and triad formation in skeletal muscle and implication in human diseases. *Skeletal Muscle*, 1(1), pp 26.

Al-Qusairi, L., Weiss, N., Toussaint, A., Berbey, C., Messaddeq, N., Kretz, C., Sanoudou, D., Beggs, A. H., Allard, B., Mandel, J. L., Laporte, J., Jacquemond, V. & Buj-Bello, A. (2009). T-tubule disorganization and defective excitation-contraction coupling in muscle fibers lacking myotubularin lipid phosphatase. *Proceedings of the National Academy of Sciences of the USA*, 106(44), 18763-8.

Alexander, S. P. H., Mathie, A. & Peters, J. A. (2011). Guide to Receptors and Channels (GRAC), 5th edition. *British Journal of Pharmacology*, 164 (1), S1-S324.

Allard, B. (2018). From excitation to intracellular Ca^{2+} movements in skeletal muscle: Basic aspects and related clinical disorders. *Neuromuscular Disorders*, 28(5), 394-401.

Allen, D. L., Roy, R. R. & Edgerton, V. R. (1999). Myonuclear domains in muscle adaptation and disease. *Muscle & Nerve*, 22(10), 1350-1360.

Alnaqeeb, M. A. & Goldspink, G. 1987. Changes in fibre type, number and diameter in developing and ageing skeletal muscle. *Journal of Anatomy*, 153.

Araya, R., Liberona, J. L., Cardenas, J. C., Riveros, N., Estrada, M., Powell, J. A., Carrasco, M. A. & Jaimovich, E. (2003). Dihydropyridine receptors as voltage sensors for a depolarization-evoked, IP3R-mediated, slow calcium signal in skeletal muscle cells. *Journal of General Physiology*, 121(1), 3-16.

Asano, T., Ishizuka, T., Morishima, K. & Yawo, H. (2015). Optogenetic induction of contractile ability in immature C2C12 myotubes. *Scientific Reports*, 5(8317).

Ashworth, R. & Brennan, C. (2005). Use of transgenic zebrafish reporter lines to study calcium signalling in development. *Briefings in Functional Genomics*, 4(2), 186-193.

Avdesh, A., Chen, M., Martin-Iverson, M. T., Mondal, A., Ong, D., Rainey-Smith, S., Taddei, K., Lardelli, M., Groth, D. M., Verdile, G. & Martins, R. N. (2012). Regular care and maintenance of a zebrafish (Danio rerio) laboratory: an introduction. *Journal of Visualized Experiments: JoVE*, (69), e4196-e4196.

Avila, G., O'Brien, J. J. & Dirksen, R. T. (2001). Excitation--contraction uncoupling by a human central core disease mutation in the ryanodine receptor. *Proceedings of the National Academy of Sciences of the United States of America*, 98(7), 4215-4220.

Bach, L., Michaelson, L. V., Haslam, R., Bellec, Y., Gissot, L., Marion, J., Da Costa, M., Boutin, J.-P., Miquel, M., Tellier, F., Domergue, F., Markham, J. E., Beaudoin, F., Napier, J. A. & Faure, J.-D. (2008). The very-long-chain hydroxy fatty acyl-CoA dehydratase PASTICCINO2 is essential and limiting for plant development. *Proceedings of the National Academy of Sciences*, 105(38).

Bailey, K. (1946). Tropomyosin: a New Asymmetric Protein Component of Muscle. *Nature*, 157(3986), 368-369.

Bailey, K. (1948). Tropomyosin: a new asymmetric protein component of the muscle fibril. *The Biochemical Journal*, 43(2), 271-279.

Bajaj, P., Bashir, R., Zorlutuna, P., Reddy, B., Jr., Millet, L., Wei, C. & Bao, G. (2011). Patterning the differentiation of C2C12 skeletal myoblasts. *Integrative Biology*, 3(9), 897-909.

Balog, E. M. & Gallant, E. M. (1999). Modulation of the sarcolemmal L-type current by alteration in SR Ca^{2+} release. *The American Journal of Physiology*, 276(1).

Barnett, M. W. & Larkman, P. M. (2007). The action potential. *Practical Neurology*, 7(3).

Barrientos, G., Sanchez-Aguilera, P., Jaimovich, E., Hidalgo, C. & Llanos, P. (2017). Membrane Cholesterol in Skeletal Muscle: A Novel Player in Excitation-Contraction Coupling and Insulin Resistance. *Journal of Diabetes Research*, 8.

Bassett, D. I. & Currie, P. D. (2003). The zebrafish as a model for muscular dystrophy and congenital myopathy. *Human Molecular Genetics*, 2.

Bate-Smith, E. C. & Bendall, J. R. (1947). Rigor mortis and adenosine-triphosphate. *Journal of Physiology*, 106(2), 177-85.

Baur, L. A., O'Connor, J., Pan, D. A., Kriketos, A. D. & Storlien, L. H. (1998). The fatty acid composition of skeletal muscle membrane phospholipid: its relationship with the type of feeding and plasma glucose levels in young children. *Metabolism*, 47(1), 106-12.

Beard, N. A., Casarotto, M. G., Wei, L., Varsányi, M., Laver, D. R. & Dulhunty, A. F. (2005). Regulation of ryanodine receptors by calsequestrin: effect of high luminal Ca^{2+} and phosphorylation. *Biophysical Journal*, 88(5), 3444-3454.

Beckonert, O., Keun, H. C., Ebbels, T. M., Bundy, J., Holmes, E., Lindon, J. C. & Nicholson, J. K. (2007). Metabolic profiling, metabolomic and metabonomic procedures for NMR spectroscopy of urine, plasma, serum and tissue extracts. *Nature Protocols*, 2(11), 2692-703.

Bentzinger, C. F., Wang, Y. X. & Rudnicki, M. A. (2012). Building muscle: molecular regulation of myogenesis. *Cold Spring Harbour Perspective Biology*, 4(2).

Berberoglu, M. A., Gallagher, T. L., Morrow, Z. T., Talbot, J. C., Hromowyk, K. J., Tenente, I. M., Langenau, D. M. & Amacher, S. L. (2017). Satellite-like cells contribute to pax7-dependent skeletal muscle repair in adult zebrafish. *Developmental Biology*, 424(2), 162-180.

Berbey, C., Weiss, N., Legrand, C. & Allard, B. (2009). Transient receptor potential canonical type 1 (TRPC1) operates as a sarcoplasmic reticulum calcium leak channel in skeletal muscle. *Journal of Biological Chemistry*, 284(52), 36387-94.

Berchtold, M. W., Brinkmeier, H. & Muntener, M. (2000). Calcium ion in skeletal muscle: its crucial role for muscle function, plasticity, and disease. *Physiological Reviews*, 80(3), pp 1215-65.

Bers, D. M. (2014). 16 - Excitation-Contraction Coupling. In: Zipes, D. P. & Jalife, J. *Cardiac Electrophysiology: From Cell to Bedside* (Sixth Edition). Philadelphia: W.B. Saunders.

Bevilacqua, J. A., Monnier, N., Bitoun, M., Eymard, B., Ferreiro, A., Monges, S., Lubieniecki, F., Taratuto, A. L., Laquerriere, A., Claeys, K. G., Marty, I., Fardeau, M., Guicheney, P., Lunardi, J. & Romero, N. B. (2011). Recessive RYR1 mutations cause unusual congenital myopathy with prominent nuclear internalization and large areas of myofibrillar disorganization. *Neuropathology and Applied Neurobiology*, 37(3), 271-84.

Bhandari, S., Lee, J. N., Kim, Y.-I., Nam, I.-K., Kim, S.-J., Kim, S.-J., Kwak, S., Oh, G.-S., Kim, H.-J., Yoo, H. J., So, H.-S., Choe, S.-K. & Park, R. (2016). The fatty acid chain elongase, Elovl1, is required for kidney and swim bladder development during zebrafish embryogenesis. *Organogenesis*, 12(2), 78-93.

Bitoun, M., Bevilacqua, J. A., Prudhon, B., Maugenre, S., Taratuto, A. L., Monges, S., Lubieniecki, F., Cances, C., Uro-Coste, E., Mayer, M., Fardeau, M., Romero, N. B. & Guicheney, P. (2007). Dynamin 2 mutations cause sporadic centronuclear myopathy with neonatal onset. *Annals of Neurology*, 62(6), 666-70.

Bitoun, M., Maugenre, S., Jeannet, P. Y., Lacene, E., Ferrer, X., Laforet, P., Martin, J. J., Laporte, J., Lochmuller, H., Beggs, A. H., Fardeau, M., Eymard, B., Romero, N. B. & Guicheney, P. (2005). Mutations in dynamin 2 cause dominant centronuclear myopathy. *Nature Genetics*, 37(11), 1207-1209.

Blaauw, B., Schiaffino, S. & Reggiani, C. (2013). Mechanisms modulating skeletal muscle phenotype. *Comprative Physiology*, 3(4), pp 1645-87.

Blanco, A. & Blanco, G. (2017). Chapter 11 - Membranes. In: Blanco, A. & Blanco, G. (eds.) *Medical Biochemistry*. Academic Press.

Bley, T., Gaillard, C., Bilzer, T., Braund, K. G., Faissler, D., Steffen, F., Cizinauskas, S., Neumann, J., Vogtli, T., Equey, R. & Jaggy, A. (2002). Genetic aspects of Labrador retriever myopathy. *Research in Veterinary Science*, 73(3), 231-6.

Blondelle, J., Ohno, Y., Gache, V., Guyot, S., Storck, S., Blanchard-Gutton, N., Barthelemy, I., Walmsley, G., Rahier, A., Gadin, S., Maurer, M., Guillaud, L., Prola, A., Ferry, A., Aubin-Houzelstein, G., Demarquoy, J., Relaix, F., Piercy, R. J., Blot, S., Kihara, A., Tiret, L. & Pilot-Storck, F. (2015). HACD1, a regulator of membrane composition and fluidity, promotes myoblast fusion and skeletal muscle growth. *Journal of Molecluar Cell Biology*, 7(5), 429-40.

Blot S, T. L., Devillaire A, Fardeau I & PA D. (2002). Phenotypic Description of a Canine Centronuclear Myopathy. *Journal of Neurological Science*s, 199(S9).

Bohm, J., Vasli, N., Malfatti, E., Le Gras, S., Feger, C., Jost, B., Monnier, N., Brocard, J., Karasoy, H., Gerard, M., Walter, M. C., Reilich, P., Biancalana, V., Kretz, C., Messaddeq, N., Marty, I., Lunardi, J., Romero, N. B. & Laporte, J. (2013). An integrated diagnosis strategy for congenital myopathies. *PLoS One,* 8(6), e67527.

Bonsignorio, D., Perego, L., Del Giacco, L. & Cotelli, F. (1996). Structure and macromolecular composition of the zebrafish egg chorion. *Zygote*, 4(2), 101-8.

Borchman, D., Tang, D. & Yappert, M. C. (1999). Lipid composition, membrane structure relationships in lens and muscle sarcoplasmic reticulum membranes. *Biospectroscopy*, 5(3), 151-167.

Boutchueng-Djidjou, M., Belleau, P., Bilodeau, N., Fortier, S., Bourassa, S., Droit, A., Elowe, S. & Faure, R. (2018). A type 2 diabetes disease module with a high collective influence for Cdk2 and PTPLAD1 is localized in endosomes. *PLoS One*, 13(10).

Boutchueng-Djidjou, M., Collard-Simard, G., Fortier, S., Hébert, S. S., Kelly, I., Landry, C. R. & Faure, R. L. (2015). The Last Enzyme of the De Novo Purine Synthesis Pathway 5-aminoimidazole-4-carboxamide Ribonucleotide Formyltransferase/IMP Cyclohydrolase (ATIC) Plays a Central Role in Insulin Signaling and the Golgi/Endosomes Protein Network. *Molecular & Cellular Proteomics*, 14(4), 1079-1092.

Braarud, H. C., Markhus, M. W., Skotheim, S., Stormark, K. M., Froyland, L., Graff, I. E. & Kjellevold, M. (2018). Maternal DHA Status during Pregnancy Has a Positive Impact on Infant Problem Solving: A Norwegian Prospective Observation Study. *Nutrients*, 10(5), 12.

Bragato, C., Gaudenzi, G., Blasevich, F., Pavesi, G., Maggi, L., Giunta, M., Cotelli, F. & Mora, M. (2016). Zebrafish as a Model to Investigate Dynamin 2-Related Diseases. *Scientific Reports*, 6(20466).

Braun, T. & Gautel, M. (2011). Transcriptional mechanisms regulating skeletal muscle differentiation, growth and homeostasis. *Nature Reviews in Molecular Cell Biology*, 12(6), 349-61.

Brennan, C., Mangoli, M., Dyer, C. E. F. & Ashworth, R. (2005). Acetylcholine and calcium signalling regulates muscle fibre formation in the zebrafish embryo. *Journal of Cell Science*, 118(22), 5181.

Brinkmeier, H. (2011). TRP channels in skeletal muscle: gene expression, function and implications for disease. *Advances in Experimental Medicine and Biology*, 704, 749-58.

Briolay, A., Jaafar, R., Nemoz, G. & Bessueille, L. (2013). Myogenic differentiation and lipid-raft composition of L6 skeletal muscle cells are modulated by PUFAs. *Biochimica et Biophysica Acta*, 1828(2), 602-13.

Brolinson, A., Fourcade, S., Jakobsson, A., Pujol, A. & Jacobsson, A. (2008). Steroid hormones control circadian Elovl3 expression in mouse liver. *Endocrinology*, 149(6), 3158-66.

Brown, D. A. & London, E. (2000). Structure and Function of Sphingolipid- and Cholesterol-rich Membrane Rafts. *Journal of Biological Chemistry*, 275(23), 17221-17224.

Bryson-Richardson, R. J. & Currie, P. D. (2008). The genetics of vertebrate myogenesis. *Nature Reviews in Genetics*, 9(8), 632-46.

Buckingham, M. (1992). Making muscle in mammals. *Trends in Genetics*, 8(4), 144-8.

Buj-Bello, A., Laugel, V., Messaddeq, N., Zahreddine, H., Laporte, J., Pellissier, J.-F. & Mandel, J.-L. (2002). The lipid phosphatase myotubularin is essential for skeletal muscle maintenance but not for myogenesis in mice. *Proceedings of the National Academy of Sciences*, 99(23), 15060.

Buzgar N., A. A. I., Buzatu A (2009). Romanian Database of Raman Spectroscopy *[http://rdrs.uaic.ro/*].

Cadot, B., Gache, V. & Gomes, E. R. (2015). Moving and positioning the nucleus in skeletal muscle - one step at a time. *Nucleus*, 6(5), 373-81.

Campiglio, M., Kaplan, M. M. & Flucher, B. E. (2018). STAC3 incorporation into skeletal muscle triads occurs independent of the dihydropyridine receptor. *Journal of Cellular Physiology*, 233(12), 9045-9051.

Cardenas, C., Muller, M., Jaimovich, E., Perez, F., Buchuk, D., Quest, A. F. & Carrasco, M. A. (2004). Depolarization of skeletal muscle cells induces phosphorylation of cAMP response element binding protein via calcium and protein kinase Calpha. *Journal of Biological Chemistry*, 279(37), 39122-31.

Carozzi, A. J., Ikonen, E., Lindsay, M. R. & Parton, R. G. (2000). Role of cholesterol in developing T-tubules: analogous mechanisms for T-tubule and caveolae biogenesis. *Traffic*, 1(4), 326-41.

Carroll, D. (2011). Genome engineering with zinc-finger nucleases. *Genetics*, 188(4), 773-782.

Cassandrini, D., Trovato, R., Rubegni, A., Lenzi, S., Fiorillo, C., Baldacci, J., Minetti, C., Astrea, G., Bruno, C., Santorelli, F. M. & Italian Network on Congenital, M. (2017). Congenital myopathies: clinical phenotypes and new diagnostic tools. *Italian journal of pediatrics*, 43(1), 101-101.

Celichowski, J. (2000). Mechanisms underlying the regulation of motor unit contraction in the skeletal muscle. *Journal of Physiology and Pharmacology*, 51(1), 17-33.

Ceyhan-Birsoy, O., Agrawal, P. B., Hidalgo, C., Schmitz-Abe, K., DeChene, E. T., Swanson, L. C., Soemedi, R., Vasli, N., Iannaccone, S. T., Shieh, P. B., Shur, N., Dennison, J. M., Lawlor, M. W., Laporte, J., Markianos, K., Fairbrother, W. G., Granzier, H. & Beggs, A. H. (2013). Recessive truncating titin gene, mutations presenting as centronuclear myopathy. *Neurology*, 81(14),1205.

Chen, Y. H., Lee, W. C., Cheng, C. H. & Tsai, H. J. (2000). Muscle regulatory factor gene: zebrafish (Danio rerio) myogenin cDNA. *Comparative Biochemistry and Physiology*, 127(1), 97-103.

Clarke, N. F. (2011). Congenital fiber-type disproportion. *Seminars in Pediatric Neurology*, 18(4), 264-71.

Collins, C. A. & Morgan, J. E. (2003). Duchenne's muscular dystrophy: animal models used to investigate pathogenesis and develop therapeutic strategies. *International Journal of Experimental Pathology*, 84(4), 165-172.

Conceicao, M. S., Vechin, F. C., Lixandrao, M., Damas, F., Libardi, C. A., Tricoli, V., Roschel, H., Camera, D. & Ugrinowitsch, C. (2018). Muscle Fiber Hypertrophy and Myonuclei Addition: A Systematic Review and Meta-analysis. *Medicine and Science in Sports and Exercise*, 50(7), 1385-1393.

Cong, X., Doering, J., Grange, R. W. & Jiang, H. (2016). Defective excitation-contraction coupling is partially responsible for impaired contractility in hindlimb muscles of Stac3 knockout mice. *Scientific Reports*, 6.

Cooke, R. (1986). The mechanism of muscle contraction. *Critical Reviews in Biochemistry and Molecular Biology*, 21(1), 53-118.

Cooper, C. A., Handy, R. D. & Bury, N. R. (2006). The effects of dietary iron concentration on gastrointestinal and branchial assimilation of both iron and cadmium in zebrafish (Danio rerio). *Aquatic Toxicology*, 79(2), 167-175.

Corry, B. (2006). Understanding ion channel selectivity and gating and their role in cellular signalling. *Molecular BioSystems*, 2(11), 527-535.

Coste, B., Houge, G., Murray, M. F., Stitziel, N., Bandell, M., Giovanni, M. A., Philippakis, A., Hoischen, A., Riemer, G., Steen, U., Steen, V. M., Mathur, J., Cox, J., Lebo, M., Rehm, H., Weiss, S. T., Wood, J. N., Maas, R. L., Sunyaev, S. R. & Patapoutian, A. (2013). Gain-of-function mutations in the mechanically activated ion channel PIEZO2 cause a subtype of Distal Arthrogryposis. *Proceedings of the National Academy of Sciences of the United States of America*, 110(12), 4667-4672.

Courilleau, D., Chastre, E., Sabbah, M., Redeuilh, G., Atfi, A. & Mester, J. (2000). B-ind1, a novel mediator of Rac1 signaling cloned from sodium butyrate-treated fibroblasts. *Journal of Biological Chemistry*, 275(23), 17344-8.

Cowling, B. S., Prokic, I., Tasfaout, H., Rabai, A., Humbert, F., Rinaldi, B., Nicot, A. S., Kretz, C., Friant, S., Roux, A. & Laporte, J. (2017). Amphiphysin (BIN1) negatively regulates dynamin 2 for normal muscle maturation. *Journal of Clinical Investigation*, 127(12), 4477-4487.

Cowling, B. S., Toussaint, A., Amoasii, L., Koebel, P., Ferry, A., Davignon, L., Nishino, I., Mandel, J.-L. & Laporte, J. (2011). Increased Expression of Wild-Type or a Centronuclear Myopathy Mutant of Dynamin 2 in Skeletal Muscle of Adult Mice Leads to Structural Defects and Muscle Weakness. *The American Journal of Pathology*, 178(5), 2224-2235.

Cowling, B. S., Toussaint, A., Muller, J. & Laporte, J. (2012). Defective Membrane Remodeling in Neuromuscular Diseases: Insights from Animal Models. *PLOS Genetics*, 8(4), e1002595.

Cox, G. A., Phelps, S. F., Chapman, V. M. & Chamberlain, J. S. (1993). New mdx mutation disrupts expression of muscle and nonmuscle isoforms of dystrophin. *Nature Genetics*, 4(87).

Cox, D. L. N. a. M. C. (2012). *Lehninger: Principles of Biochemistry* (6th edn), 23(6), 293-294.

Crilly, S., Njegic, A., Laurie, S. E., Fotiou, E., Hudson, G., Barrington, J., Webb, K., Young, H. L., Badrock, A. P., Hurlstone, A., Rivers-Auty, J., Parry-Jones, A. R., Allan, S. M. & Kasher, P. R. (2018). Using zebrafish larval models to study brain injury, locomotor and neuroinflammatory outcomes following intracerebral haemorrhage. *F1000 Research*, 7(1617-1617).

Danos, N. & Ward, A. B. (2012). The homology and origins of intermuscular bones in fishes: phylogenetic or biomechanical determinants? *Biological Journal of the Linnean Society*, 106(3), 607-622.

Dayal, A., Schrötter, K., Pan, Y., Föhr, K., Melzer, W. & Grabner, M. (2017). The Ca^{2+} influx through the mammalian skeletal muscle dihydropyridine receptor is irrelevant for muscle performance. *Nature Communications*, 8(1), 475.

den Hertog, J. (2005). Chemical genetics: Drug screens in Zebrafish. *Bioscience Reports*, 25(5-6), 289-97.

Deng, W., Sun, H., Liu, Y., Tao, D., Zhang, S. & Ma, Y. (2009). Molecular cloning and expression analysis of a zebrafish novel zinc finger protein gene rnf141. *Genetics and molecular biology*, 32(3), 594-600.

Denic, V. & Weissman, J. S. (2007). A molecular caliper mechanism for determining very long-chain fatty acid length. *Cell*, 130(4), 663-77.

Denniss, A., Dulhunty, A. F. & Beard, N. A. (2018). Ryanodine receptor Ca^{2+} release channel post-translational modification: Central player in cardiac and skeletal muscle disease. *International Journal of Biochemistry & Cell Biology*, 101.

Devoto, S. H., Melancon, E., Eisen, J. S. & Westerfield, M. (1996). Identification of separate slow and fast muscle precursor cells in vivo, prior to somite formation. *Development*, 122(11), 3371-80.

DiFranco, M., Herrera, A. & Vergara, J. L. (2011). Chloride currents from the transverse tubular system in adult mammalian skeletal muscle fibers. *The Journal of general physiology*, 137(1), 21-41.

Dooley, K. & Zon, L. I. (2000). Zebrafish: a model system for the study of human disease. *Current Opinions in Genetics and Development*, 10(3), 252-6.

Dowling, J. J., Low, S. E., Busta, A. S. & Feldman, E. L. (2010). Zebrafish MTMR14 is required for excitation–contraction coupling, developmental motor function and the regulation of autophagy. *Human Molecular Genetics*, 19(13), 2668-2681.

Dowling, J. J., Vreede, A. P., Low, S. E., Gibbs, E. M., Kuwada, J. Y., Bonnemann, C. G. & Feldman, E. L. (2009). Loss of myotubularin function results in T-tubule disorganization in zebrafish and human myotubular myopathy. *PLoS Genetics*, 5(2), pp e1000372.

Driever, W., Solnica-Krezel, L., Schier, A. F., Neuhauss, S. C., Malicki, J., Stemple, D. L., Stainier, D. Y., Zwartkruis, F., Abdelilah, S., Rangini, Z., Belak, J. & Boggs, C. (1996). A genetic screen for mutations affecting embryogenesis in zebrafish. *Development*, 123.

Dueñas, M. E., Essner, J. J. & Lee, Y. J. (2017). 3D MALDI Mass Spectrometry Imaging of a Single Cell: Spatial Mapping of Lipids in the Embryonic Development of Zebrafish. *Scientific Reports*, 7(1), 14946.

Dulhunty, A. F. (2006). Excitation–contraction coupling from the 1950s into the new millennium. *Clinical and Experimental Pharmacology and Physiology*, 33(9), 763-772.

Durieux, A.-C., Vignaud, A., Prudhon, B., Viou, M. T., Beuvin, M., Vassilopoulos, S., Fraysse, B., Ferry, A., Lainé, J., Romero, N. B., Guicheney, P. & Bitoun, M. (2010). A centronuclear myopathy-dynamin 2 mutation impairs skeletal muscle structure and function in mice. *Human Molecular Genetics*, 19(24), 4820-4836.

Duttaroy, A. K. (2009). Transport of fatty acids across the human placenta: a review. *Progress in Lipid Research*, 48(1), 52-61.

Ebashi, S. & Kodama, A. (1965). A new protein factor promoting aggregation of tropomyosin. *Journal of Biochemistry*, 58(1), 107-8.

Ehler, E. & Gautel, M. 2008. The sarcomere and sarcomerogenesis. *Adv Exp Med Biol*, 642(1-14.

Emwas, A. H. (2015). The strengths and weaknesses of NMR spectroscopy and mass spectrometry with particular focus on metabolomics research. *Methods in Molecular Biology*, 1277.

Engel, A. G., Gomez, M. R. & Groover, R. V. (1971). Multicore disease. A recently recognized congenital myopathy associated with multifocal degeneration of muscle fibers. *Mayo Clinic Proceedings*, 46(10), 666-81.

Essén, B., Jansson, E., Henriksson, J., Taylor, A. W. & Saltin, B. (1975). Metabolic Characteristics of Fibre Types in Human Skeletal Muscle. *Acta Physiologica Scandinavica*, 95(2), 153-165.

Fahlke, C. (2011). Chloride channels take center stage in a muscular drama. *The Journal of General Physiology*, 137(1), 17-19.

Falcone, S., Roman, W., Hnia, K., Gache, V., Didier, N., Lainé, J., Auradé, F., Marty, I., Nishino, I., Charlet-Berguerand, N., Romero, N. B., Marazzi, G., Sassoon, D., Laporte, J. & Gomes, E. R. (2014). N-WASP is required for Amphiphysin-2/BIN1-dependent nuclear positioning and triad organization in skeletal muscle and is involved in the pathophysiology of centronuclear myopathy. *EMBO Molecular Medicine*, 6(11), 1455-1475.

Flemming, P. K., Dedman, A. M., Xu, S.-Z., Li, J., Zeng, F., Naylor, J., Benham, C. D., Bateson, A. N., Muraki, K. & Beech, D. J. (2006). Sensing of Lysophospholipids by TRPC5 Calcium Channel. *Journal of Biological Chemistry*, 281(8), 4977-4982.

Flucher, B. E. & Andrews, S. B. (1993). Characterization of spontaneous and action potential-induced calcium transients in developing myotubes in vitro. *Cytoskeleton*, 25(2), 143-57.

Folker, E. S. & Baylies, M. K. (2013). Nuclear positioning in muscle development and disease. *Frontiers in Physiology*, 4.

Formigli, L., Sassoli, C., Squecco, R., Bini, F., Martinesi, M., Chellini, F., Luciani, G., Sbrana, F., Zecchi-Orlandini, S., Francini, F. & Meacci, E. (2009). Regulation of transient receptor potential canonical channel 1 (TRPC1) by sphingosine 1-phosphate in C2C12 myoblasts and its relevance for a role of mechanotransduction in skeletal muscle differentiation. *Journal of Cell Science*, 122(9), 1322-1333.

Fraher, D., Sanigorski, A., Mellett, Natalie A., Meikle, Peter J., Sinclair, Andrew J. & Gibert, Y. (2016). Zebrafish Embryonic Lipidomic Analysis Reveals that the Yolk Cell Is Metabolically Active in Processing Lipid. *Cell Reports*, 14(6), 1317-1329.

Franzini-Armstrong, a. & Jorgensen, A. O. (1994). Structure and Development of E-C Coupling Units in Skeletal Muscle. *Annual Review of Physiology*, 56(1), 509-534.

Fregosi, R. F. & Ludlow, C. L. (2013). Activation of upper airway muscles during breathing and swallowing. *Journal of Applied Physiology*, 116(3), 291-301.

Gagnon, J. A., Valen, E., Thyme, S. B., Huang, P., Ahkmetova, L., Pauli, A., Montague, T. G., Zimmerman, S., Richter, C. & Schier, A. F. (2014). Efficient Mutagenesis by Cas9 Protein-Mediated Oligonucleotide Insertion and Large-Scale Assessment of Single-Guide RNAs. *PloS One*, 9(5), e98186.

Gaigg, B., Timischl, B., Corbino, L. & Schneiter, R. (2005). Synthesis of sphingolipids with very long chain fatty acids but not ergosterol is required for routing of newly synthesized plasma membrane ATPase to the cell surface of yeast. *Journal of Biological Chemistry*, 280(23), 22515-22.

Gibbs, E. M., Davidson, A. E., Trickey-Glassman, A., Backus, C., Hong, Y., Sakowski, S. A., Dowling, J. J. & Feldman, E. L. (2013a). Two Dynamin-2 Genes Are Required for Normal Zebrafish Development. *PloS One*, 8(2), e55888.

Gibbs, E. M., Horstick, E. J. & Dowling, J. J. (2013b). Swimming into prominence: the zebrafish as a valuable tool for studying human myopathies and muscular dystrophies. *The FEBS Journal*, 280(17), 4187-4197.

Goebel, H. H. (2003). Congenital myopathies at their molecular dawning. *Muscle & Nerve*, 27(5), 527-548.

Grounds, M. D., Terrill, J. R., Radley-Crabb, H. G., Robertson, T., Papadimitriou, J., Spuler, S. & Shavlakadze, T. (2014). Lipid Accumulation in Dysferlin-Deficient Muscles. *The American Journal of Pathology*, 184(6), 1668-1676.

Gutierrez-Martin, Y., Martin-Romero, F. J. & Henao, F. (2005). Store-operated calcium entry in differentiated C2C12 skeletal muscle cells. *Biochimica et Biophysica Acta (BBA) - Biomembranes*, 1711(1), 33-40.

Guyon, J. R., Steffen, L. S., Howell, M. H., Pusack, T. J., Lawrence, C. & Kunkel, L. M. (2007). Modeling human muscle disease in zebrafish. *Biochimica et Biophysica Acta*, 1772(2), 205-15.

Hall, Z. W. & Sanes, J. R. (1993). Synaptic structure and development: The neuromuscular junction. *Cell*, 72.

Hamill, O. P., Marty, A., Neher, E., Sakmann, B. & Sigworth, F. J. (1981). Improved patch-clamp techniques for high-resolution current recording from cells and cell-free membrane patches. *Pflugers Archiv*, 391(2), 85-100.

Hamilton, S. L. (2005). Ryanodine receptors. *Cell Calcium*, 38(3-4), 253-60.

Harayama, T. & Riezman, H. (2018). Understanding the diversity of membrane lipid composition. *Nature Reviews in Molecular Cell Biology*, 19(5), 281-296.

Harkewicz, R., Du, H., Tong, Z., Alkuraya, H., Bedell, M., Sun, W., Wang, X., Hsu, Y. H., Esteve-Rudd, J., Hughes, G., Su, Z., Zhang, M., Lopes, V. S., Molday, R. S., Williams, D. S., Dennis, E. A. & Zhang, K. (2012). Essential role of ELOVL4 protein in very long chain fatty acid synthesis and retinal function. *Journal of Biological Chemistry*, 287(14), 11469-80.

Heasman, J. (2002). Morpholino oligos: making sense of antisense? *Developmental Biology*, 243(2), 209-14.

Helland, I. B., Smith, L., Saarem, K., Saugstad, O. D. & Drevon, C. A. (2003). Maternal Supplementation With Very-Long-Chain n-3 Fatty Acids During Pregnancy and Lactation Augments Children's IQ at 4 Years of Age. *Pediatrics*, 111(1), e39.

Henry, C. A., McNulty, I. M., Durst, W. A., Munchel, S. E. & Amacher, S. L. (2005). Interactions between muscle fibers and segment boundaries in zebrafish. *Developmental Biology*, 287(2), 346-60.

Hernandez-Ochoa, E. O. & Schneider, M. F. (2018). Voltage sensing mechanism in skeletal muscle excitation-contraction coupling: coming of age or midlife crisis*? Skeletal Muscle*, 8(20).

Hille, F., Richter, H., Wong, S. P., Bratovic, M., Ressel, S. & Charpentier, E. (2018). The Biology of CRISPR-Cas: Backward and Forward. *Cell*, 172(6), 1239-1259.

Hogan, B. M., Verkade, H., Lieschke, G. J. & Heath, J. K. (2008). Manipulation of gene expression during zebrafish embryonic development using transient approaches. *Methods in Molecular Biology*, 469.

Horstick, E. J., Gibbs, E. M., Li, X., Davidson, A. E. & Dowling, J. J. (2013). Analysis of embryonic and larval zebrafish skeletal myofibers from dissociated preparations. *Journal of visualized experiments: JoVE,* 81, e50259-e50259.

Howe, K., Clark, M. D., Torroja, C. F., Torrance, J., Berthelot, C., Muffato, M., Collins, J. E., Humphray, S., McLaren, K., Matthews, L., McLaren, S., Sealy, I., Caccamo, M., Churcher, C., Scott, C., Barrett, J. C., Koch, R., Rauch, G.-J., White, S., Chow, W., Kilian, B., Quintais, L. T., Guerra-Assunção, J. A., Zhou, Y., Gu, Y., Yen, J., Vogel, J.-H., Eyre, T., Redmond, S., Banerjee, R., Chi, J., Fu, B., Langley, E., Maguire, S. F., Laird, G. K., Lloyd, D., Kenyon, E., Donaldson, S., Sehra, H., Almeida-King, J., Loveland, J., Trevanion, S., Jones, M., Quail, M., Willey, D., Hunt, A., Burton, J., Sims, S., McLay, K., Plumb, B., Davis, J., Clee, C., Oliver,

K., Clark, R., Riddle, C., Elliott, D., Threadgold, G., Harden, G., Ware, D., Begum, S., Mortimore, B., Kerry, G., Heath, P., Phillimore, B., Tracey, A., Corby, N., Dunn, M., Johnson, C., Wood, J., Clark, S., Pelan, S., Griffiths, G., Smith, M., Glithero, R., Howden, P., Barker, N., Lloyd, C., Stevens, C., Harley, J., Holt, K., Panagiotidis, G., Lovell, J., Beasley, H., Henderson, C., Gordon, D., Auger, K., Wright, D., Collins, J., Raisen, C., Dyer, L., Leung, K., Robertson, L., Ambridge, K., Leongamornlert, D., McGuire, S., Gilderthorp, R., Griffiths, C., Manthravadi, D., Nichol, S., Barker, G., et al. (2013). The zebrafish reference genome sequence and its relationship to the human genome. *Nature*, 496(498).

Hruscha, A., Krawitz, P., Rechenberg, A., Heinrich, V., Hecht, J., Haass, C. & Schmid, B. (2013). Efficient CRISPR/Cas9 genome editing with low off-target effects in zebrafish. *Development*, 140(24), 4982-7.

Huxley, A. F. (1957). Muscle Structure and Theories of Contraction. *Progress in Biophysics and Biophysical Chemistry*, 7.

Huxley, H. & Hanson, J. (1954). Changes in the Cross-Striations of Muscle during Contraction and Stretch and their Structural Interpretation. *Nature*, 173(973).

Igarashi, M., Ma, K., Chang, L., Bell, J. M. & Rapoport, S. I. (2008). Rat heart cannot synthesize docosahexaenoic acid from circulating alpha-linolenic acid because it lacks elongase-2. *Journal of Lipid Research*, 49(8), 1735-45.

Ikeda, M., Kanao, Y., Yamanaka, M., Sakuraba, H., Mizutani, Y., Igarashi, Y. & Kihara, A. (2008). Characterization of four mammalian 3-hydroxyacyl-CoA dehydratases involved in very long-chain fatty acid synthesis. *FEBS Letters*, 582(16), 2435-40.

Infantolino, B. W., Ellis, M. J. & Challis, J. H. (2010). Individual Sarcomere Lengths in Whole Muscle Fibers and Optimal Fiber Length Computation. *The Anatomical Record*, 293(11), 1913-1919.

Ito, K., Komazaki, S., Sasamoto, K., Yoshida, M., Nishi, M., Kitamura, K. & Takeshima, H. (2001). Deficiency of triad junction and contraction in mutant skeletal muscle lacking junctophilin type 1. *The Journal of Cell Biology*, 154(5), 1059-1067.

Jacquemond, V. (1997). Indo-1 fluorescence signals elicited by membrane depolarization in enzymatically isolated mouse skeletal muscle fibers. *Biophysical Journal*, 73(2), 920-928.

Jakobsson, A., Westerberg, R. & Jacobsson, A. (2006). Fatty acid elongases in mammals: Their regulation and roles in metabolism. *Progress in Lipid Research*, 45(3), 237-249.

Jing, L. (2012). Culture, Differentiation and Transfection of C2C12 Myoblasts. *Bio-protocol*, 2(10), e172.

Joung, J. K. & Sander, J. D. (2013). TALENs: a widely applicable technology for targeted genome editing. Nature reviews. *Molecular cell biology*, 14(1), 49-55.

Jungbluth, H., Cullup, T., Lillis, S., Zhou, H., Abbs, S., Sewry, C. & Muntoni, F. (2010). Centronuclear myopathy with cataracts due to a novel dynamin 2 (DNM2) mutation. *Neuromuscular Disorders*, 20(1), 49-52.
Jungbluth, H. & Gautel, M. (2014). Pathogenic mechanisms in centronuclear myopathies. *Frontiers in Aging Neuroscience*, 6.

Jungbluth, H., Treves, S., Zorzato, F., Sarkozy, A., Ochala, J., Sewry, C., Phadke, R., Gautel, M. & Muntoni, F. (2018). Congenital myopathies: disorders of excitation-contraction coupling and muscle contraction. *Nature Reviews Neurology*, 14(3), 151-167.

Jungbluth, H., Wallgren-Pettersson, C. & Laporte, J. (2008). Centronuclear (myotubular) myopathy. Orphanet *Journal of Rare Disease*, 3(26).

Jungbluth, H., Zhou, H., Sewry, C. A., Robb, S., Treves, S., Bitoun, M., Guicheney, P., Buj-Bello, A., Bönnemann, C. & Muntoni, F. (2007). Centronuclear myopathy due to a de novo dominant mutation in the skeletal muscle ryanodine receptor (RYR1) gene. *Neuromuscular Disorders*, 17(4), 338-345.

Kabashi, E., Brustein, E., Champagne, N. & Drapeau, P. (2011). Zebrafish models for the functional genomics of neurogenetic disorders. *Biochimica et Biophysica Acta (BBA) - Molecular Basis of Disease*, 1812(3), 335-345.

Karunasekara, Y., Rebbeck, R. T., Weaver, L. M., Board, P. G., Dulhunty, A. F. & Casarotto, M. G. (2012). An alpha-helical C-terminal tail segment of the skeletal L-type Ca^{2+} channel beta1a subunit activates ryanodine receptor type 1 via a hydrophobic surface. *FASEB Journal*, 26(12), 5049-59.

Kasher, P. R., Jenkinson, E. M., Briolat, V., Gent, D., Morrissey, C., Zeef, L. A. H., Rice, G. I., Levraud, J.-P. & Crow, Y. J. (2015). Characterization of samhd1 Morphant Zebrafish Recapitulates Features of the Human Type I Interferonopathy Aicardi-Goutières Syndrome. *The Journal of Immunology*, 194(6), 2819.

Kassar-Duchossoy, L., Giacone, E., Gayraud-Morel, B., Jory, A., Gomes, D. & Tajbakhsh, S. (2005). Pax3/Pax7 mark a novel population of primitive myogenic cells during development. *Genes and Development*, 19(12), 1426-31.

Keynes, R., Aidley, D., & Huang, C. (2011). Frontmatter. *In Nerve and Muscle*. Cambridge: Cambridge University Press

Kiens, B. (2006). Skeletal Muscle Lipid Metabolism in Exercise and Insulin Resistance. *Physiological Reviews*, 86(1), 205-243.

Kihara, A. (2012). Very long-chain fatty acids: elongation, physiology and related disorders. *Journal of Biochemistry*, 152(5), 387-95.

Kihara, A. (2014). Sphingosine 1-phosphate is a key metabolite linking sphingolipids to glycerophospholipids. *Biochimica et Biophysica Acta (BBA) - Molecular and Cell Biology of Lipids*, 1841(5), 766-772.

Kihara, A., Sakuraba, H., Ikeda, M., Denpoh, A. & Igarashi, Y. (2008). Membrane topology and essential amino acid residues of Phs1, a 3-hydroxyacyl-CoA dehydratase involved in very long-chain fatty acid elongation. *Journal of Biological Chemistry*, 283(17), 11199-209.

Kim, D. H., Sun, Y., Yun, S., Kim, B., Hwang, C. N., Nelson, B. & Lee, S. H. (2004). Mechanical property characterization of the zebrafish embryo chorion. *Conference Proceedings IEEE Engineering in Medicine and Biology Science*, 7.

Kim, J.-B., Kim, S.-J., Kang, S.-Y., Yi, J. W. & Kim, S.-M. (2014). The large-conductance calcium-activated potassium channel holds the key to the conundrum of familial hypokalemic periodic paralysis. *Korean Journal of Pediatrics*, 57(10), pp 445-450.

Kimmel, C. B., Ballard, W. W., Kimmel, S. R., Ullmann, B. & Schilling, T. F. (1995). Stages of embryonic development of the zebrafish. *Developmental Dynamics*, 203(3), 253-310.

Kinsella, J. E. (1990). Lipids, Membrane Receptors, and Enzymes: Effects of Dietary Fatty Acids. *Journal of Parenteral and Enteral Nutrition*, 14(5S), 200S-217S.

Koch, M. C., Steinmeyer, K., Lorenz, C., Ricker, K., Wolf, F., Otto, M., Zoll, B., Lehmann-Horn, F., Grzeschik, K. H. & Jentsch, T. J. (1992). The skeletal muscle chloride channel in dominant and recessive human myotonia. *Science*, 257(5071), 797-800.

Kok, F. O., Shin, M., Ni, C. W., Gupta, A., Grosse, A. S., van Impel, A., Kirchmaier, B. C., Peterson-Maduro, J., Kourkoulis, G., Male, I., DeSantis, D. F., Sheppard-Tindell, S., Ebarasi, L., Betsholtz, C., Schulte-Merker, S., Wolfe, S. A. & Lawson, N. D. (2015). Reverse genetic screening reveals poor correlation between morpholino-induced and mutant phenotypes in zebrafish. *Developmental Cell*, 32(1), 97-108.

Komazaki, S., Nishi, M., Takeshima, H. & Nakamura, H. (2001). Abnormal formation of sarcoplasmic reticulum networks and triads during early development of skeletal muscle cells in mitsugumin29-deficient mice. *Development, Growth & Differentiation*, 43(6), 717-723.

Konishi, H., Okuda, A., Ohno, Y. & Kihara, A. (2010). Characterization of HACD1 K64Q mutant found in arrhythmogenic right ventricular dysplasia patients. *Journal of Biochemistry*, 148(5), 617-22.

Kramer, J. W., Hegreberg, G. A., Bryan, G. M., Meyers, K. & Ott, R. L. (1976). A muscle disorder of Labrador retrievers characterized by deficiency of type II muscle fibers. *Journal of the American Veterinary Medical Association*, 169(8), 817-20.

Krüger, J., Kunert-Keil, C., Bisping, F. & Brinkmeier, H. (2008). Transient receptor potential cation channels in normal and dystrophic mdx muscle. *Neuromuscular Disorders*, 18(6), 501-513.

Kurth, F., Franco-Obregon, A., Casarosa, M., Kuster, S. K., Wuertz-Kozak, K. & Dittrich, P. S. (2015). Transient receptor potential vanilloid 2-mediated shear-stress responses in C2C12 myoblasts are regulated by serum and extracellular matrix. *FASEB Journal*, 29(11), pp 4726-4737.

Ladbrooke, B. D. & Chapman, D. (1969). Thermal analysis of lipids, proteins and biological membranes. A review and summary of some recent studies. *Chemistry Physics Lipids*, 3(4), 304-56.

Laforêt, P. & Vianey-Saban, C. (2010). Disorders of muscle lipid metabolism: Diagnostic and therapeutic challenges. *Neuromuscular Disorders*, 20(11), 693-700.

Lanner, J. T., Georgiou, D. K., Joshi, A. D. & Hamilton, S. L. (2010). Ryanodine receptors: structure, expression, molecular details, and function in calcium release. *Cold Spring Harbour Perspectives in Biology*, 2(11).

Laporte, J., Hu, L. J., Kretz, C., Mandel, J. L., Kioschis, P., Coy, J. F., Klauck, S. M., Poustka, A. & Dahl, N. (1996). A gene mutated in X-linked myotubular myopathy defines a new putative tyrosine phosphatase family conserved in yeast. *Nature Genetics*, 13(2), 175-82.

Laporte, J., Guiraud-Chaumeil, C., Vincent, M. C., Mandel, J. L., Tanner, S. M., Liechti-Gallati, S., Wallgren-Pettersson, C., Dahl, N., Kress, W., Bolhuis, P. A., Fardeau, M., Samson, F. & Bertini, E. (1997). Mutations in the MTM1 gene implicated in X-linked myotubular myopathy. ENMC International Consortium on Myotubular Myopathy. European Neuro-Muscular Center. *Human Molecular Genetics*, 6(9), 1505-11.

Lauritzen, L., Hansen, H. S., Jorgensen, M. H. & Michaelsen, K. F. (2001). The essentiality of long chain n-3 fatty acids in relation to development and function of the brain and retina. *Progress in Lipid Research*, 40(1-2), 1-94.

Le Poul, E., Loison, C., Struyf, S., Springael, J. Y., Lannoy, V., Decobecq, M. E., Brezillon, S., Dupriez, V., Vassart, G., Van Damme, J., Parmentier, M. & Detheux, M. (2003). Functional characterization of human receptors for short chain fatty acids and their role in polymorphonuclear cell activation. *Journal of Biological Chemistry*, 278(28), 25481-9.

Lee, E., Marcucci, M., Daniell, L., Pypaert, M., Weisz, O. A., Ochoa, G. C., Farsad, K., Wenk, M. R. & De Camilli, P. (2002). Amphiphysin 2 (Bin1) and T-tubule biogenesis in muscle. *Science*, 297(5584), 1193-6.

Lee, E. H., Cherednichenko, G., Pessah, I. N. & Allen, P. D. (2006). Functional coupling between TRPC3 and RyR1 regulates the expressions of key triadic proteins. *Journal of Biological Chemistry*, 281(15), 10042-8.

Lee, J. H., Tachibana, H., Morinaga, Y., Fujimura, Y. & Yamada, K. (2009). Modulation of proliferation and differentiation of C2C12 skeletal muscle cells by fatty acids. *Life Sciences*, 84(13-14), 415-20.

Lee, U. S. & Cui, J. (2010). BK channel activation: structural and functional insights. *Trends in Neurosciences*, 33(9), 415-423.

Leech, C. A. & Holz, G. G. T. (1994). Application of patch clamp methods to the study of calcium currents and calcium channels. *Methods in Cell Biology*, 40.

Leikina, E., Melikov, K., Sanyal, S., Verma, S. K., Eun, B., Gebert, C., Pfeifer, K., Lizunov, V. A., Kozlov, M. M. & Chernomordik, L. V. (2013). Extracellular annexins and dynamin are important for sequential steps in myoblast fusion. *Journal of Cell Biology*, 200(1), 109-23.

Leonard, A. E., Pereira, S. L., Sprecher, H. & Huang, Y.-S. (2004). Elongation of long-chain fatty acids. *Progress in Lipid Research*, 43(1), 36-54.

Li, D., Gonzalez, O., Bachinski, L. L. & Roberts, R. (2000). Human protein tyrosine phosphatase-like gene: expression profile, genomic structure, and mutation analysis in families with ARVD. *Gene*, 256(1-2), 237-243.

Li, J., King, N. C. & Sinoway, L. I. (2003). ATP concentrations and muscle tension increase linearly with muscle contraction. *Journal of Applied Physiology*, 95(2), 577-583.

Li, J., Vosegaard, T. & Guo, Z. (2017). Applications of nuclear magnetic resonance in lipid analyses: An emerging powerful tool for lipidomics studies. *Progress in Lipid Research*, 68.

Li, L. & Dixon, J. E. (2000). Form, function, and regulation of protein tyrosine phosphatases and their involvement in human diseases. *Seminars in Immunology*, 12(1), 75-84.

Li, W., Sandhoff, R., Kono, M., Zerfas, P., Hoffmann, V., Ding, B. C.-H., Proia, R. L. & Deng, C.-X. (2007). Depletion of ceramides with very long chain fatty acids causes defective skin permeability barrier function, and neonatal lethality in ELOVL4 deficient mice. *International Journal of Biological Sciences*, 3(2), 120-128.

Lieschke, G. J. & Currie, P. D. (2007). Animal models of human disease: zebrafish swim into view. *Nature Reviews Genetics*, 8(5), 353-67.

Lin, X., Yang, X., Li, Q., Ma, Y., Cui, S., He, D., Lin, X., Schwartz, R. J. & Chang, J. (2012). Protein tyrosine phosphatase-like A regulates myoblast proliferation and differentiation through MyoG and the cell cycling signaling pathway. *Molecular Cell Biology*, 32(2), 297-308.

Liu, J., Zhou, Y., Qi, X., Chen, J., Chen, W., Qiu, G., Wu, Z. & Wu, N. (2017). CRISPR/Cas9 in zebrafish: an efficient combination for human genetic diseases modeling. *Human Genetics*, 136(1), 1-12.

Livak, K. J. & Schmittgen, T. D. (2001). Analysis of relative gene expression data using real-time quantitative PCR and the 2(-Delta Delta C(T)) Method. *Methods*, 25(4), 402-8.

Lorenzon, P., Giovannelli, A., Ragozzino, D., Eusebi, F. & Ruzzier, F. (1997). Spontaneous and Repetitive Calcium Transients in C2C12 Mouse Myotubes during In Vitro Myogenesis. *European Journal of Neuroscience*, 9(4), 800-808.

Louis, M., Zanou, N., Van Schoor, M. & Gailly, P. (2008). TRPC1 regulates skeletal myoblast migration and differentiation. *Journal of Cell Science*, 121(Pt 23), 3951-9.

Maier, F., Demmelmair, H., Fugmann, M., Hellmuth, C., Lechner, A., Koletzko, B. & Uhl, O. (2016). Contribution of glycerophospholipids and sphingomyelin to the circulating NEFA. *Prostaglandins, Leukotrienes and Essential Fatty Acids*, 110.

Majczenko, K., Davidson, Ann E., Camelo-Piragua, S., Agrawal, Pankaj B., Manfready, Richard A., Li, X., Joshi, S., Xu, J., Peng, W., Beggs, Alan H., Li, Jun Z., Burmeister, M. & Dowling, James J. (2012). Dominant Mutation of CCDC78 in a Unique Congenital Myopathy with Prominent Internal Nuclei and Atypical Cores. *The American Journal of Human Genetics*, 91(2), 365-371.

Manabe, Y., Miyatake, S., Takagi, M., Nakamura, M., Okeda, A., Nakano, T., Hirshman, M. F., Goodyear, L. J. & Fujii, N. L. (2012). Characterization of an Acute Muscle Contraction Model Using Cultured C2C12 Myotubes. *Plos One*, 7(12), 10.

Mandrell, D., Truong, L., Jephson, C., Sarker, M. R., Moore, A., Lang, C., Simonich, M. T. & Tanguay, R. L. (2012). Automated zebrafish chorion removal and single embryo placement: optimizing throughput of zebrafish developmental toxicity screens. *Journal of Laboratory Automation*, 17(1), 66-74.

Manhart, A., Windner, S., Baylies, M. & Mogilner, A. (2018). Mechanical positioning of multiple nuclei in muscle cells. *Plos Computational Biology*, 14(6), 25.

Marshall, A., T Blakney, G., Chen, T., K Kaiser, N., M McKenna, A., P Rodgers, R., M Ruddy, B. & Xian, F. (2013). Mass resolution and mass accuracy: how much is enough? *Mass Spectrometry* (Tokyo, Japan), 2(Spec Iss), S0009-S0009.

Marty, I. & Fauré, J. (2016). Excitation-Contraction Coupling Alterations in Myopathies. *Journal of Neuromuscular Diseases*, 3(4), 443-453.

Maurer M, B. J., Pele M, Barthelemy I, Blot S, Aubin-Houzelstein G, Storck-Pilot F & Tiret L. (2010). The PTPLA gene, mutated in a dog model of centronuclear myopathy, is prone to a physiological tissue specific alternative splicing that produces isoforms with putatively distinct structural and functional properties. *Proceedings of the XIIth International Congress on Neuromuscular diseases*, Naples, Italy.

Maurer, M., Mary, J., Guillaud, L., Fender, M., Pelé, M., Bilzer, T., Olby, N., Penderis, J., Shelton, G. D., Panthier, J.-J., Thibaud, J.-L., Barthélémy, I., Aubin-Houzelstein, G., Blot, S., Hitte, C. & Tiret, L. (2012). Centronuclear Myopathy in Labrador Retrievers: A Recent Founder Mutation in the PTPLA Gene Has Rapidly Disseminated Worldwide. *PloS One*, 7(10), e46408.

Maxfield, F. R. & Tabas, I. (2005). Role of cholesterol and lipid organization in disease. *Nature*, 438(7068), 612-21.

Maxfield, F. R. & van Meer, G. (2010). Cholesterol, the central lipid of mammalian cells. *Current Opinion in Cell Biology*, 22(4), 422-429.

McCurley, A. T. & Callard, G. V. (2008). Characterization of housekeeping genes in zebrafish: male-female differences and effects of tissue type, developmental stage and chemical treatment. *BMC Molecular Biology*, 9(1), 102.

McKenna, M. J., Bangsbo, J. & Renaud, J.-M. (2008). Muscle K^+, Na^+, and Cl^- disturbances and Na^+-K^+ pump inactivation: implications for fatigue. *Journal of Applied Physiology*, 104(1), 288-295.

McKerrell, R. E. & Braund, K. G. (1987). Hereditary myopathy in Labrador Retrievers: clinical variations. *Journal of Small Animal Practice*, 28(6), 479-489.

McMahon, D. K., Anderson, P. A., Nassar, R., Bunting, J. B., Saba, Z., Oakeley, A. E. & Malouf, N. N. (1994). C2C12 cells: biophysical, biochemical, and immunocytochemical properties. *American Journal of Physiology-Cell Physiology*, 266(6), C1795-C1802.
McMillin, M. J., Below, J. E., Shively, K. M., Beck, A. E., Gildersleeve, H. I., Pinner, J., Gogola, G. R., Hecht, J. T., Grange, D. K., Harris, D. J., Earl, D. L., Jagadeesh, S., Mehta, S. G., Robertson, S. P., Swanson, J. M., Faustman, E. M., Mefford, H. C., Shendure, J., Nickerson, D. A., Bamshad, M. J. & University of Washington Center for Mendelian, G. (2013). Mutations in ECEL1 cause distal arthrogryposis type 5D. *American Journal of Human Genetics*, 92(1), 150-156.

Mehravar, M., Shirazi, A., Nazari, M. & Banan, M. (2019). Mosaicism in CRISPR/Cas9-mediated genome editing. *Developmental Biology*, 445(2), 156-162.

Meyer, A. & Schartl, M. (1999). Gene and genome duplications in vertebrates: the one-to-four (-to-eight in fish) rule and the evolution of novel gene functions. *Current Opinions in Cell Biology*, 11(6), 699-704.

Molino, D., Van der Giessen, E., Gissot, L., Hematy, K., Marion, J., Barthelemy, J., Bellec, Y., Vernhettes, S., Satiat-Jeunemaitre, B., Galli, T., Tareste, D. & Faure, J. D. (2014). Inhibition of very long acyl chain sphingolipid synthesis modifies membrane dynamics during plant cytokinesis. *Biochimica et Biophysica Acta*, 1842(10), 1422-30.

Monroig, O., Rotllant, J., Cerda-Reverter, J. M., Dick, J. R., Figueras, A. & Tocher, D. R. (2010). Expression and role of Elovl4 elongases in biosynthesis of very long-chain fatty acids during zebrafish Danio rerio early embryonic development. *Biochimica et Biophysica Acta*, 1801(10), 1145-54.

Monroig, O., Rotllant, J., Sanchez, E., Cerda-Reverter, J. M. & Tocher, D. R. (2009). Expression of long-chain polyunsaturated fatty acid (LC-PUFA) biosynthesis genes during

zebrafish Danio rerio early embryogenesis. *Biochimica et Biophysica Acta*, 1791(11), 1093-101.

Moon, Y. A., Hammer, R. E. & Horton, J. D. (2009). Deletion of ELOVL5 leads to fatty liver through activation of SREBP-1c in mice. *Journal of Lipid Research*, 50(3), 412-23.

Moon, Y. A. & Horton, J. D. (2003). Identification of two mammalian reductases involved in the two-carbon fatty acyl elongation cascade. *Journal of Biological Chemistry*, 278(9), 7335-43.

Moon, Y. A., Shah, N. A., Mohapatra, S., Warrington, J. A. & Horton, J. D. (2001). Identification of a mammalian long chain fatty acyl elongase regulated by sterol regulatory element-binding proteins. *Journal of Biological Chemistry*, 276(48), pp 45358-66.

Morales, P. E., Bucarey, J. L. & Espinosa, A. (2017). Muscle Lipid Metabolism: Role of Lipid Droplets and Perilipins. *Journal of Diabetes Research*.

Morgan, R. S., Walmsley, G., Dyer, S., O'Brien, F., Staunton, C., Blondelle, J., Tiret, L., Piercy, R. & Barrett-Jolley, R. (2018). Ion Channel Activity in a 3-hydroxyacyl-coA dehydratase 1 (HACD1) Deficient Muscle Cell Line. *The FASEB Journal*, 32(1t), lb484-lb484.

Moritz, B., Becker, P. B. & Göpfert, U. (2015). CMV promoter mutants with a reduced propensity to productivity loss in CHO cells. *Scientific Reports*, 5(16952).

Muhammad, E., Reish, O., Ohno, Y., Scheetz, T., Deluca, A., Searby, C., Regev, M., Benyamini, L., Fellig, Y., Kihara, A., Sheffield, V. C. & Parvari, R. (2013). Congenital myopathy is caused by mutation of HACD1. *Human Molecular Genetics*, 22(25), 5229-36.

Mukai, A., Kurisaki, T., Sato, S. B., Kobayashi, T., Kondoh, G. & Hashimoto, N. (2009). Dynamic clustering and dispersion of lipid rafts contribute to fusion competence of myogenic cells. *Experimental Cell Research*, 315(17), 3052-3063.

Nance, J. R., Dowling, J. J., Gibbs, E. M. & Bönnemann, C. G. (2012). Congenital myopathies: an update. *Current Neurology and Neuroscience Reports*, 12(2), 165-174.

Nasiadka, A. & Clark, M. D. (2012). Zebrafish breeding in the laboratory environment. *ILAR Journal*, 53(2), 161-8.

Nicolson, G. L. & Ash, M. E. (2017). Membrane Lipid Replacement for chronic illnesses, aging and cancer using oral glycerolphospholipid formulations with fructooligosaccharides to restore phospholipid function in cellular membranes, organelles, cells and tissues. *Biochimica et Biophysica Acta (BBA) - Biomembranes*, 1859(9), 1704-1724.

Nicot, A.-S., Toussaint, A., Tosch, V., Kretz, C., Wallgren-Pettersson, C., Iwarsson, E., Kingston, H., Garnier, J.-M., Biancalana, V., Oldfors, A., Mandel, J.-L. & Laporte, J. (2007).

Mutations in amphiphysin 2 (BIN1) disrupt interaction with dynamin 2 and cause autosomal recessive centronuclear myopathy. *Nature Genetics*, 39(1134).

Nishida, M. & MacKinnon, R. (2002). Structural Basis of Inward Rectification: Cytoplasmic Pore of the G Protein-Gated Inward Rectifier GIRK1 at 1.8 Å Resolution. *Cell*, 111(7), 957-965.

Nori A, Valle G, Bortoloso E, Turcato F & Volpe P. (2006). Calsequestrin targeting to sarcoplasmic
reticulum of skeletal muscle fibers. *American Journal of Physiology - Cell Physiology* 291, C245-253.

North, K. (2008). What's new in congenital myopathies? *Neuromuscular Disorders*, 18(6), 433-442.

North, K. N. & Clarke, N. F. (2003). Congenital Fiber Type Disproportion—30 Years On. Journal of *Neuropathology & Experimental Neurology*, 62(10), 977-989.

North, K. N., Wang, C. H., Clarke, N., Jungbluth, H., Vainzof, M., Dowling, J. J., Amburgey, K., Quijano-Roy, S., Beggs, A. H., Sewry, C., Laing, N. G. & Bonnemann, C. G. (2014). Approach to the diagnosis of congenital myopathies. *Neuromuscular Disorders*, 24(2), 97-116.

Nugteren, D. H. (1965). The enzymic chain elongation of fatty acids by rat-liver microsomes. *Biochimica et Biophysica Acta*, 106(2), 280-90.

O'Grady, G. L., Best, H. A., Sztal, T. E., Schartner, V., Sanjuan-Vazquez, M., Donkervoort, S., Abath Neto, O., Sutton, R. B., Ilkovski, B., Romero, N. B., Stojkovic, T., Dastgir, J., Waddell, L. B., Boland, A., Hu, Y., Williams, C., Ruparelia, A. A., Maisonobe, T., Peduto, A. J., Reddel, S. W., Lek, M., Tukiainen, T., Cummings, B. B., Joshi, H., Nectoux, J., Brammah, S., Deleuze, J. F., Ing, V. O., Ramm, G., Ardicli, D., Nowak, K. J., Talim, B., Topaloglu, H., Laing, N. G., North, K. N., MacArthur, D. G., Friant, S., Clarke, N. F., Bryson-Richardson, R. J., Bonnemann, C. G., Laporte, J. & Cooper, S. T. (2016). Variants in the Oxidoreductase PYROXD1 Cause Early-Onset Myopathy with Internalized Nuclei and Myofibrillar Disorganization. *American Journal of Human Genetics*, 99(5), 1086-1105.

Obara, K., Kojima, R. & Kihara, A. (2013). Effects on vesicular transport pathways at the late endosome in cells with limited very long-chain fatty acids. *Journal of Lipid Research*, 54(3), 831-42.

Obukhov, A. G. & Nowycky, M. C. (2004). TRPC5 activation kinetics are modulated by the scaffolding protein ezrin/radixin/moesin-binding phosphoprotein-50 (EBP50*). Journal of Cellular Physiology*, 201(2), 227-235.

Ohno, Y., Suto, S., Yamanaka, M., Mizutani, Y., Mitsutake, S., Igarashi, Y., Sassa, T. & Kihara, A. (2010). ELOVL1 production of C24 acyl-CoAs is linked to C24 sphingolipid synthesis. *Proceedings of the National Academy of Sciences*, 107(43), 18439.

Osseni, A., Sebastien, M., Sarrault, O., Baudet, M., Coute, Y., Faure, J., Fourest-Lieuvin, A. & Marty, I. (2016). Triadin and CLIMP-63 form a link between triads and microtubules in muscle cells. *Journal of Cell Science*, 129(20), 3744-3755.

Paglia, G., Kliman, M., Claude, E., Geromanos, S. & Astarita, G. (2015). Applications of ion-mobility mass spectrometry for lipid analysis. *Analytical and Bioanalytical Chemistry*, 407(17), 4995-5007.

Paolini, C., Protasi, F. & Franzini-Armstrong, C. (2004). The relative position of RyR feet and DHPR tetrads in skeletal muscle. *Journal of Molecular Biology*, 342(1), 145-53.

Parton, R. G., Way, M., Zorzi, N. & Stang, E. (1997). Caveolin-3 Associates with Developing T-tubules during Muscle Differentiation. *The Journal of Cell Biology*, 136(1), 137.

Pavlath, G. K., Rich, K., Webster, S. G. & Blau, H. M. (1989). Localization of muscle gene products in nuclear domains. *Nature*, 337(6207), 570-3.

Pelé, M., Tiret, L., Kessler, J.-L., Blot, S. & Panthier, J.-J. (2005). SINE exonic insertion in the PTPLA gene leads to multiple splicing defects and segregates with the autosomal recessive centronuclear myopathy in dogs. *Human Molecular Genetics*, 14(11), 1417-1427.

Phelps, H. A. & Neely, M. N. (2005). Evolution of the zebrafish model: from development to immunity and infectious disease. *Zebrafish*, 2(2), 87-103.

Pierson, C. R., Tomczak, K., Agrawal, P., Moghadaszadeh, B. & Beggs, A. H. (2005). X-linked myotubular and centronuclear myopathies. *Journal of Neuropathology & Experimental Neurology*, 64(7), 555-64.

Pitt, J. J. (2009). Principles and applications of liquid chromatography-mass spectrometry in clinical biochemistry. *The Clinical Biochemistry Reviews*, 30(1), 19-34.

Polster, A., Nelson, B. R., Papadopoulos, S., Olson, E. N. & Beam, K. G. (2018). Stac proteins associate with the critical domain for excitation-contraction coupling in the II-III loop of Ca(V)1.1. *Journal of General Physiology*, 150(4), 613-624.

Postlethwait, J., Amores, A., Force, A. & Yan, Y. L. (1999). The zebrafish genome. *Methods in Cell Biology*, 60.

Prives, J. & Shinitzky, M. (1977). Increased membrane fluidity precedes fusion of muscle cells. *Nature*, 268.

Quinlivan, V. H. & Farber, S. A. (2017). Lipid Uptake, Metabolism, and Transport in the Larval Zebrafish. *Frontiers in Endocrinology*, 8.

Rabionet, M., Bayerle, A., Jennemann, R., Heid, H., Fuchser, J., Marsching, C., Porubsky, S., Bolenz, C., Guillou, F., Grone, H. J., Gorgas, K. & Sandhoff, R. (2015). Male meiotic

cytokinesis requires ceramide synthase 3-dependent sphingolipids with unique membrane anchors. *Human Molecular Genetics*, 24(17), 4792-808.

Rebbeck, R. T., Karunasekara, Y., Gallant, E. M., Board, P. G., Beard, N. A., Casarotto, M. G. & Dulhunty, A. F. (2011). The β(1a) subunit of the skeletal DHPR binds to skeletal RyR1 and activates the channel via its 35-residue C-terminal tail. *Biophysical Journal*, 100(4), 922-930.

Riezman, H. (2007). The long and short of fatty acid synthesis. *Cell*, 130(4), 587-8.

Robin, G. & Allard, B. (2012). Dihydropyridine receptors actively control gating of ryanodine receptors in resting mouse skeletal muscle fibres. *Journal of Physiology*, 590(23), 6027-36.

Roe, C. R., Sweetman, L., Roe, D. S., David, F. & Brunengraber, H. (2002). Treatment of cardiomyopathy and rhabdomyolysis in long-chain fat oxidation disorders using an anaplerotic odd-chain triglyceride. *The Journal of Clinical Investigation*, 110(2), 259-269.

Roman, W. & Gomes, E. R. (2018). Nuclear positioning in skeletal muscle. *Seminars in Cell & Developmental Biology*, 82.

Romero, N. B. & Laporte, J. (2013). *Muscle Disease: Pathology and Genetics*, 2: Wiley-Blackwell.

Rosenhouse-Dantsker, A., Mehta, D. & Levitan, I. (2012). Regulation of ion channels by membrane lipids. *Comprehensive Physiology*, 2(1), 31-68.

Ross, J. A., Levy, Y., Svensson, K., Philp, A., Schenk, S. & Ochala, J. (2018). SIRT1 regulates nuclear number and domain size in skeletal muscle fibers. *Journal of Cellular Physiology*, 233(9), 7157-7163.

Rossi, A. E. & Dirksen, R. T. (2006). Sarcoplasmic reticulum: the dynamic calcium governor of muscle. *Muscle Nerve*, 33(6), 715-31.

Rossi, D., Barone, V., Giacomello, E., Cusimano, V. & Sorrentino, V. (2008). The sarcoplasmic reticulum: an organized patchwork of specialized domains. *Traffic* (Copenhagen, Denmark), 9(7), 1044-1049.

Rubakhin, S. S., Romanova, E. V., Nemes, P. & Sweedler, J. V. (2011). Profiling metabolites and peptides in single cells. *Nature Methods*, 8(4 Suppl), S20-9.

Sabha, N., Volpatti, J. R., Gonorazky, H., Reifler, A., Davidson, A. E., Li, X., Eltayeb, N. M., Dall'Armi, C., Di Paolo, G., Brooks, S. V., Buj-Bello, A., Feldman, E. L. & Dowling, J. J. (2016). PIK3C2B inhibition improves function and prolongs survival in myotubular myopathy animal models. *Journal of Clinical Investigation*, 126(9), 3613-25.

Sabourin, J., Lamiche, C., Vandebrouck, A., Magaud, C., Rivet, J., Cognard, C., Bourmeyster, N. & Constantin, B. (2009). Regulation of TRPC1 and TRPC4 cation channels requires an

alpha1-syntrophin-dependent complex in skeletal mouse myotubes. *Journal of Biological Chemistry*, 284(52), 36248-61.

Saint-Amant, L. & Drapeau, P. (1998). Time course of the development of motor behaviors in the zebrafish embryo. *Journal of Neurobiology*, 37(4), 622-32.

Sander, J. D. & Joung, J. K. (2014). CRISPR-Cas systems for editing, regulating and targeting genomes. *Nature Biotechnology*, 32(4), 347-55.

Sandow, A. (1952). Excitation-contraction coupling in muscular response. *The Yale Journal of Biology and Medicine*, 25(3), 176-201.

Sarasamma, S., Varikkodan, M. M., Liang, S. T., Lin, Y. C., Wang, W. P. & Hsiao, C. D. (2017). Zebrafish: A Premier Vertebrate Model for Biomedical Research in Indian Scenario. *Zebrafish*, 14(6), 589-605.

Sassa, T. & Kihara, A. (2014). Metabolism of very long-chain Fatty acids: genes and pathophysiology. *Biomolecules & Therapeutics* (Seoul), 22(2), 83-92.

Sassa, T., Ohno, Y., Suzuki, S., Nomura, T., Nishioka, C., Kashiwagi, T., Hirayama, T., Akiyama, M., Taguchi, R., Shimizu, H., Itohara, S. & Kihara, A. (2013). Impaired epidermal permeability barrier in mice lacking elovl1, the gene responsible for very-long-chain fatty acid production. *Molecular Cell Biology*, 33(14), 2787-96.

Sawai, M., Uchida, Y., Ohno, Y., Miyamoto, M., Nishioka, C., Itohara, S., Sassa, T. & Kihara, A. (2017). The 3-hydroxyacyl-CoA dehydratases HACD1 and HACD2 exhibit functional redundancy and are active in a wide range of fatty acid elongation pathways. *Journal of Biological Chemistry*, 292(37), 15538-15551.

Schartner, V., Romero, N. B., Donkervoort, S., Treves, S., Munot, P., Pierson, T. M., Dabaj, I., Malfatti, E., Zaharieva, I. T., Zorzato, F., Abath Neto, O., Brochier, G., Lornage, X., Eymard, B., Taratuto, A. L., Bohm, J., Gonorazky, H., Ramos-Platt, L., Feng, L., Phadke, R., Bharucha-Goebel, D. X., Sumner, C. J., Bui, M. T., Lacene, E., Beuvin, M., Labasse, C., Dondaine, N., Schneider, R., Thompson, J., Boland, A., Deleuze, J. F., Matthews, E., Pakleza, A. N., Sewry, C. A., Biancalana, V., Quijano-Roy, S., Muntoni, F., Fardeau, M., Bonnemann, C. G. & Laporte, J. (2017). Dihydropyridine receptor (DHPR, CACNA1S) congenital myopathy. *Acta Neuropathologica*, 133(4), 517-533.

Schiaffino, S. & Reggiani, C. (2011). Fiber types in mammalian skeletal muscles. *Physiology Review*, 91(4), 1447-531.

Schmidt, R., Strähle, U. & Scholpp, S. (2013). Neurogenesis in zebrafish – from embryo to adult. *Neural Development*, 8(1), 3.

Schneiter, R., Hitomi, M., Ivessa, A. S., Fasch, E. V., Kohlwein, S. D. & Tartakoff, A. M. (1996). A yeast acetyl coenzyme A carboxylase mutant links very-long-chain fatty acid

synthesis to the structure and function of the nuclear membrane-pore complex. *Molecular Cell Biology*, 16(12), 7161-72.

Schuldiner, M., Collins, S. R., Thompson, N. J., Denic, V., Bhamidipati, A., Punna, T., Ihmels, J., Andrews, B., Boone, C., Greenblatt, J. F., Weissman, J. S. & Krogan, N. J. (2005). Exploration of the function and organization of the yeast early secretory pathway through an epistatic miniarray profile. *Cell*, 123(3), 507-19.

Schultz, C., Neef, A. B., Gadella, T. W., Jr. & Goedhart, J. (2010). Labeling lipids for imaging in live cells. *Cold Spring Harbour Protocols*, (7).

Scott, W., Stevens, J. & Binder–Macleod, S. A. (2001). Human Skeletal Muscle Fiber Type Classifications. *Physical Therapy*, 81(11), 1810-1816.

Shenkman, B. S., Turtikova, O. V., Nemirovskaya, T. L. & Grigoriev, A. I. (2010). Skeletal muscle activity and the fate of myonuclei. *Acta Naturae*, 2(2), 59-66.

Sigruener, A., Kleber, M. E., Heimerl, S., Liebisch, G., Schmitz, G. & Maerz, W. (2014). Glycerophospholipid and Sphingolipid Species and Mortality: The Ludwigshafen Risk and Cardiovascular Health (LURIC) Study. *PloS One*, 9(1), e85724.

Smith, D. L. & Plowman, S. A. (2007). Chapter 2 - Understanding Muscle Contraction, In *Exercise Physiology for Health, Fitness, and Performance*, (ed 2), San Francisco.

Smith, L. L., Beggs, A. H. & Gupta, V. A. (2013). Analysis of skeletal muscle defects in larval zebrafish by birefringence and touch-evoke escape response assays. *Journal of Visualiszed Experiments (JoVE)*, 82), e50925.

Smith, L. L., Gupta, V. A. & Beggs, A. H. (2014). Bridging integrator 1 (Bin1) deficiency in zebrafish results in centronuclear myopathy. *Human Molecular Genetics*, 23(13), 3566-3578.

Sotgia, F., Woodman, S. E., Bonuccelli, G., Capozza, F., Minetti, C., Scherer, P. E. & Lisanti, M. P. (2003). Phenotypic behavior of caveolin-3 R26Q, a mutant associated with hyperCKemia, distal myopathy, and rippling muscle disease. *American Journal of Physiology - Cell Physiology*, 285(5), C1150-60.

Sparrow, J., Hughes, S. M. & Segalat, L. (2008). Other Model Organisms for Sarcomeric Muscle Diseases. In: Laing, N. G. (ed.) *Sarcomere and Skeletal Muscle Disease.* Berlin: Springer-Verlag Berlin.

Sperelakis, N. (1987). Electrophysiology of calcium antagonists. *Juornal of Molecular Cell Cardiology*, 19 (Suppl 2).

Spiro, A. J., Shy, G. & Gonatas, N. K. (1966). Myotubular myopathy: Persistence of fetal muscle in an adolescent boy. *Archives of Neurology*, 14(1), 1-14.

Stefanyk, L. E., Coverdale, N., Roy, B. D., Peters, S. J. & LeBlanc, P. J. (2010). Skeletal Muscle Type Comparison of Subsarcolemmal Mitochondrial Membrane Phospholipid Fatty Acid Composition in Rat. *Journal of Membrane Biology*, 234(3), 207-215.

Streisinger, G., Walker, C., Dower, N., Knauber, D. & Singer, F. (1981). Production of clones of homozygous diploid zebra fish (Brachydanio rerio). *Nature*, 291.

Suchyna, T. M., Markin, V. S. & Sachs, F. (2009). Biophysics and structure of the patch and the gigaseal. *Biophysical Journal*, 97(3), 738-747.

Summerton, J. (1999). Morpholino antisense oligomers: the case for an RNase H-independent structural type. *Biochimica et Biophysica Acta*, 1489(1), 141-58.

Syeda, R., Qiu, Z., Dubin, A. E., Murthy, S. E., Florendo, M. N., Mason, D. E., Mathur, J., Cahalan, S. M., Peters, E. C., Montal, M. & Patapoutian, A. (2016). LRRC8 Proteins Form Volume-Regulated Anion Channels that Sense Ionic Strength. *Cell*, 164(3), 499-511.

Tajsharghi, H., Thornell, L. E., Lindberg, C., Lindvall, B., Henriksson, K. G. & Oldfors, A. (2003). Myosin storage myopathy associated with a heterozygous missense mutation in MYH7. *Annals of Neurology*, 54(4), 494-500.

Takeshima, H., Komazaki, S., Nishi, M., Iino, M. & Kangawa, K. (2000). Junctophilins: a novel family of junctional membrane complex proteins. *Molecular Cell*, 6(1), 11-22.

Takeshima, H., Nishi, M., Iwabe, N., Miyata, T., Hosoya, T., Masai, I. & Hotta, Y. (1994). Isolation and characterization of a gene for a ryanodine receptor/calcium release channel in Drosophila melanogaster. *FEBS Letters*, 337(1), 81-7.

Tanaka, H., Harauma, A., Takimoto, M. & Moriguchi, T. (2015). Association between very long chain fatty acids in the meibomian gland and dry eye resulting from n-3 fatty acid deficiency. *Prostaglandins, Leukotrienes and Essential Fatty Acids (PLEFA)*, 97.

Tanaka, S., Ono, Y. & Sakamoto, K. (2017). DCEBIO facilitates myogenic differentiation via intermediate conductance Ca^{2+} activated K^{+} channel activation in C2C12 myoblasts. *Journal of Pharmacological Sciences*, 133(4), 276-279.

Thisse, B., Thisse, C. (2004). Fast Release Clones: A High Throughput Expression Analysis. ZFIN Direct Data Submission. [*http://zfin.org*].

Tidball, J. G., Dorshkind, K. & Wehling-Henricks, M. (2014). Shared signaling systems in myeloid cell-mediated muscle regeneration. *Development*, 141(6), 1184.

Tiers, G. V. D. (1958). Reliable Proton Nuclear Resonance Shielding Values by "Internal Referencing" with Tetramethyl-silane. *The Journal of Physical Chemistry*, 62(9), 1151-1152.

Tiller, K. E. & Tessier, P. M. (2015). Advances in Antibody Design. *Annual Review of Biomedical Engineering*, 17.

Tiret, L., Blot, S., Kessler, J. L., Gaillot, H., Breen, M. & Panthier, J. J. (2003). The cnm locus, a canine homologue of human autosomal forms of centronuclear myopathy, maps to chromosome 2. *Human Genetics*, 113(4), 297-306.

Tjondrokoesoemo, A., Park, K. H., Ferrante, C., Komazaki, S., Lesniak, S., Brotto, M., Ko, J.-K., Zhou, J., Weisleder, N. & Ma, J. (2011). Disrupted Membrane Structure and Intracellular Ca^{2+} Signaling in Adult Skeletal Muscle with Acute Knockdown of Bin1. *PloS One*, 6(9), pp e25740.

Todd, J. J., Razaqyar, M. S., Witherspoon, J. W., Lawal, T. A., Mankodi, A., Chrismer, I. C., Allen, C., Meyer, M. D., Kuo, A., Shelton, M. S., Amburgey, K., Niyazov, D., Fequiere, P., Bönnemann, C. G., Dowling, J. J. & Meilleur, K. G. (2018). Novel Variants in Individuals with RYR1-Related Congenital Myopathies: *Genetic, Laboratory, and Clinical Findings. Frontiers in Neurology*, 9(118).

Tondeur, S., Pangault, C., Le Carrour, T., Lannay, Y., Benmahdi, R., Cubizolle, A., Assou, S., Pantesco, V., Klein, B., Hamamah, S., Schved, J. F., Fest, T. & De Vos, J. (2010). Expression map of the human exome in CD34+ cells and blood cells: increased alternative splicing in cell motility and immune response genes. *PLoS One*, 5(2), e8990.

Toscano, A., Emmanuele, V., Savarese, M., Musumeci, O., Torella, A., Conca, E., Moggio, M., Nigro, V. & Rodolico, C. (2017). Pseudo-dominant inheritance of a novel homozygous HACD1 mutation associated with congenital myopathy: The first caucasian family. *Neuromuscular Disorders*, 27.

Tosch, V., Rohde, H. M., Tronchere, H., Zanoteli, E., Monroy, N., Kretz, C., Dondaine, N., Payrastre, B., Mandel, J. L. & Laporte, J. (2006). A novel PtdIns3P and PtdIns(3,5)P2 phosphatase with an inactivating variant in centronuclear myopathy. *Human Molecular Genetics*, 15(21), 3098-106.

Toussaint, A., Cowling, B. S., Hnia, K., Mohr, M., Oldfors, A., Schwab, Y., Yis, U., Maisonobe, T., Stojkovic, T., Wallgren-Pettersson, C., Laugel, V., Echaniz-Laguna, A., Mandel, J. L., Nishino, I. & Laporte, J. (2011). Defects in amphiphysin 2 (BIN1) and triads in several forms of centronuclear myopathies. *Acta Neuropathology*, 121(2), 253-66.

Tvrdik, P., Westerberg, R., Silve, S., Asadi, A., Jakobsson, A., Cannon, B., Loison, G. & Jacobsson, A. (2000). Role of a new mammalian gene family in the biosynthesis of very long chain fatty acids and sphingolipids. *Journal of Cell Biology*, 149(3), 707-18.

Uwanogho, D. A., Hardcastle, Z., Balogh, P., Mirza, G., Thornburg, K. L., Ragoussis, J. & Sharpe, P. T. (1999). Molecular cloning, chromosomal mapping, and developmental expression of a novel protein tyrosine phosphatase-like gene. *Genomics*, 62(3), 406-16.

Vainzof, M., Ayub-Guerrieri, D., Onofre, P. C., Martins, P. C., Lopes, V. F., Zilberztajn, D., Maia, L. S., Sell, K. & Yamamoto, L. U. (2008). Animal models for genetic neuromuscular diseases. *Journal of Molecular Neuroscience*, 34(3), 241-8.

Valdes De Hoyos, A., Hoz-Rodriguez, L., Arzate, H. & Narayanan, A. S. (2012). Isolation of protein-tyrosine phosphatase-like member-a variant from cementum. *Journal of Dental Research*, 91(2), 203-9.

Valentim, A. M., van Eeden, F. J., Strähle, U. & Olsson, I. A. S. (2016). Euthanizing zebrafish legally in Europe: Are the approved methods of euthanizing zebrafish appropriate to research reality and animal welfare? *EMBO Reports*, 17(12), 1688-1689.

van den Berg, R. A., Hoefsloot, H. C. J., Westerhuis, J. A., Smilde, A. K. & van der Werf, M. J. (2006). Centering, scaling, and transformations: improving the biological information content of metabolomics data. *BMC Genomics*, 7.

van Meer, G. & de Kroon, A. I. P. M. (2011). Lipid map of the mammalian cell. *Journal of Cell Science*, 124(1).

van Meer, G., Voelker, D. R. & Feigenson, G. W. (2008). Membrane lipids: where they are and how they behave. Nature reviews. *Molecular Cell Biology*, 9(2), 112-124.

Vasireddy, V., Uchida, Y., Salem, J. N., Kim, S. Y., Mandal, M. N. A., Reddy, G. B., Bodepudi, R., Alderson, N. L., Brown, J. C., Hama, H., Dlugosz, A., Elias, P. M., Holleran, W. M. & Ayyagari, R. (2007). Loss of functional ELOVL4 depletes very long-chain fatty acids (≥C28) and the unique ω-O-acylceramides in skin leading to neonatal death. *Human Molecular Genetics*, 16(5), 471-482.

Vega, A. V., Ramos-Mondragon, R., Calderon-Rivera, A., Zarain-Herzberg, A. & Avila, G. (2011). Calcitonin gene-related peptide restores disrupted excitation-contraction coupling in myotubes expressing central core disease mutations in RyR1. *Journal of Physiology*, 589(19), 4649-69.

Veldman, M. B. & Lin, S. (2008). Zebrafish as a developmental model organism for pediatric research. *Pediatric Research*, 64(5), 470-6.

Velica, P. & Bunce, C. M. (2011). A quick, simple and unbiased method to quantify C2C12 myogenic differentiation. *Muscle Nerve*, 44(3), 366-70.

Venkatachalam, K., Luo, J. & Montell, C. (2014). Evolutionarily conserved, multitasking TRP channels: lessons from worms and flies. *Handbook of Experimental Pharmacology*, 223.

Vergara, C., Latorre, R., Marrion, N. V. & Adelman, J. P. (1998). Calcium-activated potassium channels. *Current Opinions in Neurobiology*, 8(3), 321-9.

Vuckovic, D. (2018). Bioanalytical techniques in lipidomics. *Bioanalysis*, 10(5), 273-274.

Wakashima, T., Abe, K. & Kihara, A. (2014). Dual functions of the trans-2-enoyl-CoA reductase TER in the sphingosine 1-phosphate metabolic pathway and in fatty acid elongation. *Journal of Biological Chemistry*, 289(36), 24736-48.

Wallace, M. A., Della Gatta, P. A., Ahmad Mir, B., Kowalski, G. M., Kloehn, J., McConville, M. J., Russell, A. P. & Lamon, S. (2016). Overexpression of Striated Muscle Activator of Rho Signaling (STARS) Increases C2C12 Skeletal Muscle Cell Differentiation. *Frontiers in Physiology*, 7.

Wallgren-Pettersson, C. & Laing, N. G. (2000). Report of the 70th ENMC International Workshop: nemaline myopathy, 11-13 June 1999, Naarden, The Netherlands. *Neuromuscular Disorders*, 10(4-5), 299-306.

Walmsley, G. L. (2013). Pathophysiology of Canine Centronuclear Myopathy. University of London.

Walmsley, G. L., Blot, S., Venner, K., Sewry, C., Laporte, J., Blondelle, J., Barthelemy, I., Maurer, M., Blanchard-Gutton, N., Pilot-Storck, F., Tiret, L. & Piercy, R. J. (2017). Progressive Structural Defects in Canine Centronuclear Myopathy Indicate a Role for HACD1 in Maintaining Skeletal Muscle Membrane Systems. *American Journal of Pathology*, 187(2), 441-456.

Wang, B., Pelletier, J., Massaad, M. J., Herscovics, A. & Shore, G. C. (2004). The Yeast Split-Ubiquitin Membrane Protein Two-Hybrid Screen Identifies BAP31 as a Regulator of the Turnover of Endoplasmic Reticulum-Associated Protein Tyrosine Phosphatase-Like B. *Molecular and Cellular Biology*, 24(7), 2767-2778.

Wang, C., Wang, M. & Han, X. (2015). Applications of mass spectrometry for cellular lipid analysis. *Molecular BioSystems*, 11(3), 698-713.

Wang, Y., Botolin, D., Christian, B., Busik, J., Xu, J. & Jump, D. B. (2005). Tissue-specific, nutritional, and developmental regulation of rat fatty acid elongases. *Journal of Lipid Research*, 46(4), 706-15.

Wang, Y., Li, X., Duan, H., Fulton, T. R., Eu, J. P. & Meissner, G. (2009). Altered stored calcium release in skeletal myotubes deficient of triadin and junctin. *Cell Calcium*, 45(1), 29-37.

Wang, Y., Xu, L., Duan, H., Pasek, D. A., Eu, J. P. & Meissner, G. (2006). Knocking down type 2 but not type 1 calsequestrin reduces calcium sequestration and release in C2C12 skeletal muscle myotubes. *Journal of Biological Chemistry*, 281(22), 15572-81.

Watt, M. J. & Hoy, A. J. (2011). Lipid metabolism in skeletal muscle: generation of adaptive and maladaptive intracellular signals for cellular function. *American Journal of Physiology-Endocrinology and Metabolism*, 302(11), E1315-E1328.

White, R. J., Collins, J. E., Sealy, I. M., Wali, N., Dooley, C. M., Digby, Z., Stemple, D. L., Murphy, D. N., Billis, K., Hourlier, T., Fullgrabe, A., Davis, M. P., Enright, A. J. & Busch-Nentwich, E. M. (2017). A high-resolution mRNA expression time course of embryonic development in zebrafish. *Elife*, *6*.

Widén, C. & Barclay, C. J. (2006). ATP splitting by half the cross-bridges can explain the twitch energetics of mouse papillary muscle. *The Journal of physiology*, 573(Pt 1), 5-15.

Wienken, C. J., Baaske, P., Duhr, S. & Braun, D. (2011). Thermophoretic melting curves quantify the conformation and stability of RNA and DNA. *Nucleic Acids Research*, 39(8), e52-e52.

Wilson-Sanders, S. E. (2011). Invertebrate Models for Biomedical Research, Testing, and Education. *ILAR Journal*, 52(2), 126-152.

Worley, B. & Powers, R. (2013). Multivariate Analysis in Metabolomics. *Current Metabolomics*, 1(1), 92-107.

Wu, H. H., Brennan, C. & Ashworth, R. (2011). Ryanodine receptors, a family of intracellular calcium ion channels, are expressed throughout early vertebrate development. *BMC research notes*, 4(541-541.

Xia, J. & Wishart, D. S. (2011). Web-based inference of biological patterns, functions and pathways from metabolomic data using MetaboAnalyst. *Nature Protocols*, 6(743).

Yaffe, D. (1968). Retention of differentiation potentialities during prolonged cultivation of myogenic cells. *Proceedings of the National Academy of Sciences USA*, 61(2), 477-83.

Yaffe, D. & Saxel, O. R. A. (1977). Serial passaging and differentiation of myogenic cells isolated from dystrophic mouse muscle. *Nature*, 270(5639), 725-727.

Yang, K. & Han, X. (2016). Lipidomics: Techniques, Applications, and Outcomes Related to Biomedical Sciences. *Trends in Biochemical Sciences*, 41(11), 954-969.

Yazawa, T., Naganuma, T., Yamagata, M. & Kihara, A. (2013). Identification of residues important for the catalysis, structure maintenance, and substrate specificity of yeast 3-hydroxyacyl-CoA dehydratase Phs1. *FEBS Letters*, 587(6), 804-9.

Yeon, S. Y., Jo, Y. S., Choi, E. J., Kim, M. S., Yoo, N. J. & Lee, S. H. (2018). Frameshift Mutations in Repeat Sequences of ANK3, HACD4, TCP10L, TP53BP1, MFN1, LCMT2, RNMT, TRMT6, METTL8 and METTL16 Genes in Colon Cancers. *Pathology & Oncology Research*, 24(3), 617-622.

Ytterberg, S. R. (1991). Animal models of myopathy. *Current Opinions in Rheumatology*, 3(6), 934-40.

Zadravec, D., Brolinson, A., Fisher, R. M., Carneheim, C., Csikasz, R. I., Bertrand-Michel, J., Boren, J., Guillou, H., Rudling, M. & Jacobsson, A. (2010). Ablation of the very-long-chain fatty acid elongase ELOVL3 in mice leads to constrained lipid storage and resistance to diet-induced obesity. *FASEB Journal*, 24(11), 4366-77.

Zadravec, D., Tvrdik, P., Guillou, H., Haslam, R., Kobayashi, T., Napier, J. A., Capecchi, M. R. & Jacobsson, A. (2011). ELOVL2 controls the level of n-6 28:5 and 30:5 fatty acids in testis, a prerequisite for male fertility and sperm maturation in mice. *Journal of Lipid Research*, 52(2), 245-55.

Zaharieva, I. T., Thor, M. G., Oates, E. C., van Karnebeek, C., Hendson, G., Blom, E., Witting, N., Rasmussen, M., Gabbett, M. T., Ravenscroft, G., Sframeli, M., Suetterlin, K., Sarkozy, A., D'Argenzio, L., Hartley, L., Matthews, E., Pitt, M., Vissing, J., Ballegaard, M., Krarup, C., Slordahl, A., Halvorsen, H., Ye, X. C., Zhang, L. H., Lokken, N., Werlauff, U., Abdelsayed, M., Davis, M. R., Feng, L., Phadke, R., Sewry, C. A., Morgan, J. E., Laing, N. G., Vallance, H., Ruben, P., Hanna, M. G., Lewis, S., Kamsteeg, E. J., Mannikko, R. & Muntoni, F. (2016). Loss-of-function mutations in SCN4A cause severe foetal hypokinesia or 'classical' congenital myopathy. *Brain*, 139(3), 674-91.

Zammit, P. S. (2008). All muscle satellite cells are equal, but are some more equal than others? *Journal of Cell Science*, 121(18), 2975-82.

Zammit, P. S., Relaix, F., Nagata, Y., Ruiz, A. P., Collins, C. A., Partridge, T. A. & Beauchamp, J. R. (2006). Pax7 and myogenic progression in skeletal muscle satellite cells. *Journal of Cell Science*, 119(9), 1824-32.

Zanou, N., Mondin, L., Fuster, C., Seghers, F., Dufour, I., de Clippele, M., Schakman, O., Tajeddine, N., Iwata, Y., Wakabayashi, S., Voets, T., Allard, B. & Gailly, P. (2015). Osmosensation in TRPV2 dominant negative expressing skeletal muscle fibres. *Journal of Physiology*, 593(17), 3849-63.

Zanou, N., Shapovalov, G., Louis, M., Tajeddine, N., Gallo, C., Van Schoor, M., Anguish, I., Cao, M. L., Schakman, O., Dietrich, A., Lebacq, J., Ruegg, U., Roulet, E., Birnbaumer, L. & Gailly, P. (2010). Role of TRPC1 channel in skeletal muscle function. *American Journal of Physiology - Cell Physiology*, 298(1), C149-62.

Zeituni, E. M. & Farber, S. A. (2016). Studying Lipid Metabolism and Transport During Zebrafish Development. *Methods in Molecular Biology*, 1451.

Zhang, Y., Chen, H. S., Khanna, V. K., De Leon, S., Phillips, M. S., Schappert, K., Britt, B. A., Browell, A. K. & MacLennan, D. H. (1993). A mutation in the human ryanodine receptor gene associated with central core disease. *Nature Genetics*, 5(1), 46-50.

Zhou, H., Jungbluth, H., Sewry, C. A., Feng, L., Bertini, E., Bushby, K., Straub, V., Roper, H., Rose, M. R., Brockington, M., Kinali, M., Manzur, A., Robb, S., Appleton, R., Messina, S., D'Amico, A., Quinlivan, R., Swash, M., Muller, C. R., Brown, S., Treves, S. & Muntoni, F. (2007). Molecular mechanisms and phenotypic variation in RYR1-related congenital myopathies. *Brain*, 1308), 2024-36.

Zhu, S., Wang, Z., Zhang, Z., Wang, J., Li, Y., Yao, L., Mei, Q. & Zhang, W. (2014). PTPLAD2 is a tumor suppressor in esophageal squamous cell carcinogenesis. *FEBS Letters*, 588(6), 981-9.

Zivotic, I., Djuric, T., Stankovic, A., Ivancevic, I., Koncar, I., Milasinovic, D., Stankovic, G., Alavantic, D. & Zivkovic, M. (2018a). The HACD4 haplotype as a risk factor for atherosclerosis in males. *Gene*, 641.

Zivotic, I., Duric, T., Stankovic, A., Stankovic, G., Milasinovic, D., Dekleva, M., Markovic Nikolic, N., Alavantic, D. & Zivkovic, M. (2018b). HACD4 haplotype confers risk of myocardial infarction among males in the population of Serbia. *Atherosclerosis*, 275.

Appendices

Appendix 1: Alignment of zebrafish *hacd* sequences

Figure A1.1: Amino acid sequence alignment for zebrafish transcripts: *hacd1* (ENSDART00000157873), *hacd2* (ENSDART00000133998), *hacd3* (ENSDART00000006300) and *hacd4* (ENSDART00000157618) generated in CLC Workbench (Qiagen). Transmembrane region is annotated by the grey bar, the PTPL domain by a pink bar and essential amino acids (tyrosine and glutamate) have been annotated in blue. Conservation of residues indicated by pink bars along the bottom of alignment rows, with gaps within the sequence indicated with (-).

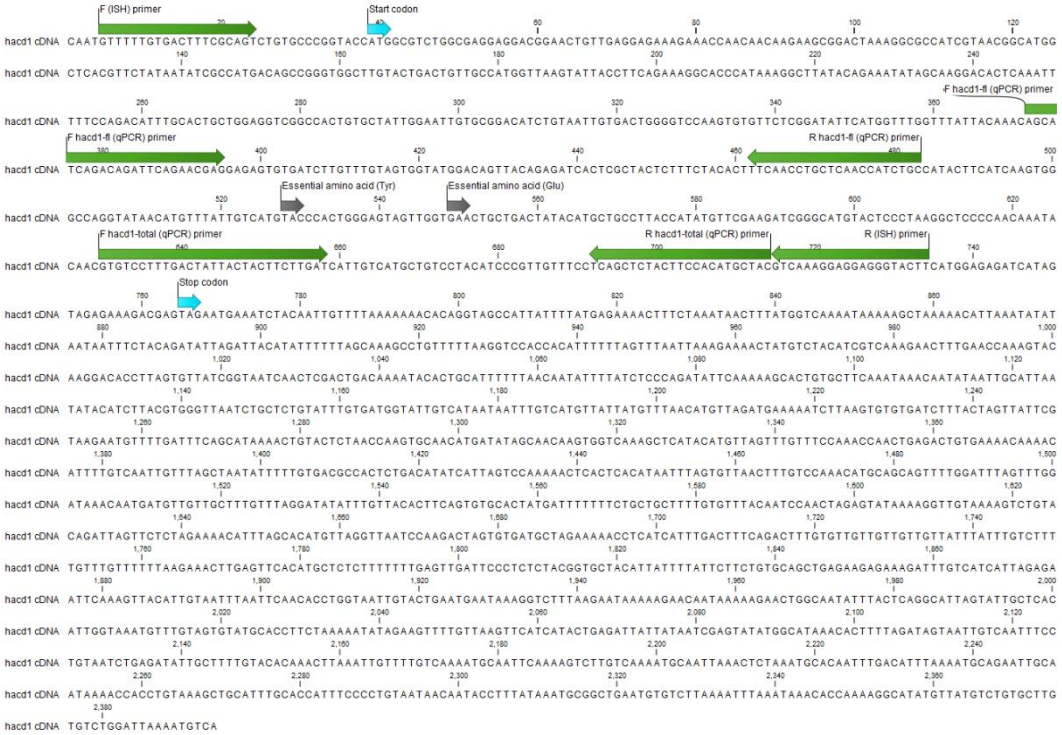

Figure A1.2: Annotated zebrafish *hacd1* sequence. Primers for both whole-mount *in situ* hybridisation and qRT-PCR (both *hacd1-total* and *hacd1-fl*) are annotated in green start and stop codon in blue and essential amino acids in grey.

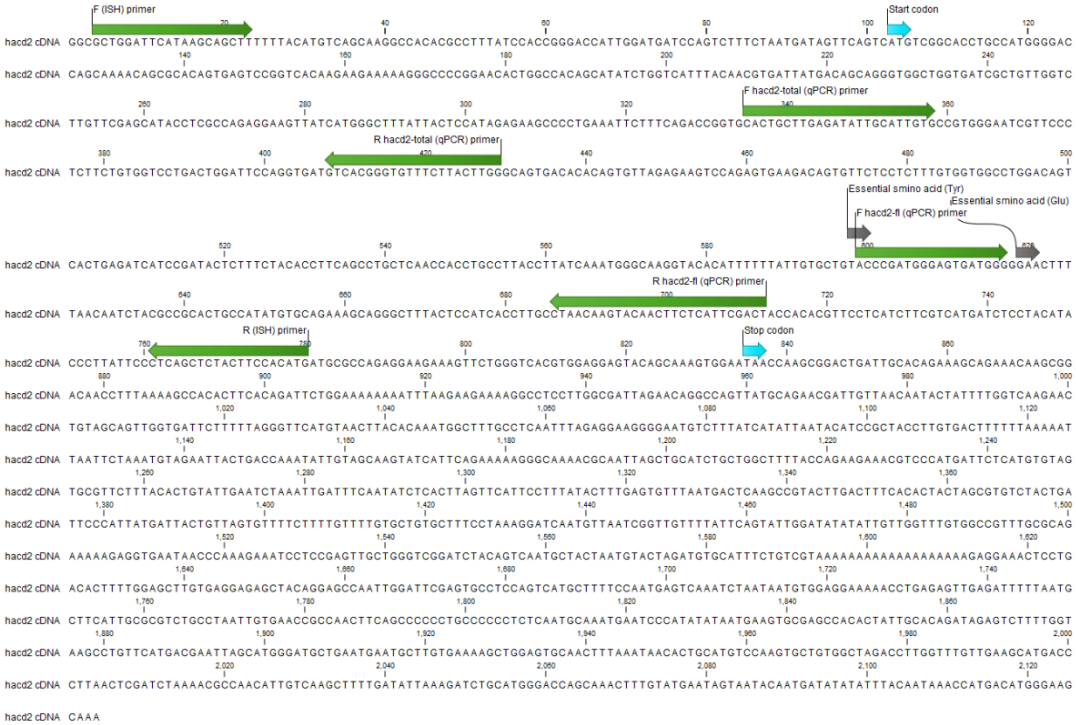

Figure A1.3: Annotated zebrafish *hacd2* sequence. Primers for both whole-mount *in situ* hybridisation and qRT-PCR (both *hacd2-total* and *hacd2-fl*) are annotated in green start and stop codon in blue and essential amino acids in grey.

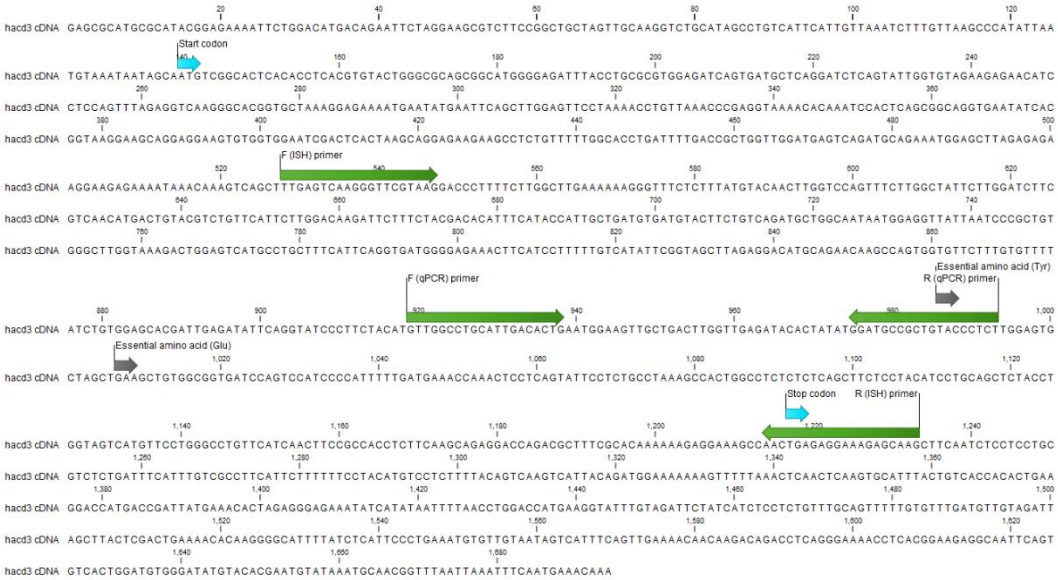

Figure A1.4: Annotated zebrafish *hacd3* sequence. Primers for both whole-mount *in situ* hybridisation and qRT-PCR are annotated in green start and stop codon in blue and essential amino acids in grey.

Figure A1.5: Annotated zebrafish *hacd4* sequence. Primers for both whole-mount *in situ* hybridisation and qRT-PCR are annotated in green start and stop codon in blue and essential amino acids in grey.

Appendix 2: Alignment of mouse (C2C12) *Hacd* sequences

Figure A2.1: Amino acid sequence alignment for murine transcripts: *Hacd1* (ENSMUST00000114753.7), *Hacd2* (ENSMUST00000061156.9), *Hacd3* (ENSMUST00000036615.6) and *Hacd4* (ENSMUST00000030221.2) generated in CLC Workbench (Qiagen). The PTPL domain is annotated by a pink bar the transmembrane region is annotated by a grey bar and essential amino acids (tyrosine and glutamate) have been annotated in blue. Conservation of residues indicated by pink bars along the bottom of alignment rows, with gaps within the sequence indicated with (-).

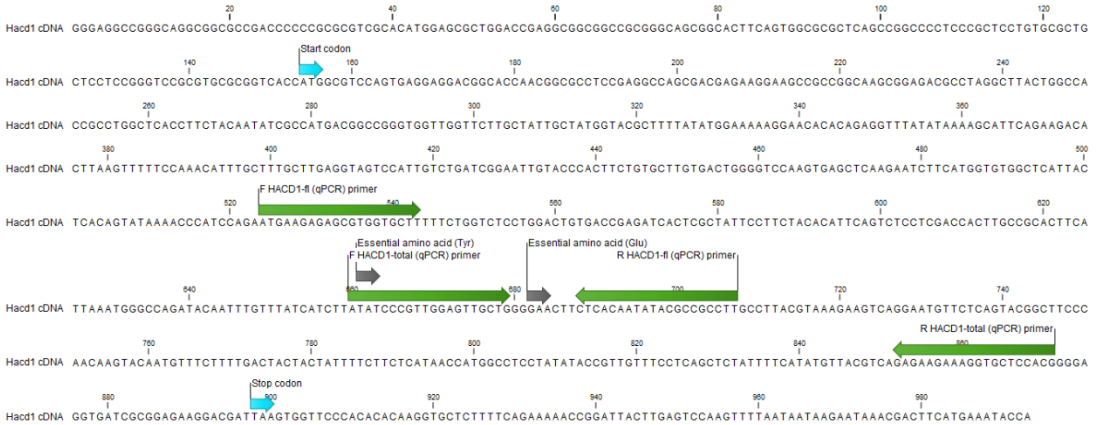

Figure A2.2: Annotated mouse *Hacd1* sequence. Primers for both whole-mount *in situ* hybridisation and qRT-PCR (both *Hacd1-total* and *Hacd1-fl*) are annotated in green start and stop codon in blue and essential amino acids in grey.

Figure A2.3: Annotated mouse *Hacd2* sequence. Primers for both whole-mount *in situ* hybridisation and qRT-PCR are annotated in green start and stop codon in blue and essential amino acids in grey.

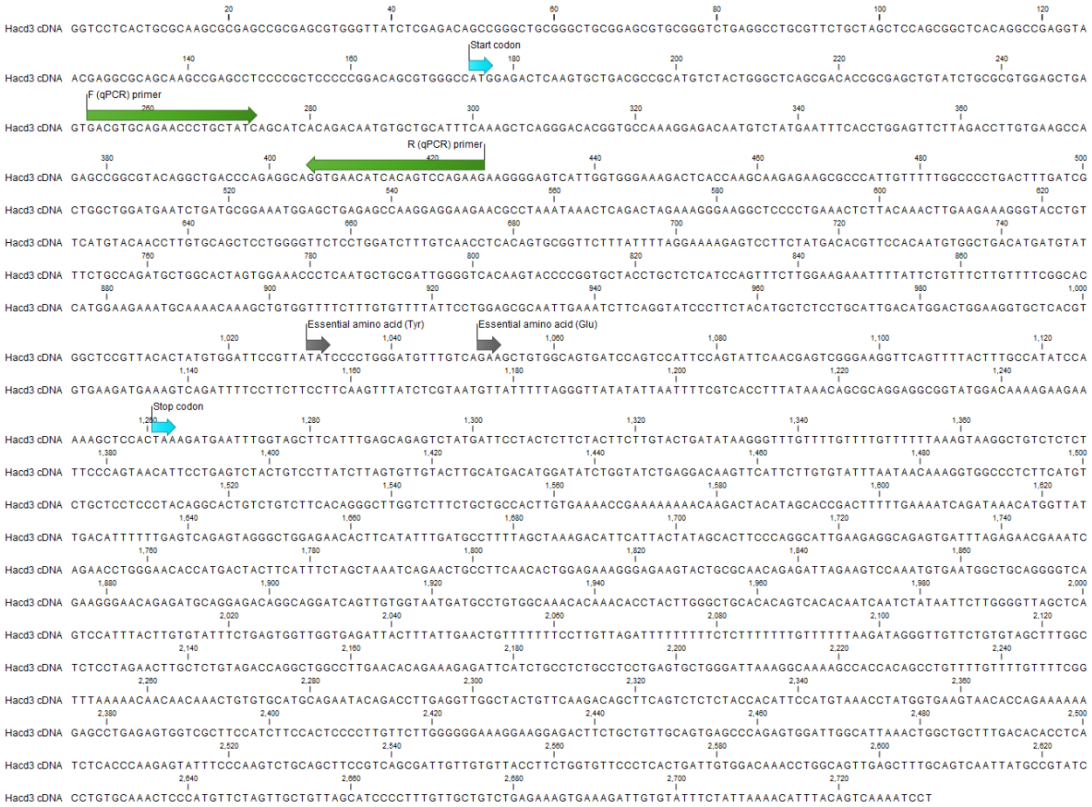

Figure A2.4: Annotated mouse *Hacd3* sequence. Primers for both whole-mount *in situ* hybridisation and qRT-PCR are annotated in green start and stop codon in blue and essential amino acids in grey.

Figure A2.5: Annotated mouse *Hacd4* sequence. Primers for both whole-mount *in situ* hybridisation and qRT-PCR are annotated in green start and stop codon in blue and essential amino acids in grey.

Appendix 3: Normalisation methods for ^{1}H-NMR lipidomics of zebrafish samples

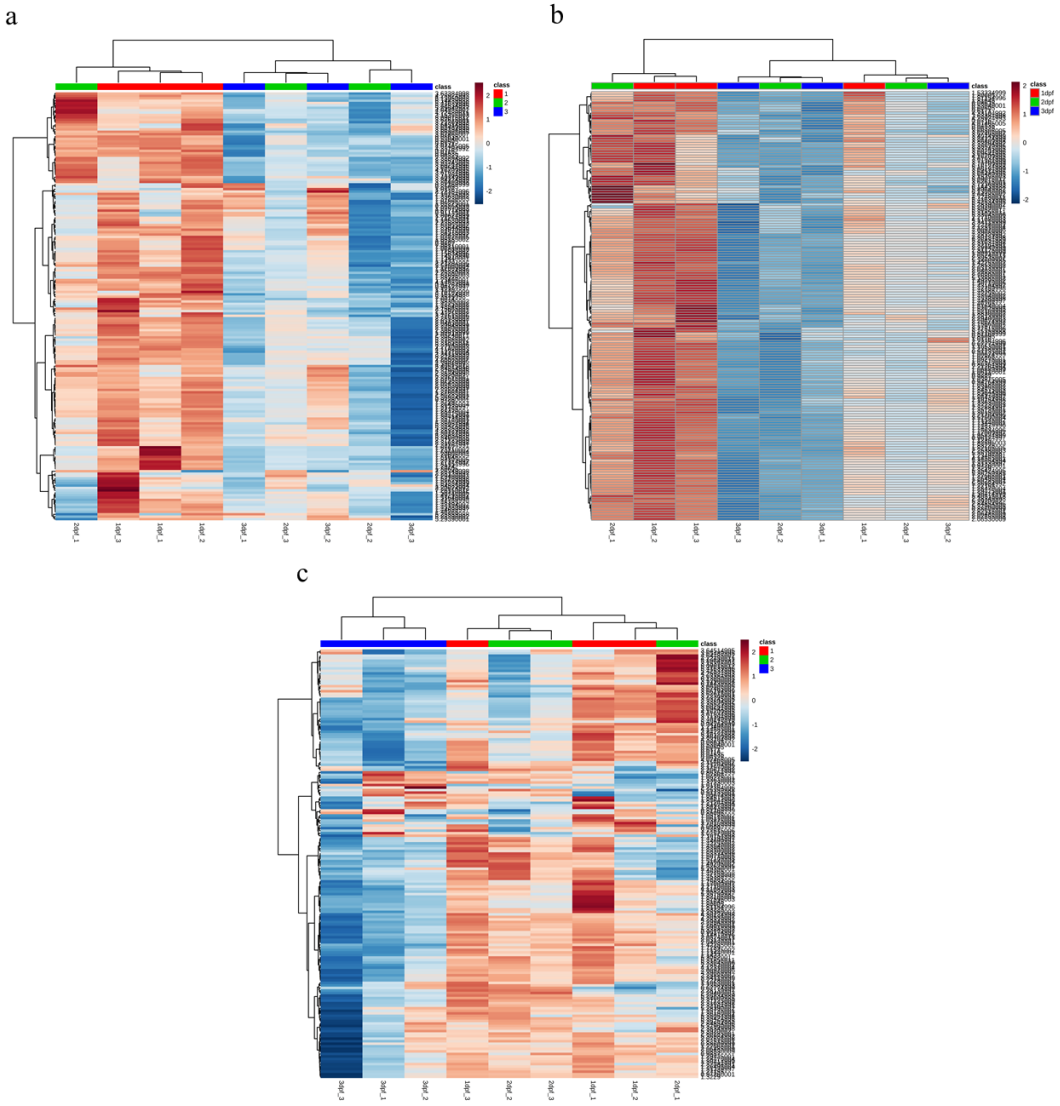

Figure A3.1: Comparison of normalisation methods for zebrafish samples using heat map analysis. (a) non-normalised heat map, (b) PQN normalised and (c) samples normalised to CH^{3}. Normalisation to CH3 was chosen in the end after examining heat maps as PQN normalisation skewed the data.